

SCHOOL OF PHYSICAL SCIENCES

Department of Applied Physics

**MICROSTRUCTURAL DESIGN AND
CHARACTERISATION OF ALUMINA/CALCIUM-
HEXALUMINATE COMPOSITES**

Dwi Asmi

**This thesis is presented as part of the requirements for the award of the
Degree of Doctor of Philosophy of Curtin University of Technology**

January 2001

DECLARATION

I hereby declare that this submission is my own work, and that to the best of my knowledge contains no material previously published or written by another person, or material which to a substantial extent has not been accepted for the award of any other degree of a university or other institute of higher learning, except where due to acknowledgment is made in the text.

Dwi Asmi

ACKNOWLEDGMENTS

I want to express my gratitude to many individuals who contributed to making this PhD thesis possible.

I would like to thank to my principal supervisor, Dr I. M. Low for his encouragement and guidance during the course of this work. I would also like to thank my associate supervisor, Professor Brian O'Connor for his encouragement, consistent support and for his expert advice on synchrotron diffraction Rietveld analysis. Thanks to Dr Brendan McGann for his assistance and efforts as thesis committee chairperson.

The financial support provided by the World Bank through Development of Undergraduate Education (DUE) Project University of Lampung, Indonesia during the course of this PhD project is greatly acknowledged.

Thanks also to Professor Deyu Li, for sharing his knowledge on diffraction science and on Rietveld analysis. Thanks to Dr Shane Kennedy of the Australian Nuclear Science and Technology Organisation (ANSTO) Neutron Scattering Group for his assistance in the design of the neutron diffraction experiments and for his invaluable discussions and advice on neutron diffraction Rietveld refinements. I also thank Dr Andrew Studer and Mr Merv Perry of ANSTO for their technical assistance. Thanks to Mr Sammy Leong of ANSTO for taking SEM and EDS images. I would like to express my gratitude to the Australian Institute of Nuclear Science and Engineering (AINSE) for funding the travel and access costs for the neutron diffraction Experiments (Grants # 98/010 & #99/030).

I would like to acknowledge the generous assistance given by the Australian National Beamline Facility, Tsukuba, Japan, and Dr James Hestor for assistance and advice on synchrotron radiation diffraction. Special thanks to Profs. H. Tsubakino and A. Yamamoto of the Himeji Institute of Technology, Japan, for providing facilities to conduct the TEM observations.

I would like to thank Mrs Carmel McManus, Mrs Tiffany Car, Mr David Prior and Mr Glen Lawson for their assistance. Thanks also go out to the Curtin

Materials Research Group for their support. Thanks to all my colleagues from University of Lampung, who supported and believed in me during this study and throughout the years.

Last but not least, I would like to thank my parents and my father- and mother-in-law. I would like to say special thanks to my husband, Ismono, and my sons, Aris and Alhusni, for their everlasting love, understanding, and support during my study.

ABSTRACT

A study was conducted to investigate a novel route to low cost processing of alumina/calcium-hexaluminate (A/CA₆) composites. The objectives of this study were to: (a) develop A/CA₆ and β -spodumene modified A/CA₆ composites using an *in-situ* reaction sintering method and functionally-graded A/CA₆ using an infiltration technique, and (b) evaluate the effects of CA₆ platelets on the ensuing physical and mechanical properties. The study has revealed that the processing procedures played an important role in the microstructural development of A/CA₆ composites. The microstructure-property relationships of these materials were found to be strongly influenced by the presence of CA₆ phase.

The A/CA₆ composites were synthesised by *in-situ* reaction sintering of alumina powder and (0, 5, 15, 30, 50 and 100 wt%) CA₆ precursor. The phase relations and development of this system were monitored using quantitative x-ray diffraction (XRD) and neutron diffraction (ND). Rietveld analysis which showed the CA₆ content to increase in proportion with the increase of CA₆ precursor added. The XRD study revealed that the CA and CA₂ phases started to develop at approximately 1000 and 1100°C and transformed to CA₆ phase at 1400°C. Similarly, the dynamic high temperature ND study showed that the corresponding calcium aluminates phases commenced to develop at 1000°C and 1200°C and then eventually transformed to CA₆ at 1400°C. The presence of the *plate-like* CA₆ grains in the system was revealed by the back-scattered SEM imaging and confirmed by the Ca x-ray map. Although the presence of CA₆ caused the reduction of hardness, the fracture toughness of A/CA₆ composites were improved when compared with alumina. It was found that the presence of CA₆ hindered the processes of sintering and densification in alumina matrix.

The use of β -spodumene had been investigated as a liquid-phase-sintering aid for the densification of A/CA₆ composites. XRD, ND, differential thermal analysis (DTA), scanning electron microscopy (SEM) and Vickers indentation were used to

characterise the effects of β -spodumene on the phase relations, densification, microstructure and mechanical properties. The results showed that the presence of β -spodumene had a profound influence on the phase relations, densification and microstructure of A/CA₆ composites. Quantitative XRD and ND Rietveld analysis showed that the addition of > 2.5 wt% β -spodumene caused the reduction of CA₆ content due to the formation of β -quartz solid solution. The reduction of porosity in the presence of β -spodumene suggests that it may be used as an effective sintering aid for improving the densification of A/CA₆ composites. However improvements in hardness and fracture toughness were not achieved probably due to the presence of large spherical pores as well as the formation of recrystallised β -spodumene and β -quartz solid solution.

A functionally-graded alumina/calcium-hexaluminate (A/CA₆) composite was successfully synthesised through infiltration of porous alumina preform with a solution containing calcium-acetate. The infiltration kinetics of liquid into porous alumina preform had also been investigated. It was found that the infiltration rate equation proposed by Washburn is most suitable for describing the effects of preform sintering temperature, viscosity and multiple infiltrations on the infiltration characteristics. The influence of applied pressure is consistent with the model proposed by Darcy, where the applied pressure enhances the infiltration rate behaviour. Key parameters for the optimum processing conditions of preforms for subsequent infiltration have also been identified.

The graded composition character of the functionally-graded A/CA₆ composites were characterised by XRD and synchrotron diffraction (SRD). Depth-profiling of compositions with XRD and SRD Rietveld refinement showed that the concentration of CA₆ decreased with depth, while that of Al₂O₃ increased with depth. Both XRD and SRD results showed that CA and CA₂ phases formed initially at 1000°C and 1300°C, respectively, but remained stable even at 1400°C, before eventually transformed to CA₆ at 1650°C. These results are consistent with those of dynamic high temperature ND data.

The graded microstructure was revealed by SEM back-scattered imaging whereby the content of CA_6 platelets was most abundant near the surface and decreased with increasing depth towards the bulk. The presence of CA_6 phase in the composite fired at $1400^{\circ}C$ was also confirmed by the transmission electron microscopy (TEM) observation in conjunction with energy dispersive spectroscopy (EDS). The hardness results of the graded material showed that the graded-region was softer than the non-graded region as a result of the presence of softer CA_6 phase in the former. However, the fracture toughness in the graded region was found to be higher than the non-graded region which might be attributed to the display of toughening processes such as crack deflection and grain bridging.

TABLES OF CONTENTS

	Page
Acknowledgments	i
Abstract	iii
Table of Contents	vi
List of Figures	xii
List of Tables	xxvi
1. INTRODUCTION	1
1.1 Research Background	1
1.2 Research Significance and Objectives	4
1.2.1 Research Significance	4
1.2.2 Research Objectives	5
1.3 Research Plan	6
1.4 Structure of Thesis	6
2. LITERATURE REVIEW	9
2.1 Introduction	9
2.2 Alumina-Based Ceramic Composites	9
2.2.1 Alumina	9
2.2.2 The CaO-Al ₂ O ₃ System	10
<i>Phase Diagram of the CaO-Al₂O₃ System</i>	12
<i>Crystal Structure of Calcium-monoaluminate – CA</i>	14
<i>Crystal structure of Calcium-dialuminate – CA₂</i>	15
<i>Crystal structure of Calcium-hexaluminate – CA₆</i>	16
<i>Formation and Properties of Calcium-hexaluminate – CA₆</i>	18

2.2.3 <i>In-situ</i> Reaction Sintering	21
2.2.4 The Al_2O_3 - CA_6 System	22
2.3 Microstructural Design of Ceramics for Improved Mechanical Reliability	27
2.4 β -Spodumene	31
2.5 Functionally-Graded Materials (FGMs)	33
2.5.1 Introduction	33
2.5.2 Fundamental Concepts of Functionally-Graded Materials (FGMs)	33
2.5.3 Fabrication Methods for producing Functionally-Graded Materials (FGMs)	36
2.5.4 Infiltration Processing of Functionally-Graded-Materials (FGMs)	38
<i>Infiltration Kinetics and Modeling</i>	39
2.5.5 Development of FGM-Based Alumina Composites at Curtin University	42
<i>Aluminium Titanate/Alumina (AT/A) System</i>	43
<i>Aluminium Titanate/Zirconia-Alumina (AT/ZA) System</i>	44
3. EXPERIMENTAL METHODS	46
3.1 Introduction	46
3.2 Processing	46
3.2.1 Powder and Liquid Precursor Preparations	46
<i>Alumina (α-Al_2O_3)</i>	47
<i>Calcium carbonate (CaCO_3) and β-spodumene ($\text{Li}_2\text{O} \cdot \text{Al}_2\text{O}_3 \cdot 4\text{SiO}_2$)</i>	48
<i>Calcium-hexaluminate (CA_6) Precursor</i>	48
<i>Liquid Precursor (Calcium acetate)</i>	48
3.2.2 Preparation of Ceramic Composites	49
<i>In-situ Reaction-Sintering of A/CA_6 Composites</i>	49
<i>β-spodumene modified A/CA_6 Composites</i>	52
<i>Functionally graded Al_2O_3/CA_6 Composites</i>	54

<i>Infiltration Kinetics</i>	54
3.3 Heat-treatment Schedules and Densification of A/CA ₆ Composites	56
3.4 Characterisation	56
3.4.1 Particle Size Analysis	56
3.4.2 Analysis of Phase Composition and Development	57
<i>X-ray Diffraction (XRD) Analysis</i>	57
<i>Synchrotron Radiation Diffraction (SRD) Analysis</i>	57
<i>Neutron Diffraction (ND) Analysis</i>	58
<i>Qualitative Phase Analysis</i>	59
<i>Rietveld Phase Composition Analysis</i>	60
3.4.3 Microstructural Examination	67
<i>Scanning Electron Microscopy (SEM)</i>	67
<i>Transmission Electron Microscopy (TEM)</i>	67
3.5 Properties Evaluation	68
3.5.1 Physical and Thermal Properties	68
<i>Shrinkage, Porosity, and Density</i>	68
<i>Thermal Expansion and Shrinkage Behaviour</i>	69
<i>Young's Modulus</i>	69
<i>Viscosity and Surface Tension</i>	69
<i>Differential Thermal and Gravimetric Analysis (DTA and TG)</i>	70
3.5.2 Mechanical Properties	71
<i>Hardness and Fracture Toughness</i>	71
 4. SYNTHESIS OF <i>IN-SITU</i> REACTION SINTERED ALUMINA/ CALCIUM-HEXALUMINATE (A/CA ₆) COMPOSITES	 73
4.1 Introduction	73
4.2 Results and Discussion	74
4.2.1 Raw Material Evaluation	74
4.2.2 Analysis of Phase Composition and Development	79

<i>X-ray Diffraction (XRD) Analysis</i>	79
<i>Neutron Diffraction (ND) Analysis</i>	85
<i>Rietveld Phase Composition Analysis</i>	91
4.2.3 Microstructural Analysis	106
4.2.4 Physical and Thermal Properties	110
<i>Shrinkage, Porosity, and Density</i>	110
<i>Thermal Expansion and Shrinkage Behaviour</i>	113
<i>Young's Moduli</i>	114
<i>Differential Thermal and Gravimetric Analysis (DTA and TG)</i>	116
4.2.5 Mechanical Properties	119
<i>Vickers Hardness</i>	119
<i>Fracture Toughness</i>	123
4.3 Summary	126
 5. SYNTHESIS OF β-SPODUMENE MODIFIED ALUMINA/ CALCIUM-HEXALUMINATE (A/CA₆) COMPOSITES	 128
5.1 Introduction	128
5.2 Results and Discussion	129
5.2.1 Raw Material Evaluation	129
5.2.2 Phase Composition Analysis	134
<i>X-ray Diffraction (XRD) Analysis</i>	134
<i>Neutron Diffraction (ND) Analysis</i>	136
<i>Rietveld Phase Composition Analysis</i>	137
5.2.3 Microstructural Analysis	144
Scanning Electron Microscopy (SEM)	144
5.2.4 Physical and Thermal Properties	150
<i>Shrinkage, Porosity, and Density</i>	150
<i>Thermal Expansion and Shrinkage Behaviour</i>	152
<i>Differential Thermal and Gravimetric Analysis (DTA and TG)</i>	154

5.2.5 Mechanical Properties	156
<i>Vickers Hardness</i>	156
<i>Fracture Toughness</i>	157
5.3 Summary	158
 6. FUNCTIONALLY-GRADED ALUMINA/CALCIUM- HEXALUMINATE (A/CA₆) COMPOSITES	 159
6.1 Introduction	159
6.2 Results and Discussion	160
6.2.1 Infiltration Kinetics	160
6.2.2 Analysis of Phase Composition and Development	168
<i>X-ray Diffraction (XRD) Analysis</i>	168
<i>Synchrotron Radiation Diffraction (SRD) Analysis</i>	184
<i>High-Temperature Neutron Diffraction (HTND) Analysis</i>	193
6.2.3 Microstructural Analysis	199
<i>Scanning Electron Microscopy (SEM)</i>	199
<i>Transmission Electron Microscopy (TEM)</i>	200
6.2.4 Physical and Thermal Properties	202
<i>Weight Gain, Density, Porosity and Shrinkage</i>	202
<i>Thermal Expansion and Shrinkage Behaviour</i>	204
<i>Differential Thermal and Gravimetric Analysis (DTA and TG)</i>	206
6.2.5 Mechanical Properties	210
<i>Vickers Hardness</i>	210
<i>Fracture Toughness</i>	213
6.3 Summary	216

7	CONCLUSIONS AND FUTURE WORK	219
7.1	Conclusions	219
7.1.1	Synthesis and Properties of <i>In-situ</i> Reaction Sintered Alumina/Calcium-Hexaluminate (A/CA ₆) Composites	219
7.1.2	Synthesis and Properties of β-spodumene modified Alumina/ Calcium-Hexaluminate (A/CA ₆) Composites	220
7.1.3	Synthesis and Properties of Functionally-Graded Alumina/ Calcium-Hexaluminate (A/CA ₆) Composites	221
7.2	Future Work	223
	REFERENCES	225
	LIST OF PUBLICATIONS ARISING FROM THESIS	246
	APPENDICES	249
	Appendix A - Crystallographic Data	250
	Appendix B - Rietveld Refinement Patterns	258

LIST OF FIGURES

Figure	Title	Page
2.1.	Crystal structure of α -Al ₂ O ₃ (ICSD # 73725) projected on the (a) (001) and (b) (210) planes. The ion sizes are drawn in proportion to the ionic radii, i.e. 0.55 Å for Al ³⁺ and 1.35 Å for O ²⁻ . Plotted using the software package 'PowderCell' (1999).	11
2.2.	Phase diagram for the CaO-Al ₂ O ₃ system. After Nurse, Welch and Majumdar (1965).	13
2.3.	Crystal structure of CA (ICSD # 260) projected on the (010) plane. The ion sizes are drawn in proportion to the ionic radii, i.e. 1.05 Å for Ca ²⁺ , 0.55 Å for Al ³⁺ and 1.35 Å for O ²⁻ .	14
2.4.	Crystal structure of CA ₂ (ICSD # 16191) projected on the (001) plane. The ion sizes are drawn in proportion to the ionic radii, i.e. 1.05 Å for Ca ²⁺ , 0.55 Å for Al ³⁺ and 1.35 Å for O ²⁻ .	15
2.5.	Crystal structure of CA ₆ (ICSD # 34394) projected on the (a) (001) and (b) (210) planes. The ion sizes are drawn in proportion to the ionic radii, i.e. 1.05 Å for Ca ²⁺ , 0.55 Å for Al ³⁺ and 1.35 Å for O ²⁻ .	17
2.6.	Flexural strength for the hot-pressed CA ₆ ceramics as a function of temperature. Legends: HP _⊥ = surface perpendicular to the hot-pressing direction, HP _∥ = surface parallel to the hot-pressing direction. After Nagaoka, Kanzaki, and Yamaoka (1990).	20
2.7.	Variation of room-temperature fracture toughness for the CA ₆ ceramics, sintered at 1500 – 1650 °C. Error bars indicate two estimated standard deviations (2σ). Redrawn after Criado and De Aza (1991).	20

2.8.	Schematic diagram for the production of ceramic composite, consisting of a matrix (C) and inclusions (D), through <i>in-situ</i> reaction sintering of a compacted mixture of two powders (A and B). After Rahaman (1995).	21
2.9.	Schematic diagram for the reaction mechanism of the Al_2O_3 and CA to form CA_6 : (a) Solid-state reaction, and (b) Solution-precipitation. After An and Soni (1990).	24
2.10.	Hardness of Al_2O_3 - CA_6 composite as a function of CA_6 content (vol%). Error bars indicate two estimated standard deviations (2σ). Redrawn after Criado, Pena and Cabalero (1988).	25
2.11.	Fracture toughness of Al_2O_3 - CA_6 composite as a function of CA_6 content (vol%). Error bars indicate two estimated standard deviations (2σ). Redrawn after Criado, Pena and Cabalero (1988).	25
2.12.	Flexural strength of Al_2O_3 - CA_6 composite as a function of CA_6 content (vol%). Error bars indicate two estimated standard deviations (2σ). Redrawn after Criado, Pena and Cabalero (1988).	26
2.13.	Plots of strength as a function of indentation load for (○) equiaxed and (●) platelet composites. Shaded boxes at the left represent strength of unindented specimens and specimens where failure did not initiate at the indent. After An and Chan (1996).	27
2.14.	Comparison of strength-crack size and fracture toughness-crack size relationships for materials exhibiting non-R-curve and R-curve behaviour. After Harmer, Chan and Miller (1992).	29
2.15.	Crystal structure of β -spodumene (ICSD # 14235) projected on the (001) plane. The ion sizes are drawn in proportion to the ionic radii, i.e. 0.4 Å for Si^{4+} , 0.55 Å for Al^{3+} , 1.35 Å for O^{2-} , and 0.7 Å for Li^+ .	32
2.16.	Conceptual diagram of functionally-graded materials for the relaxation of thermal stress. After Koizumi and Niino (1995).	35

2.17.	Comparison of (a) structure, (b) composition, and (c) properties of functionally graded materials and uniform bilayer materials. After Choy (1996).	35
2.18.	Approach for a functionally-graded material (FGM) development. Redrawn after Koizumi and Watanabe (1997).	36
2.19.	Vickers hardness of AT/A as a function distance at a load of 30 N. After Low (1998).	44
2.20.	Energy dispersive x-ray microanalysis of Ti K α , Al K α , and Zr K α as a function of depth for functionally graded AT/ZA composites. Error bars indicate 2 x estimated standard deviations. After Pratapa (1997).	45
3.1.	Processing of <i>in-situ</i> reaction sintered A/CA ₆ composites.	51
3.2.	Processing of β -spodumene modified A/CA ₆ composites.	53
3.3.	Liquid infiltration processing of functionally-graded A/CA ₆ composites.	55
3.4.	Schematic diagram of the crack due to Vickers indentation.	71
4.1.	Particle size distributions for the as-received Al ₂ O ₃ and CaCO ₃ , and processed CaCO ₃ powders.	76
4.2.	Particle size distributions for the processed CA5, CA15, CA30, CA50, and CA ₆ precursor powders.	78
4.3.	X-ray powder diffraction pattern of the as-received Al ₂ O ₃ powder using CuK α radiation. The peaks are labeled A for α -Al ₂ O ₃ and the associated numbers are the PDF file intensity.	78
4.4.	X-ray powder diffraction pattern of the as-received CaCO ₃ powder using CuK α radiation. The peaks are labeled \blacktriangledown for CaCO ₃ and the associated numbers are the PDF file intensity. The most intense CaCO ₃ line (\blacktriangledown 100) has a count rate of 14000 cps.	78

4.5.	Room-temperature x-ray diffraction (XRD) patterns for CA0, CA5, C15, CA30, CA50, and CA100 samples.	80
4.6.	Expanded views of the XRD patterns in Figure 4.5 for CA0, CA5, and C15 in (b) and CA30, CA50, and CA100 in (a). Legends: A = α -Al ₂ O ₃ and x = CA ₆ .	81
4.7.	Room-temperature x-ray diffraction (XRD) patterns for CA100, fired at 1000 - 1600 °C for 2h.	83
4.8.	Expanded views of the XRD patterns in Figure 4.7 for CA100 from 1000 to 1200 °C in (b) and 1300 to 1400 °C in (a). Legends A = α -Al ₂ O ₃ , o = CaO, ▲ = CA, ● = CA ₂ .	84
4.8.	(Continued) Expanded views of the XRD patterns in Figure 4.7 for CA100 from 1450 to 1600 °C in (c). Legends A = α -Al ₂ O ₃ , ● = CA ₂ , x = CA ₆ .	85
4.9.	Room-temperature neutron diffraction (ND) patterns for CA0, CA5, C15, CA30, CA50 and CA100 samples.	87
4.10.	Expanded views of the ND patterns in Figure 4.9 for CA0, CA5, and C15 in (b), and CA30, CA50, and CA100 in (a). Legends: A = α -Al ₂ O ₃ and x = CA ₆ .	88
4.11.	High-temperature neutron diffraction (HTND) patterns for CA100 sample from 1000 to 1600 °C.	89
4.12.	Expanded views of the HTND patterns in Figure 4.11 for CA100 from 1000 to 1200 °C in (b) and 1300 to 1400 °C in (a). Legends A = α -Al ₂ O ₃ , o = CaO, ▲ = CA and ● = CA ₂ .	90
4.12.	(Continued) Expanded views of the HTND patterns in Figure 4.11 for CA100 from 1450 to 1600 °C in (c). Legends A = α -Al ₂ O ₃ , ● = CA ₂ , x = CA ₆ .	91
4.13.	XRD Rietveld difference plots for A/CA ₆ composites: (a) CA15 and (b) CA30. The observed data are shown by a (+) sign, and the calculated data by a solid line. Vertical line represents the positions	

- of diffraction lines for α -Al₂O₃ and CA₆. The green line below the vertical line is the difference profile. 93
- 4.14. ND Rietveld difference plots for A/CA₆ composites: (a) CA15 and (b) CA30. The observed data are shown by a (+) sign, and the calculated data by a solid line. Vertical line represents the positions of diffraction lines for α -Al₂O₃, and CA₆. The green line below the vertical line is the difference profile. 94
- 4.15. Relationship between the CA₆ composition (wt%) derived from Rietveld refinement with x-ray diffraction (XRD) patterns versus the CA₆ (wt%) as-weighed in A/CA₆ composite. Error bars indicate two estimated standard deviations (2 σ). 97
- 4.16. Relationship between the CA₆ composition (wt%) derived from Rietveld refinement with neutron diffraction (ND) patterns versus the CA₆ (wt%) as-weighed in A/CA₆ composite. Error bars indicate two estimated standard deviations (2 σ). 97
- 4.17. XRD Rietveld difference plots for CA100 sample fired at (a) 1000 °C and (b) 1350 °C. The observed data are shown by a (+) sign, and the calculated data by a solid line. Vertical line represents the positions of diffraction lines for α -Al₂O₃, CA and CaO in (a) and α -Al₂O₃ and CA₂ in (b), respectively. The green line below the vertical lines is the difference profile. 100
- 4.18. HTND Rietveld difference plots for CA100 sample fired at (a) 1000 °C and (b) 1350 °C. The observed data are shown by a (+) sign, and the calculated data by a solid line. Vertical line represents the positions of diffraction lines for α -Al₂O₃, CA and CaO in (a), and α -Al₂O₃ and CA₂ in (b). The green line below the vertical lines is the difference profile. 101

4.19.	Variation in the Rietveld analysis values for the relative phase composition (wt%) of the CA100 sample obtained from XRD data in (a) and HTND in (b) as a function of temperature. Error bars are too small to include.	105
4.20.	SEM micrograph for CA5 sample. Polished surface was thermally etched at 1350 °C for 30 minutes. Back-scattered image in (a) and Ca x-ray map image in (b). (Inset: image of an area showing the presence of abnormal alumina grain growth in the A/CA ₆ composite).	107
4.21.	SEM micrograph for CA30 sample. Polished surface was thermally etched at 1350 °C for 30 minutes. Back-scattered image in (a) and Ca x-ray map image in (b).	108
4.22.	Al x-ray map images for CA5 in (a) and CA30 in (b). Polished surface was thermally etched at 1350 °C for 30 minutes.	109
4.23.	Shrinkage as a function of CA ₆ content for CA0, CA5, CA15, CA30, and CA100 samples. Error bars indicate two estimated standard deviations (2σ).	110
4.24.	Porosity as a function of CA ₆ content for CA0, CA5, CA15, CA30, and CA100 samples. Error bars indicate two estimated standard deviations (2σ).	111
4.25.	Density as a function of CA ₆ content for CA0, CA5, CA15, CA30, and CA100 samples. Error bars indicate two estimated standard deviations (2σ).	112
4.26.	Thermal expansion and shrinkage behaviour for the α-Al ₂ O ₃ (CA0) and A/CA ₆ (CA30), between 20 - 1500 °C. T _{dens} indicates the temperature at which densification commences and S _{max} indicates the maximum shrinkage.	114

4.27.	Young's modulus as a function of CA ₆ content for the compositions CA0, CA5, CA15, CA30, CA50, and CA100. Error bars indicate two estimated standard deviations (2σ).	115
4.28.	Thermal analysis for the CA100 sample from 20 to 1500 °C: (a) DTA and (b) TG.	117
4.29.	Thermal analysis for the as-received CaCO ₃ powder from 20 - 1500 °C: (a) DTA and (b) TG.	118
4.30.	Variation of Vickers hardness as a function of CA ₆ content for an applied load of 98 N. Error bars indicate two estimated standard deviations (2σ).	120
4.31.	Variation of Vickers hardness versus applied load for CA0, CA5, and CA15 samples. Error bars indicate two estimated standard deviations (2σ).	120
4.32.	Variation of indentation size as a function of the applied load for the CA0, CA5, and CA15 samples. The solid line indicates the best fit satisfying Equation 4.8. Error bars (2σ) have only been shown for one of the data sets to aid clarity.	123
4.33.	Variation of the fracture toughness as a function of CA ₆ content for an applied load of 98 N. Error bars indicate two estimated standard deviations (2σ).	124
4.34.	Variation of the fracture toughness as function of load for the CA0, CA5, and CA15 samples. Error bars indicate two estimated standard deviations (2σ).	125
5.1.	Particle size distributions for the as-received and processed β-spodumene powders.	130
5.2.	Particle size distributions for the milled CAS0, CAS2.5, CAS10 and CAS15 powders.	131

- 5.3a. Measured x-ray powder diffraction patterns for the as-received β -spodumene powders using CuK α radiation. The peaks are labelled s (β -spodumene). The associated number is the PDF file intensity. 133
- 5.3b. Quality of the Rietveld pattern-fitting results for the as-received β -spodumene. The observed data are shown by a (+) sign and the calculated data by a solid line. Vertical line represents the positions of diffraction lines for $\text{Li}_2\text{O} \cdot \text{Al}_2\text{O}_3 \cdot 4\text{SiO}_2$. The green line below the vertical lines is the difference plot. 133
- 5.4. Room-temperature x-ray diffraction (XRD) patterns for CAS0, CAS2.5, CAS10 and CAS15 samples. Legends A = α - Al_2O_3 , x = CA_6 , s = β -spodumene and q = β -quartz solid solution. 135
- 5.5. Room-temperature neutron diffraction (ND) patterns for CAS0, CAS2.5, CAS10 and CAS15 samples. Legends A = α - Al_2O_3 , x = CA_6 , s = β -spodumene and q = β -quartz solid solution. 136
- 5.6. XRD Rietveld difference plots for β -spodumene modified A/ CA_6 composite: (a) CAS0 and (b) CAS10. The observed data are shown by a (+) sign, and the calculated data by a solid line. Vertical line represents the positions of diffraction lines for α - Al_2O_3 and CA_6 in (a) and α - Al_2O_3 , β -quartz, β -spodumene and CA_6 in (b). The green line below the vertical lines is the difference plot. 139
- 5.7. ND Rietveld difference plots for β -spodumene modified A/ CA_6 composite: (a) CAS0 and (b) CAS10. The observed data are shown by a (+) sign, and the calculated data by a solid line. Vertical line represents the positions of diffraction lines for α - Al_2O_3 and CA_6 in (a) and α - Al_2O_3 , β -quartz, β -spodumene and CA_6 in (b). The green line below the vertical lines is the difference profile. 140
- 5.8. Variations of phase composition (wt%) of α - Al_2O_3 and CA_6 in (a) and β -quartz and β -spodumene in (b) obtained from XRD and ND data as a function of β -spodumene content (wt%). 143

- 5.9. SEM micrograph for the CAS0 sample. Polished surface was thermally etched at 1350 °C for 30 minutes. (a) Back-scattered electron image. Legends: A = alumina, CA₆ = calcium hexaluminate and P = porosity. 145
- 5.9. (Continued) SEM micrograph for the CAS0 sample. Polished surface was thermally etched at 1350 °C for 30 minutes. (b) Ca x-ray image and (c) Al x-ray image. 146
- 5.10. SEM micrograph for the CAS2.5 sample. Polished surface was thermally etched at 1350 °C for 30 minutes. (a) Backscattered electron image and (b) Ca x-ray image. Legends: A = alumina, CA₆ = calcium hexaluminate and P = porosity. 147
- 5.10. (Continued) SEM micrograph for the CAS2.5 sample. Polished surface was thermally etched at 1350 °C for 30 minutes. (c) Al x-ray image. 148
- 5.11. SEM micrograph for the CAS2.5 sample. Polished surface was thermally etched at 1350 °C for 30 minutes. (a) Backscattered electron image and (b) Al x-ray image. Legends: A = alumina and P = porosity. 149
- 5.12. Shrinkage for compositions CAS0, CAS2.5, CAS10 and CAS15 samples. Error bars indicate two estimated standard deviations (2σ). 150
- 5.13. Porosity for compositions CAS0, CAS2.5, CAS10, and CAS15 samples. Error bars indicate two estimated standard deviations (2σ). 151
- 5.14. Density for compositions CAS0, CAS2.5, CAS10 and CAS15 samples. Error bars indicate two estimated standard deviations (2σ). 152
- 5.15. Thermal expansion and shrinkage behaviour for CAS2.5 and CAS15 samples. T_{dens} indicates the temperature at which

densification commences and S_{\max} indicates the maximum shrinkage.	153
5.16. Thermal analysis for the CAS2.5 and CAS15 samples between 20 and 1500 °C: (a) DTA and (b) TG.	155
5.17. Variation of hardness as a function of β -spodumene content for an applied load of 98 N. Error bars indicate two estimated standard deviations (2σ).	156
5.18. Variation of fracture toughness as a function of β -spodumene content for an applied load of 98 N. Error bars indicate two estimated standard deviations (2σ).	157
6.1. Variations of apparent porosity for the alumina preforms as a function of temperature. Error bars indicate two estimated standard deviations (2σ).	160
6.2. Variations of bulk density for the alumina preforms as a function of temperature. Error bars indicate two estimated standard deviations (2σ).	161
6.3. Square height (h^2) as a function of infiltration time (t) for the infiltration of water into alumina preform.	164
6.4. Square height (h^2) as a function of infiltration time (t) for the infiltration of water and calcium acetate into alumina preform.	165
6.5. Square height (h^2) as a function of infiltration time (t) for the infiltration of water into alumina preform under vacuum and non-vacuum.	166
6.6. Square height (h^2) as a function of infiltration time (t) for the first and second infiltration of calcium acetate into alumina preform.	167
6.7. Room-temperature XRD patterns for the alumina control sample and for the functionally-graded A/CA ₆ composites obtained by the <i>gradual polishing</i> method.	170

- 6.8. Expanded views of the XRD patterns in Figure 6.7 for alumina and functionally-graded A/CA₆ composites obtained by the gradual polishing method at depths of 0 – 0.2 mm in (b) and 0.4 – 0.8 mm in (a). Legends A = α -Al₂O₃ and x = CA₆. 171
- 6.9. Room-temperature XRD patterns for the functionally-graded A/CA₆ composites obtained by the slicing method at various depths (Layers 1 – 4). 172
- 6.10. Room-temperature XRD patterns for the functionally-graded A/CA₆ composites heat-treated at various temperatures as obtained by slicing method. 173
- 6.11. Expanded views of the XRD patterns in Figure 6.10 for the functionally-graded A/CA₆ composites heat-treated at 1000 – 1300 °C in (b) and 1350 – 1650 °C in (a). Legends A = α -Al₂O₃, \blacktriangle = CA, \bullet = CA₂, and x = CA₆. 174
- 6.12. XRD Rietveld difference plots for the alumina control sample. The observed data are shown by a (+) sign, and the calculated data by the solid line. Vertical lines represent the positions of diffraction lines for α -Al₂O₃. The green line below the vertical line is the difference profile. 175
- 6.13. XRD Rietveld difference plots for the functionally-graded A/CA₆ composite obtained by gradual polishing at the depth of 0.5 mm in (a) and slicing method at layer 2 (2 – 4 mm) in (b). The observed data are shown by a (+) sign, and the calculated data by the solid line. Vertical line represents the positions of diffraction lines for α -Al₂O₃ and CA₆. The green line below the vertical line is the difference profile. 176
- 6.14. XRD Rietveld difference plots for the functionally-graded A/CA₆ composite at 1000 °C in (a) and 1400 in (b). The observed data are shown by a (+) sign, and the calculated data by the solid line.

- Vertical line represents the positions of diffraction lines for α - Al_2O_3 and CA in (a) and α - Al_2O_3 , CA_2 , CA_6 and CA in (b). The green line between the vertical line is the difference profile. 177
- 6.15. Variations of weight concentrations (wt %) for α - Al_2O_3 and CA_6 in functionally graded A/ CA_6 composites obtained by the gradual polishing method in (a) and the slicing method in (b). Error bars indicate two estimated standard deviations (2σ). 181
- 6.16. Variation of weight concentrations (wt%) from Rietveld refinement with XRD data for the functionally graded A/ CA_6 composites as a function of temperature. Error bars too small to include. 183
- 6.17. SRD patterns for the functionally graded A/ CA_6 composites for layers 1 – 4 (a) imaging plate 1, $2\theta = 10 - 45^\circ$ and (b) imaging plate 2, $2\theta = 50 - 80^\circ$. The graded composition samples were obtained by *slicing method*. Legends A = α - Al_2O_3 , x = CA_6 , and u = unknown. 185
- 6.18. SRD Rietveld difference plots for layer 4 of the functionally-graded A/ CA_6 composites: (a) imaging plate 1 and (b) imaging plate 2. The observed data are shown by a (+) sign, and the calculated data by the solid line. Vertical lines represent the positions of diffraction lines of α - Al_2O_3 and CA_6 . The green line below the vertical line is the difference profile. 186
- 6.18. (Continued) SRD Rietveld difference plots for layer 4 of the functionally-graded A/ CA_6 composites: (c) imaging plate 3 and (d) imaging plate 4. The observed data are shown by a (+) sign, and the calculated data by the solid line. Vertical lines represent the positions of diffraction lines of α - Al_2O_3 and CA_6 . The green line below the vertical line is the difference profile. 187

- 6.19. Variation of weight concentrations (wt%) for the α -Al₂O₃ and CA₆ phases in the functionally-graded A/CA₆ composites for layers 1 – 4 obtained by SRD data. Error bars too small to include. 190
- 6.20. SRD patterns for the functionally-graded A/CA₆ composites at 1000 – 1300 °C in (b) and 1350 – 1650 °C in (a). Legends A = α -Al₂O₃, ▲ = CA, ● = CA₂, x = CA₆ and u = unknown. 192
- 6.21. HTND patterns for the functionally-graded A/CA₆ composites heat-treated at various temperatures. 194
- 6.22. Expanded views of the HTND views patterns for the functionally-graded A/CA₆ composites at RT, 1050, 1100 and 1200 °C in (b) and at 1300, 1350 and 1400 °C in (a). Legends A = α -Al₂O₃, ▲ = CA, ● = CA₂ and x = CA₆. 195
- 6.23. HTND Rietveld difference plots for the functionally-graded A/CA₆ composite at 1050 °C in (a) and 1400 °C in (b). The observed data are shown by a (+) sign, and the calculated data by the solid line. Vertical line represents the positions of diffraction lines for α -Al₂O₃ and CA in (a) and α -Al₂O₃, CA₂ and CA₆ in (b). The green line between the vertical line is the difference profile. 196
- 6.24. Variation of weight concentrations (wt%) from Rietveld refinement with HTND data for the functionally-graded A/CA₆ composites as a function of temperature. Error bars too small to include. 198
- 6.25. Typical microstructure of functionally-graded A/CA₆ composite as viewed in the SEM. The lighter grains are CA₆. 200
- 6.26. TEM micrograph of CA₆ in functionally-graded A/CA₆ composite calcined at 1400 °C for 0.5h as revealed by (a) bright field imaging, (b) SAD and (c) the corresponding EDS chart. 201
- 6.27. Thermal expansion and shrinkage behaviour for the functionally graded A/CA₆ composites and alumina for the temperature range

20-1500°C. T_{dens} indicates the temperature at which densification commences and S_{max} indicates the maximum shrinkage.	205
6.28. Thermal analysis for the calcium acetate from 20 to 1000 °C: (a) DTA and (b) TG.	208
6.29. Thermal analysis for the functionally-graded A/CA ₆ composites from 20 to 1000 °C: (a) DTA and (b) TG.	209
6.30. Variation of Vickers hardness as a function of distance for the FGM sample at applied load of 98 N. Shaded box at the left represents the average Vickers hardness for the control sample. Error bars indicate two estimated standard deviations (2σ).	211
6.31. Variation of Vickers hardness as a function of applied load for the FGM at (0 – 5 mm) and (12 – 17 mm) distances and control samples. Error bars indicate two estimated standard deviations (2σ).	212
6.32. Variation of fracture toughness as a function of distance for the FGM sample for an applied load of 98 N. Shaded box at the left represents the average fracture toughness for the control sample. Error bars indicate two estimated standard deviations (2σ).	214
6.33. Back-scattered SEM micrographs of Vickers indentation for the functionally graded A/CA ₆ composites showing crack deflection (labelled as ‘D’) and grain-bridging (labelled as ‘G’).	215

LIST OF TABLES

Table	Title	Page
2.1.	Fabrication methods and examples of functionally graded materials. After Hirai (1996).	37
3.1.	Chemical compositions (wt %) of starting raw materials.	47
3.2.	Formulations of various <i>in-situ</i> reaction sintered A/CA ₆ composites.	50
3.3.	Formulations of various β -spodumene modified A/CA ₆ composites.	52
3.4.	PDF files used for qualitative phase analysis of the XRD, SRD and ND patterns.	59
3.5.	ICSD files used in the Rietveld refinement of XRD, SRD and ND data.	65
4.1.	Milling time and particle sizes data for the as-received Al ₂ O ₃ and CaCO ₃ , and processed CaCO ₃ powders.	77
4.2.	Particle size data for processed CA ₆ precursor, CA5, CA15, CA30, and CA50 powders after milling for 3h.	77
4.3.	Figures-of-merit from Rietveld refinement with XRD data for CA0, CA5, CA15, CA30, CA50 and CA100 samples.	95
4.4.	Figures-of-merit from Rietveld refinement with ND data for CA0, CA5, CA15, CA30, CA50 and CA100 samples.	95
4.5.	Relative phase composition from Rietveld refinement with XRD data for CA0, CA5, CA15, CA30, CA50, and CA100 samples.	96
4.6.	Relative phase compositions from Rietveld refinement with ND data for CA0, CA5, CA15, CA30, CA50, and CA100 samples.	96
4.7.	Figures-of-merit from Rietveld refinement with XRD data for CA100 sample.	102

4.8.	Figures-of-merit from Rietveld refinement with HTND data for CA100 sample.	102
4.9.	Relative phase compositions determined from Rietveld refinement with XRD data for CA100 sample.	103
4.10.	Relative phase compositions determined from Rietveld refinement with HTND data for CA100 sample.	104
4.11.	Average thermal expansion coefficient for the A/CA ₆ composite (CA30) and α -Al ₂ O ₃ (CA0), between 20 – 1000 °C.	113
4.12.	Variation of \square_0 , \square_1 and \square_2 parameters derived from Equation 4.8 for CA0, CA5, and CA15 samples.	122
5.1.	Milling time and particle size data for the as-received and processed β -spodumene powders.	130
5.2.	Particle size data for the CAS0, CAS2.5, CAS10, and CAS15 processed powders after milling for 3h.	131
5.3.	Figures-of-merit from Rietveld refinement with XRD data for CA0, CAS2.5, CA10 and CA15 samples.	141
5.4.	Figures-of-merit from Rietveld refinement with ND data for CA0, CAS2.5, CA10 and CA15 samples.	141
5.5.	Relative phase composition (wt%) from Rietveld refinement with XRD data for CAS0, CAS2.5, CAS10 and CAS15 samples.	142
5.6.	Relative phase composition (wt%) from Rietveld refinement with ND data for CAS0, CAS2.5, CAS10 and CAS15 samples.	142
5.7.	Average thermal expansion coefficient for CAS0, CAS2.5, CAS15, and alumina samples, at 20 – 1000 °C.	154
6.1.	Apparent porosity and bulk density of the alumina preform pre-sintered at 900, 1000, 1100, and 1100 °C.	161
6.2.	Resistance against infiltration cracking by the various preforms.	162
6.3.	Viscosity and surface tension of water and calcium acetate solution.	162

6.4.	Figures-of-merit from Rietveld refinement with XRD data for the alumina and graded A/CA ₆ composite obtained by gradual polishing and slicing methods.	179
6.5.	Relative phase compositions from Rietveld refinements with XRD data for the sintered alumina and graded A/CA ₆ samples obtained by gradual polishing and slicing methods.	180
6.6.	Figures-of-merit from Rietveld refinement with XRD data for the functionally-graded A/CA ₆ composite, sintered at 1000 – 1650 °C for 0.5h.	182
6.7.	Relative phase compositions from Rietveld refinements with XRD data for the functionally-graded A/CA ₆ composites, sintered at 1000 – 1650 °C for 0.5h.	183
6.8.	Figures-of-merit from Rietveld refinement with SRD data for the functionally graded A/CA ₆ composite obtained by slicing method.	189
6.9.	Relative phase compositions (wt%) from Rietveld refinements with SRD data for the functionally-graded A/CA ₆ composites obtained by slicing method.	190
6.10.	Figures-of-merit from Rietveld refinement with HTND data for the functionally graded A/CA ₆ composite.	197
6.11	Relative phase compositions from Rietveld refinements with HTND data for the functionally-graded A/CA ₆ composites.	198
6.12.	Weight gain, density, porosity, and shrinkage for the A/CA ₆ (FGM) and alumina (control) samples.	202
6.13.	Average thermal expansion coefficient for the functionally graded A/CA ₆ composites, A/CA ₆ composites produced by <i>in-situ</i> reaction sintering and alumina control sample, between 20 – 1000 °C.	205

CHAPTER 1

INTRODUCTION

1.1 Research Background

Ceramic composites are attracting increasing attention because of the broader diversity particularly improvement in properties, which they can frequently provide. It is well known that the unique properties of ceramic composites depend on their microstructure; therefore, design or tailoring of composite microstructure to achieve improved or novel properties presents processing challenges. From the processing point of view, there is growing interest in the microstructural design of toughened ceramics with microstructures exhibiting *plate-like* grain morphologies. This microstructure type can be achieved by a simple strategy, viz. by dispersing a suitable second phase in a matrix. The presence of second phases in the microstructure can act as effective bridging sites in the wake of crack, hence resulting in improved fracture resistance (Becher 1991). Theoretical considerations as well as experimental results show that the most effective reinforcement could be achieved by second phase particles with a *plate-like* morphology and high aspect ratios (Pezzoti 1993; Pezoti *et al.* 1996). The increase in fracture toughness is also dependent on differences in the physical properties of the second phase and the matrix, such as thermal expansion mismatch or elastic modulus. Second phase phases with lower thermal expansion than that of the alumina matrix may enhance the effectiveness and density of the bridges as observed in alumina/aluminium titanate composites (Padture, Bennison, and Chan 1993). Increasing the volume fraction and particle size of the second phase enhances flaw tolerance of the material, however it is limited by spontaneous microcracking of the matrix (Lawn *et al.* 1993; Padture *et al.* 1993).

The concept of *in-situ* or *self-reinforcement* has been well demonstrated for silicon carbide (SiC) ceramics by pressureless liquid-phase sintering (Padture 1994;

Lee, Kim and Kim 1994; Padture and Lawn 1994) and silicon nitride (Si_3N_4) ceramics (Li and Yamanis 1989; Salem *et al.* 1992; Hirosaki, Akimune, and Mitomo 1993) where highly elongated SiC and Si_3N_4 grains, respectively, are grown within the matrix to impart considerable improvements in the fracture toughness and Weibull modulus. By judiciously adjusting the composition through simultaneous additions of SrO and Al_2O_3 to ZrO_2 , a microstructure of strontium hexaluminate ($\text{SrO} \cdot 6\text{Al}_2\text{O}_3$) platelets within the Ce-TZP matrix can be produced with much improved hardness and strength (Culter *et al.* 1991). Strengths of over 500 MPa and hardness up to 14 GPa, with fracture toughness in excess of $15 \text{ MPa} \cdot \text{m}^{1/2}$ have been achieved in these composites.

Chen and Chen (1992) showed that $\alpha\text{-Al}_2\text{O}_3$ can be toughened by growth of *in-situ* hexaluminate platelets ($\text{LaAl}_{11}\text{O}_{18}$, $\text{LaMgAl}_{11}\text{O}_{19}$, $\text{SrAl}_{12}\text{O}_{19}$, and $\text{Na}_2\text{MgAl}_{12}\text{O}_{17}$) within the alumina matrix. Although up to 40% improvement in fracture toughness was achieved for alumina composites containing 30 vol % hexaluminate platelets, the maximum toughness being intrinsically limited by the strength of these layered compounds. By adopting a unique microstructural control, Yasuoka *et al.* (1995) achieved strengths of over 600 MPa and fracture toughness in excess of $6 \text{ MPa} \cdot \text{m}^{1/2}$ for alumina composites containing both elongated Al_2O_3 grains and $\text{LaAl}_{11}\text{O}_{18}$ platelets.

Calcium-hexaluminate, $\text{CaAl}_{12}\text{O}_{19}$ (CA_6), is a promising compound as a second phase in alumina-based composites because it is thermodynamically compatible with alumina matrix and it has the same average thermal expansion coefficient, i.e. approximately $8.5 \times 10^{-6} \text{ }^\circ\text{C}^{-1}$. However its thermal expansion behaviour is highly anisotropic, i.e. $\alpha_a = 7.3 \times 10^{-6} \text{ }^\circ\text{C}^{-1}$, $\alpha_c = 11.8 \times 10^{-6} \text{ }^\circ\text{C}^{-1}$ (Criado, Caballero, and Pena 1987). Hence, thermal expansion mismatch between alumina and CA_6 may be expected. Considerable effort has been devoted to the study of CA_6 as a component of refractory materials (Criado, Caballero, and Pena 1987; Criado and De Aza 1991). However, there exist few studies that deal with the fabrication and characterisation of $\text{Al}_2\text{O}_3\text{-CA}_6$ dense composites for structural applications (An,

Chan, and Soni 1996; An and Chan 1996). In a series of studies, An and Chan (1996) and An, Chan and Soni (1996) demonstrated that CA_6 can be prepared as a reinforcing phase in alumina matrices. They found that the incorporation of 30 vol % platelets CA_6 grains that develop *in-situ* during processing in alumina matrix resulted in enhanced toughening and damage tolerance. However, they did not study in detail the phase development of CA_6 within the alumina matrix by x-ray diffraction, neutron diffraction, and thermal analysis. Also, the effect of CA_6 content on the densification behaviour and mechanical properties of alumina has not been reported.

Functionally-graded materials (FGMs) are a relatively new class of the composite materials, which exhibit a progressive change in structure, composition, and properties as a function of spatial direction within the material (Hirai 1996). A variety of methods to produce graded materials and examples of these materials have been well documented in the literature (Sasaki and Hirai 1991; Hirai 1996). Recently, one of the extremely useful methods for designing new graded materials with unique microstructural, physical and thermal properties has been developed at Curtin University. This method is liquid infiltration, which includes the immersing of porous powder compact with suitable infiltrants followed by heat-treatment to produce a dense multi-phase body. The microstructural elements in this material are tailored to provide graded compositions and generate different modes of strengthening and toughening. The unique mechanical performance of both flaw tolerance and wear resistance for FGMs produced using infiltration techniques has been well demonstrated in graded mullite/ZTA (Low *et al.* 1993; Low, Skala, and Li 1993) and AT/ZTA (Low, Skala, and Zhou 1996; Pratapa and Low 1996; Pratapa, O'Connor and Low 1997). In these systems the host body is encased with a graded layer of mullite or AT through full infiltration. The heterogeneous layer of graded mullite/alumina, mullite/ZTA, and AT/ZTA provides excellent toughness, while the homogeneous alumina or ZTA layer retains strength and wears resistance. The presence of graded phase in the heterogeneous layer has an added advantage of minimising the macroscopic residual stresses which may cause de-bonding or

cracking at interfaces, or hinder the densification process. Recent work at Curtin University by Asmi, Low and Sitepu (1997) and Asmi and Low (1998) in the synthesised of functionally-graded alumina/calcium-hexaluminate (A/CA_6) composites using partial infiltration technique has shown that there is improvement in the physical and mechanical behaviour of alumina composites containing 5 - 50 wt% calcium-hexaluminate (CA_6) composites.

In the present work emphasis was placed on designing, fabricating, characterising, and understanding of novel alumina/calcium-hexaluminate (A/CA_6) and β -spodumene modified A/CA_6 composites produced using *in-situ* reaction sintering, and functionally-graded A/CA_6 composites produced using infiltration techniques with prospect of both wear and damage tolerance. Accordingly, the results of the study would be of use in the developments of alumina-based composites materials processing technologies associated with characterisation procedures, in special relation to the role of microstructure on damage-tolerance.

1.2 Research Significance and Objectives

1.2.1 Research Significance

This research represents a significant conceptual advance in the design, fabrication and understanding of novel alumina/calcium-hexaluminate (A/CA_6) composites with the prospect of enhancing both wear and damage resistance. It has combined innovative processing methodology with a new materials design concept for improving mechanical reliability. The *in-situ* reaction sintering method and infiltration processes were developed to produce A/CA_6 composites with high mechanical performance and controlled microstructure. This research has also lead to the microstructural design of functionally graded A/CA_6 with highly specific multi-functional properties, which is becoming essential for use in high performance applications. The research on the rudiments of the infiltration process itself gave

valuable information pertaining to the kinetics of infiltration of liquids into porous bodies.

1.2.2 Research Objectives

The primary objective of this research project was to produce novel A/CA₆ composites with high mechanical performance via microstructural control. The presence of CA₆ in this system was expected to improve the mechanical properties. The specific objectives of the research were:

- 1) To study the phase compositions and developments of *in-situ* reaction sintered A/CA₆, β -spodumene modified A/CA₆, and functionally-graded A/CA₆ composites.
- 2) To determine the formation temperatures of calcium aluminates (i.e. CA, CA₂, and CA₆) which occur during calcination of A/CA₆ composites.
- 3) To examine the effect of β -spodumene on the phase composition, microstructure, and property relationships of A/CA₆ composite with the aim of achieving optimum mechanical performance.
- 4) To study the kinetics of infiltration of liquid into a porous body and the use of this technique to fabricate functionally-graded A/CA₆ composites.
- 5) To design alumina-based ceramic matrix composites with graded calcium-hexaluminate (CA₆) to impart flaw tolerance.
- 6) To study the graded composition profiles, microstructures, and property relationships of functionally-graded A/CA₆ composites with the purpose of achieving high mechanical performance.
- 7) To compare the phase developments, microstructures, physical and mechanical properties for the A/CA₆ system, which are produced by *in-situ* reaction sintering and infiltration methods.

1.3 Research Plan

Based on the significance and objectives stated in section 1.2, the proposed research plan in this study are as follows:

- 1) Selection and evaluation of raw materials to produce *in-situ* reaction sintered A/CA₆, β -spodumene modified A/CA₆, and functionally-graded A/CA₆ composites.
- 2) Fabrication of A/CA₆ and β -spodumene modified A/CA₆ using an *in-situ* reaction-sintering process and functionally-graded A/CA₆ using an infiltration technique.
- 3) Characterisation of the phase compositions and graded composition profiles for the composites using room-temperature x-ray diffraction (XRD) and neutron diffraction (ND), high-temperature neutron diffraction (HTND) and room-temperature synchrotron radiation diffraction (SRD).
- 4) Study the kinetics of infiltration of liquid into porous alumina preforms.
- 5) Evaluation of selected physical and mechanical properties viz. shrinkage, porosity, density, thermal expansion and shrinkage behaviour, and hardness and fracture toughness.
- 6) Evaluation of microstructure development using scanning electron microscopy and transmission electron microscopy.

1.4 Structure of Thesis

The studies reported in this thesis were concentrated on the microstructural design, synthesis, characterisation, physical and mechanical measurements of novel A/CA₆ composites produced by the *in-situ* reaction sintering and an innovative infiltration process. This thesis is divided into 7 chapters.

Chapter 1 describes the background to the research topic, the statement of the significance and objectives, and the research plan.

Chapter 2 reviews the literature of the theoretical backgrounds associated with the research topic. This topic involves alumina-based ceramic composites, design of ceramic composites with high mechanical performance and microstructural control, and functionally graded materials (FGMs).

Chapter 3 describes the experimental strategy in the research, which was developed to achieve the objectives. The experimental procedure begins with processing strategy to produce composites of high density, desired microstructure and phase distribution. Descriptions of the sintering, characterisation, and property evaluation then follow.

Chapter 4 presents the results on the synthesis, phase composition and development, physical and mechanical properties for A/CA₆ composites that were produced by the conventional reaction sintering technique. This begins with an evaluation of the raw materials. The use of XRD, ND and dynamic HTND, SEM, DTA and TG analysis, dilatometry, and Vickers indentation to characterise A/CA₆ composites are then presented. Quantitative phase compositions from Rietveld analysis results are also presented.

Chapter 5 presents the results on the synthesis, phase composition and development, physical and mechanical properties of β -spodumene modified A/CA₆ composites, which were produced by the conventional reaction sintering technique. Evaluation of the raw material was initially described. The experimental results from XRD, ND, SEM, DTA and TG analysis, dilatometry, and Vickers indentation are then presented. Quantitative phase compositions from Rietveld analysis with XRD and ND data are also presented.

Chapter 6 presents the results on the infiltration kinetics, the graded composition profiles and phase developments, the physical and mechanical properties for functionally graded A/CA₆ composite, which were produced by an

infiltration technique. This chapter begins with the study of the kinetic infiltration of liquid into porous alumina preform. The experimental results from XRD, SRD, ND, and HTND, SEM, TEM, DTA and TG analysis, dilatometry and Vickers indentation are then presented. Quantitative phase compositions from Rietveld analysis with XRD, SRD and HTND data are also presented.

Finally, in Chapter 7, the conclusions of the study are presented together with recommendations for future research work.

CHAPTER 2

LITERATURE REVIEW

2.1 Introduction

The theoretical backgrounds associated with the research topic are reviewed in this chapter. This topic involves alumina-based ceramic composites and functionally graded materials (FGMs). Calcium hexaluminate (CA_6) is the reinforced phase in the alumina matrix to produce alumina/calcium-hexaluminate (A/ CA_6) composites, therefore reviews on both are also presented. β -spodumene was chosen as sintering aid to densify A/ CA_6 composites, so review on this material is considered. Both *in-situ* reaction sintering and infiltration techniques were used to manufacture A/ CA_6 composites, therefore brief reviews on both topics are also presented.

2.2 Alumina-Based Ceramic Composites

2.2.1 Alumina

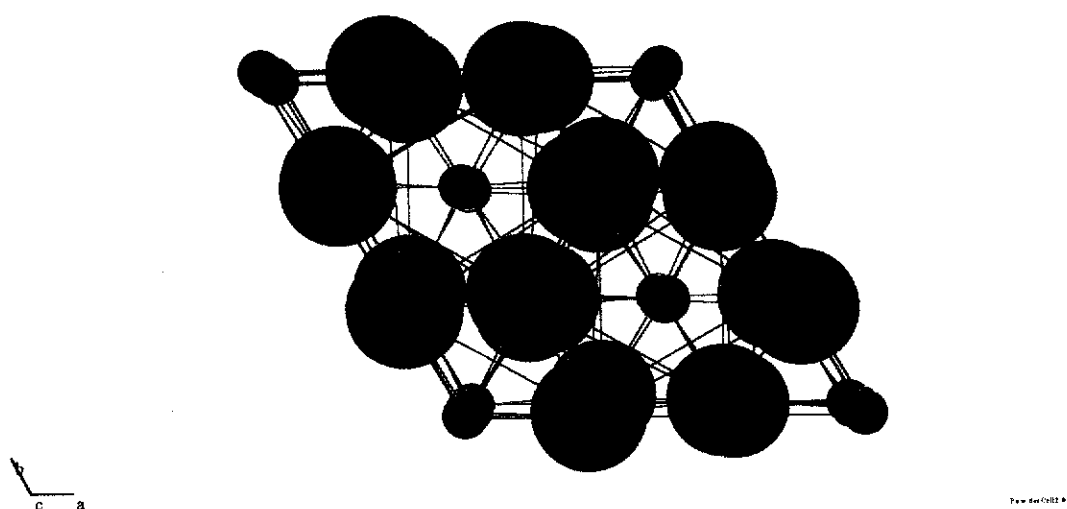
Alumina is most extensively used non-transforming monolithic ceramic due to the easy and relatively cheap technology for its production and also due to its remarkable properties (Munro 1997). Pure alumina is chemically inert and possesses high stability, excellent compressive strength and creep resistance up to high-temperatures (Munro 1997; Chevalier *et al.* 1997). The melting point of α - Al_2O_3 is 2050 ± 4 °C (Munro 1997). This makes alumina an excellent material for application in industry, medicine, electronics and many others. A variety of alumina materials are commercially available for these applications, with alumina contents ranging from 85 % to 99.99 % alumina. In addition to alumina content, these commercial materials also can vary in bulk density, impurity content, and other microstructural

characteristics such as grain size and grain boundary microstructure (Dörre and Hübner 1984).

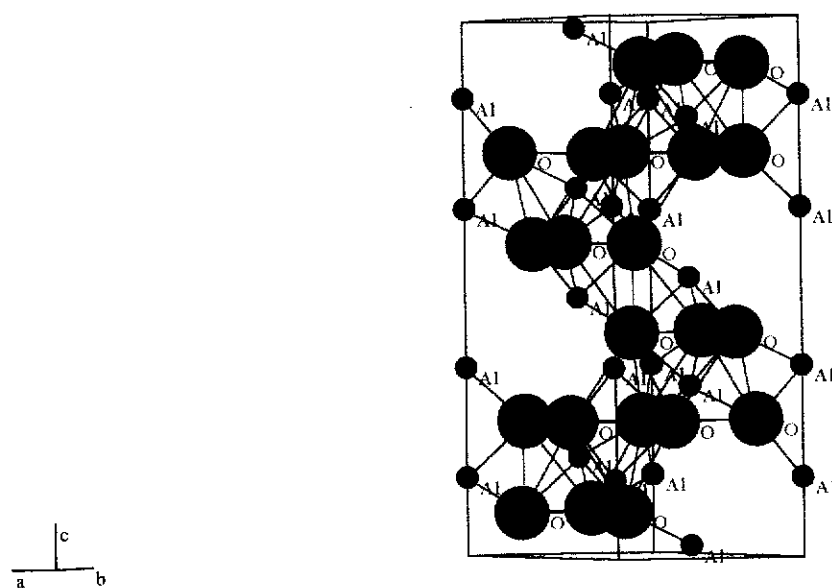
Aluminium oxide, Al_2O_3 is found in several crystallographic forms, for example α , β , and γ (Misra 1986). The most prevalent and widely used in structural engineering is denoted as α - Al_2O_3 or termed corundum in mineral form and sapphire as the single crystal (Dörre and Hübner 1984). The structure parameters of α - Al_2O_3 (space group R3c) proposed by Maslen, Streltsov and streltsova (1993) – ICSD # 73725 (see Appendix A), have been employed in the present study, because of the high quality data reported. Both synchrotron diffraction ($\lambda = 0.7$ and 0.9 \AA) and x-ray diffraction ($\text{MoK}\alpha$, $\lambda = 0.71069 \text{ \AA}$) data were collected with two small crystals. The two sets of results are consistent. Figure 2.1 shows the crystal structure of α - Al_2O_3 , based on the model proposed by Maslen, Streltsov and streltsova (1993), projected on the (a) (001) and (b) (120) planes, which is plotted using the software package 'Powder Cell' program version 2.3 for Windows (Kraus and Nolze 1999). The ion sizes are drawn in proportion to the ionic radii, i.e. 0.55 \AA for Al^{3+} and 1.35 \AA for O^{2-} . The structure consists of planes of close-packed oxygen ions in the A-B-A-B sequence interleaved with planes of aluminium ions in an a-b-c-a-b-c sequence. A hexagonal crystallographic cell is formed from repeating sequence A-a-B-b-A-c-B-a-A-b-B-c. Lattice parameters of α - Al_2O_3 are $a = 4.7540(5) \text{ \AA}$ and $c = 12.9820(6) \text{ \AA}$, related to a theoretical density of 3.997 g/cm^3 (Maslen, *et al.* 1993).

2.2.2 The $\text{CaO-Al}_2\text{O}_3$ System

The calcium aluminates of the $\text{CaO-Al}_2\text{O}_3$ system are an extensive family of compounds that exhibit the diverse structural chemistry of aluminium (Tas 1998). It contains a number of stable intermediate compounds such as C_3A , C_{12}A , CA , CA_2 , and CA_6 , of which CA_6 is the richest in alumina. The compound formulation employed in this study is the conventional cement notation, i.e. $\text{C} = \text{CaO}$, and $\text{A} = \text{Al}_2\text{O}_3$, thus $\text{CA} = \text{CaO} \cdot \text{Al}_2\text{O}_3$, $\text{CA}_2 = \text{CaO} \cdot 2 \text{ Al}_2\text{O}_3$, and $\text{CA}_6 = \text{CaO} \cdot 6 \text{ Al}_2\text{O}_3$, etc.



(a)



(b)

Figure 2.1. Crystal structure of $\alpha\text{-Al}_2\text{O}_3$ (ICSD # 73725) projected on the (a) (001) and (b) (210) planes. The ion sizes are drawn in proportion to the ionic radii, i.e. 0.55 \AA for Al^{3+} and 1.35 \AA for O^{2-} . Plotted using the software package 'PowderCell' (Kraus and Nolze 1999).

The CaO-Al₂O₃ system has been used as an important constituent in the high alumina cement, steel, and ceramic industries (Parker and Sharp 1982; Kopanda and Maczura 1990). New applications have emerged in optical and structural ceramics. Owing to their good photosensitive properties, some of the amorphous calcium-aluminates are promising candidates for used in information storage device (Goktas and Weinberg 1991; Wallenberg, Weston and Brown 1991). Calcium aluminates offer a very good host lattice, which can be doped with suitable ions to develop solid-state lasers and high temperature ceramic sensors after proper densification. In addition, crystalline calcium aluminates have been used in high strength and high toughness ceramic-polymer composite materials (Birchall, Horward and Kendal 1981).

Phase Diagram of the CaO-Al₂O₃ System

The phase equilibrium studies on the CaO-Al₂O₃ system has been investigated by a number of researchers (Shepherd, Rankin and Wright 1909; Rankin and Wright 1915; Nurse, Welch and Majumdar 1965). However differences of opinion still exist on several points. Shepherd, Rankin and Wright (1909) made the first study of the CaO-Al₂O₃ phase diagram. Rankin and Wright (1915) later made some adjustments of the invariant temperature. They indicated the presence of four compounds: C₃A, C₅A₃, CA, and C₃A₅. Langerquist *et al.* (1937) in x-ray studies identified C₅A₃ as C₁₂A₇ and C₃A₅ as CA₂, and they reported a new high alumina phase C₃A₁₆. From microscopic study this later compound was identified as CA₆ (Filonenko and Lavrov 1949). Determinations of the phase diagram have also been made by Chatterjee and Zhomoidin (1972) and Imlach and Glasser (1968). However, Haldstet (1990) suggests the CaO-Al₂O₃ phase diagram as proposed by Nurse, Welch and Majumdar (1965) is the most widely used for predicting phase behaviour. The phase diagram of the binary CaO-Al₂O₃ system shown in Figure 2.2 is the basis for the effective manufacture of high alumina cements and refractory castables (Nurse, Welch and Majumdar 1965). Of particular interest in this system are CA,

CA₂ and CA₆ phases. The CA phase melts incongruently at 1602 °C to yield CA₂ and liquid. The CA₂ was found to melt incongruently at 1762 °C to CA₆ and liquid, and the CA₆ was observed to melt incongruently at 1830 °C to Al₂O₃ and liquid (Nurse, Welch and Majumdar 1965).

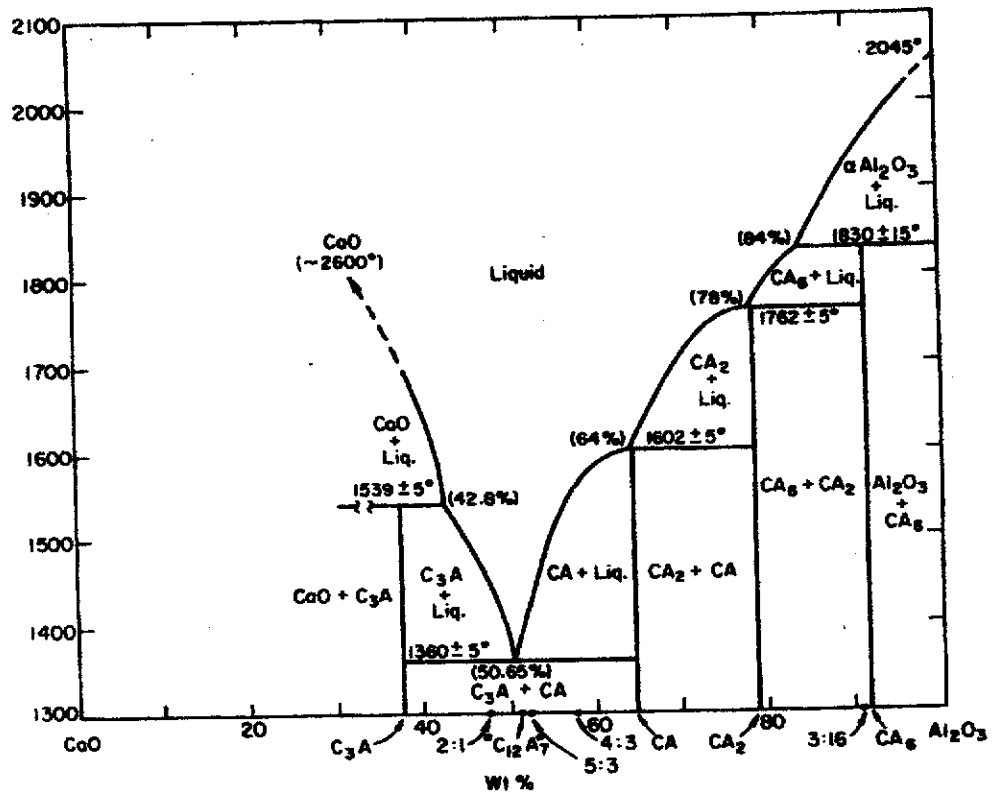


Figure 2.2. Phase diagram for the CaO-Al₂O₃ system. After Nurse, Welch and Majumdar (1965).

Crystal Structure of Calcium Monoaluminate - CA

The crystal structure of calcium monoaluminate – $\text{CaO} \cdot \text{Al}_2\text{O}_3$ (CA) was determined by Dougill (1957) and confirmed as similar to β -tridymite (a three dimensional arrangement of AlO_4 tetrahedra with Ca accommodated in the cavities). The space group was reported as P21/n. Hörkner and Müller-Buschaum (1976) re-examined the crystal structure of CA by single crystal x-ray data. They reported the structure has monoclinic crystal structure. The space group belongs to P21/n, and Ca has lattice cell parameters $a = 8.7000 \text{ \AA}$, $b = 8.0920 \text{ \AA}$, $c = 15.1910 \text{ \AA}$ and $\beta = 90.2^\circ$. The structure of CA projected on the (010) plane as proposed by Hörkner and Müller-Buschaum (ICSD # 260) is plotted in Figure 2.3. The ion sizes are drawn in proportion to the ionic radii, i.e. 1.05 \AA for Ca^{2+} , 0.55 \AA for Al^{3+} , and 1.35 \AA for O^{2-} . The crystal structure data for CA are presented in Appendix A.

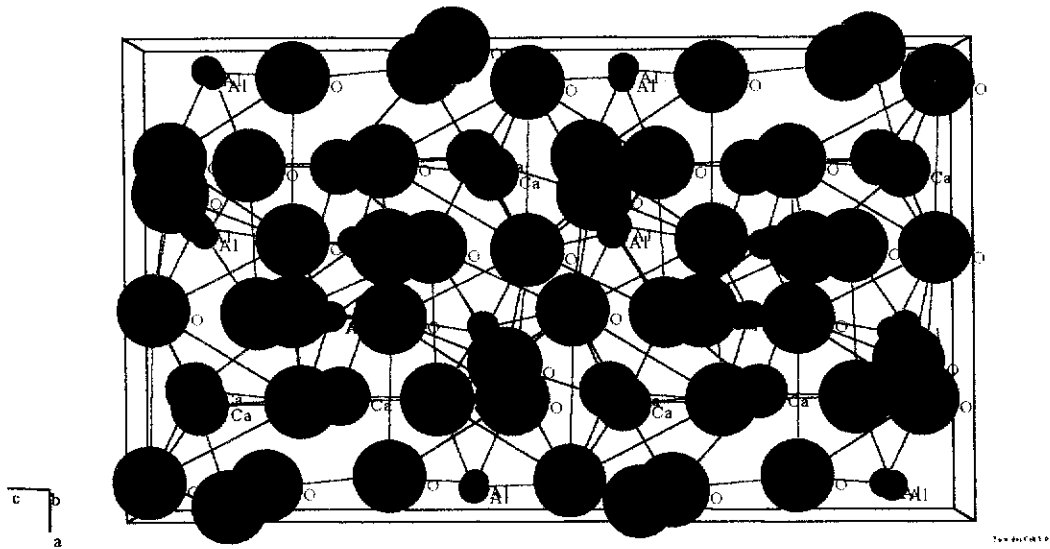


Figure 2.3. Crystal structure of CA (ICSD # 260) projected on the (010) plane. The ion sizes are drawn in proportion to the ionic radii, i.e. 1.05 \AA for Ca^{2+} , 0.55 \AA for Al^{3+} and 1.35 \AA for O^{2-} .

Crystal Structure of Calcium Dialuminate – CA₂

There has been a certain amount of controversy over the exact crystal structure for the calcium dialuminate phase – CaO.2Al₂O₃ (CA₂). Boyko and Winsy (1958) proposed the crystal structure of CA₂ as isomorphous monoclinic crystals with the space group C2/c. Ponomarev, Kheiker and Belov (1970) confirmed the CA₂ phase as monoclinic with a space group C12/c1 and it has lattice parameters $a = 12.8666 \text{ \AA}$, $b = 8.8790 \text{ \AA}$, $c = 5.5440 \text{ \AA}$, and $\beta = 106.8^\circ$. The structure of CA₂ projected on the (001) plane as proposed by Ponomarev, Kheiker and Belov (ICSD # 73725) is plotted in Figure 2.4. The ion sizes are drawn in proportion to the ionic radii, i.e. 1.05 \AA for Ca²⁺, 0.55 \AA for Al³⁺, and 1.35 \AA for O²⁻. The crystal structure data for CA₂ are presented in Appendix A.

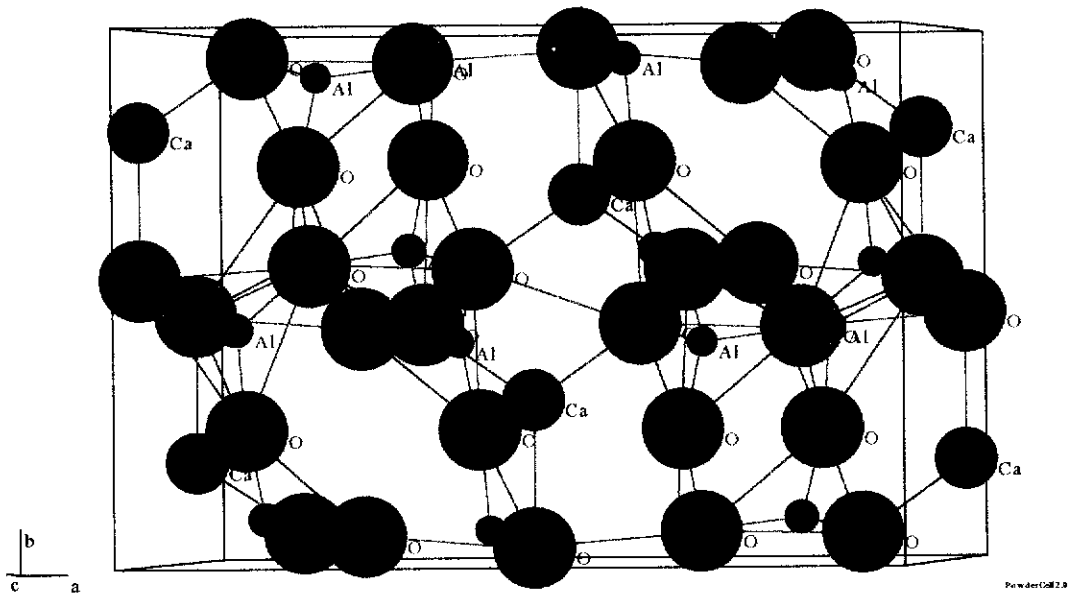


Figure 2.4. Crystal structure of CA₂ (ICSD # 16191) projected on the (001) plane. The ion sizes are drawn in proportion to the ionic radii, i.e. 1.05 \AA for Ca²⁺, 0.55 \AA for Al³⁺ and 1.35 \AA for O²⁻.

Crystal Structure of Calcium-Hexaluminate - CA₆

Calcium hexaluminate, CA₆ (hibonite) is a layered compound having the magnetoplumbite structure. The crystal structure of CA₆ was first studied by Kato and Saalfeld (1968), and confirmed to be isostructural with the mineral magnetoplumbite. The structure belongs to the hexagonal space group P6₃/mmc (Kato and Saalfeld 1968; Utsunomiya *et al.* 1988). The magnetoplumbite (CA₆) structure consists of spinel blocks and conduction layers, which are stacked alternatively to form a sort of layer structure. Spinel blocks are composed only of Al³⁺ and O²⁻ ions, and have the same rigid structure as spinel. Large cations such as Ca²⁺ are usually located in the spacious conduction layer, which has a mirror symmetry plane. According to Iyi, Takekawa and Kimura (1989), the charge and the radius of the large cations in the conduction layer determine the structure type of hexaluminate. The conduction layer decreases not only due to the decrease of the radii of the Ca²⁺ cations, but also because of the population increase. However, the spinel block thickness increases according to the increase in the amount of Al³⁺ defect within the spinel block. The structure of CA₆ projected on the (001) and (210) planes as proposed by Kato and Saalfeld (ICSD # 34394) is plotted in Figure 2.5. The ion sizes are drawn in proportion to the ionic radii, i.e. 1.05 Å for Ca²⁺, 0.55 Å for Al³⁺, and 1.35 Å for O²⁻. The crystal structure data for CA₆ are presented in Appendix A.

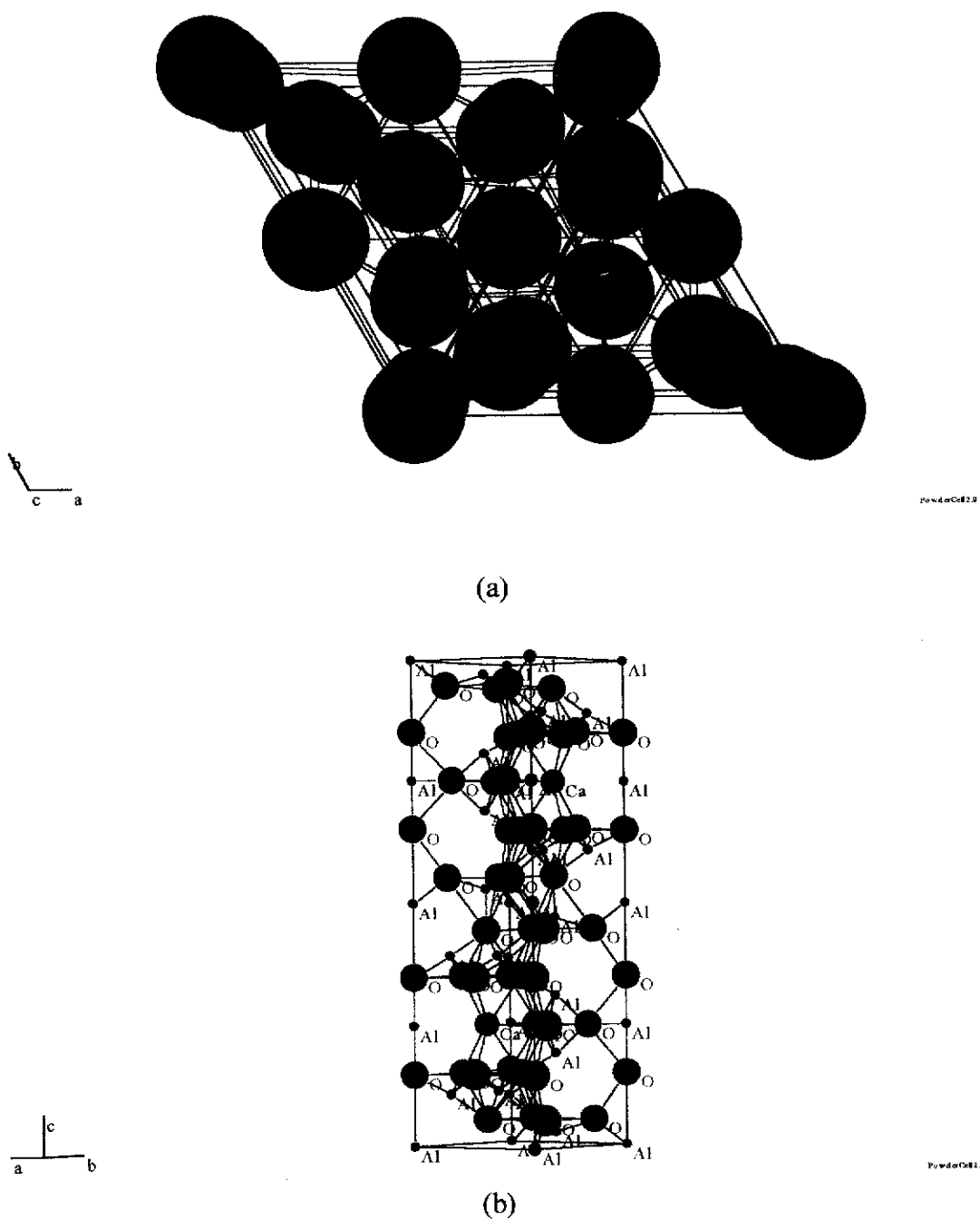


Figure 2.5. Crystal structure of CA_6 (ICSD # 34394) projected on the (a) (001) and (b) (210) planes. The ion sizes are drawn in proportion to the ionic radii, i.e. 1.05 \AA for Ca^{2+} , 0.55 \AA for Al^{3+} and 1.35 \AA for O^{2-} .

Formation and Properties of Calcium-Hexaluminate - CA₆

CA₆ has been successfully fabricated using solid-state and sol-gel techniques. Mendoza, Freese and Moore (1988) found that the optimum calcination of CA₆ from alumina powder and calcium hydroxide is approximately at 1400 °C. Cinibulk and Hay (1996) studied the evolution of the CA₆ phase from alumina sols that contained calcium acetate. They reported that, after firing the gelled sols at 1200 °C, the major phase observed was CA₆ with additional minor phases of α -Al₂O₃ and CA₂. Fired at 1400 °C, an almost single phase of CA₆ was obtained, with traces of α -Al₂O₃ and CA₂ still displayed.

The morphology of CA₆ grains is dependent on the processing route used. Criado, Pena and Caballero (1988) demonstrated that the CA₆ grains exhibit platelet morphology when CA₆ is obtained by reaction sintering of Al₂O₃ and CaCO₃ powders because of the presence of a eutectic CaO-Al₂O₃ melt at 1360 °C. This result agrees with those obtained by De Jonghe, Schmid and Chang (1984) that used the reaction between Al₂O₃ and CaO-Al₂O₃ melt. However, the solid state sintering with previously synthesised CA₆ powders showed equiaxed grain morphology. In a study by Nagaoka, Kanzaki and Yamaoka (1990) two types of CA₆ morphologies were found, i.e. elongated grains in the surface parallel to the hot-pressing direction and equiaxed grains in the surface perpendicular to the hot-pressing direction.

The information on the thermal expansion is essential in the understanding of a material at high temperatures. Brooksbank (1970) studied the thermal expansion behaviour of calcium aluminate as inclusions in chromium steel at temperatures between 0 °C and 800 °C by using dilatometer for CA and CA₂ and high temperature x-ray diffraction for CA₆. The average thermal expansion coefficient obtained was $6.5 \times 10^{-6} \text{ }^{\circ}\text{C}^{-1}$ for CA and $5.0 \times 10^{-6} \text{ }^{\circ}\text{C}^{-1}$ for CA₂. The results for CA₆ have been reported to be $\alpha_a = 7.6 \times 10^{-6} \text{ }^{\circ}\text{C}^{-1}$ and $\alpha_c = 11.8 \times 10^{-6} \text{ }^{\circ}\text{C}^{-1}$, the mean thermal expansion coefficient of $8.8 \times 10^{-6} \text{ }^{\circ}\text{C}^{-1}$ close to the result reported by Floyd (1964) of $8.35 \times 10^{-6} \text{ }^{\circ}\text{C}^{-1}$. Mendoza, Freese and Moore (1988) also used a dilatometer to investigate the thermal expansion behaviour of CA₆ in the series of calcium

aluminate system. A heating rate of 5 °C/minute between 25 °C to 1000 °C was employed, and the value of $8.5 \times 10^{-6} \text{ }^{\circ}\text{C}^{-1}$ obtained is in a good agreement with those reported earlier by Floyd (1964) and Brooksbank (1970).

Nagaoka, Kanzaki and Yamaoka (1990) studied the mechanical properties of hot-pressed calcium-hexaluminate. The calcium-hexaluminate was observed to have an aspect ratio of 1.6 and with a preferred c-axis orientation perpendicular to the hot-pressing direction. It has a flexural strength of approximately 600 MPa at room temperature and 400 MPa at 1300 °C. These values are higher than the value of 289 MPa reported by Criado, Caballero and Pena (1987). Figure 2.6 shows the temperature dependence of flexural strength of calcium-hexaluminate (Nagaoka, Kanzaki and Yamaoka 1990). The hardness (H_v) and fracture toughness (K_{IC}) parallel to the hot-pressing direction were 13.1 GPa and $3.4 \text{ MPa}\cdot\text{m}^{1/2}$, whereas that perpendicular to the hot-pressing direction were 13.4 GPa and $3.0 \text{ MPa}\cdot\text{m}^{1/2}$. The fracture toughness values are lower than those reported by Criado, Caballero and Pena (1987) and by Mendoza, Freese and Moore (1988) due to the lower aspect ratio of the calcium-hexaluminate. Figure 2.7 shows the variation of fracture toughness at room temperature for the calcium-hexaluminate ceramics, sintered at 1500 – 1650 °C (Criado and De Aza 1991).

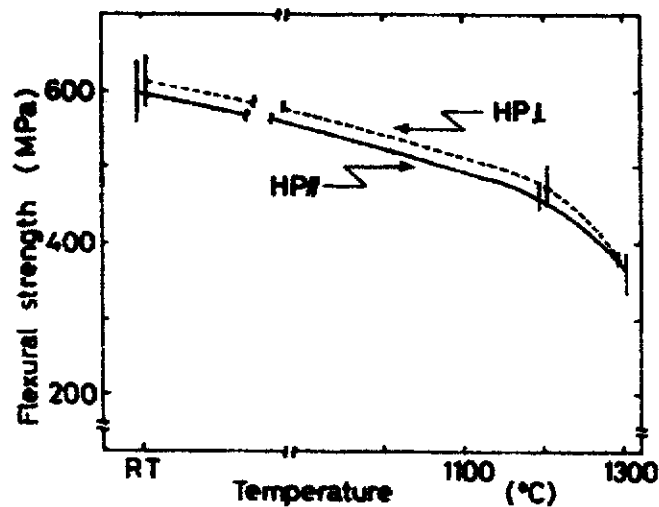


Figure 2.6. Flexural strength for the hot-pressed CA_6 ceramics as a function of temperature. Legends: HP_\perp = surface perpendicular to the hot-pressing direction, HP_\parallel = surface parallel to the hot-pressing direction. After Nagaoka, Kanzaki, and Yamaoka (1990)

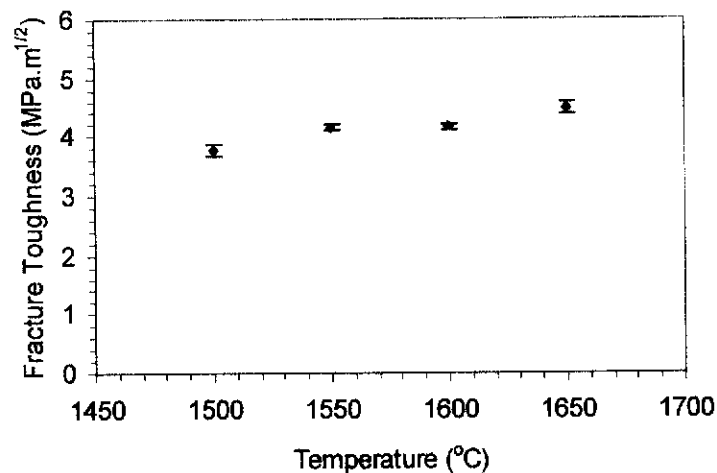


Figure 2.7. Variation of room-temperature fracture toughness for the CA_6 ceramics, sintered at 1500 – 1650 °C. Error bars indicate two estimated standard deviations (2σ). Redrawn after Criado and De Aza (1991)

2.2.3 *In-situ* Reaction Sintering

In-situ reaction sintering is a firing process in which the chemical reaction of the starting materials and the densification of the powder compact are both achieved in a single heat-treatment step (Rahaman 1995). The basic concept for the production of a composite by the *in-situ* reaction sintering technique is shown in Figure 2.8. During firing, reaction between the two starting materials (i.e. A and B) and densification occur to produce a polycrystalline solid consisting of two phases (i.e. C and D) given by:

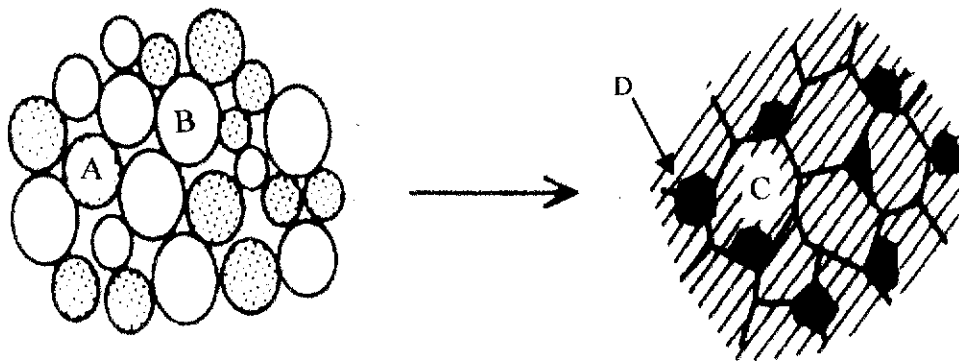
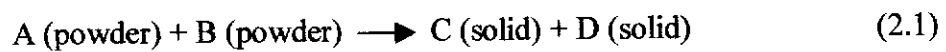
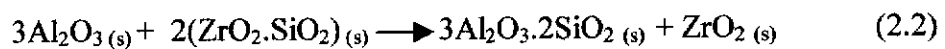


Figure 2.8. Schematic diagram for the production of ceramic composite, consisting of a matrix (C) and inclusions (D), through *in-situ* reaction sintering of a compacted mixture of two powders (A and B). After Rahaman (1995).

One of the examples for the application of Equation 2.1 is the reaction between alumina and zircon to produce mullite and zirconia (Wallace, Petzow and Claussen 1984):



In this process, a dense product of mullite with fine zirconia inclusions is obtained. A two-stage process is used with densification at about 1450 °C followed by anneal above 1500 °C to form the mullite-ZrO₂. Boch, Chartier and Giry (1990) demonstrated that with 0.4 µm particles 97 % theoretical density could be achieved after 30 min at 1540 °C, whereas with a 3 µm starting powder only 88 % density was achieved after 10 h at the same temperature. The mechanical strength of the composite (400 MPa) was higher than that of the unreinforced mullite prepared by hot pressing (270 MPa) (Claussen and Jahn 1980). The resulting microstructure consisted of a mullite matrix with both intragranular and intergranular zirconia particles.

The concept of *in-situ* reaction sintering has also been successfully demonstrated for enhancing the mechanical properties of alumina-based ceramic composites. For examples Al₂O₃/Ce-TZP (Cutler and Mayhew 1991), Al₂O₃/hexaluminate platelets (LaAl₁₁O₁₈, LaMgAl₁₁O₁₉, SrAl₁₂O₁₉, and Mg₂NaAl₁₅O₂₅) (Chen and Chen 1992), Al₂O₃/LaAl₁₁O₁₈ (Yasuoka *et al.* 1995; Jang and Kishi 1998), and Al₂O₃/CA₆ (Criado, Caballero and Pena 1987; An and Chan 1996; An, Chan and Soni 1996; Maschio and Pezzotti 1999; Asmi and Low 1998; Asmi *et al.* 1999). An and Chan (1996) suggested that two main advantages can be obtained from the processing of ceramic composites via the *in-situ* reaction sintering approach, i.e. (i) it is relatively easy to achieve high densities, and (ii) potential health hazards due to handling of whiskers are avoided. Of particular interest related to the present study is the Al₂O₃/CA₆ system, therefore a review on this system is given in the following section.

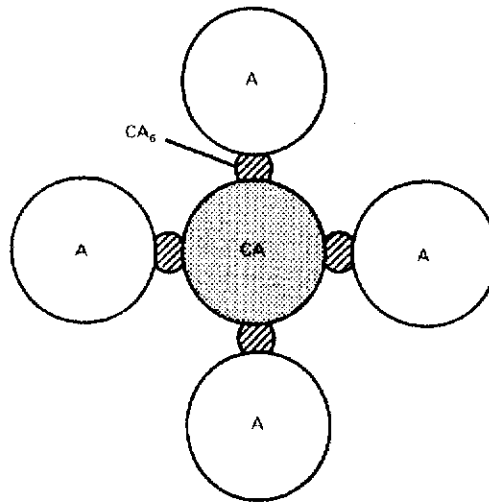
2.2.4 The Al₂O₃-CA₆ System

In recent years, Al₂O₃-CA₆ composites have been widely studied as structural materials since it was found that Al₂O₃ containing *plate-like* CA₆ grains showed a more pronounced R-curve behaviour than a composite contains equiaxed grains (An

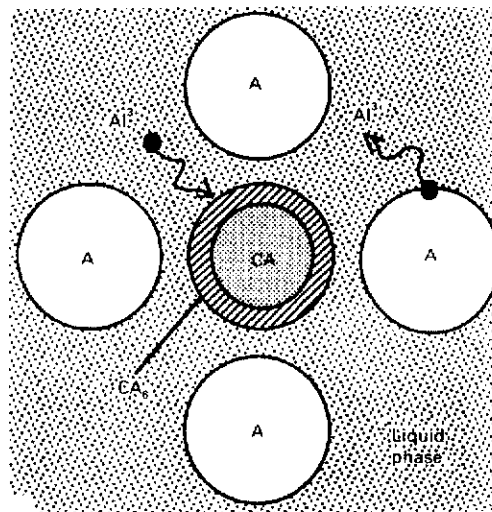
and Chan 1996). CA_6 has been chosen as a reinforcing phase in alumina matrix by virtue of (i) its chemical compatibility and (ii) its mechanical and thermal expansion properties (Criado, Caballero, and Pena 1987, Chan and Soni 1996, An and Chan 1996, Criado, Asmi and Low 1998, and Asmi *et al.* 1999). CA_6 has also been used for coating alumina fibers (Cinibulk 1994, 1995) due to its easily cleaved crystallographic basal planes oriented parallel to the fiber-matrix interface. This weak interface is used to deflect cracks, therefore toughening the composite.

Chan and Soni (1996) studied the effect of processing conditions on the morphology of CA_6 in $Al_2O_3/30$ vol% CA_6 composites. They used two different starting raw materials, i.e. (i) Al_2O_3 and $CaCO_3$, and (ii) Al_2O_3 and CaO . Anorthite- $CaAl_2Si_2O_8$ (1.0 vol %) was used as sintering aid. The use of $CaCO_3$ as the starting powder was found to result in *plate-like* CA_6 grains, in contrast to CaO which gave equiaxed CA_6 grains. They postulated that the difference in CA_6 morphologies could be attributed to two different mechanisms in the reaction of Al_2O_3 and CA to form CA_6 , i.e. (i) solid state reaction between Al_2O_3 and CA grains, and (ii) solution-precipitation (see Figure 2.9). The solid-state reaction resulted in the formation of equiaxed CA_6 grains, whereas solution-precipitation favoured the development of *plate-like* grains. One vol % $CaAl_2Si_2O_8$ -anorthite did not play an important role in the development of CA_6 morphology.

Several researchers have studied the mechanical properties of Al_2O_3 - CA_6 composites. Criado, Pena and Cabalero (1987) reported that the addition of CA_6 (i.e. 4.21, 6.37, 12.69, and 25.15 vol %) has no influence on the fracture toughness; however it was found that the flexural strength decreased by approximately 20 % when compared with Al_2O_3 due to the anisotropic grain growth of CA_6 phase. The hardness, fracture toughness, and flexural strength of various Al_2O_3 - CA_6 composites manufactured by reaction sintering of Al_2O_3 and $CaCO_3$ are shown in Figures 2.10, 2.11, and 2.12.



(a)



(b)

Figure 2.9. Schematic diagram for the reaction mechanism showing of the Al_2O_3 and CA to form CA_6 : (a) Solid-state reaction, and (b) Solution-precipitation. After An and Soni (1996).

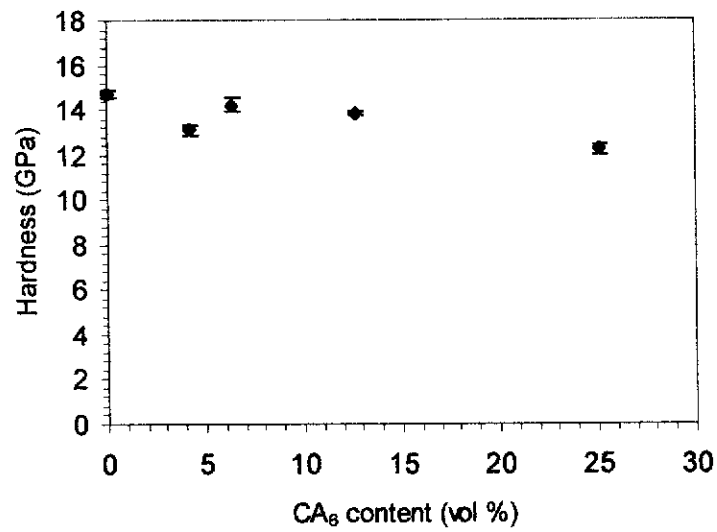


Figure 2.10. Hardness of Al₂O₃-CA₆ composite as a function of CA₆ content (vol %). Error bars indicate two estimated standard deviations (2σ). Redrawn after Criado, Pena and Cabalero (1988).

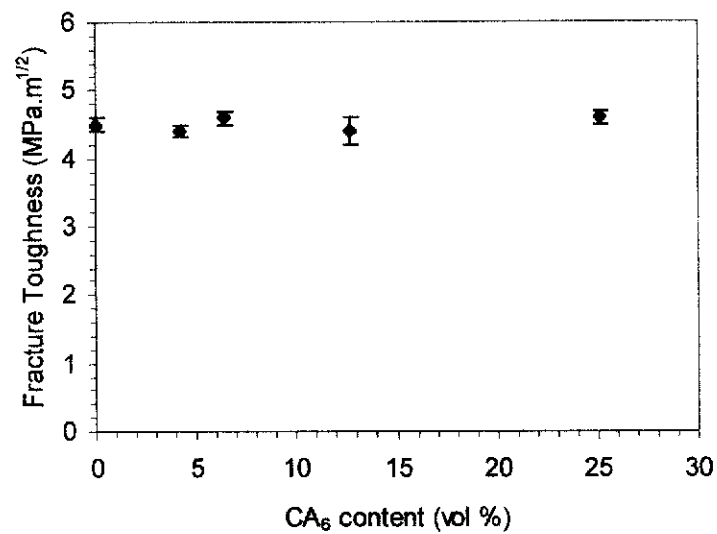


Figure 2.11. Fracture toughness of Al₂O₃-CA₆ composite as a function of CA₆ content (vol %). Error bars indicate two estimated standard deviations (2σ). Redrawn after Criado, Pena and Cabalero (1988).

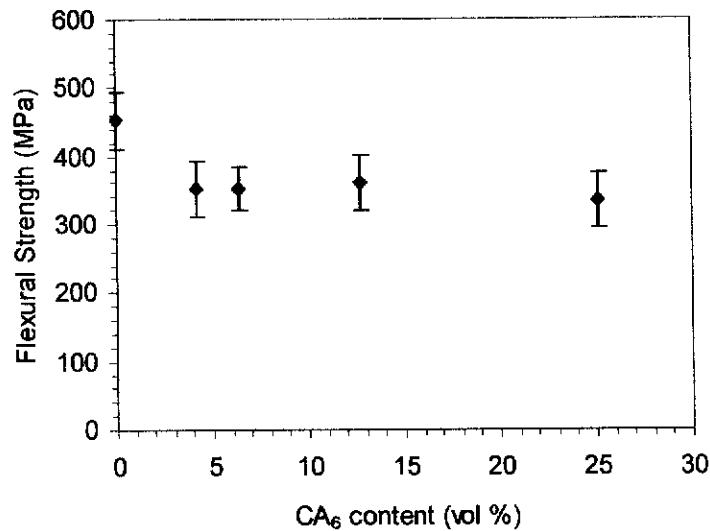


Figure 2.12. Flexural strength of Al_2O_3 - CA_6 composite as a function of CA_6 content (vol %). Error bars indicate two estimated standard deviations (2σ). Redrawn after Criado, Pena and Cabalero (1988).

An and Chan (1996) reported that the mechanical properties of Al_2O_3 can be improved by the *in-situ* formation of 30 vol % CA_6 . It has been shown that the increase in aspect ratio of CA_6 grains increases the crack growth resistance, and the crack morphology is planar when CA_6 grains are equiaxed, and tortuous when they are plates (An and Chan 1996; An, Chan and Chan 1998). The mechanical behaviour of A/30 vol % CA_6 composites was evaluated using the indentation strength technique. The measured fracture strength as a function of indentation load for the equiaxed and platelet composites is shown in Figure 2.13. Each data point on the plot represents the mean of at least five specimens. The error bars are the standard deviation limits for each data point and the solid straight line through the data corresponds to the classical Griffith result for a material with a single-valued toughness, i.e. $P^{1/3}$ dependence, which is indicative of flaw-tolerance or R-curve behaviour. As can be seen from Figure 2.13, the strength data for equiaxed (\square) and

platelet (\square) composites clearly differed in terms of their tendency to plateau at the lower indentation load region, in that the platelet composite shows more pronounced flaw-tolerance behaviour.

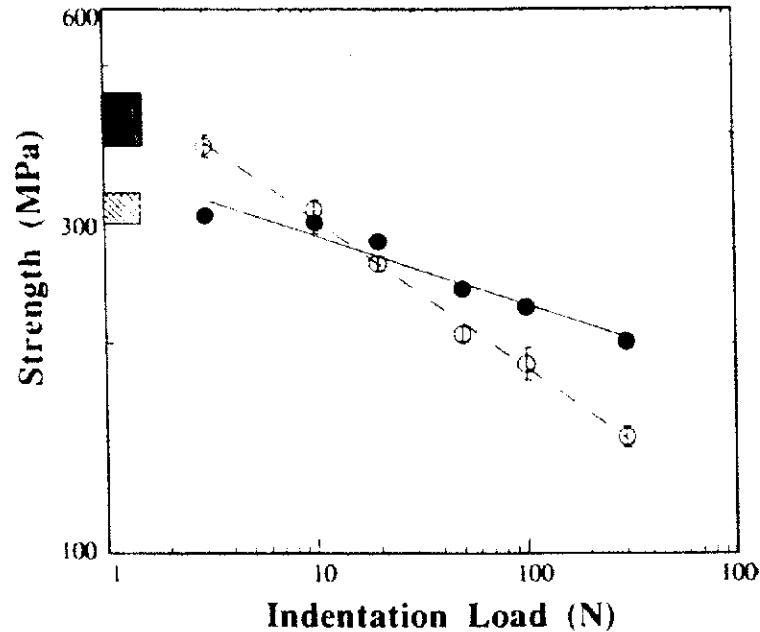


Figure 2.13. Plots of strength as a function of indentation load for (\square) equiaxed and (\circ) platelet composites. Shaded boxes at the left represent strength of unindented specimens and specimens where failure did not initiate at the indent. After An and Chan (1996).

2.3 Microstructural Design of Ceramics for Improved Mechanical Reliability

In the past, significant attention was given to the development of composites in order to limit the brittle nature of ceramics. In general, composites consist of a ceramic matrix and a homogeneously distributed second phase, which could have a spherical, *plate-like* or *needle-like* morphology. The second phase interacts with a propagating crack by deflecting the crack front or bridging the crack wake resulting in an enhancement of fracture toughness of the composite in comparison to

monolithic materials. Theoretical considerations as well as experimental results show that the dispersed second phase with a *plate-like* morphology enhances fracture toughness. The increase in fracture toughness is dependent on differences in the physical properties of the second phase and the matrix, for example thermal expansion mismatch or elastic modulus (Hoffmann 1994).

The governing principle of processing high strength polycrystalline ceramics is to achieve a flaw free material. This has led to development of highly sinterable, pure powders and their use to make fired ceramics with fewer flaws and hence higher mechanical strength (Harmer, Chan and Miller 1992). While this *flaw elimination* approach is important it is now realised that design of *flaw tolerant* ceramics for improved mechanical reliability is a more realistic and useful aim. In the flaw tolerance approach the microstructure is designed to promote crack bridging behind a propagating crack tip which leads, ideally, to the strength being independent of flaw size (Bennison and Lawn 1989) so-called *R-curve behaviour*. A major advantage of such behaviour is that strength is less sensitive to processing defect. Such behaviour, however, requires a multiphase, heterogeneous microstructure.

Major toughening mechanisms in fibre and whisker-reinforced ceramic matrix composites are elastic bridging and frictional pullout of reinforcements behind a propagating crack tip (Lee and Rainforth 1994). It is now recognised that these processes are also responsible for flaw tolerance in unreinforced ceramics such as alumina and silicon nitride. R-curve behaviour, manifests as an increase in fracture toughness as a crack grows, arises from bridging grains being wedged in the microstructure by internal compressive stresses. In non-cubic materials these wedging stresses are augmented by thermal expansion mismatch between adjacent grains. The extent of fracture toughness increase depends on such microstructural features as the size and shape of the bridging grains, the spacing between the bridges, and the residual stress field surrounding the bridging sites (Bennison and Lawn 1989). Isolated, elongated grains introduced into the microstructure are most effective in causing the R-curve behaviour. Figure 2.14 shows a comparison of

strength-crack size and fracture toughness-crack size relationships for ceramics exhibiting non-R-curve and R-curve behaviour. For non-R-curve ceramics, the strength decreases with increasing flaw size. R-curve materials, however, exhibit a range of crack sizes over which fracture strength (σ_f) is invariant, i.e. they are flaw tolerant. For non-R-curve ceramics, the fracture toughness is a constant independent of crack size. For R-curve ceramics the toughness increases with crack size (Harmer, Chan and Miller 1992).

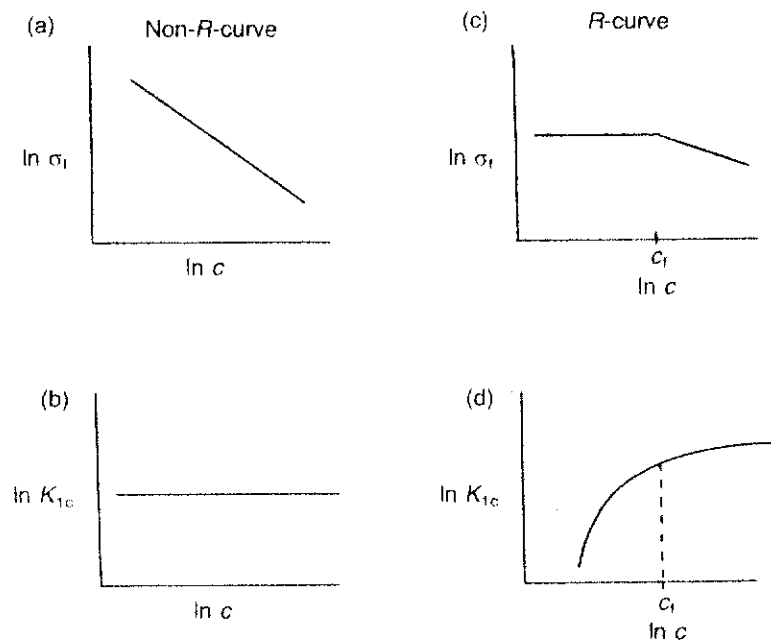


Figure 2.14. Comparison of strength-crack size and fracture toughness-crack size relationships for materials exhibiting non-R-curve and R-curve behaviour. After Harmer, Chan and Miller (1992).

In mono-phase materials, such as alumina, it has been demonstrated that one way to enhance the microstructural bridging is to increase the grain size (Chantikul, Bennison and Lawn 1990). This method is effective by increasing the grain pullout distance and, therefore, promoting flaw tolerance. However, the improvement is often achieved at the expense of strength for small flaws. A more effective approach is by *in-situ* forming of elongated grain reinforcements where significant

improvements in flaw tolerance and toughening have been achieved in silicon nitride (Li and Yamanis 1989). However, the technique for the *in-situ* formation of such duplex microstructures is based largely on empiricism.

A new approach to improving the flaw tolerance of ceramic materials is to augment the clamping stresses on the bridging grains by increasing the magnitude of the grain boundary residual stresses. In mono-phase materials, this approach is limited by the degree of anisotropy, since this determines the maximum possible mismatch in thermal expansion coefficient between neighboring grains. However, in two-phase materials, there is much greater flexibility. The residual stresses may be enhanced by the addition of a second phase whose thermal expansion coefficient shows the desired degree mismatch with that of the matrix. The mechanical behaviour of such two phase composites have been studied by several researchers (Faber, Iwagoshi and Gosh 1988; Liu and Ownby 1991; Taya *et al.* 1990). Padture, Bennison, and Chan (1993) reported that the addition of aluminium titanate to alumina results in improved flaw tolerance compared to mono-phase alumina. These improvements in the flaw tolerance are sought through enhancement of the local residual stress level.

The importance of the role of residual stresses in determining R-curve behaviour was clearly demonstrated in the alumina/anorthite systems (Padture and Chan 1992). They reported alumina/anorthite composites with intergranular crystalline phase showed more-pronounced R-curve behaviour than alumina/anorthite composite with glassy phase. This result can be explained with the respect to the crack bridging model. In the case of alumina/anorthite with glassy phase, viscous flow of the glassy second phase would be expected to allow the relaxation of the residual stresses. This in turn would reduce the effectiveness of grain bridging.

The dispersion of controlled heterogeneous microstructure in the matrix has also shown to be beneficial in the enhancement of the R-curve behaviour of ceramic materials. Lutz, Claussen and Swain (1991) reported that the dispersion of microstructural pressure zone consisting of alumina and monoclinic zirconia led to

recently been successfully used as a liquid-phase sintering aid for the densification of alumina (Latella, Burton and O'Connor 1995), mullite (Low *et al.* 1997, Low, Suherman and Phillips 1997), and aluminium titanate (Shi and Low 1998) ceramics. More recently, the addition of 15 wt % β -spodumene to alumina has been demonstrated to produce thermal shock resistant ceramics (Bayuseno, Latella and O'Connor 1999).

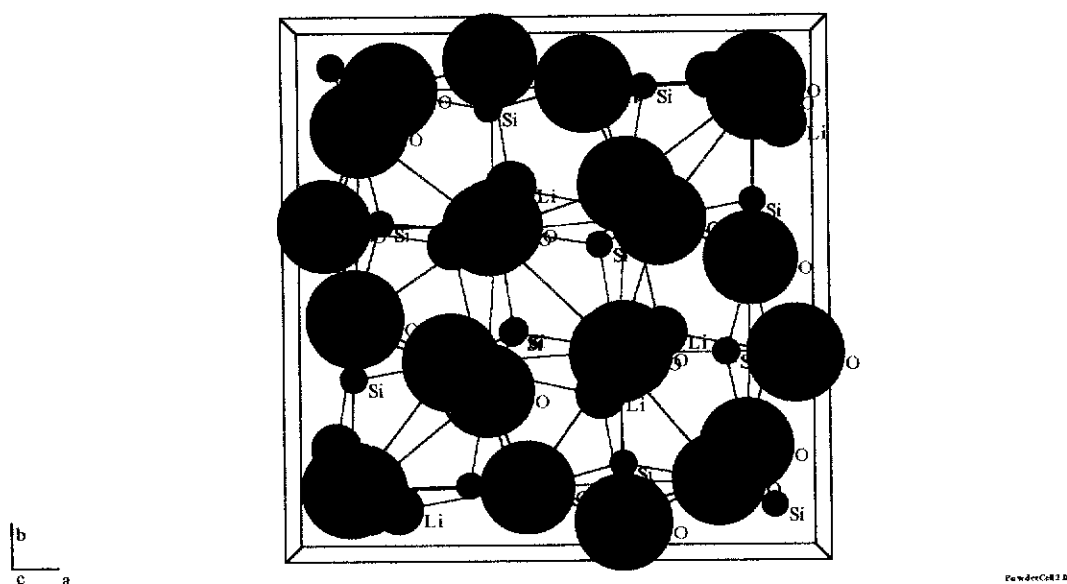


Figure 2.15. Crystal structure of β -spodumene (ICSD # 14235) projected on the (001) plane. The ion sizes are drawn in proportion to the ionic radii, i.e. 0.4 Å for Si^{4+} , 0.55 Å for Al^{3+} , 1.35 Å for O^{2-} , and 0.7 Å for Li^{+} .

2.5 Functionally-Graded Materials (FGMs)

2.5.1 Introduction

Design of functionally-graded materials (FGMs) is a novel concept for recognition of innovative properties or functions that cannot be achieved by conventional homogeneous materials (Koizumi 1992). Functionally graded materials are materials with a smooth gradient in one or more properties, which is essential for their function. The property gradient is usually caused by a gradient in chemical composition or microstructure. These materials are wide spread in nature, for example graded structures are found in the culms of bamboo and barley and many other plants. However, it was only in 1984 that the concept of functionally-graded materials (FGMs) has been developed by Niino and co-workers who were searching for materials capable of withstanding the high heat fluxes occurring during re-entry of space vehicles. In general, this material consists of one material on one side, a second material on the other, and an intermediate layer between them whose structure, composition and morphology vary smoothly from one material to the other at the micron level (Kawasaki and Watanabe 1997). Since then, it has been recognised that the concept of a property gradation can be useful in many applications where one component has to fulfil contrasting requirements in different positions and a joint is inappropriate.

From the context mentioned above, this section first describes briefly the fundamental concept of FGMs. Then, the general fabrication methods for producing them. Following this, the infiltration processing of FGMs with a brief explanation of infiltration kinetics and modeling. Finally, FGM-based alumina composites developed at Curtin University will also be described.

2.5.2 Fundamental Concepts of Functionally-Graded Materials (FGMs)

As outlined in section 2.4.1 the concept of functionally-graded materials (FGMs) was initially proposed in 1984 as a means of tailoring a superheat resistant material of a type aimed for superior thermal stress relaxation (Koizumi 1992). This

type of FGM is required to possess not only high oxidation resistance and thermal shock resistance but also have superior thermal stress relaxation and thermal barrier characteristics. In this way, the FGM concept was expected to be applicable to materials for functional uses as well as structural applications. Since then, interest in FGMs has grown rapidly and about 200 possibilities of utilizing FGM concept have been proposed (Koizumi 1997).

Figure 2.16 shows a conceptual diagram of functionally-graded materials, taking into account the relaxation of thermal stress (Koizumi and Niino 1995). For the surface that contacts high temperature gases at thousands of degrees ($> 2000\text{ }^{\circ}\text{K}$), ceramics are candidate materials used to provide adequate heat resistance. Whereas, for the other surface that provides cooling as low as $1000\text{ }^{\circ}\text{K}$, metallic materials are used to furnish the necessary thermal conductivity and mechanical strength. Furthermore, the composition of these materials is formulated to provide optimum distribution of composition, structure, and porosity to effectively relax thermal stress. The continuously changing in composition or structural elements within this material can occur not only in thickness direction but also width direction. The comparison of structure, composition, and properties of functionally-graded materials and uniform bilayer materials is shown in Figure 2.17. A typical FGM possesses systematic but continuous variation in composition and microstructure across the material, resulting in a gradual change in properties from one surface to another.

Recently, Kawasaki and Watanabe (1997) have identified two essential aspects to be considered in the design of functionally-graded material. The first aspect includes the tailoring of chemical composition and microstructure on the basis of property distribution to achieve the desired function. The second aspect involves the availability of fabrication processing with excellent reproducibility as an advanced technology for gradient. In order to achieve the two of them, the materialization system approach should be applied. As shown in figure 2.18, the approach for FGM development consists of a loop of three processes, material design, fabrication and evaluation that are linked closely together.

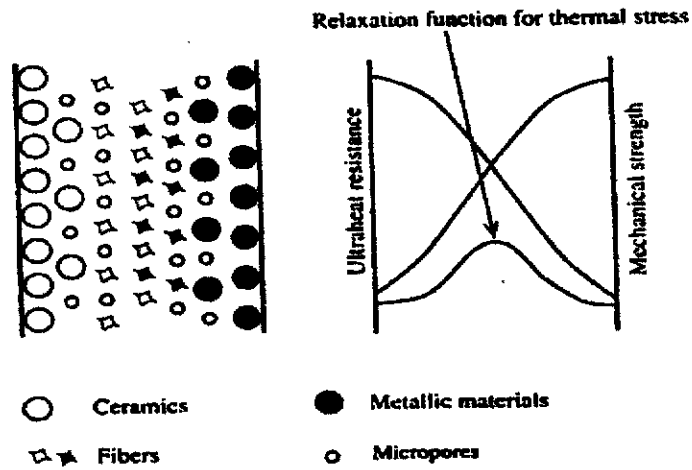


Figure 2.16. Conceptual diagram of functionally-graded materials for the relaxation of thermal stress. After Koizumi and Niino (1995).

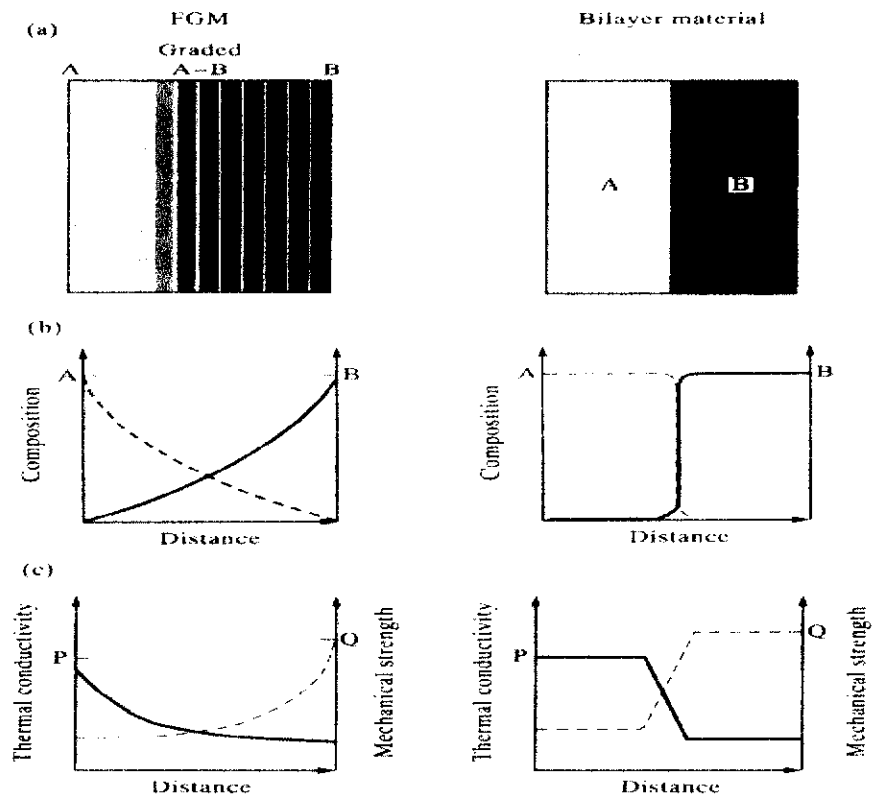


Figure 2.17. Comparison of (a) structure, (b) composition and (c) properties of functionally-graded materials and uniform bilayer materials. After Choy (1996).

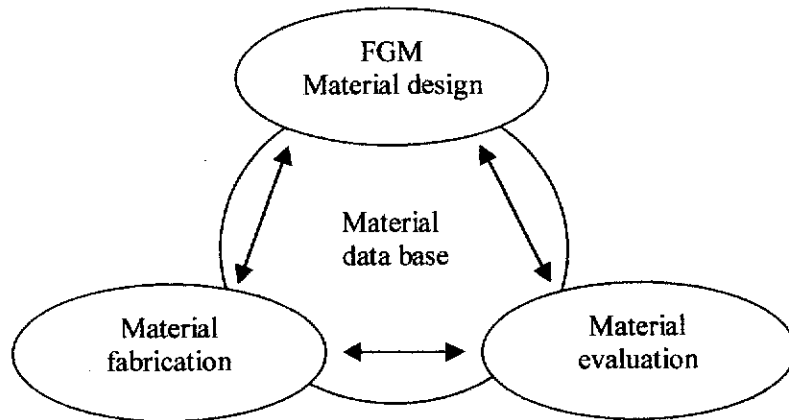


Figure 2.18. Approach for a functionally-graded material (FGM) development. Redrawn after Koizumi and Watanabe (1997).

2.5.3 Fabrication Methods for Producing Functionally-Graded Materials (FGMs)

The fabrication of functionally-graded materials (FGMs) has been successfully demonstrated through a variety of methods. The most important objective in the fabrication of a FGM is to achieve a well-controlled not only distribution of composition but also other necessary elements such as microstructure, crystal structure, and pores (Hirai 1996). In other words, for a FGM system, it is necessary to fully consider the relationships between the material characteristics and structures before selecting the method of fabrications. The fabrication processes can be classified into three approaches, i.e. gas, liquid, and solid. Typical fabrication methods and examples of FGMs are presented in Table 2.1.

Table 2.1. Fabrication methods and examples of functionally-graded materials
(After Hirai 1996)

Method	Examples
<i>Vapor phase methods</i>	
CVD (Chemical Vapor Deposition)	SiC/C, TiC/C, SiC/TiC, BN/Si ₃ N ₄ , SiC/TiC-SiC, SiO ₂ /SiO ₂ (GeO ₂)
CVI (Chemical Vapor Infiltration)	SiC/C, TiB ₂ /SiC
Ion plating	TiN/Ti, TiC/Ti, CrN/Cr
Chemical gas reaction	SiC/C
<i>Liquid phase methods</i>	
Sol-gel	SiO ₂ /TiO ₂ , SiO ₂ /GeO ₂
Molten metal infiltration	SiC/C, W/Cu, Al ₂ O ₃ /Al, SS/Cu
Electro-depositing	Cu/CuZn, Cu/CuNi, ZrO ₂ + Ni/Ni, SiC/C
Electro-plating	Cu/CuZn, Cu/CuNi
Plasma spraying	PSZ/NiCrAlY, PSZ/NiCrAl, PSZ/NiCr, PSZ/SS
Centrifugal casting	SiC/Al
<i>Solid phase methods</i>	
<i>(a) Powder stacking methods</i>	
Centrifugal	ZrO ₂ /NiCr
Spraying	PSZ/SS
Powder Infiltration	Al ₂ O ₃ /Ni
Slip casting	ZrO ₂ /Ni, ZrO ₂ /SS, Al ₂ O ₃ /W, Al ₂ O ₃ /ZrO ₂ , Al ₂ O ₃ /Al ₂ TiO ₅ ,
<i>(b) Sintering methods</i>	
Sintering, Hot-pressing (HP), and Hot-isostatic pressing (HIP)	PSZ/SS, YSZ/Mo, Al ₂ O ₃ /Ni, MgONi, SiC-AlN/AlN/Mo, AlN/Ni, AlN/Al, Si ₃ N ₄ /Mo
Plasma activated	PSZ/TiAl, PSZ/Ti, YSZ/SS
Self-propagating high-temperature synthesis (SHS)	TiB ₂ /Cu, TiB ₂ /Ni, TiC/NiAl, TiC/Ni, AlN/Al, AlN/Ni, Cr ₃ C ₂ /Ni, Cr ₃ C ₂ /TiC
Diffusion and reaction	ZrO ₂ /Al ₂ O ₃ , PZT/NiNb, SiC/C, Al ₂ O ₃ /Sn/Nb/Sn/Al ₂ O ₃ , Ti ₅ Si ₃ /Ti, ZrSi ₂ /Zr

2.4.4 Infiltration Processing of Functionally-Graded Materials (FGMs)

Infiltration is the term commonly applied to the physical process of liquid- or gas-phase entry into the porous media through the surface. This mechanism has been studied by many researchers in the fields of soil physics (Carman 1956), chemistry (Kubo *et al.* 1972), powder technology (Sendlak and Rhines 1958) and powder metallurgy (Obuchi and Watanabe 1970). Recently, liquid- or gas-phase infiltration of preforms has now emerged as a very useful technique for the processing of composite materials. The former involves the use of a low viscosity liquid such as sols, metal- or polymer-melts. The latter is concerned primarily with the use of chemical vapor deposition. A variety of infiltration techniques have been developed for the processing of composites and these include vacuum (Chung and Lin 1996; Chung, Chang and Lin 1999), high pressure (Liu 1996; Cardinal, R'Mili and Merle 1998), spontaneous (Aghajania and Nagelberg 1996; Xi *et al.* 1996; Trumble 1998) and chemical vapour (Ofori and Sotirchos 1997; Kawase *et al.* 1999). For instance, metal matrix composites (MMC) are commonly fabricated by vacuum or pressure infiltration of preforms with molten metals (Vassel *et al.* 1996). Similarly, a ceramic-matrix ceramic (CMC) can also be easily synthesized by pressure infiltration of preforms with either a liquid- or a gas- phase precursor (Riccieli and Marshall 1994). Using this infiltration process, it is possible to design new materials not only with unique microstructures (i.e. graded, multiphase, microporous, etc) but also unique thermomechanical properties (i.e. graded functions, designed residual strains, thermal shock, etc).

Liquid infiltration was chosen in this study for several reasons. Firstly, its cost-effectively and versatility. Secondly, this method has been successfully used for the preparation of multiphase ceramic composite materials. For examples mullite/alumina composites developed by Marple and Green (1990, 1991, 1993), the mullite/zirconia-toughened alumina (ZTA), AT/alumina and AT/mullite/ZTA systems developed by Low and co-workers (Low *et al.* 1993, 1994, 1996; Pratapa and Low 1996). Recently, the CA₆/alumina system has been developed by Asmi and

Low (Asmi and Low 1998; Asmi *et al.* 1999). Finally, this method brings two advantages when compared to the commonly used powder. Firstly, in terms of preparation where only monophase porous ceramic host is needed therefore problems with homogeneous mixing of several constituents in a multicomponent system can be avoided. Secondly, the density of the ceramic green body increases after infiltration due to filling of the open pores with the product of infiltrant, therefore, higher density products with lower shrinkage after sintering can be achieved (Galusek and Majling 1995).

Infiltration Kinetics and Modeling

The theoretical analysis of liquid penetration through porous ceramic preforms depends on two considerations. First, the nature of the porosity, specifically the spatial variation pores size in the preform, the tortuosity and the connectivity on the porous network influence the penetration. Second, due to the change in the permeability of the preform, segregation of solutes and discontinuous deposition of reaction products (Asthana, Rohatgi, and Tewari 1992). No comprehensive literature exists at present that deal with these entire factors, although empirical manipulation of process variables to achieve some control on structure and properties of infiltrated ceramic composites has been possible.

The study of infiltration processes has been one of the main goals for the investigation of infiltration behaviour. Washburn (1921) modelled the rate of infiltration by assuming porous media to be a constant cross section capillary. In the case of good wetting, the liquid-vapor surface within a single pore channel will develop a concave curvature (meniscus) depending on the contact angle and the pore size. Across the meniscus a pressure difference called capillary pressure builds up, driving the liquid into the porous preform. Under this assumption, the flow in a capillary follows the Poiseuille's law (Von Mises and Fredricks 1971), which states that

$$\frac{dV}{dt} = \frac{\pi r^4 dp}{8\mu h} \quad (2.3)$$

where dV is the volume of liquid which in time dt flows through a length, l , of a capillary having a radius, r . μ is the viscosity of liquid and dp is the total effective pressure acting to force the liquid along the capillary. So, by considering

$$dV = \pi r^2 dl \quad (2.4)$$

and the capillary pressure, dp by the following Young-Kelvin equation:

$$dp = \frac{2\gamma \cos\theta}{r} \quad (2.5)$$

where γ is the surface tension of liquid and θ is the contact angle between the liquid and the preform, Equation 2.3 may be written in terms of a velocity:

$$\frac{dl}{dt} = \frac{r\gamma \cos\theta}{4\eta l} \quad (2.6)$$

Integration of Equation 2.6 will give the expression for the relationship between the length of infiltration as a function of time:

$$l^2 = \left(\frac{r\gamma \cos\theta}{2\eta} \right) t \quad (2.7)$$

Dullien, El-Sayed and Batra (1977) applied Equation 2.7 (Washburn model) to a real porous media, in which the effective channel radius was defined by taking into consideration the varying segments of a real porous media. Einset (1996) used the effective radius to replace the average pore radius in the Washburn equation, giving a successful explanation of the parabolic behaviour of the infiltrations of

several organic solvents into compact formed from a mixture of carbon and silicon carbide powders.

Scheidegger (1974) has also described the flow of liquid into a porous media by capillary pressure using the Darcy equation:

$$l^2 = \left(\frac{2kP}{\eta} \right) t \quad (2.8)$$

where $P = P_c + P_a - P_i$ are the capillary pressure, the applied pressure, and the pressure of displaced gas, respectively. When the powder compact is modeled using identical spheres of diameter d with a relative density ρ and the porosity modeled with an equivalent capillary of radius r , the capillary pressure is given by

$$P_c = \frac{2\gamma \cos \theta}{r} = \frac{6\gamma \cos \theta}{d(1-\rho)} \quad (2.9)$$

In Equation 2.8, k is the permeability of porous media and is commonly expressed by the Kozeny-Carman equation (Tu and Lange 1995):

$$k = \frac{d^2(1-\rho)^3}{36 T \rho^2} \quad (2.10)$$

where T is a constant that defines the shape and tortuosity of the pore channel.

When a powder compact contains air, the expression for gas diffusion is given by the Fick's law (Geiger and Poirier 1980):

$$l^2 = (2D\beta P_i) t \quad (2.11)$$

where D is the diffusion coefficient of the gas within the liquid and β is Henry's constant. The flow of liquid due to capillary pressure dominates initially which will be followed by gas diffusion once the gas within the body is sufficiently compressed, despite the fact that both processes occur concurrently (Lange, Tu and Evans 1995). Tu and Lange (1995) studied the kinetics of infiltration of a solution precursor into silicon nitride preforms and proposed that the infiltration process involved two parabolic stages, i.e. the initial stage could be described by Darcy's law and the final stage fitted by Fick's law. The opposing internal pressure of the compressed gas (P_i) is primarily responsible for the formation of a composition gradient within the body.

Based on the Darcy's fundamental principle and the Kozeny-Carman equation (Carman 1956), Semlak and Rhines (1958) and Yokota *et al.* (1980) have also developed similar infiltration rate equations, which are respectively

$$l^2 = \frac{2}{\pi} \left(\frac{r \cos \theta_{\infty}}{2\eta} \right) t \quad (2.12)$$

$$l^2 = \frac{2}{\sqrt{5}} \left(\frac{p\gamma r \cos \theta_{\infty}}{\eta} \right) t \quad (2.13)$$

where r , θ_{∞} , p , γ , and η are respectively average pore radius, equilibrium contact angle, porosity, surface tension of liquid, and viscosity of infiltrant.

2.4.5 Development of FGM-Based Alumina Composites at Curtin University

Over the last four years, Dr. Low and his research students at Curtin have investigated a new generation of functionally graded materials using the various liquid infiltration techniques. The design of these FGMs involved the fabrication of pre-sintered porous preform, followed by its infiltration into a liquid infiltrant and

Aluminium Titanate/Alumina (AT/A) System

The functionally graded aluminium titanate/alumina (AT/A) system has been successfully demonstrated using the infiltration technique (Low, Skala, and Zhou 1996; Low 1998; Skala 2000). Tetraethyl orthotitanate (TEOT, a TiO₂-rich organic solution) was used as infiltrant. Sintering at 1550 °C for 4 h was applied to the specimens to allow the formation of alumina titanate/alumina and densification of the specimens. The formation of alumina titanate occurred according to the reaction:



The graded profile composition was characterised by elemental dot-mapping and electron microprobe analysis. Both Ti and Si x-ray maps revealed the graded nature of material.

The Vickers hardness profile at a load of 30 N for the FGM from the homogeneous alumina layer to the graded AT/A layer is presented in Figure 2.19. The gradual reduction in hardness from the alumina interface verifies the presence of a continuous AT concentration gradient in the graded layer. The decrease in hardness commensurates with an increase in abundance of softer AT phase away from the interface (Low 1998).

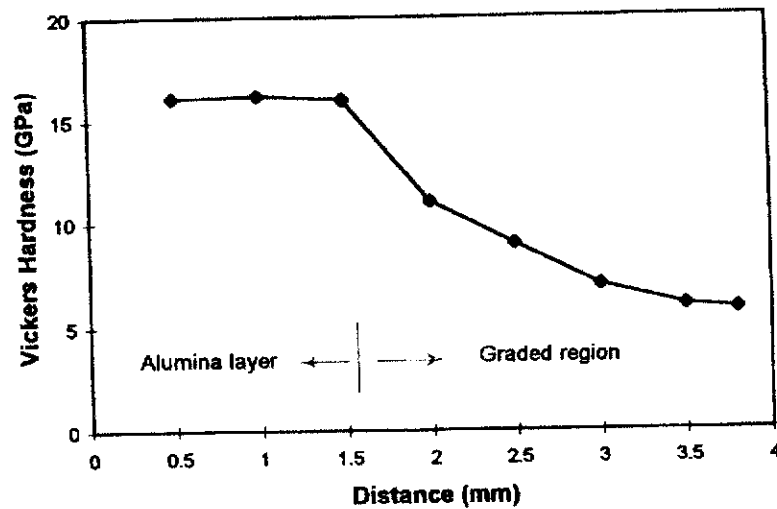


Figure 2.19. Vickers hardness of AT/A as a function of distance at a load of 30 N. After Low 1998.

Aluminium Titanate/Zirconia-Alumina (AT/ZA) System

The functionally graded aluminium-titanate/zirconia-alumina (AT/ZA) system has been studied using infiltration of alumina-zirconia (AZ) preform with a solution of TiCl_4 (Pratapa 1997; Pratapa, Low and O'Connor 1998). Sintering at 1550°C for 3 h was employed to produce densification of the material. The graded character of the FGM was confirmed by a graded composition as revealed by quantitative XRD and scanning electron microscopy. The gradual decrease of AT with increasing depth showed that the material exhibited a graded compositional character. The graded compositional character was also characterised qualitatively using energy dispersive x-ray microanalysis (see Figure 2.20). It was found that titanium emissions reduce with increasing depth, whereas those of aluminium and zirconium are nearly constant (Pratapa 1997). This results show that infiltration has led to the formation of a graded microstructure.

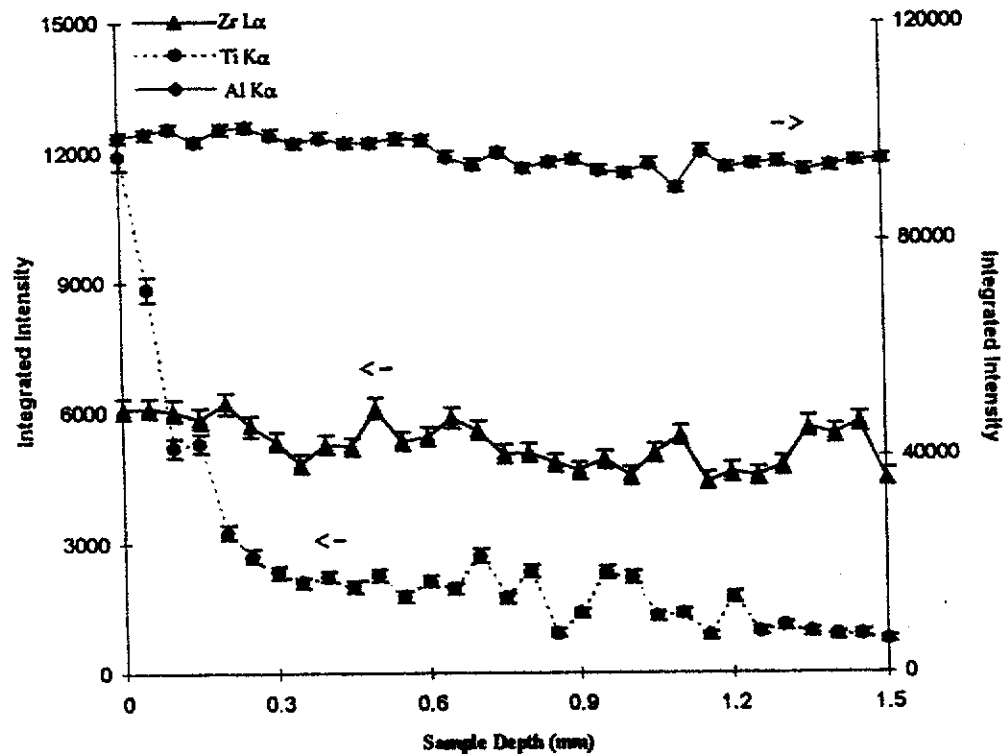


Figure 2.20. Energy dispersive x-ray microanalysis of Ti K α , Al K α , and Zr K α as a function of depth for functionally graded AT/ZA composites. Error bars indicate 2 x estimated standard deviations. After Pratapa (1997).

The functionally graded AT/ZA system exhibits unique properties (i.e. graded thermal and mechanical properties). Pratapa (1997) found that the surface is soft damage tolerant as indicated by its load-dependent hardness and has a low thermal expansion (i.e. $5.6 \times 10^{-6} \text{ }^{\circ}\text{C}^{-1}$). In contrast the core is harder and it has a higher thermal expansion (i.e. $7.4 \times 10^{-6} \text{ }^{\circ}\text{C}^{-1}$). Therefore, this unique property is very useful where two extremely different properties are desired.

CHAPTER 3

EXPERIMENTAL METHODS

3.1 Introduction

This chapter describes the experimental strategy in the research which was developed to achieve the objectives. The experimental procedures associated with the research objectives are described. These procedures were concerned with the fabrication and design of novel alumina/calcium-hexaluminate (A/CA₆) ceramic composites with both wear and damage resistance. An *in-situ* reaction sintering method and an *innovative* infiltration process were developed to produce A/CA₆ ceramic composites with high mechanical performance and controlled microstructure. There were three crucial components of the experimental procedure: processing, characterisation, and properties evaluation.

3.2 Processing

A crucial goal of the processing strategy was to produce composites of high density, desired microstructure and phase distribution. The various steps used to produce the required materials are outlined in the following sections.

3.2.1 Powder and Liquid Precursor Preparations

Commercial Al₂O₃ (A1000SG grade ALCOA USA), CaCO₃ (analytical UNIVAR), calcined β -spodumene (Li₂O.Al₂O₃.4SiO₂) supplied by Gwalia Consolidated Ltd., Western Australia, and calcium acetate (Unilab chemicals) was used as raw materials. Table 3.1 shows the chemical composition of the raw materials. The median particle sizes for as received alumina, calcium carbonate and β -spodumene powders were 0.54 μ m, 15.53 μ m, and 18.83 μ m, respectively. Accordingly, no milling trials were performed on the alumina powder, however

substantial milling of the calcium carbonate and β -spodumene powders was required prior to processing of the composites. The procedure of powder and liquid precursor preparation to produce A/CA₆ composites is described below.

Table 3.1. Chemical compositions (wt%) of starting raw materials

	Alumina	Calcium carbonate	β -spodumene
Al ₂ O ₃	99.7		27.0
CaCO ₃		99.5	
SiO ₂	<0.01		64.0
TiO ₂	<0.01		0.02
Fe ₂ O ₃	0.03	0.005	0.16
CaO	0.05		0.04
MgO	<0.01	0.1	0.02
Na ₂ O	0.06	0.01	0.19
K ₂ O	0.06	0.05	0.05
SO ₄		0.01	
Li ₂ O			8.10
P ₂ O ₅	<0.01		0.11
LOI	0.46	<0.5	0.3

Alumina (α -Al₂O₃)

Alumina powder for fabrication of composite was obtained by wet ball milling Al₂O₃ (A1000SG grade ALCOA USA) with 3 wt% propylene glycol as antiflocculant. An analytical balance (FX-300, A & D Company) with an accuracy 0.01 g was used to weigh batch formulations of 200 g of alumina. The powder was mixed with 150 ml methanol and turbula milled for 3 h with 3 mm diameter high purity alumina media. The slurry obtained was then dried in an oven at 60 °C for 24 h. The powder cake was then ground to a fine powder using a mortar and pestle, followed by screening with 150 μ m, 75 μ m and 45 μ m grid-size sieves.

Calcium carbonate (CaCO_3) and β -spodumene ($\text{Li}_2\text{O} \cdot \text{Al}_2\text{O}_3 \cdot 4\text{SiO}_2$)

These materials were processed by a similar procedure used to prepare the alumina powder. The as-received raw materials had a relatively broad size distribution and a median particle size of 15.53 μm , and 18.83 μm , respectively. Hence, controlling the initial particle size by milling was required in these powders before processing of composites. The milling time was increased to 5 h for calcium carbonate and 8 h for β -spodumene. Particle size analysis was determined before and after milling using a laser scattering instrument.

Calcium-hexaluminate (CA_6) Precursor

The powder precursor of CA_6 was prepared from a well-mixed 6:1 mixture of processed alumina and calcium carbonate powders. The mixed powders were prepared using the same milling procedure described above. The powder mixture was then calcined at 900°C for 2 h to decompose the calcium carbonate. This step was taken to remove the CO_2 which might otherwise be trapped and hinder the processes of sintering and densification. The calcined precursor CA_6 powder was then again homogenised by following the similar procedure milling described above. Several milligram powders were then sent to the Division of Minerals CSIRO, Bentley Western Australia for particle size analysis. The chemical analysis of CA_6 precursor was not evaluated at this stage.

Liquid Precursor (Calcium acetate)

The liquid precursor was prepared by dissolving 26.8 g of calcium acetate powder in 100 ml deionised water. The liquid precursor mixture was stirred for 1 h using a magnetic stirrer followed by ultrasonic stirring for 0.5 h. In order to determine the temperature at which the calcium acetate decomposed to CaO , 15 ml of the solutions were allowed to settle for 48 h at room temperature and the gel allowed to dry at 80 °C in oven for 3 days. The cake was then ground to a fine powder using a mortar and pestle. Simultaneous DTA and TGA measurements on the

powder were carried out on a Netzsch STA-409C instrument in nitrogen atmosphere at a heating rate of $10\text{ }^{\circ}\text{C min}^{-1}$ with an empty reference.

3.2.2 Preparation of Ceramic Composites

Two different processing routes were used to fabricate the ceramic composites. A conventional reaction-sintering method was used to prepare *in-situ* A/(0 - 100) wt% CA_6 and β -spodumene modified A/30 wt% CA_6 composites. An innovative *infiltration technique* was employed to prepare functionally-graded A/ CA_6 composites. The details of each step are described below.

In-situ Reaction Sintered A/ CA_6 composites

Figure 3.1 shows the flowchart of the conventional processing of *in-situ* reaction sintered A/ CA_6 composites. The composites were prepared from well-mixed alumina and (5 - 50 wt%) CA_6 precursor (see section 3.2.1). The powder was mixed with 150 ml methanol and wet ball-milled for 3h with 3 mm diameter high purity alumina media. The slurry was then dried in oven at 60°C for 48 h and ground with mortar and pestle. The powder obtained was then screened with 150, 75 and $45\text{ }\mu\text{m}$ grid-size sieves. The powder mixture was then uniaxially pressed in a metal-die at 150 MPa to yield cylindrical pellets with dimensions of 5 mm height and 19 mm diameter and bar-shaped with dimensions of 5 mm depth, 10 mm width, and 60 mm length. These samples were fired in air at 1400°C for 12 h, followed by 1650°C for 2 h, and then furnace-cooled.

Table 3.2 Formulations of various *in-situ* reaction sintered A/ CA₆ composites.

Sample	Alumina (wt%)	CA ₆ (wt%)
A100	100	0
CA5	95	5
CA15	85	15
CA30	70	30
CA50	50	50
CA100	0	100

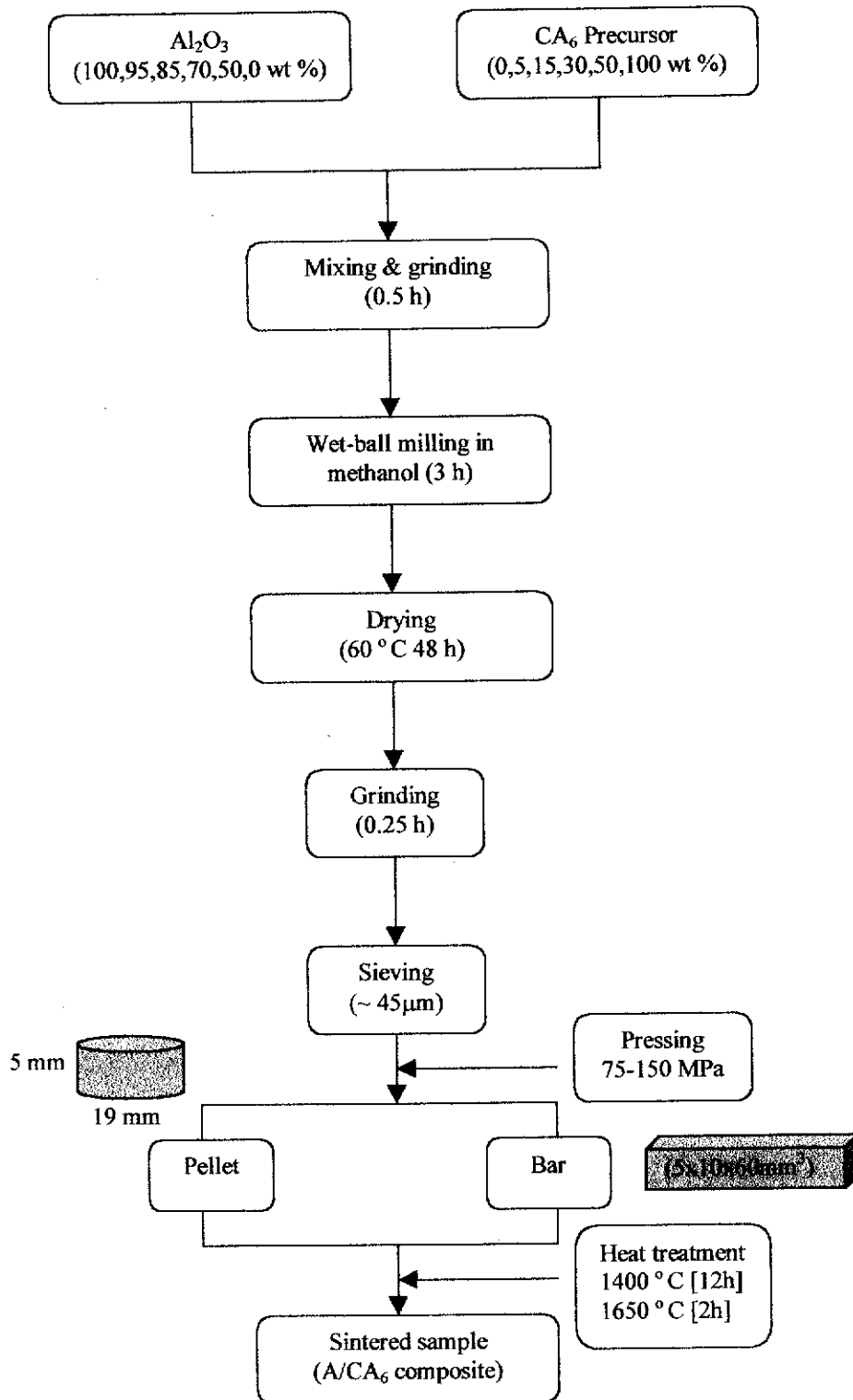


Figure 3.1. Processing of *in-situ* reaction sintered Al/CA₆ composites.

β -spodumene modified A/CA₆ Composites

This experiment was conducted to determine the influence of β -spodumene addition on the sintering and densification behaviour of A/CA₆ composites. Figure 3.2 shows the flowchart of the processing of β -spodumene modified A/CA₆ composites.

To synthesise β -spodumene modified A/CA₆ composites, the processed alumina powder was wet ball-milled in methanol for 3 h with 30 wt% of CA₆ precursor and 0, 2.5, 5, 10, 15 wt% of spodumene. The slurry was then dried in oven at 60 °C for 48 h and ground with mortar and pestle. The obtained powder was then screened through a 175, 75 and 45 μ m sieved, followed by uniaxially-pressing in a metal die at 150 MPa to yield cylindrical pellets 5 mm high and 19 mm in diameter and also rectangular bars with dimensions 5mm depth, 10 mm width, and 60 mm in length. These samples were fired in air at 1400 °C for 12 h, followed by 1650 °C for 2 h, and then furnace-cooled.

Table 3.3. Formulations of various β -Spodumene modified A/CA₆ Composites.

Sample	A/CA ₆ precursor (wt%)	β -spodumene (wt%)
CAS0	100	0
CAS2	97.5	2.5
CAS5	95	5
CA10	90	10
CA15	85	15

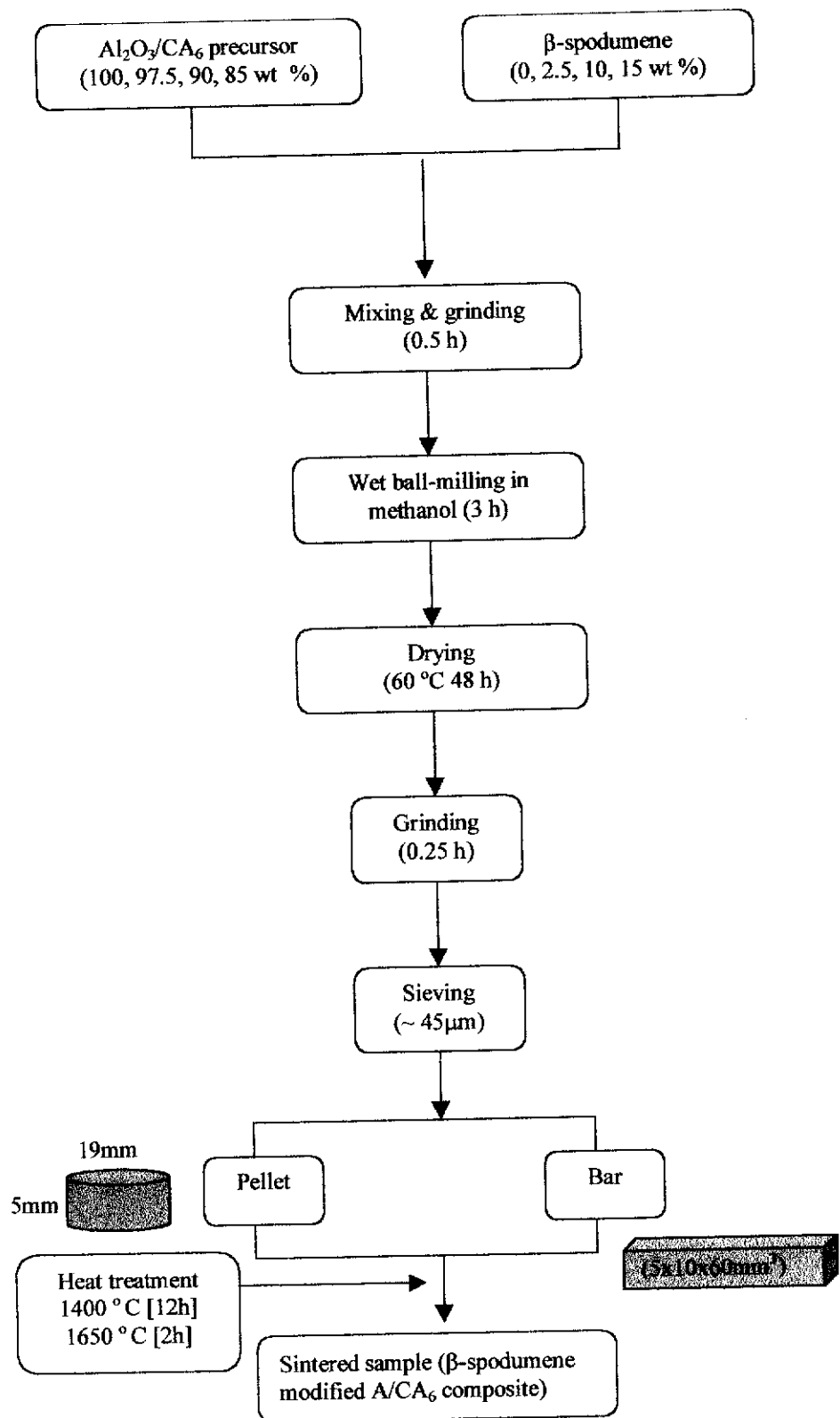


Figure 3.2. Processing of β -spodumene modified A/CA₆ composites.

Functionally-Graded A/CA₆ Composites

Figure 3.3 shows the schematic flowchart of the *liquid-infiltration* method for fabrication of functionally-graded alumina/calcium-hexaluminate composites. The same processed alumina powder (see section 3.2.1) was used to prepare the porous alumina preforms for subsequent infiltration. Preforms were fabricated by uniaxial pressing of alumina powder at 75 MPa to yield a bar sample of dimensions 5x12x60 mm³. For applications where the aim is to maximise the amount of CA₆ incorporated into Al₂O₃ matrix, it is desirable that the preform has a high volume fraction of porosity. For this reason, a trial partial sintering (see section 3.3) at a temperature ranging 900 - 1200 °C for 2 h was used to increase the strength and retain the porosity (~ 41 - 47%) of the preform prior to infiltration.

Infiltration of the porous preform was conducted at room temperature. To produce a functionally-graded material (FGM), the sample was immersed partially in a solution of calcium acetate (Unilab Chemicals) for 5 h. In order to ascertain the formation of each of calcium aluminate phases (CA, CA₂, and CA₆) a fully infiltrated alumina preform was conducted for 8h. The infiltrated preform was then dried at room temperature for 24 h prior to heat-treatment in a high temperature furnace at 1400 °C for 12 h, followed by 1650 °C for 2 h, and then furnace-cooled.

Infiltration Kinetics

The kinetics of infiltrating a liquid precursor into alumina preforms were studied using water and an aqueous solution of calcium acetate. Infiltration measurements of previously evacuated (0.1 torr) preforms were performed either in vacuum or in an ambient condition. In the former, the bottom of the preform was slightly immersed in a beaker containing the solution within a chamber evacuated to 0.1 torr throughout the measurement. The height of infiltrant rise was recorded visually as a function of time. The effect of preform sintering temperatures, liquid type, vacuum and non-vacuum and multiple infiltrations on the infiltration behaviour were also investigated.

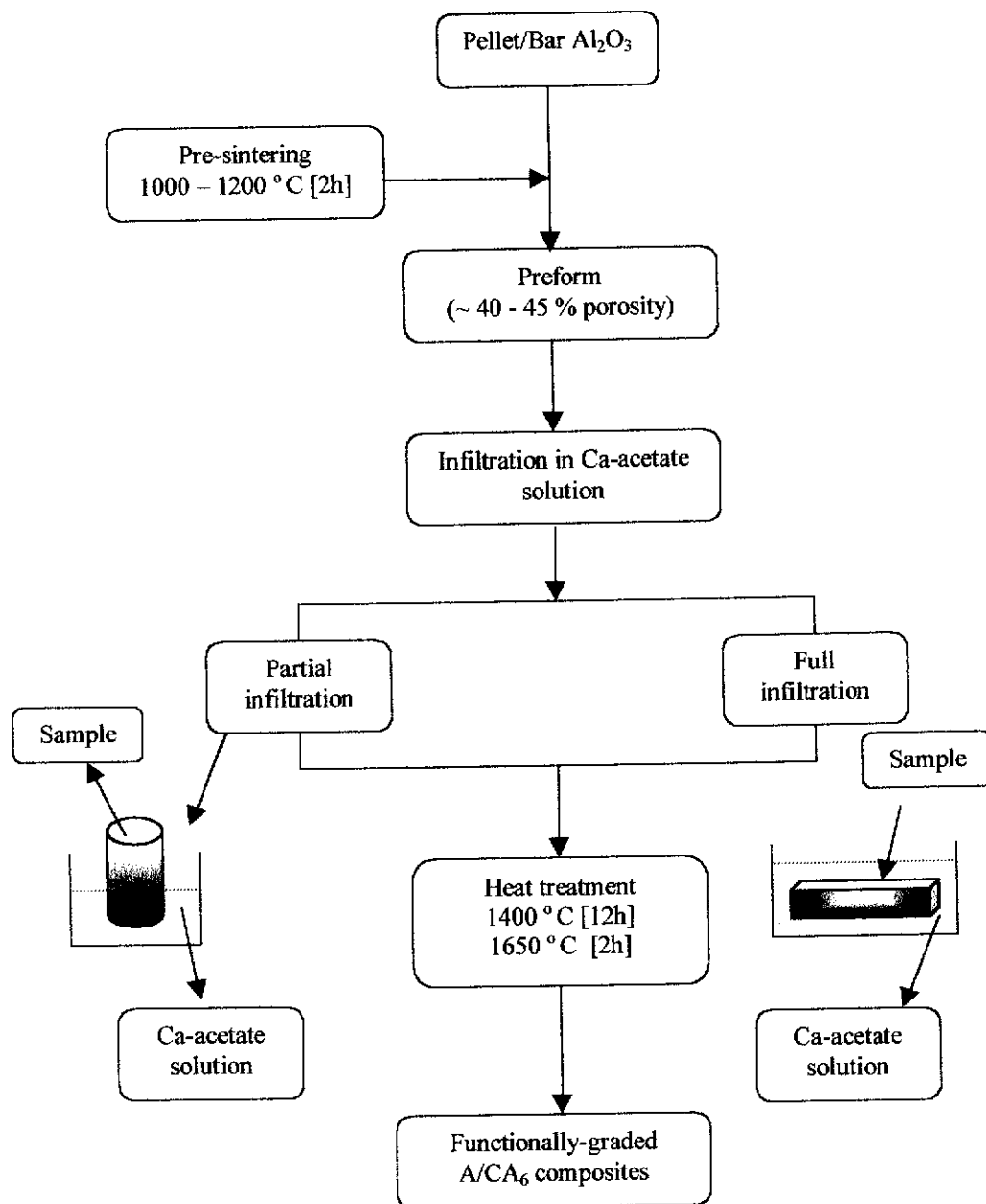


Figure 3.3. Liquid infiltration processing of functionally-graded A/CA₆ composites.

3.3 Heat Treatment Schedules and Densification of A/CA₆ Composites

Samples were fired in a high-temperature furnace (Model HT 04/17, Ceramic Engineering). The samples were placed on a 99.9 % alumina tray and coated with alumina powder to prevent sticking. The heat treatment schedules conducted in each case were system-specific, as summarised below:

(i) Partial sintering of porous Al₂O₃ preform:

200 °C/h to 450 °C dwell 30 minute

300 °C/h to 900-1200 °C dwell 2h

450 °C/h cool to room temperature

(ii) Formation of CA, CA₂, and CA₆

200 °C/h to 450 °C dwell 30 minute

300 °C/h to 1000-1650 °C dwell 0.5h

450 °C/min cool to room temperature

(iii) A/(0-50 wt %) CA₆ , β-spodumene modified A/(30 wt %)CA₆ , and functionally-graded A/CA₆ composites:

200 °C/h to 450 °C dwell 30 minute

300 °C/h to 1400 °C dwell 12h

300 °C/h to 1650 °C dwell 2h

450 °C/h cool to room temperature.

3.4 Characterisation

3.4.1 Particle Size Analysis

The particle size for as-received Al₂O₃, CaCO₃, and processed CA5, CA15, CA30, CA50, CA₆ precursor, CAS2.5, CAS10, and CAS15 powders was measured using a Malvern Mastersizer laser diffraction instrument at the CSIRO, Division of Minerals, Particle Analysis Service, Bentley, Western Australia. Powders were initially dispersed in water using a sodium hexamethaphosphate solution.

3.4.2 Analysis of Phase Compositions and Developments

X-ray Diffraction (XRD) Analysis

Laboratory x-ray diffraction (XRD) patterns for all heat-treated samples were conducted with an automated Siemens D500 Bragg-Brentano instrument using $\text{CuK}\alpha$ radiation ($\lambda = 0.15418 \text{ nm}$), produced at 40 kV and 30 mA over the 2θ range $5^\circ - 130^\circ$, step size 0.04 and counting time 2.4 s/step. Samples were mounted onto aluminium sample holders using a viscous adhesive and adjusted to the correct height with a glass slide. Diffraction patterns were also conducted to study the concentration depth profiles of calcium aluminates and to monitor the development of CA , CA_2 , and CA_6 . To obtain the graded composition profile, both gradual polishing and slicing methods were used. The emery paper was used to polish away the material to depths of 0.1, 0.2, 0.4, 0.5, 0.6 and 0.8 mm. For the slicing method, the sample was cut using diamond blade into consecutive slices thickness of 2 mm. In order to determine the phase developments of various calcium aluminates (i. e. CA , CA_2 , and CA_6) in reaction sintered A/CA_6 and functionally graded A/CA_6 composites at various temperatures, the selected CA100 and FGM samples were fired at temperatures between $1000 - 1600^\circ\text{C}$ for 2h.

Synchrotron Radiation Diffraction (SRD) Analysis

Synchrotron radiation diffraction was conducted to study the concentration depth-profiles of calcium-hexaluminate in functionally graded alumina/ CA_6 composites and to monitor the phase development of CA , CA_2 and CA_6 . Two processing routes were used to infiltrate the porous alumina preforms. The first was aimed at studying the concentration depth-profiles of CA_6 and it involved a partial infiltration of the preform in a solution of calcium acetate for 5 h. The partially-infiltrated preform was dried at room temperature for 24 h. The sample was then cut using diamond blade into consecutive slices thickness of 2 mm. Each of these slices was then crushed into powder using a mortar and pestle. Individual batches of powder were then placed in high purity alumina crucibles and heat-treated at 1400°C

for 12 h, followed by 1650 °C for 2h in an air atmosphere using a MoSi₂ resistance heated box furnace (Model HT 04/17, Ceramic Engineering). The second processing route was aimed at monitoring the phase development of CA, CA₂, and CA₆. The process involved fully immersing the preforms in the calcium acetate solution for 8 h, followed by over-night drying. Again, the dried preforms were crushed into powder and placed in high purity crucibles for calcining at various temperatures ranging from 1000 - 1650 °C for 2 h. The calcined powders were further milled in a high purity zirconia mould for 2 minutes to obtain finer particle size.

Synchrotron diffraction patterns for all heat-treated powders were acquired with the BIGDIFF instrument at the Australian National Beamline Facility (ANBF) at Tsukuba, Japan (Sabine *et al.* 1995; Garrett *et al.* 1995). SRD patterns in Debye-Scherrer geometry were measured using the same powdered specimens as previously employed in the XRD analysis packed in low-absorption lithium borate glass capillaries (0.3 mm diameter and all thickness 0.01 mm). The dense packing of powder in the glass capillaries was facilitated using an ultrasonic water bath. The monochromator was set to deliver a wavelength of 1.0 Å. The incident beam dimensions were set at a length of 10 mm and a width of 0.8 mm to completely immerse the specimen within the beam. The exposure time was 20 min for each specimen. Four erasable imaging plates (400 mm x 200 mm), each covering $2\theta = 40^\circ$, were used to obtain the diffraction patterns. These were digitized to produce an 8-bit image which diffraction intensities were extracted.

Neutron Diffraction (ND) Analysis

Both room-temperature and high temperature neutron diffraction were used to monitor the evolution of phase transformations within the green alumina/calcium-hexaluminate composite. Room temperature neutron diffraction was performed on samples CA0, CA5, CA15, CA30, CA50, CA100, CA2.5S, CA10S, CA15S, which had been heat-treated to 1650 °C for 2 h. High temperature neutron diffraction was employed to the selected compositions of alumina/CA₆ samples (CA100 and FGM)

at various temperatures (1000 - 1600 °C). The bar-shaped green sample with dimensions 10 x10 x 60 mm³ was initially pre-calcined at 1000 °C for 2h to increase its strength prior to the neutron study. This experiment was conducted in order to ascertain the formation temperature of each of the calcium aluminate phases. The neutron diffraction data collection was performed using a medium resolution powder diffractometer (MRPD) located at the Australian Nuclear Science and Technology Organisation (ANSTO) in Lucas Heights, NSW. The operation conditions were $\lambda = 1.667 \text{ \AA}$, 2θ range = 4 - 138°, step size = 0.1°, counting time ~ 40 - 50 s/step, monochromator of 8 Ge crystals (115 reflection), and 32 ³He detectors 4° apart.

Qualitative Phase Analysis

The phase developments for each of the compositions in A/CA₆, β -spodumene modified A/CA₆, functionally graded A/CA₆ composites, and alumina as a control samples were monitored using x-ray and neutron diffraction on the as-fired surface. Qualitative x-ray diffraction was performed by comparing the diffraction lines with standard PDF files using the search match procedure. The PDF files used for each of the phases mentioned are listed in Table 3.4.

Table 3.4. PDF file numbers used for qualitative phase analysis of the XRD, ND and SRD patterns.

Phase	Legend	PDF file
α -Al ₂ O ₃	A	42-1268
CaCO ₃	▼	05-0586
CaO	o	43-1001
CaO.Al ₂ O ₃ (CA)	▲	23-1036
CaO.2Al ₂ O ₃ (CA ₂)	●	23-1037
CaO.6Al ₂ O ₃ (CA ₆)	x	84-1613
Li ₂ O.Al ₂ O ₃ .4SiO ₂	s	35-797
Li ₂ Al ₂ Si ₃ O ₁₀	q	73-2336

Rietveld Phase Composition Analysis

It is well known that the Rietveld method (Rietveld 1967, 1969) has been used as a powerful tool for crystal structure refinements based on powder diffraction data, especially in materials science. Rietveld refinement involves the fitting of a complete experimental diffraction pattern with calculated profiles and background. A detailed description of the Rietveld method can be found in Young (1993). The Rietveld method uses crystal structure and diffraction peaks profile to generate x-ray or neutron diffraction pattern via a process of least square refinement which minimises the differences between the observed and the calculated patterns.

The least-squares procedure uses the Newton-Raphson algorithm to minimise of residual R (Young 1993):

$$R = \sum_i w_i (y_{io} - y_{ic})^2 \quad (3.1)$$

where y_{io} is the observed intensity and y_{ic} is the calculated intensity at point i , and w_i is the weighting factor for point i in the pattern which is normally set as the reciprocal of the measured intensity at point i given by:

$$w_i = \frac{1}{\sigma_i^2} \quad (3.2)$$

The calculated intensity y_{ic} at each point i in the pattern for a number of phases k is determined by summing all the contributions of neighbouring reflection and the background. The intensity of diffracted beams is dependent on the diffractometer optics. X-ray diffraction (XRD), synchrotron radiation diffraction (SRD) and neutron diffraction (ND) were employed in this research, hence the two forms of optics considered in this thesis are Bragg-Brentano and Debye-Scherrer optics.

Warren (1969) proposed the calculated intensity of diffracted beams with Bragg-Brentano optics (XRD) for infinitely thick specimens, which is given by

$$y_{ic} = KA_i \sum_{jk} m_{jk} L_{jk} |F_{jk}|^2 G_{ijk} P_{jk} \frac{C_k}{V_k^2} + y_{ib} \quad (3.3)$$

where K is the instrument constant, it is dependent on instrumental parameters and incident beam characteristics but independent of the specimen, A_i is the absorption factor, m_{jk} is the multiplicity factor, L_{jk} is the Lorentz-polarisation factor for the reflection jk , F_{jk} is the structure factor, G_{ijk} is a normalised peak profile function, P_{jk} is the preferred orientation function, C_k is the volume fraction of k and V_k is the corresponding cell volume, and y_{ib} is the background contribution for point i .

The calculated intensity of diffracted beams with Debye-Scherrer optics (SRD and ND) for cylindrical, semi-transparent specimens (Bacon 1962) is given by

$$y_{ic} = KA_i(r, \theta) v \sum_{jk} m_{jk} L_{jk} |F_{jk}|^2 G_{ijk} P_{jk} \frac{C_k}{V_k^2} + y_{ib} \quad (3.4)$$

where $A_i(r, \theta)$ is the attenuation factor for specimen radius r and Bragg θ angle, and v is the volume of specimen.

Hunter and Howard (1998) have made the simplified forms of Equations 3.3 and 3.4 as follow:

Bragg-Bentano,

$$y_{ic} = A_i \sum_{jk} s_k m_{jk} L_{jk} |F_{jk}|^2 G_{ijk} P_{jk} + y_{ib} \quad (3.5)$$

where s_k is the Rietveld scale factor, and it is given by:

$$s_k = \frac{KC_k}{\mu V_k^2} \quad (3.6)$$

Debye-Scherrer,

$$y_{ic} = A_i(r, \theta) \sum_{jk} s_k m_{jk} L_{jk} |F_{jk}|^2 G_{ijk} P_{jk} + y_{ib} \quad (3.7)$$

where s_k is the Rietveld scale factor, in this case is given by

$$s_k = \frac{vKC_k}{V_k^2} \quad (3.8)$$

The structure factor, F_k is given by the expression

$$F_k = \sum_{j=1}^n f_j \exp[2\pi i(h_k^t r_j - h_k^t B_j h_k)] \quad (3.9)$$

where f_j is the scattering factor or scattering length of atom j , and h_k , r_j and B_j are matrices representing the Miller indices, atomic coordinates and anisotropic thermal vibration parameters, respectively, and the subscript t represents matrix transposition.

The background intensity y_{ib} may be modeled using the polynomial (Rietveld 1969):

$$y_{ib} = \sum_{m=-1}^n B_m (2\theta)^m \quad (3.10)$$

where B_m are refinable parameters and 2θ is the diffraction angle. Background model were 3rd order for XRD data, 3th order for ND data, and 5th for SRD data.

The peak profile function G_{ik} may be modeled using pseudo-Voigt or Voigt peaks shape function. In the pseudo-Voigt peak shape function, G_{ik} is given by

$$G_{ik} = \gamma \frac{C_0^{1/2}}{H_k \pi} [1 + C_0 X_k^2]^{-1} + (1 + \gamma) \frac{C_1^{1/2}}{H_k \pi^{1/2}} \exp[-C_1 X_{ik}^2] \quad (3.11)$$

where $C_0 = 4$, $C_1 = 4 \ln 2$, $X_{ik} = (2\theta_i - 2\theta_k)/H_k$, γ is a refinable ‘mixing’ parameter, and H_k is the full-width at half-maximum (FWHM) of the k^{th} Bragg reflection. The variation of the peak FWHM is defined by the function described by (Caglioti *et al.* 1958):

$$H_k = (U \tan^2 \theta + V \tan \theta + W)^{1/2} \quad (3.12)$$

where U , V , and W are peak function parameters. For the Voigt peak shape function, G_{ik} is given by

$$G_{ik} = \frac{C_1^{1/2}}{H_{Gk} \pi^{1/2}} \operatorname{Re} \left[\omega \left(C_1^{1/2} X_{ik} + i C_3 \frac{H_{Lk}}{H_{Gk}} \right) \right] \quad (3.13)$$

where $C_1 = 2 \ln 2$, $C_3 = (\ln 2)^{1/2}$, H_{Gk} is the FWHM of the contributing Gaussian, H_{Lk} is the FWHM of the contributing Lorentzian, ω is the complex error function, and Re denotes its real part. The Gaussian component width varies in accordance with Equation 3.11, whereas the width of the Lorentzian component varies with $\sec \theta$ and $\tan \theta$:

$$H_{Lk} = \frac{180}{\pi} \frac{\lambda}{D} \sec(\theta) + \frac{180}{\pi} S \tan(\theta) = K_s \sec(\theta) + K_t \tan(\theta) \quad (3.14)$$

where D is the crystallite size and K is a refinable parameter. Voigt functions best approximated the peak shape obtained from ND pattern but were relatively poor approximation for XRD and SRD patterns, requiring pseudo-Voigt function to be used, as they were more suitable approximations.

The profile function can be corrected for peak asymmetry using the semi-empirical function proposed by Rietveld (1969)

$$A_{ik} = 1 - AS[\text{sign}(2\theta_i - 2\theta_k)](2\theta_i - 2\theta_k)^2 \cot \theta_k \quad (3.15)$$

where AS is the asymmetry parameter to be determined from Rietveld refinement.

The preferred orientation parameter, P_k corrects for the *plate-like* crystallites in the specimen by applying a function proposed by Dollase (1986)

$$P_k = (P^2 \cos^2 \alpha_k + P^{-1} \sin^2 \alpha_k)^{-3/2} \quad (3.16)$$

where P is a refinable parameter and α_k is the acute angle between the scattering vector and the normal to the crystallites.

The estimated standard deviations (esds) for the Rietveld refinement parameters were derived with the expression for parameter j :

$$\sigma_j = \left[M_{jj}^{-1} \frac{\sum_{i=1}^N w_i (y_{io} - y_{ic})^2}{N - P} \right] \quad (3.17)$$

where N is the number of observations, P is the number of parameters being refined and M_{jj}^{-1} is the diagonal element determined by inversion of the normal matrix with elements M_{jk} which is given by:

$$M_{jk} = -\sum_i 2w_i \left[(y_i - y_{ci}) \frac{\partial^2 y_{ci}}{\partial x_i \partial x_k} - \left(\frac{\partial y_{ci}}{\partial x_j} \right) \left(\frac{\partial y_{ci}}{\partial x_k} \right) \right] \quad (3.18)$$

where x_j and x_k are adjustable parameters.

The parameters refined for all samples were those controlling pattern intensity (scale factors), peak profile (width and shape), peak position (zero point and unit cell), background polynomial parameters, and the individual atom thermal parameters. The crystal structure models used in the calculation were taken from the Inorganic Crystal Structure Data Base (Fach Informations Zentrum and Gmelin Institut, Germany) – ICSD as shown in Table 3.5. The crystallographic data for each phase used in the refinement are presented in Appendix A. The refinements were performed by the Rietica program for Windows 95/98/NT version 1.6.5 which derives from the Hill-Howard-Hunter LHPM program (Hill, Howard and Hunter 1999). The final Rietveld scale factors were converted to the phase compositions-by-weight using the ZMV expression proposed by Hill and Howard (1987):

$$W_k = \frac{s_k (ZMV)_k}{\sum_{i=1}^n s_i (ZMV)_i} \quad (3.19)$$

where W_k is the weight fraction of phase k , s is the Rietveld scale factor, Z is the number of formula units per unit cell, M is the mass of the formula unit, and V is the unit-cell volume.

Table 3.5. ICSD files used in the Rietveld refinement of XRD, SRD and ND data.

Phase	ICSD file
α -Al ₂ O ₃	75725
CaO	75785
CaO.Al ₂ O ₃ (CA)	260
CaO.2Al ₂ O ₃ (CA ₂)	34487
CaO.6Al ₂ O ₃ (CA ₆)	34394
Li ₂ O.Al ₂ O ₃ .4SiO ₂	14235
Li ₂ Al ₂ Si ₃ O ₁₀	24897

The agreement between the observed and calculated intensities during the course of the refinement can be assessed using figures-of-merit or R-values (Young 1993; Kisi 1994) given by:

(i) The profile R factor,
$$R_p = \frac{\sum |y_{io} - y_{ic}|}{\sum y_{io}} \quad (3.20)$$

(ii) The weighted profile R factor,
$$R_{wp} = \left[\frac{\sum w_i (y_{io} - y_{ic})^2}{\sum w_i y_{io}^2} \right]^{1/2} \quad (3.21)$$

(iii) The Bragg R factor,
$$R_B = \frac{\sum |I_{ko} - I_{kc}|}{\sum I_{kc}} \quad (3.22)$$

where I_{ko} is the observed integrated intensity of reflection k calculated at the end of the refinement after apportioning each y_{io} between the contributing peaks and background when that is refined according to the calculated intensities I_{kc} .

(iv) The expected R factor,
$$R_{exp} = \left[\frac{N - P}{\sum w_i y_{io}^2} \right]^{1/2} \quad (3.23)$$

where $N-P$ is the weighed sum of squared residuals.

(v) The goodness-of-fit,
$$GOF = \frac{\sum w_i (y_{io} - y_{ic})^2}{N - P} = \left[\frac{R_{wp}}{R_{exp}} \right]^2 \quad (3.24)$$

Prince (1993) suggests that the ideal value for GOF is 1.0, if a $GOF > 1.5$ is an indication of an inappropriate model or a false minimum in the refinement. However, for phase analysis, a value of less than about 4.0 is acceptable (Kisi 1994).

The difference plots between the observed and the calculated patterns is also an important for assessing the degree of refinement. The two patterns should essentially give a flat difference for a well-refined model. The difference plots may also provide indication of the presence of undetected phase(s) or inaccuracies in the background or peak shape modelling.

3.4.3 Microstructural Examination

Scanning Electron Microscopy (SEM)

Microstructural analysis was performed on polished and thermally-etched samples. The sintered samples were cold-mounted into an epoxy resin. The cross-sections of samples were then polished using a Struers Pedamat polisher beginning with 40 μm , 15 μm , 9 μm , 6 μm , 3 μm , and finally 1 μm diamond paste. Following this the samples were removed from the resin mount by heating in a microwave oven at 200 °C, then thermally-etched at 1350 °C for 30 minutes.

The samples were mounted on an aluminium stub using a carbon conductive double side tape, then carbon-coated before placing in the SEM. The SEM imaging was conducted on a JEOL JSM-6400 with operation condition voltage of 15 - 30 kV, working distance 15 mm, and using backscattered and secondary electron detectors, and Ca- and Al-x-ray mapping. The SEM data collection was conducted at the Materials Division of ANSTO in Lucas Height, Sydney.

Transmission Electron Microscopy (TEM)

The transmission electron microscopy (JEOL) operating at 200 kV acceleration voltage, coupled with the selected area diffraction (SAD) and energy dispersive spectroscopy (EDS) were used to observe and confirm the microstructure of calcium aluminates (CA , CA_2 , and CA_6) in a functionally graded A/ CA_6 composite. Sample fired at 1400 °C for 0.5 h was used. Fine powders of the sample were sprinkled on a copper grid coated with carbon film. The TEM data collection

was conducted at the Department of Materials Science and Engineering, Himeji Institute of Technology, Himeji, Japan.

3.5 Properties Evaluation

3.5.1 Physical and Thermal Properties

Shrinkage, Density, and Porosity

The values of green compact bulk density of samples were determined by measuring the mass and the dimensions of the samples. Measurements were taken on each sample using a digital vernier caliper (Mitoyo, Japan) to an accuracy of ± 0.01 mm. The shrinkage (S_D) was determined by the percent reduction in diameter of the green compact (D_0) to the sintered sample (D) using the relation:

$$S_D = \frac{D - D_0}{D_0} \times 100 \quad (3.25)$$

The values of bulk density (D_b) and apparent porosity (P_a) of the sintered samples were determined using the Archimedes principle according to Australian Standard (AS 1774.5- 1989) with deionised water as the immersion medium. The density and porosity were calculated by following formulas:

$$\text{Bulk density,} \quad D_b = \frac{m_s}{(m_s - m_i) \times D_i} \quad (3.26)$$

$$\text{Apparent porosity,} \quad P_a = \frac{(m_s - m_d)}{(m_s - m_i)} \times 100 \quad (3.27)$$

where m_d is the mass of dried samples, m_i is the mass of the test samples, saturated with and suspended in water, m_s the mass of the test samples, saturated with water and suspended in air, D_i is the density of water at room temperature.

Thermal Expansion and Shrinkage Behaviour

Bar samples with dimensions 4 x 4 x 10 mm³ were prepared to study the thermal expansion and shrinkage behaviour. A theta 160 dilatometer was used to characterise the densification behaviour of green control samples (alumina), alumina/calcium-hexaluminate, β -spodumene modified alumina/calcium hexaluminate, and functionally graded alumina/calcium-hexaluminate composites at temperatures between 20 - 1500 °C. These experiment were conducted at the Materials Division of ANSTO in Lucas Height, Sydney.

Young's Modulus

Bar samples with dimensions 2.5 x 10 x 50 mm³ were prepared for Young's modulus measurements, which was conducted using a Grindo Sonic tester at room temperature. The faces of each of the samples were lightly ground using a 10 μ m diamond pad in order to achieve parallel surface. The Young's modulus (E) was calculated using:

$$E = 0.9468 \frac{L^3 P f^2}{d^3 w} \quad (3.28)$$

where L , d , w , P and f are the sample length, thickness, width, weight, and resonance frequency, respectively. This work was conducted at the Materials Division of ANSTO in Lucas Height, Sydney.

Viscosity and Surface Tension

The viscosity of calcium acetate solution and water was measured using an Oswald viscosimeter (model Ubbelohde Viscometer manufactured by Techniqo). The method is based on the driving force of the liquid through the vertical capillary. The viscosity, η was calculated by comparing the flow time of the standard liquid, t_s and the test liquid, t through a vertical capillary according the following equation:

$$\eta = \frac{t}{t_s} \eta_s \quad (3.29)$$

where η_s is the viscosity of the standard solution. Water was used as the standard liquid. The experiment was conducted at the Department of Applied Chemistry, Curtin University.

The surface tension of the liquids was measured using the torsion balance method. The surface tension, γ was calculated using the following equation:

$$\gamma = \frac{mg}{2(l-b)} \quad (3.30)$$

where m is the loaded mass at which the glass slide started to break away from the surface of liquid due to surface tension, g is the acceleration gravitation, l and b are the length and thickness of the glass slide. The experiment was conducted at the Department of Applied Physics, Curtin University.

Differential and Thermogravimetric Analysis (DTA and TGA)

Simultaneous DTA and TGA measurements on as-received CaCO_3 , CA100, CAS2.5, CAS15, and Ca-acetate liquid precursor were carried out on a Netzsch STA-409C instrument in nitrogen atmosphere. Specimens weighing 10 mg were placed in platinum crucible and heated to a maximum temperature of 1500 °C at a heating rate 10 °C min⁻¹ with an empty reference.

3.5.2 Mechanical Properties

Hardness and Fracture Toughness

The indentation hardness was measured using a ZWICK microhardness tester with Vickers diamond pyramid. All the samples used for indentation tests were prepared by cold-mounting in resin and diamond polishing the test surface beginning at 40 μm , 15 μm , 9 μm , 6 μm , 3 μm , and finishing with 1 μm grade diamond. The samples were indented using loads of 29.4 – 294 N, the number of indents made for a load was three. The indentation half-diagonal lengths and the radial surface crack lengths were measured directly using a micrometer attached to the sample stage. The average half-diagonal length and average radial surface crack length were used to calculate hardness and fracture toughness. Figure 3.4 shows a schematic diagram of the crack at a Vickers indentation.

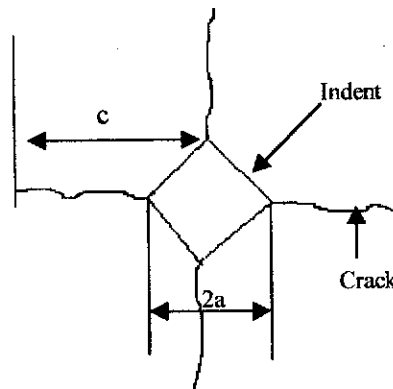


Figure 3.4. Schematic diagram of the crack due to Vickers indentation.

The hardness and fracture toughness were calculated using the following formulae (Evans and Charles 1980):

Hardness,
$$H_v = 1.8544 \frac{P}{(2a)^2} \quad (3.31)$$

where P is the load of indenter (N) and a is the half-diagonal length (m).

Fracture toughness,
$$K_{ic} = 0.16H_v \sqrt{a} \left(\frac{c}{a}\right)^{-3/2} \quad (3.32)$$

where c is the crack length (m).

CHAPTER 4

SYNTHESIS OF *IN-SITU* REACTION SINTERED ALUMINA/CALCIUM-HEXALUMINATE (A/CA₆) COMPOSITES

4.1 Introduction

Alumina has been widely used because of its excellent physical and thermomechanical properties (Dörre and Hübner 1984). Its intrinsic brittleness and relatively poor reliability however, renders the toughening of alumina ceramics an important and challenging area of study. The incorporation of secondary phases (eg. particulates, fibers or platelets) has been proven to be an easy, safe and economical toughening technique for alumina ceramics. The fracture behaviour of alumina is highly affected by its microstructure due to crack deflection, secondary microcracking and crack bridging phenomena and thermal expansion anisotropy of alumina is recognised to be responsible for these processes.

Recently, it has been demonstrated that it is possible to easily synthesise ceramic matrix composites by an *in-situ* reaction of homogeneous powders, which during densification lead to development of randomly dispersed phases with *plate-like* morphology (Chen and Chen 1992). *In-situ* formed *plate-like* grains have a favourable impact on the matrix toughness as already confirmed by both experimental and theoretical studies (Pezzoti 1993; Pezzoti *et al.* 1996).

Calcium hexaluminate (CA₆) has been introduced as a second phase in alumina-based composite due to its similar thermal expansion coefficient (see section 1.1) and thermodynamic compatibility with alumina. Reaction sintered alumina-CA₆ composites containing different CA₆ content has been successfully demonstrated (Criado, Cabalero and Pena 1987), but the toughness values obtained have so far been very modest. The fracture behaviour of alumina/30 vol % CA₆ synthesised by reaction sintering has been studied by An, Chan and Sony (1996) and

An and Chan (1996) using the indentation strength technique. They found the R-curve behaviour more pronounced for the composite containing CA_6 platelets, and this behaviour was attributed to crack bridging by the CA_6 grains. However, the high-temperature mechanical properties of such materials are expected to be poor owing to the presence of glassy phase at the grain boundaries.

In this chapter, results on the synthesis, phase composition and development, physical and mechanical properties of *in-situ* reaction sintered of alumina/calcium-hexaluminate (A/CA_6) composites are described. The characteristics and properties of A/CA_6 composites have been studied using room-temperature x-ray diffraction (XRD), room-temperature neutron diffraction (ND), high-temperature neutron diffraction (HTND), scanning electron microscopy (SEM), differential thermal and gravimetric analysis (DTA/TG), dilatometry, and Vickers indentation. Quantitative phase compositions (QPA) of A/CA_6 composites were analysed using Rietveld refinement method.

4.2 Results and Discussion

4.2.1 Raw Material Evaluation

Commercial Al_2O_3 (A1000SG grade, ALCOA USA) and $CaCO_3$ powders (analytical UNIVAR) were used as raw materials (see section 3.2.1). The chemical compositions of the starting alumina and calcium carbonate powders are shown in Table 3.1. The chemical analysis of the alumina A1000SG indicates that the material is a high purity alumina powder with the impurity of soda (Na_2O) less than 0.1 %.

The $CaCO_3$ material has low level of various oxide impurities such as Na_2O , K_2O and SO_4 except that the MgO impurity concentration is relatively higher. It has been shown that the presence of MgO was used to improve the sinterability and densification behaviour of alumina and also to restricting the abnormal grain growth (Bateman, Bennison and Harmer 1989). Therefore, the presence of impurity MgO (0.1 %) in this material was considered likely to influence the reaction-sintering mechanism and the microstructural character of fabricated A/CA_6 composites.

The particle size distribution of the as-received Al_2O_3 and CaCO_3 , and processed CaCO_3 , CA5, CA15, CA30, CA50 and precursor CA_6 were determined using the laser scattering method described in section 3.4.1. The particle size distribution results for the as-received Al_2O_3 , as-received CaCO_3 , and processed CaCO_3 are shown in Figure 4.1. A summary of the particle size data is given in Table 4.1. The mean particle size (D_{50}) of Al_2O_3 and CaCO_3 are $0.54\ \mu\text{m}$ and $15.53\ \mu\text{m}$, respectively. The particle size result indicates that ball milling of the CaCO_3 powders was difficult because the initial particle size represents a crystal size and not an agglomeration of smaller particles. However after 5 h milling the mean particle size is shown to be near a micron size.

The particle size distribution of the processed CA_6 precursor, CA5, CA15, CA30, and CA50 are shown in Figure 4.2. The milling time and distribution data are presented in Table 4.2. The particle size data presented as a function of milling time for each of the composition of CA_6 precursor, CA5, CA15, CA30, and CA50 suggest that the reduction of particle size to the specified size ($< 1\ \mu\text{m}$) could be achieved after 3 hours of ball milling.

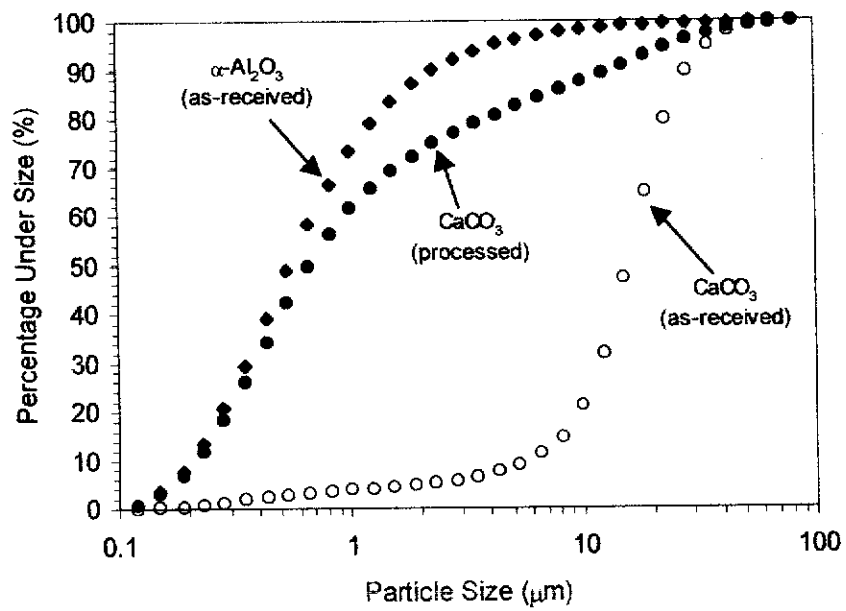


Figure 4.1. Particle size distributions for the as-received Al_2O_3 and CaCO_3 , and processed CaCO_3 powders.

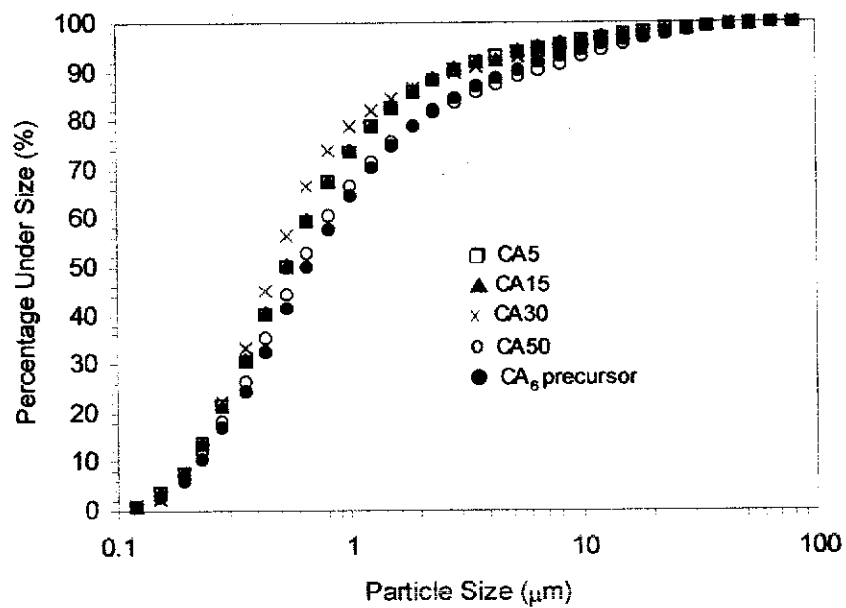


Figure 4.2. Particle size distributions for the processed CA5, CA15, CA30, CA50 and CA_6 precursor powders.

Table 4.1. Milling time and particle sizes data for the as-received Al_2O_3 and CaCO_3 and processed CaCO_3 powders.

Sample	Milling Time (h)	D ₁₀ (μm)	D ₅₀ (μm)	D ₉₀ (μm)
Al_2O_3 (as-received)	0	0.2	0.5	2.3
CaCO_3 (as-received)	0	5.8	15.5	28.3
CaCO_3 (processed)	5	0.2	0.7	13.3

Table 4.2. Particle size data for processed CA_6 precursor CA_5 , CA_{15} , CA_{30} , and CA_{50} powders after milling for 3h.

Sample	D ₁₀ (μm)	D ₅₀ (μm)	D ₉₀ (μm)
CA_6 precursor	0.2	0.7	5.0
CA_5	0.2	0.5	2.8
CA_{15}	0.2	0.5	2.7
CA_{30}	0.2	0.5	2.9
CA_{50}	0.2	0.6	6.3

Laboratory x-ray powder diffraction patterns were used to examine the crystallographic form of the raw materials and to detect the possible presence of other phases. The diffraction pattern of the as-received alumina is shown in Figure 4.3 which indicates the presence only of single-phase rhombohedral $\alpha\text{-Al}_2\text{O}_3$ [PDF file number 43-1484]. The diffraction pattern of the as-received CaCO_3 is depicted in Figure 4.4. The primary phase material is CaCO_3 [PDF file number 05-0556].

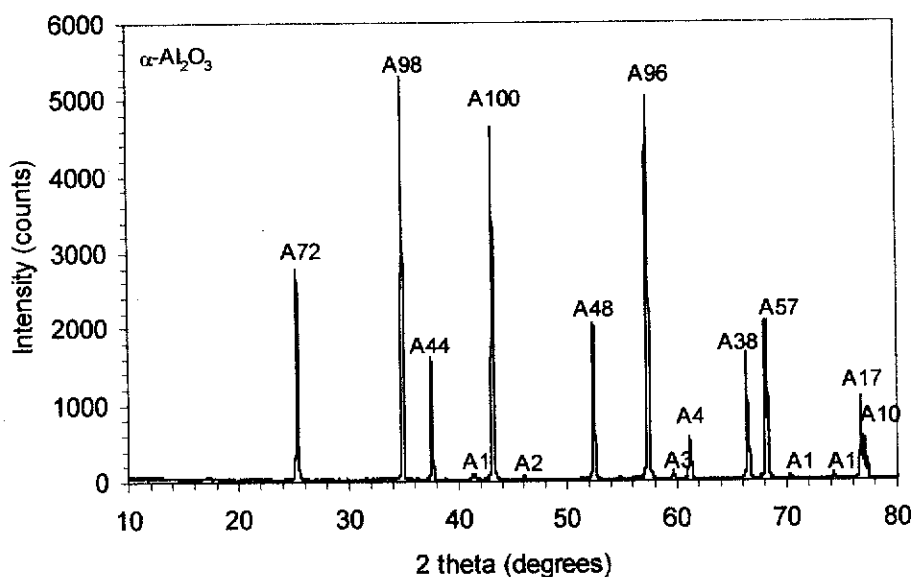


Figure 4.3. X-ray powder diffraction pattern of the as-received Al_2O_3 powder using $\text{CuK}\alpha$ radiation. The peaks are labeled A for $\alpha\text{-Al}_2\text{O}_3$ and the associated numbers are the PDF file intensity.

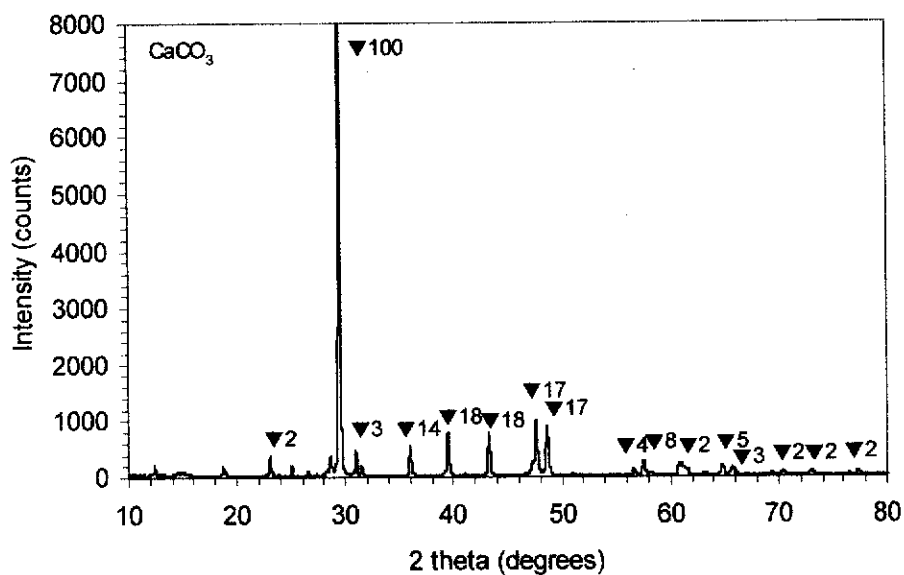


Figure 4.4. X-ray powder diffraction pattern of the as-received CaCO_3 powder using $\text{CuK}\alpha$ radiation. The peaks are labeled ▼ for CaCO_3 and the associated numbers are the PDF file intensity. The most intense CaCO_3 line (▼100) has a count rate of 14000 cps.

4.2.2 Analysis of Phase Composition and Development

Room-temperature x-ray and neutron diffraction data were used to examine the phase compositions of the *in-situ* reaction sintered A/CA₆ composites (see section 3.4.2). The high temperature neutron diffraction (HTND) technique and laboratory x-ray diffraction as described in section 3.4.2 were also employed to monitor the phase development of calcium aluminate (CA, CA₂, and CA₆) for the selected compositions of CA100 sample. A search/match procedure using the PDF file numbers 42-1268, 38-0470, for α -Al₂O₃, CaO, CA, CA₂, and CA₆, respectively was employed to identify the individual peak in each pattern prior to Rietveld analysis. The results of the phase abundance extracted from each pattern obtained are described in the following section.

X-ray Diffraction (XRD) Analysis

Figure 4.5 shows the room-temperature x-ray diffraction (XRD) patterns for the sintered A/(0-100 wt%) CA₆ samples. Expanded views of the XRD patterns for the compositions CA0, CA5, and CA15 are shown in Figure 4.6b, while those for CA30, CA50, and CA100 are shown in Figure 4.6a. The phase α -Al₂O₃ was the only phase observed for the unmodified samples. For the compositions CA5, CA15, CA30 and CA50, the phases present were α -Al₂O₃ and CA₆. However, for the composition CA100 (100 wt % CA₆) the major phase CA₆ and a trace of α -Al₂O₃ were observed. This result can be attributed to the incomplete reaction of the raw materials (Al₂O₃ and CaCO₃) to form CA₆ under the test conditions at 1650 °C for 2 h. The *in-situ* formation of CA₆ phase in A/CA₆ composites is clearly evident for each composition. The peak intensity of CA₆ increased in proportion to the content of CA₆ precursor added. In contrast, for the peak intensity for α -Al₂O₃ decreased in proportion to the content of CA₆ precursor added.

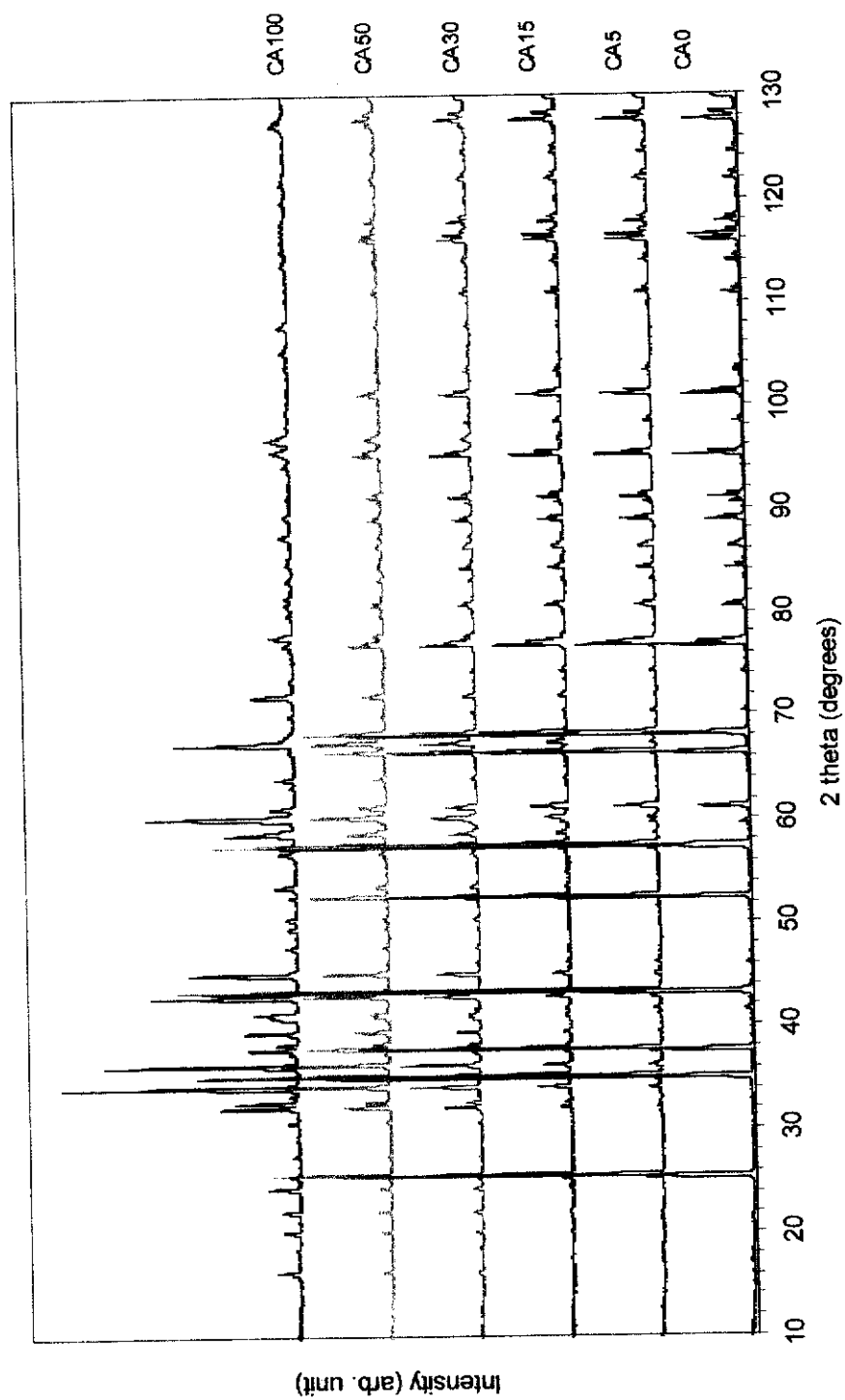
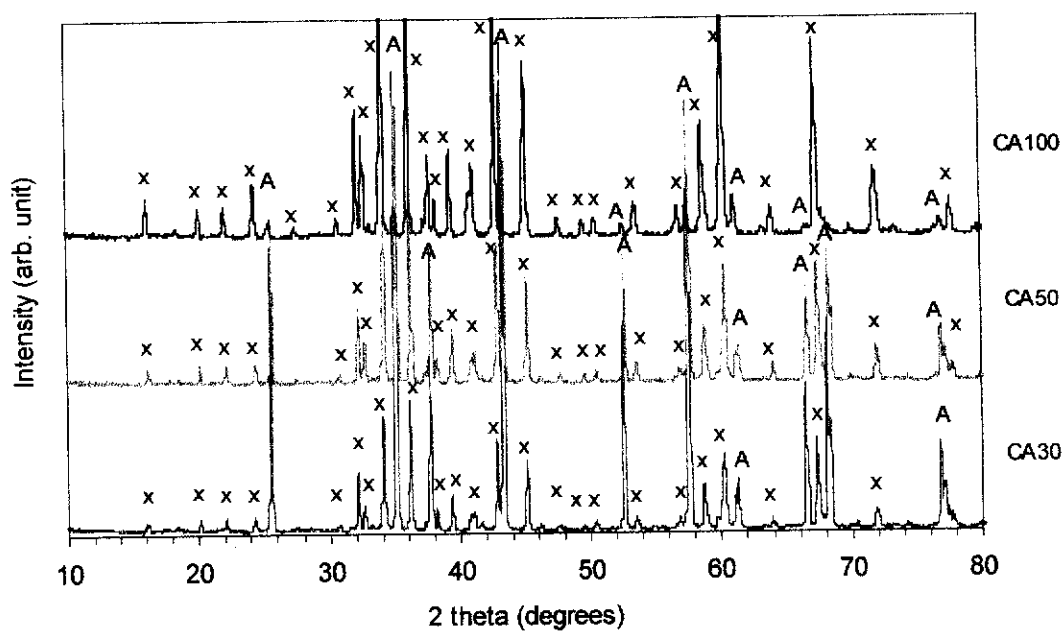
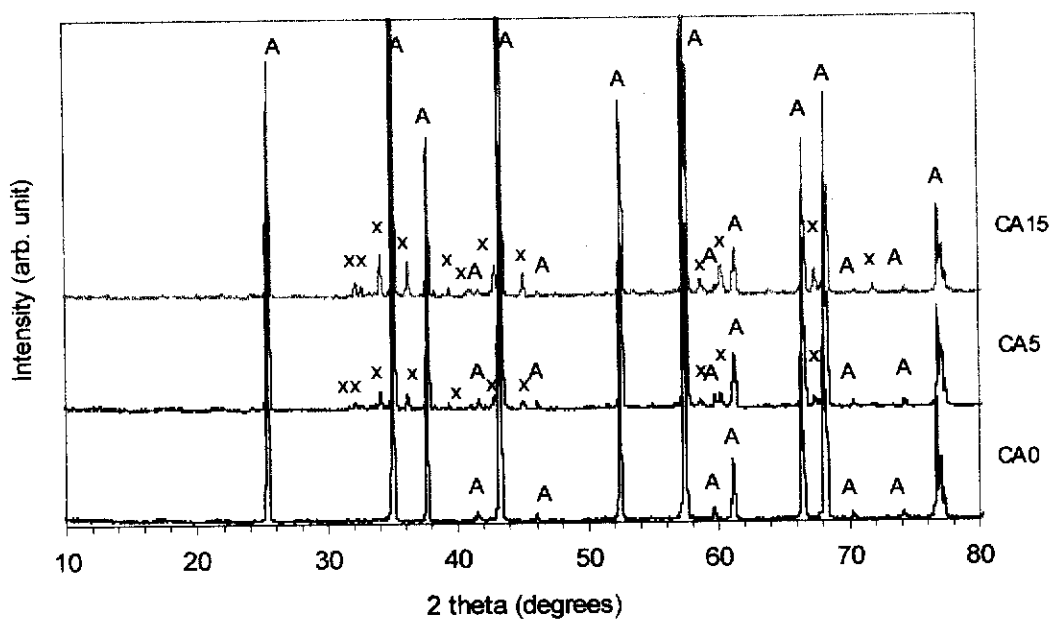


Figure 4.5. Room-temperature x-ray diffraction (XRD) patterns for CA0, CA5, CA15, CA30, CA50 and CA100 samples.



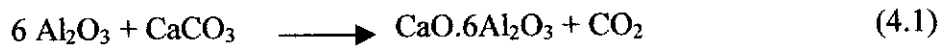
(a)



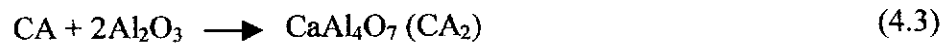
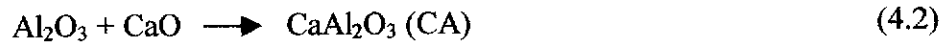
(b)

Figure 4.6. Expanded views of the XRD patterns in Figure 4.5 for CA0, CA5 and C15 in (b) and CA30, CA50 and CA100 in (a). Legends: A = α - Al_2O_3 and x = CA_6 .

Room-temperature XRD was also used to study the formation of calcium aluminates (CA, CA₂ and CA₆) in A/CA₆ composites. The CA100 sample was chosen for this experiment. The experiment was conducted by firing the materials at various temperatures between 1000 and 1600 °C for 2 h. Room-temperature XRD patterns for sintered Al₂O₃:CaCO₃ in ratio 6:1 at various temperatures are shown in Figure 4.7. Figures 4.8a, 4.8b, and 4.8c show the expanded views XRD patterns in the temperature range between 1000-1600 °C. Various phases were observed for this system. The conventional solid state reaction process for fabrication of the CA₆ compound was based on the following reaction:



However, the solid state reaction processes were usually more complex. Fired at 1000 °C for 2 h (Figure 4.8b) the phases observed were α -Al₂O₃, CaO and CA. The peak intensity for the α -Al₂O₃ phase decreased with increasing in temperature. The peak intensities for CA was also decreased with increasing in temperature and disappeared by 1300 °C, followed by the appearance of CA₂ phase at 1100 °C, which remained at temperature of 1450 °C. The formation temperatures of CA₆ occurred at approximately 1400 °C. The formation of *in-situ* CA and CA₂, and their transformation to CA₆, are believed to occur through exothermic reactions between Al₂O₃ and CaO, at 1000 – 1400 °C according to the following reactions:



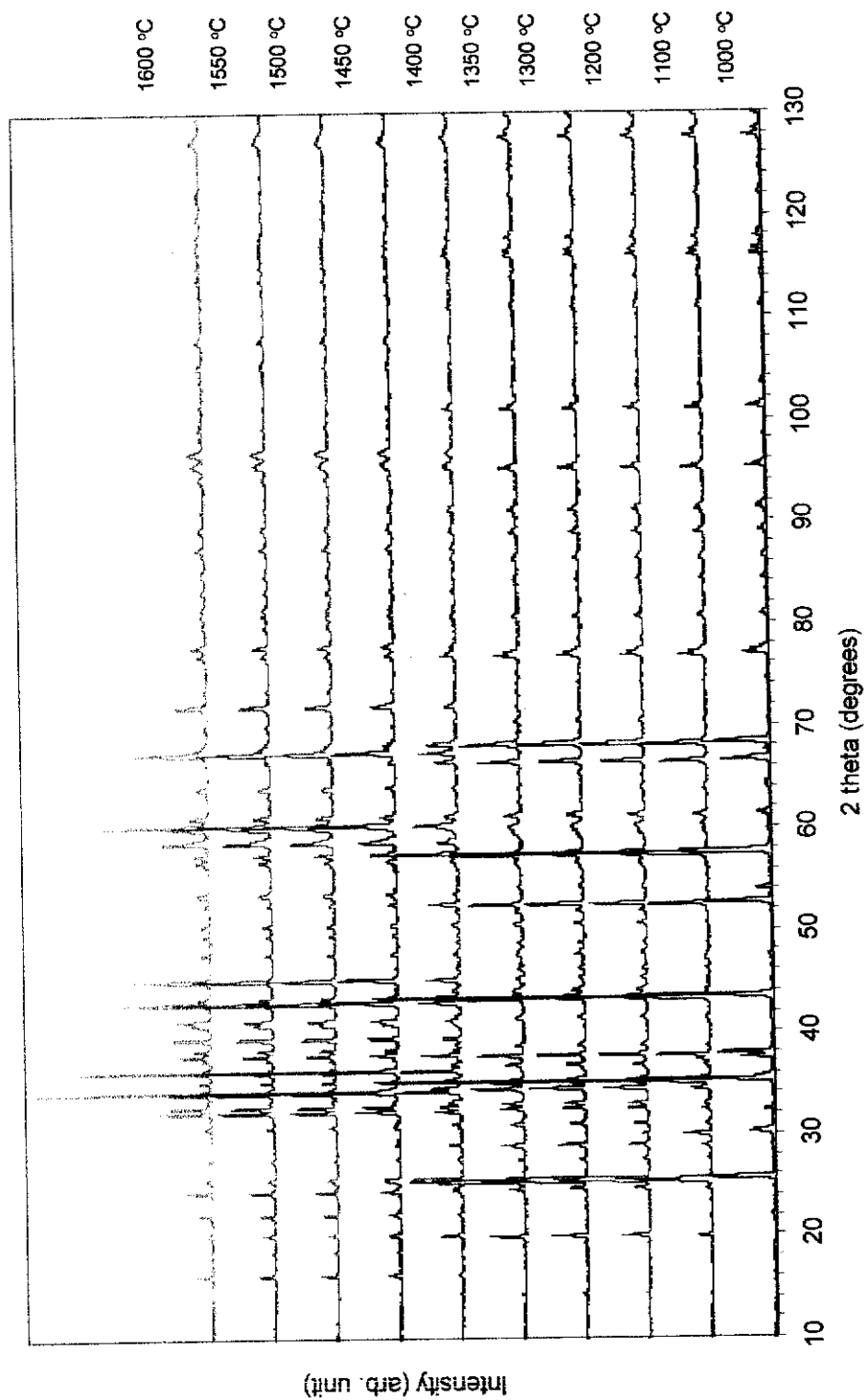
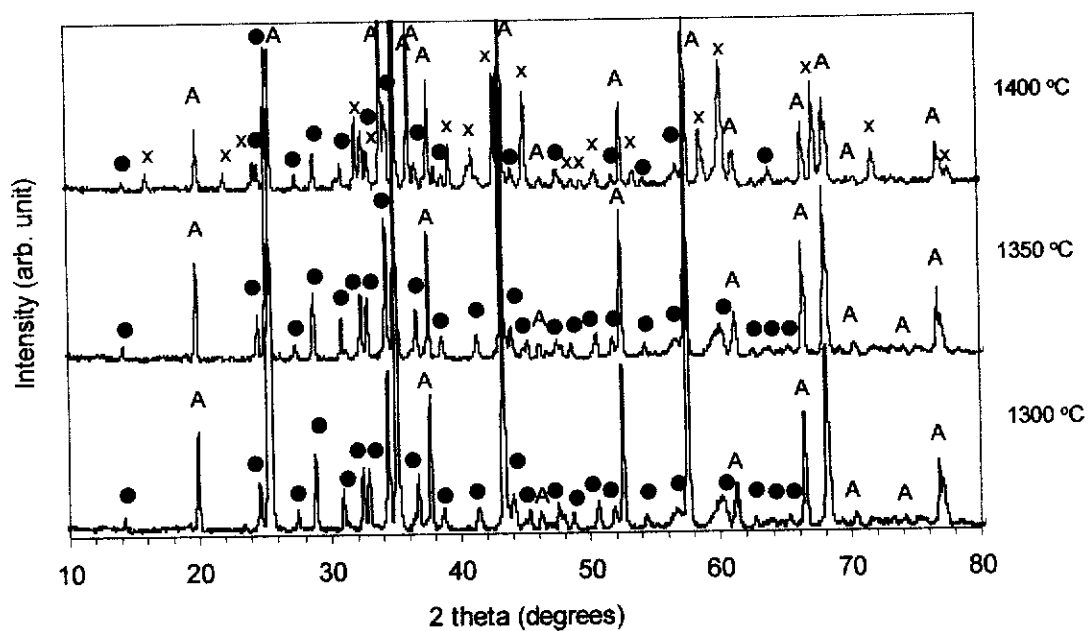
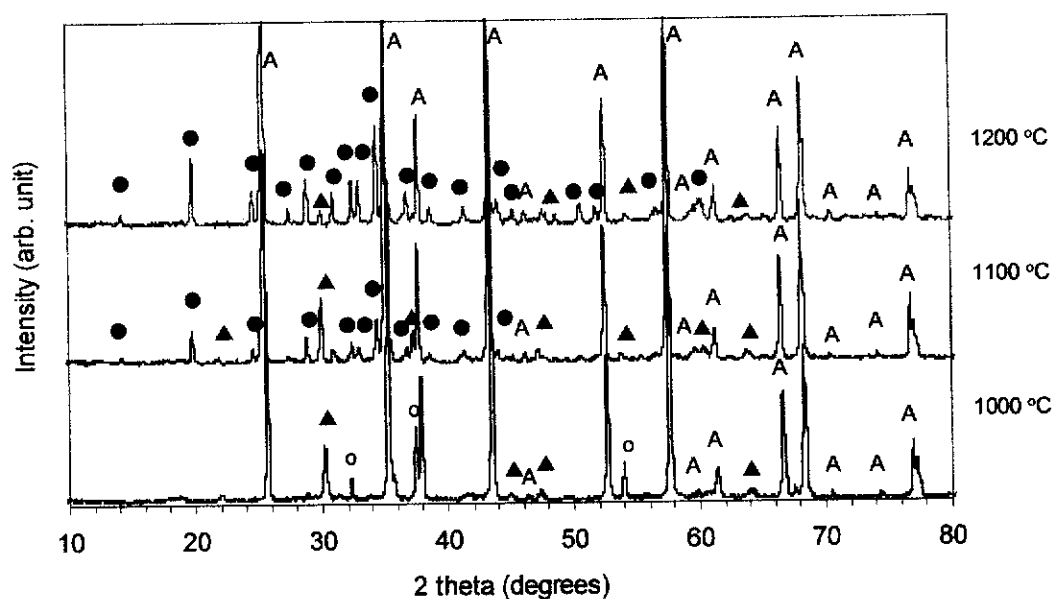


Figure 4.7. Room-temperature XRD patterns for CA100, fired at 1000 - 1600 °C for 2h.

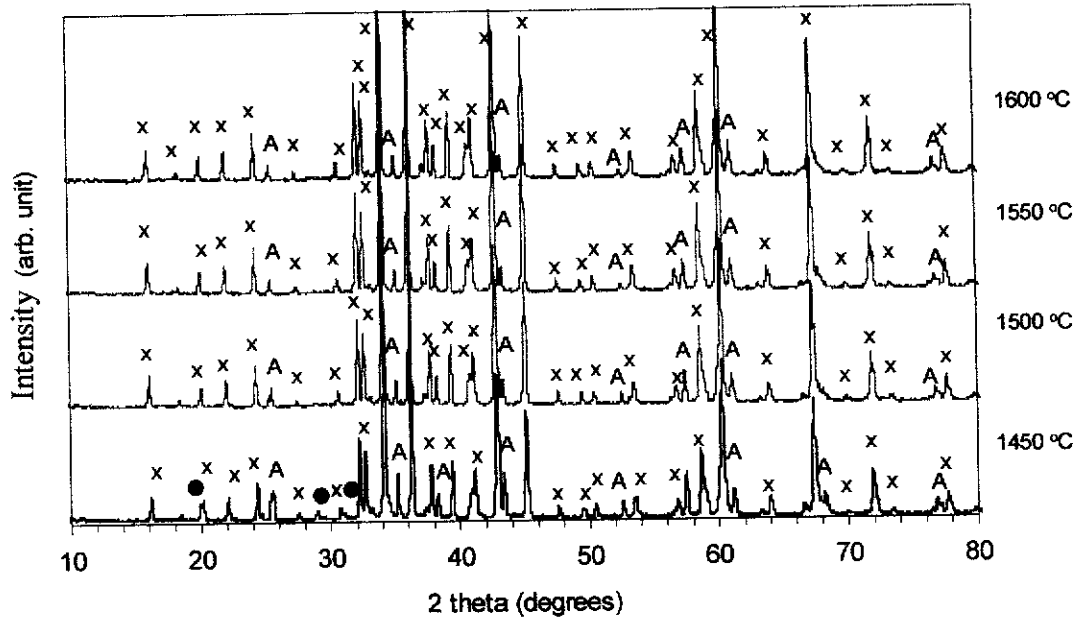


(a)



(b)

Figure 4.8. Expanded views of the XRD patterns in Figure 4.7 for CA100 from 1000 to 1200 °C in (b) and 1300 to 1400 °C in (a). Legends A = α -Al₂O₃, o = CaO, ▲ = CA, ● = CA₂.



(c)

Figure 4.8. (Continued) Expanded views of the XRD patterns in Figure 4.7 for CA100 from 1450 to 1600 °C in (c). Legends A = α - Al_2O_3 , • = CA_2 , x = CA_6 .

Traces of α - Al_2O_3 and CA_2 often accompany CA_6 in the final product as the completion of such reactions depends on the diffusion distances, i.e. on the particle sizes and the degree of mixing of the reactant powders (Cinibulk 2000). The formation of CA_6 is believed to occur via *in-situ* reactions according to Equations 4.1, 4.2, 4.3 and 4.4. Therefore, in this case, Equations 4.4 and 4.5 are important for understanding the development of elongated CA_6 grains, it being known that CA and CA_2 is the intermediate phase during the solid state formation of CA_6 .

Neutron Diffraction (ND) Analysis

Room-temperature neutron diffraction patterns for the sintered CA0, CA5, CA15, CA30, CA50, and CA100 samples are shown in Figure 4.9. Highlighted views of the ND patterns for the CA0, CA5, and CA15 are shown in Figure 4.10b, while those for the CA30, CA50, and CA100 are shown in Figure 4.10a. The α -

Al_2O_3 was the only phase obtained in the CA0 control sample, which agrees well with the x-ray diffraction results previously obtained. For the compositions CA5, CA15, CA30 and CA50, the phases observed were $\alpha\text{-Al}_2\text{O}_3$ and CA_6 , whereas the major phase CA_6 and a trace of $\alpha\text{-Al}_2\text{O}_3$ were also observed for the composition CA100 (100 wt % CA_6). The two sets of results (XRD and ND) obtained were in reasonable agreement. The incomplete reaction of the raw materials to form CA_6 at 1650 °C is attributed to the traces of $\alpha\text{-Al}_2\text{O}_3$ phase observed in the final product. The *in-situ* formation of the CA_6 phase in A/ CA_6 composites is also clearly evident for each composition. The peak intensity for the CA_6 phase increased in proportion to the amount of CA_6 precursor added, while the peak intensity for the $\alpha\text{-Al}_2\text{O}_3$ phase decreased in proportion to the amount of CA_6 precursor added.

Figure 4.11 shows the high-temperature neutron diffraction (HTND) patterns for the CA100 sample at temperatures in the range 1000 – 1600 °C. Expanded patterns are shown in Figures 4.12a, 4.12b, and 4.12c. The phases present at 1000 °C were $\alpha\text{-Al}_2\text{O}_3$, CaO, and CA. The presence of the CaO and CA phases remained until 1100 °C, and then disappeared by 1200 °C with the CA_2 phase being observed and then remaining to 1450 °C. The temperatures for CA_2 formation were 100 °C higher for the HTND data than the XRD result. The temperature formation for CA_6 occurred at approximately 1400 °C. This agrees well with the results obtained from the x-ray diffraction, synchrotron diffraction and differential thermal analysis (DTA) (Asmi *et al.* 1998). The formation of CA_6 is believed to occur via *in-situ* reactions according to Equations 4.1, 4.2, 4.3 and 4.4. Traces of $\alpha\text{-Al}_2\text{O}_3$ were also found in the final product.

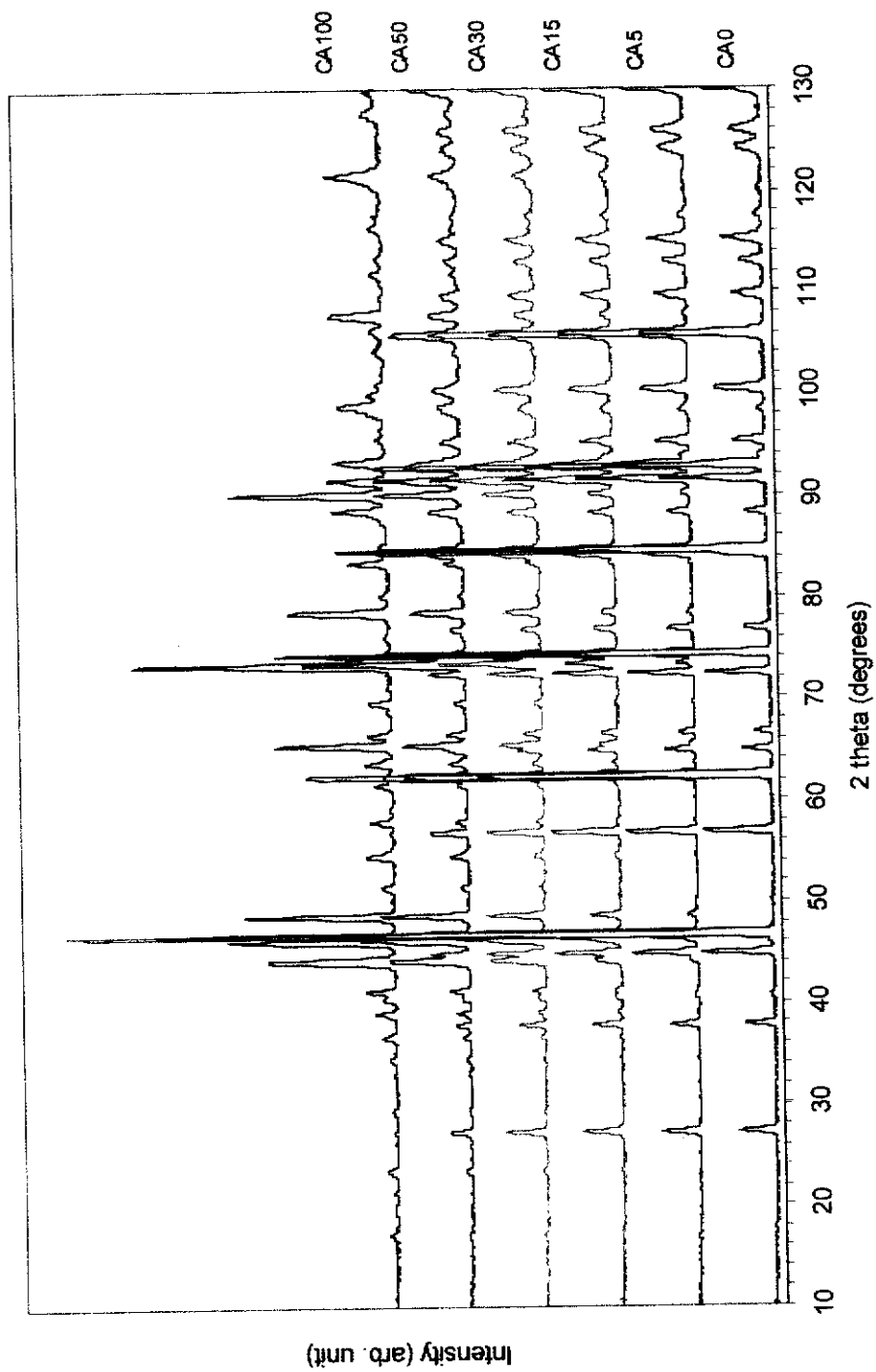
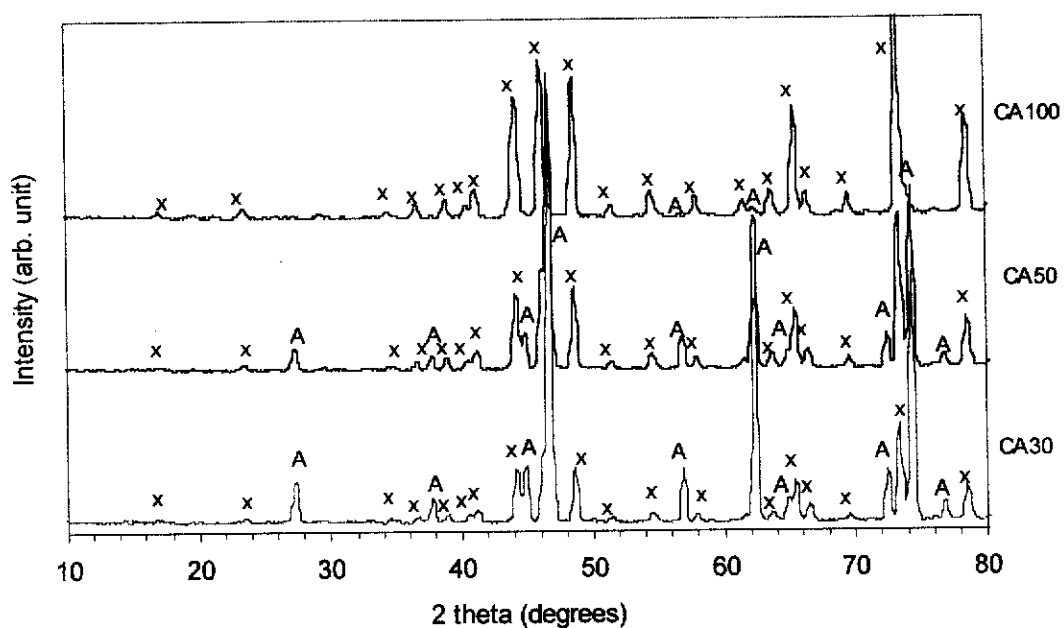
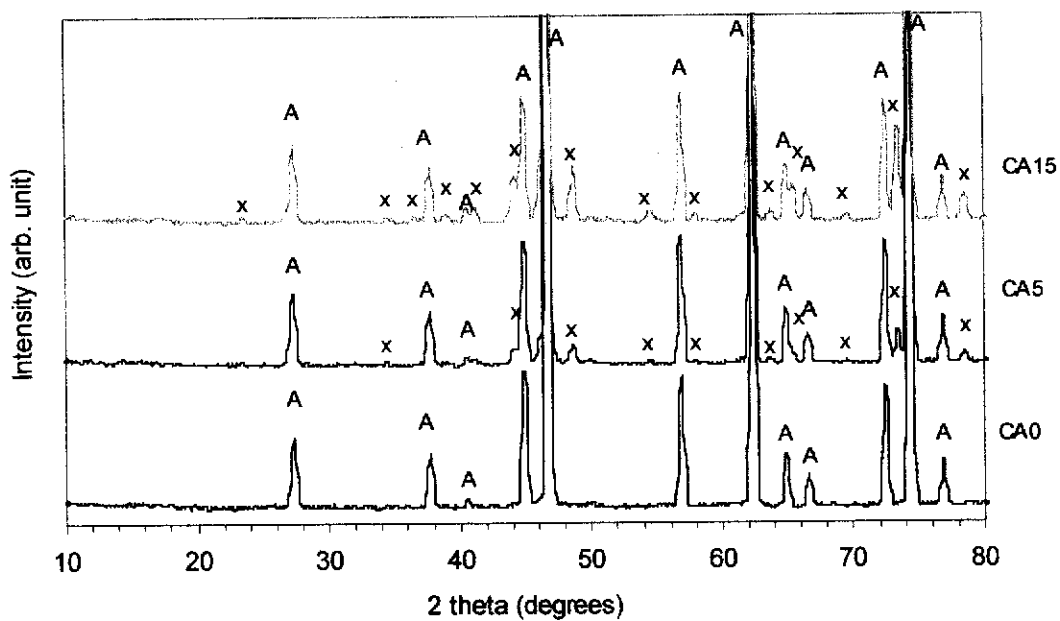


Figure 4.9. Room temperature ND patterns for CA0, CA5, CA15, CA30, CA50 and CA100 samples.



(a)



(b)

Figure 4.10. Expanded views of the ND patterns in Figure 4.9 for CA0, CA5 and C15 in (b) and CA30, CA50 and CA100 in (a). Legends: A = $\alpha\text{-Al}_2\text{O}_3$ and x = CA_6 .

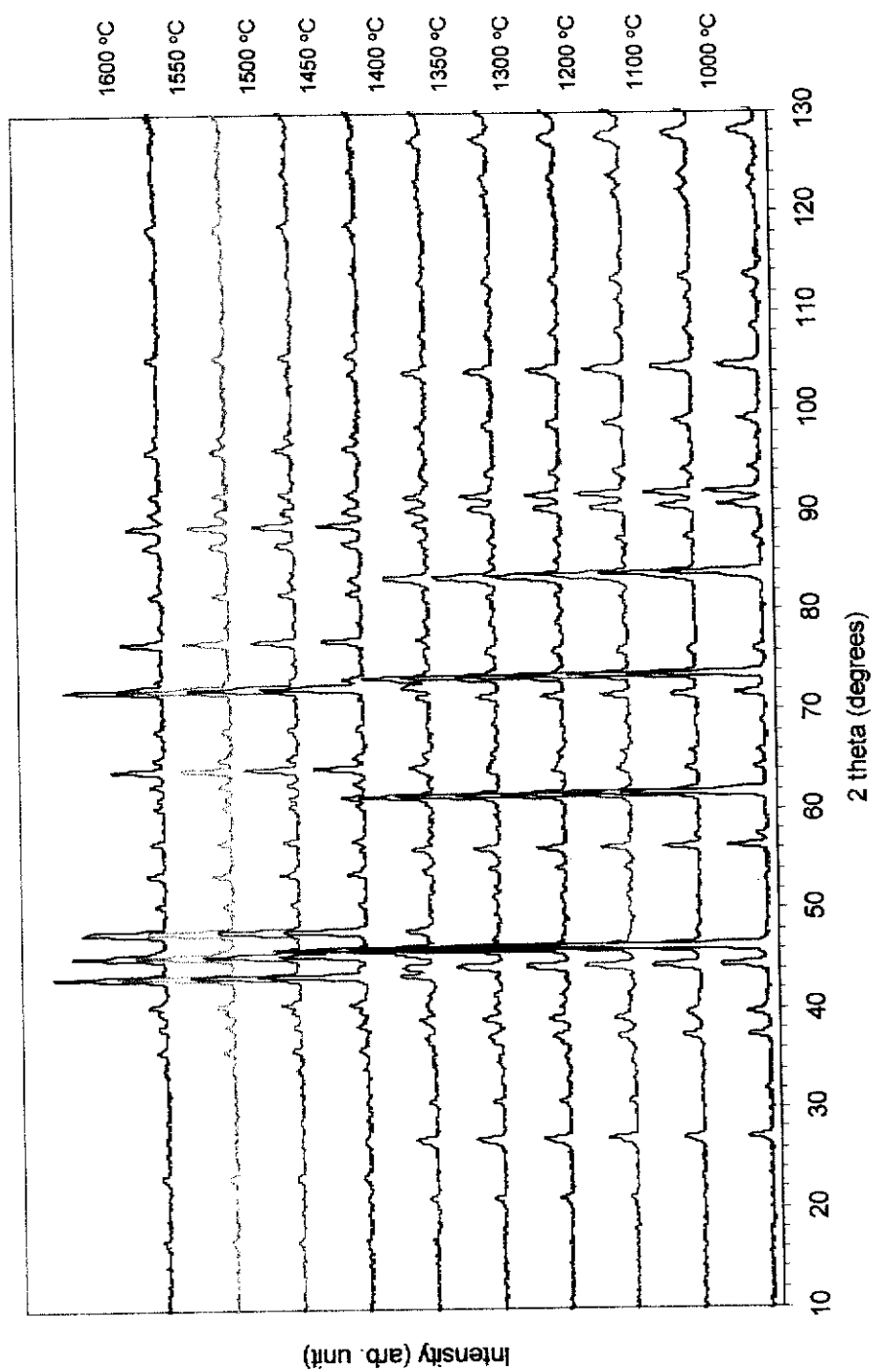
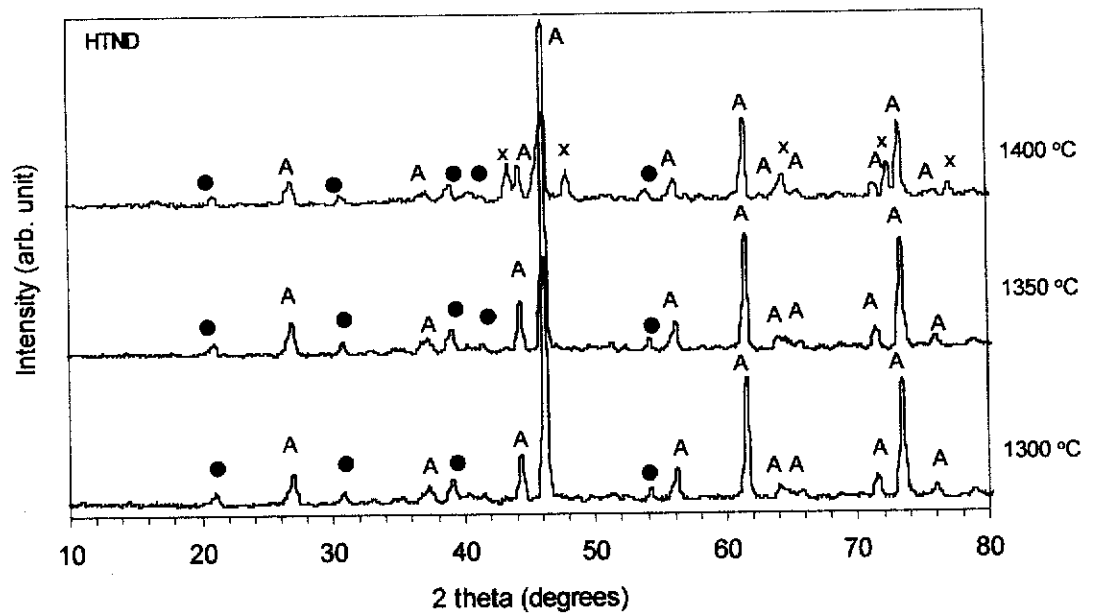
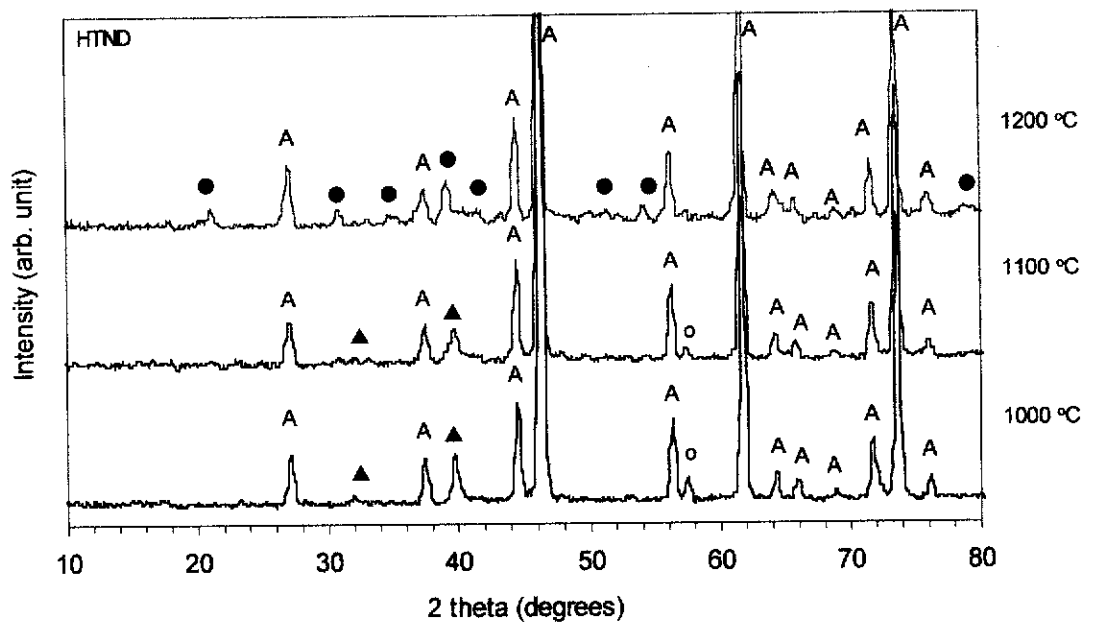


Figure 4.11. High temperature neutron diffraction (HTND) patterns for CA100 at various temperatures in the range 1000 - 1600 °C.

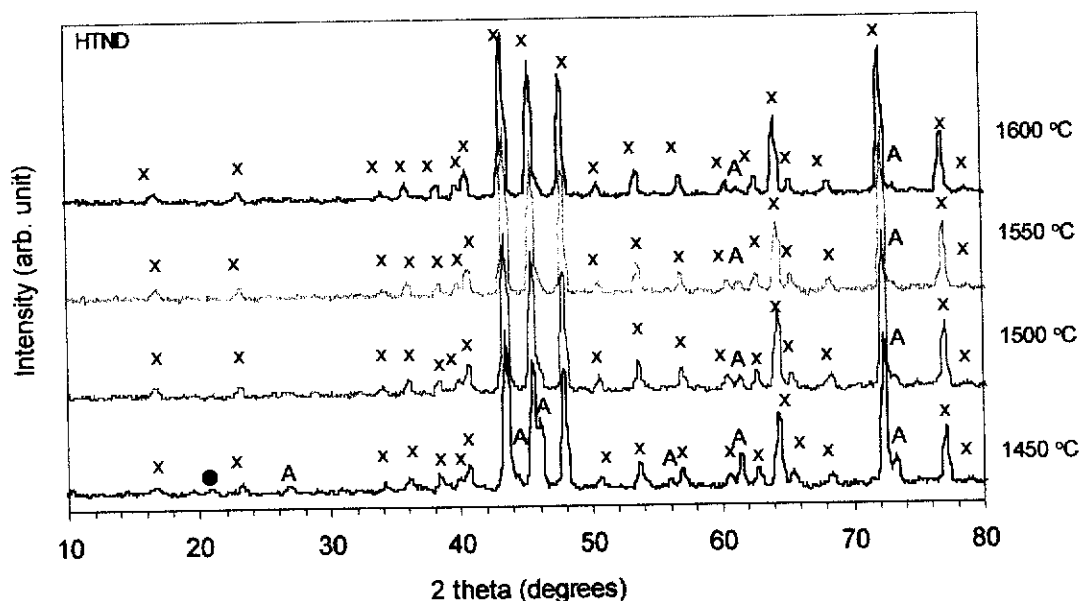


(a)



(b)

Figure 4.12. Expanded views of the HTND patterns in Figure 4.11 for CA100 from 1000 to 1200 °C in (b) and 1300 to 1400 °C in (a). Legends A = $\alpha\text{-Al}_2\text{O}_3$, o = CaO, ▲ = CA, and ● = CA_2 .



(c)

Figure 4.12. (Continued) Expanded views of the HTND patterns in Figure 4.11 for CA100 from 1450 to 1600 °C in (c). Legends A = α -Al₂O₃, ● = CA₂, x = CA₆.

Rietveld Phase Composition Analysis

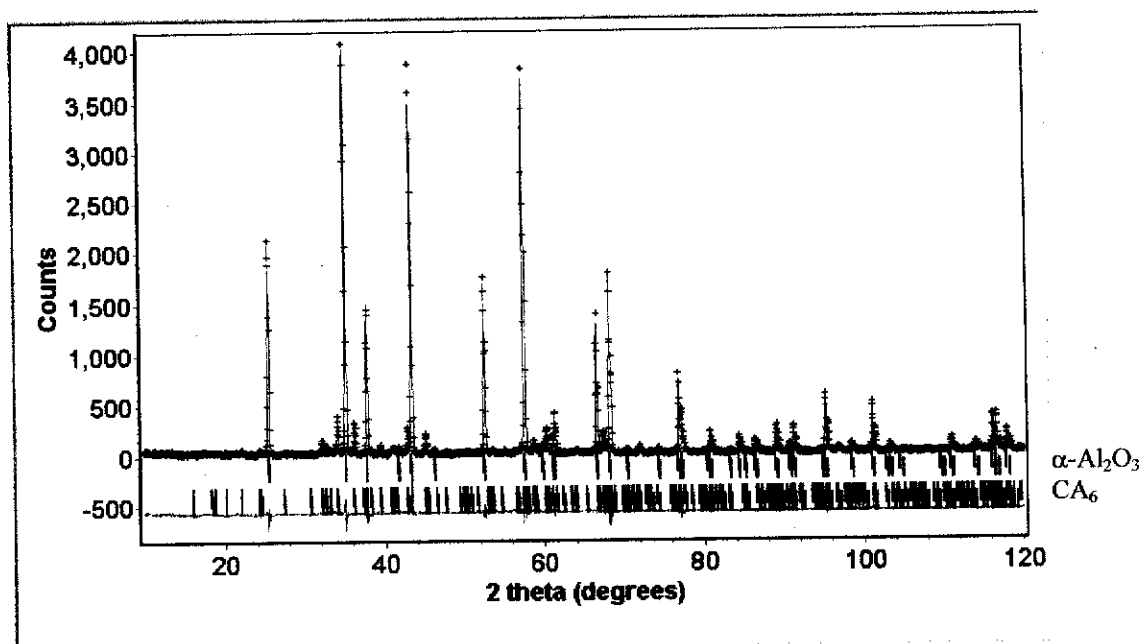
The relative phase composition values for each of the diffraction patterns for the compositions CA0, CA5, CA15, CA30, CA50 and CA100 were performed by the Rietveld method using the Rietica for Windows 95/98/NT version 1.6.5 program which derives from the Hill-Howard-Hunter LHPM program (Hill, Howard, and Hunter 1995). The crystal structures models used in the calculation were taken from the Inorganic Crystal Structure Data Base (Fach Informations Zentrum and Gmelin Institut, Germany) – ICSD # 75725, 75785, 260, 34487, 34394 for α -Al₂O₃, CaO, CA, CA₂, and CA₆, respectively. The parameters refined were those controlling pattern intensity (scale factors), peak profile (width and shape), peak position (zero point and unit cell), background polynomial parameters, and the individual atom thermal parameters. The final Rietveld scale factors were converted to the phase compositions-by-weight using Equation 3.19. The quality of the Rietveld

calculations for all samples was assessed in terms of the Rietveld difference plots and the refinement figures-of-merit.

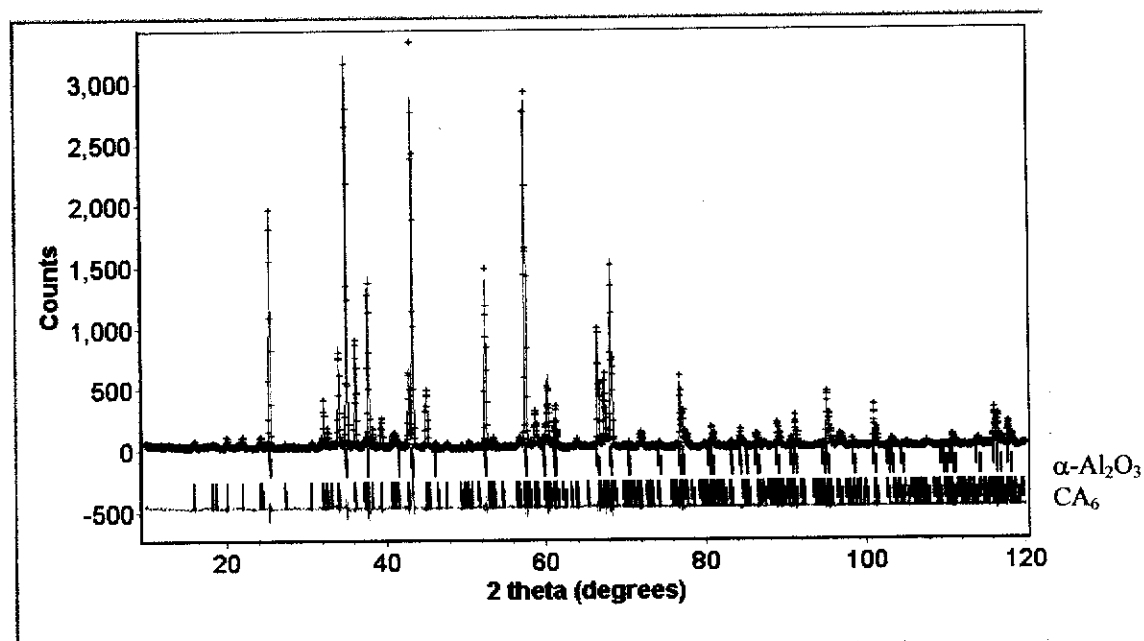
Selected output difference plots obtained from the XRD and ND patterns Rietveld calculations for CA15 and CA30 samples are shown in Figures 4.13 and 4.14. Results for the CA0, CA5, CA50 and CA100 samples are shown in Appendix B (Figures B-1, B-2, B3, and B-4). The results show no unassigned Bragg reflections, thus indicating that the correct phases were used in the Rietveld calculations. The fluctuations in the difference plots indicate reasonable fit between the observed and the calculated plot.

The figures-of-merit for CA0, CA5, CA15, CA30, CA50, and CA100 samples obtained by Rietveld analysis with the XRD and ND data are presented in Tables 4.3 and 4.4. The R_B factors for the individual phases in each composition obtained from ND is lower than that for the corresponding XRD patterns, i.e. 1.7 – 3.6 % for ND data and 3.3 – 6.9 % for the XRD data. The degree of the refinements is also demonstrated by the small goodness-of- fit (GOF) values, i.e. less than 3 %, indicating that all refinement results are acceptable (Kisi 1994).

The relative phase compositions (wt%) for CA0, CA5, CA15, CA30, CA50, and CA100 samples obtained by Rietveld analysis with the XRD and ND data are presented in Tables 4.5 and 4.6. The relative phase compositions (wt%) of CA_6 obtained from the XRD patterns agree well with the as-weighed CA_6 compositions, except for the CA15 and CA100 samples for which there are discrepancies of 3.1 and 5.1 wt% of CA_6 , respectively. However, the relative phase compositions (wt%) for CA_6 obtained with ND data show a small discrepancy of 2.7 wt% for CA_6 in the CA100 sample. This discrepancy indicates incomplete reaction of the raw materials (Al_2O_3 and $CaCO_3$) used to form *in-situ* CA_6 at 1650 °C for 2h. However, assuming that the reaction was complete, the agreement is satisfactory in general. The agreements between the weight fraction of CA_6 (wt%) obtained from the Rietveld analysis versus the as-weighed CA_6 content (wt%) are shown in Figures 4.15 and 4.16. The correlation obtained was 0.9953 for XRD and 0.9999 for ND data.

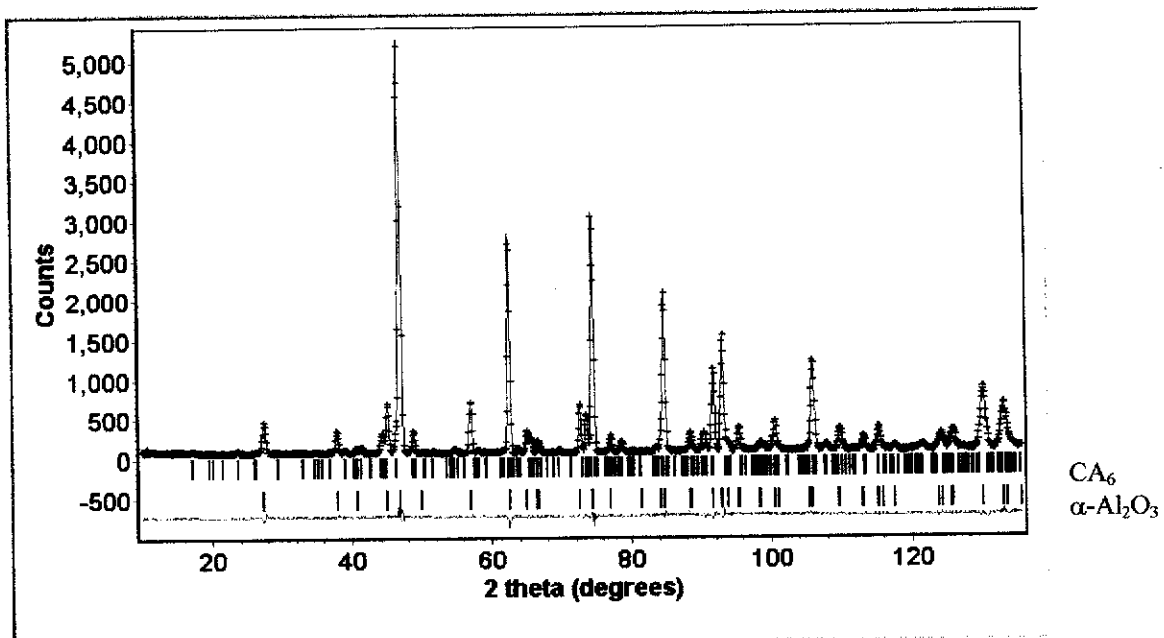


(a)

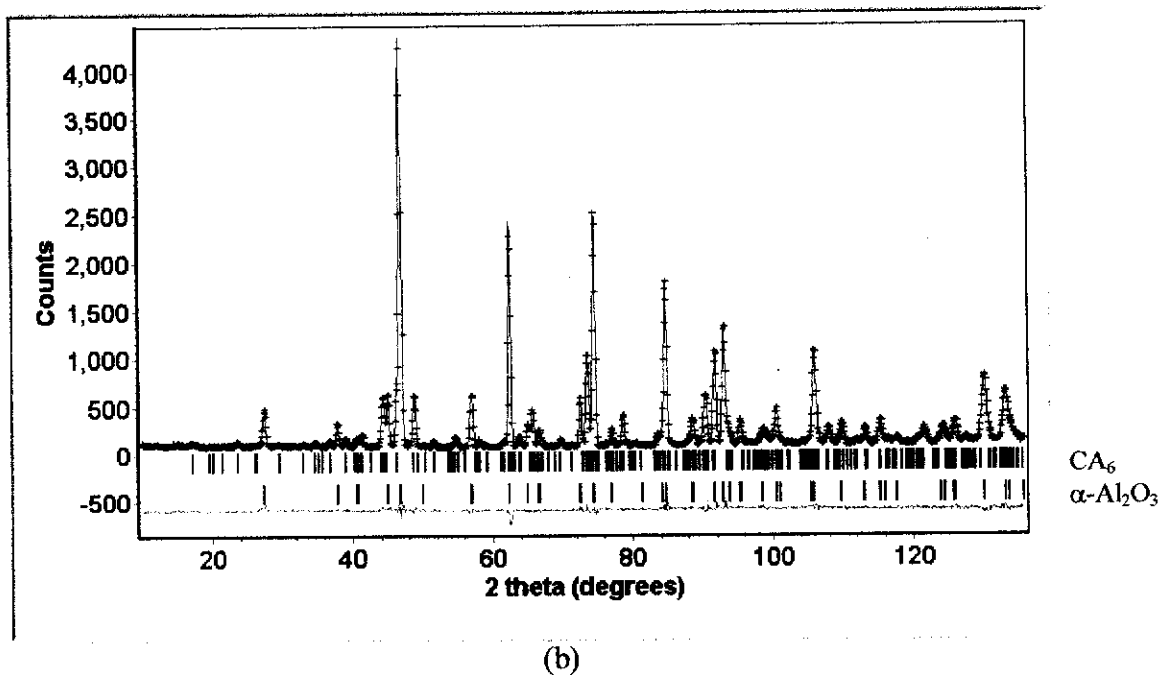


(b)

Figure 4.13. XRD Rietveld difference plots for CA15 in (a) and CA30 in (b). The observed data are shown by a (+) sign, and the calculated data by a solid line. Vertical line represents the positions of diffraction lines for α -Al₂O₃, and CA₆. The green line below the vertical line is the difference profile.



(a)



(b)

Figure 4.14. ND Rietveld difference plots for CA15 in (a) and CA30 in (b). The observed data are shown by a (+) sign, and the calculated data by a solid line. Vertical line represents the positions of diffraction lines for α -Al₂O₃, and CA₆. The green line below the vertical line is the difference profile.

Table 4.3. Figures-of-merit from Rietveld refinement with XRD data for CA0, CA5, CA15, CA30, CA50 and CA100 samples.

Sample	R _{exp}	R _{wp}	GOF	R _B α -Al ₂ O ₃	R _B CA ₆
CA0	10.8	16.4	2.3	5.0	-
CA5	10.5	15.2	2.1	3.5	6.9
CA15	10.7	14.5	1.8	3.4	5.5
CA30	10.9	14.6	1.8	3.8	4.2
CA50	11.1	14.7	1.8	3.6	4.2
CA100	10.9	14.9	1.9	3.3	4.6

Table 4.4. Figures-of-merit from Rietveld refinement with ND data for CA0, CA5, CA15, CA30, CA50 and CA100 samples.

Sample	R _{exp}	R _{wp}	GOF	R _B α -Al ₂ O ₃	R _B CA ₆
CA0	3.5	5.6	2.6	1.9	-
CA5	3.4	5.1	2.3	1.7	2.5
CA15	3.3	5.0	2.2	1.7	2.3
CA30	3.3	5.9	3.2	2.6	3.0
CA50	3.4	5.2	2.3	2.2	2.6
CA100	3.6	6.7	3.4	3.4	3.6

Table 4.5. Relative phase composition from Rietveld refinement with XRD data for CA0, CA5, CA15, CA30, CA50, and CA100 samples.

Sample	α -Al ₂ O ₃ (wt%)	CA ₆ (wt%)
CA0	100.0 (0.5)	-
CA5	94.6 (0.9)	5.4 (0.3)
CA15	88.1 (0.9)	11.9 (0.4)
CA30	68.5 (0.8)	31.5 (0.5)
CA50	48.6 (0.6)	51.4 (0.7)
CA100	5.1 (0.3)	94.9 (1.1)

Table 4.6. Relative phase compositions from Rietveld refinement with ND data for CA0, CA5, CA15, CA30, CA50, and CA100 samples.

Sample	α -Al ₂ O ₃ (wt%)	CA ₆ (wt%)
CA0	100.0 (0.5)	-
CA5	94.3 (0.8)	5.7 (0.3)
CA15	84.4 (0.7)	15.6 (0.3)
CA30	70.7 (0.7)	29.3 (0.5)
CA50	50.8 (0.5)	49.2 (0.6)
CA100	2.7 (0.3)	97.3 (1.2)

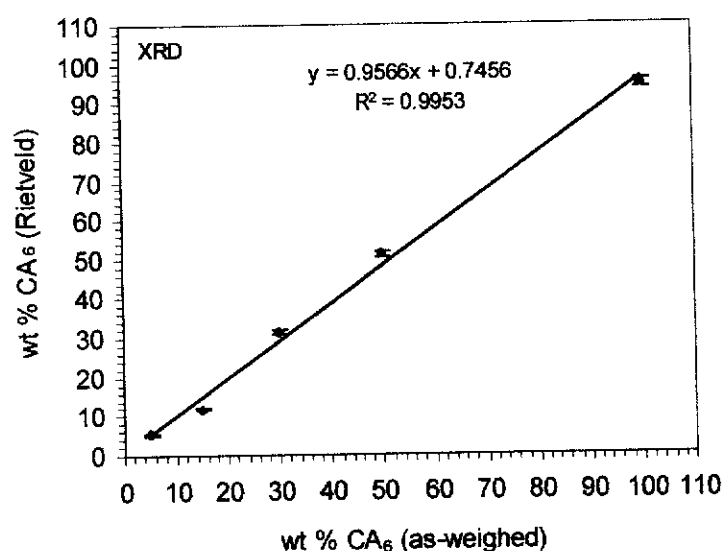


Figure 4.15. Relationship between the CA_6 composition (wt%) derived from Rietveld refinement with x-ray diffraction (XRD) patterns versus the CA_6 (wt%) as-weighed in A/ CA_6 composite. Error bars indicate two estimated standard deviations (2σ).

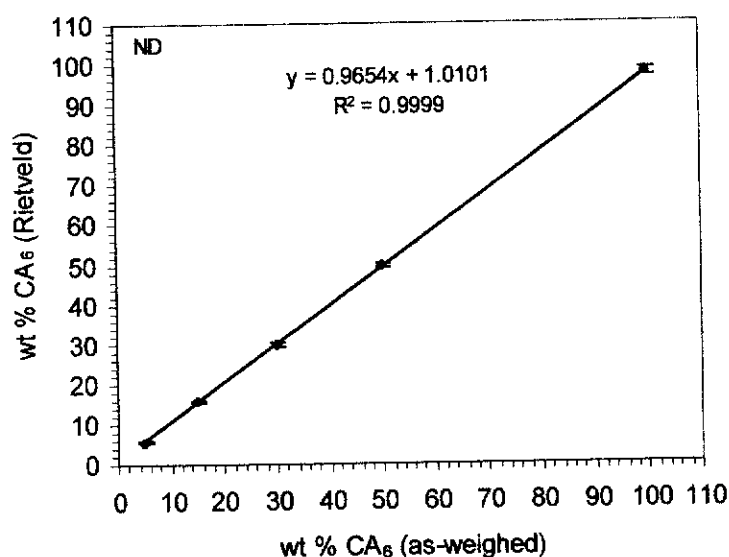


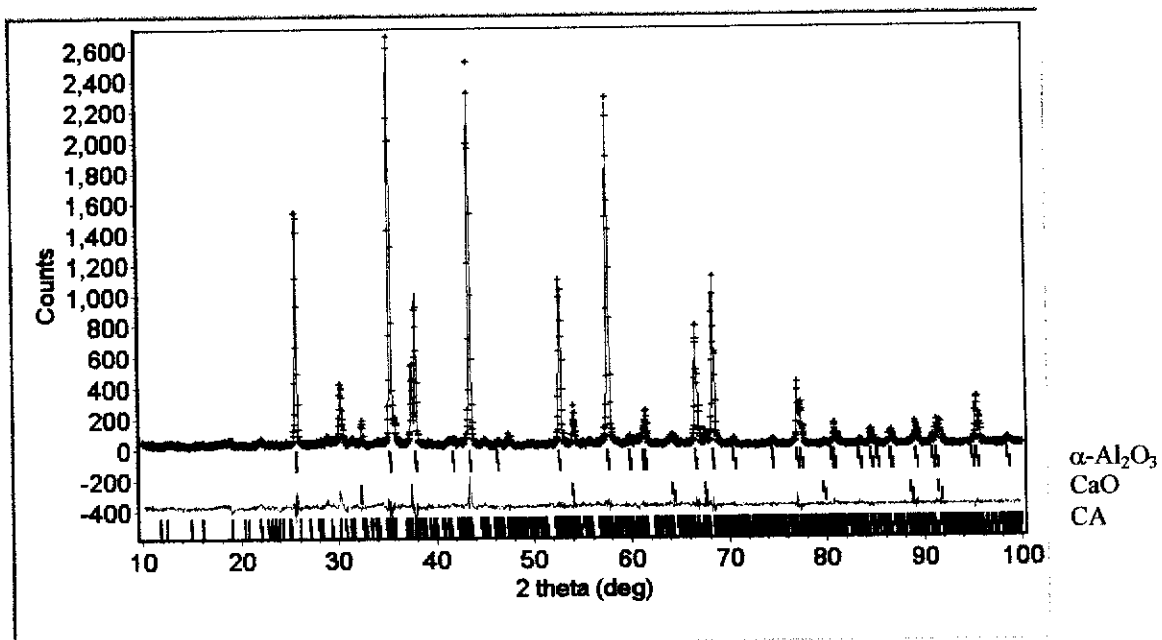
Figure 4.16. Relationship between the CA_6 composition (wt%) derived from Rietveld refinement with neutron diffraction (ND) patterns versus the CA_6 (wt%) as-weighed in A/ CA_6 composite. Error bars indicate two estimated standard deviations (2σ).

The Rietveld difference plots for CA100 sample at 1000 °C and 1350 °C obtained from XRD and ND patterns are shown in Figures 4.17 and 4.18. The difference plots for temperatures 1100, 1200, 1300, 1350, 1400, 1500, 1550 and 1600 °C are shown in Appendix B (Figures B5 - B12).

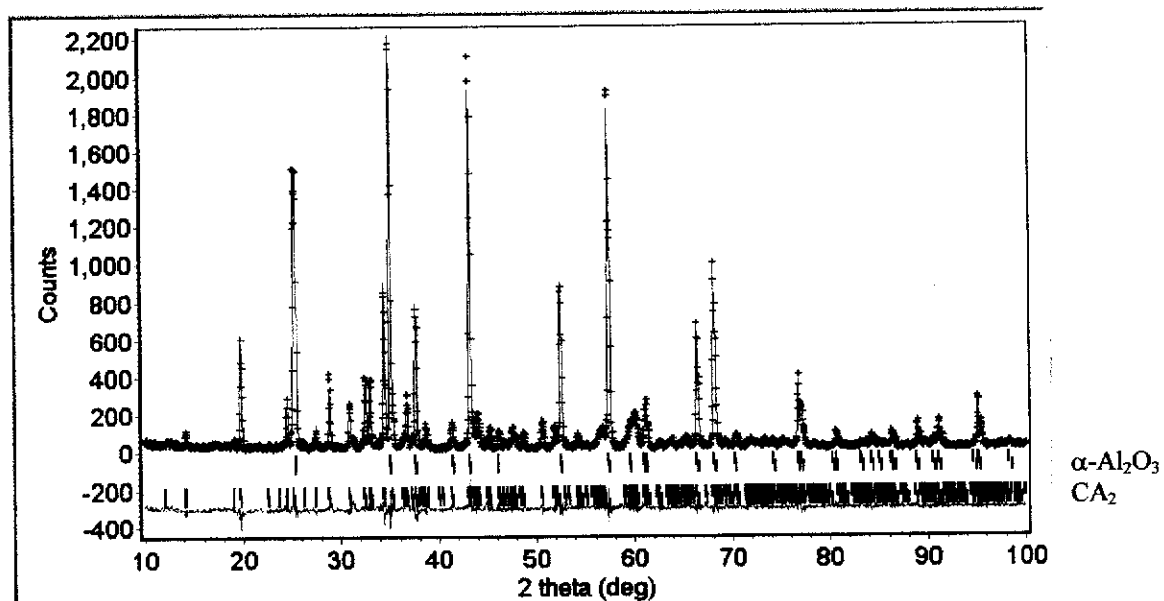
The figures-of-merit profile for CA100 sample between 1000 - 1600 °C, as determined from Rietveld refinement with room temperature XRD and HTND data are shown in Tables 4.7 and 4.8. The R_B factors for each phase in each refinement with XRD data are approximately 2.8 – 5.4 % for α -Al₂O₃, 8.2 % for CaO, 5.8 – 8.2 for CA, 4.2 – 6.3 % for CA₂, and 3.9 - 4.3 % for CA₆. The corresponding values from HTND data were lower, i.e. 1.2 – 2.6 % for α -Al₂O₃, 1.4 – 3.6 % for CaO, 3.1 – 3.9 % for CA, 3.0 – 4.3 % for CA₂, and 2.6 – 3.3 % for CA₆. The GOF values for both (XRD and HTND) were relatively low, i. e all approximately less than 2 %, indicating that the qualities of refinements are acceptable.

Tables 4.9 and 4.10 show the relative phase composition (wt%) of the CA100 sample derived from the XRD and HTND data. The variations of relative phase composition (wt%) as a function of temperature are presented in Figure 4.19. The relative phase compositions obtained from XRD patterns for the α -Al₂O₃ phase decreased markedly with increasing temperature, i.e. from 86.0(1.1) wt% at 1000 °C to 4.7(0.4) wt% at 1600 °C. The wt % of CA decreased from 10.9(0.3) – 1.9(0.2) wt% at 1100 – 1200 °C but disappeared at 1300 °C. The wt% of CA₂ increased slightly up to the temperature 1350 °C, and reached 36.0(0.7) wt% at this temperature, decreased sharply until 1450 °C then disappeared at 1500 °C. The wt% CA₆ increased markedly from 1400 to 1500 °C, i.e. 47.3(0.9) – 93.7(1.3) wt% but from 1500 to 1600 °C it increased steadily. The maximum wt% of CA₆ reached 95.6(1.2) wt% at 1550 °C. The wt% obtained from HTND data for α -Al₂O₃ phase decreased sharply with increasing temperature, i.e. from 91.4(1.5) wt% at 1000 °C to 4.3(0.8) wt% at 1600 °C. The wt% of CaO and CA showed similar behaviour from 1000 to 1100 °C, but disappeared at 1200 °C owing to the formation of the CA₂ phase. The wt% of CA₂ increased slightly up to the temperature 1350 °C and

reaching 32.0(1.2) wt% at this temperature and then decreased sharply until 1450 °C, followed by disappearance at 1500 °C. The wt% of the CA₆ increased markedly from 1400 to 1450 °C, i.e. 30.7(1.2) – 82.2(1.9) wt%, while from 1500 to 1600 °C the wt% of CA₆ increased steadily. The maximum wt% of CA₆ reached 95.7(2.3) wt% at 1600 °C.

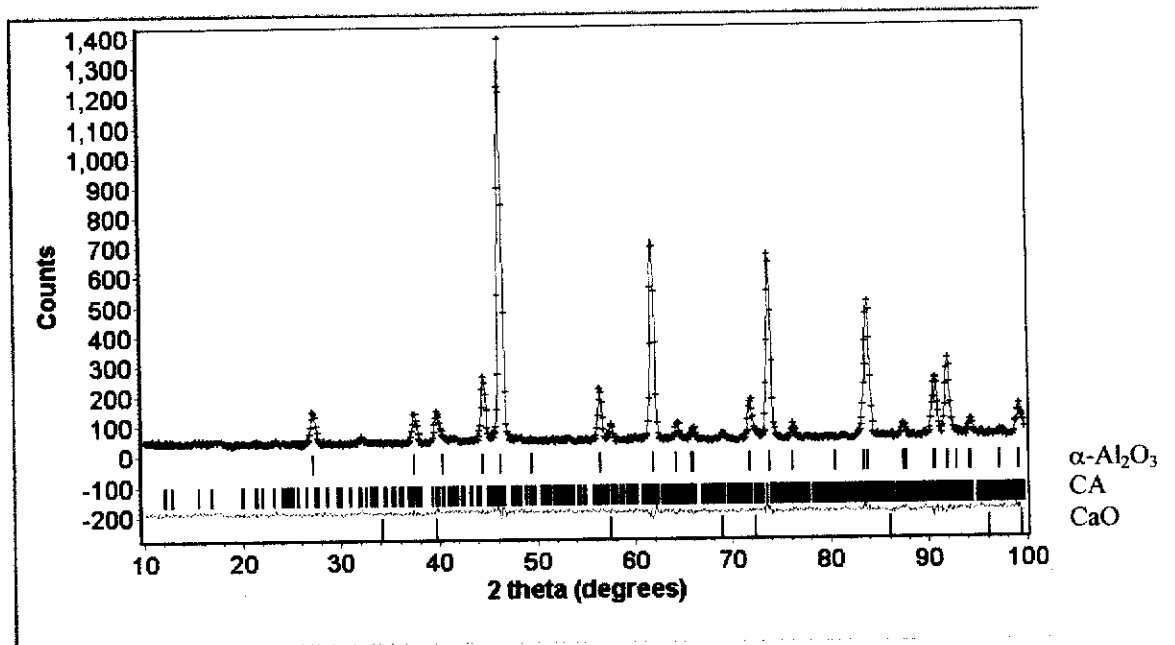


(a)

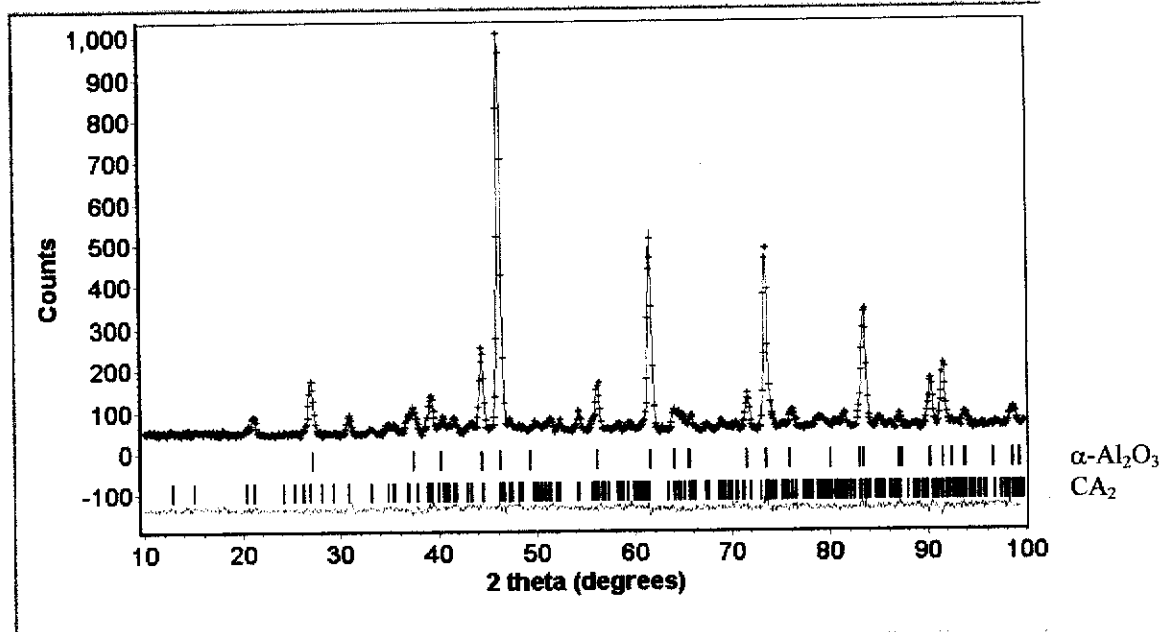


(b)

Figure 4.17. XRD Rietveld difference plots for CA100 sample fired at (a) 1000 °C and (b) 1350 °C. The observed data are shown by a (+) sign, and the calculated data by a solid line. Vertical line represents the positions of diffraction lines for α-Al₂O₃, CA and CaO in (a), and α-Al₂O₃ and CA₂ in (b), respectively. The green line below the vertical lines is the difference profile.



(a)



(b)

Figure 4.18. HTND Rietveld difference plots for the CA100 sample fired at (a) 1000 °C and (b) 1350 °C. The observed data are shown by a (+) sign, and the calculated data by a solid line. Vertical line represents the positions of diffraction lines for α -Al₂O₃, CA and CaO in (a), and α -Al₂O₃ and CA₂ in (b), respectively. The green line below the vertical lines is the difference profile.

Table 4.7. Figures-of-merit from Rietveld refinement with XRD data for CA100 sample.

Temperature (°C)	R _{exp}	R _{wp}	GOF	R _B α -Al ₂ O ₃	R _B CaO	R _B CA	R _B CA ₂	R _B CA ₆
1000	11.0	15.3	1.9	2.9	8.2	7.4	-	-
1100	10.6	15.2	2.0	2.9	-	8.2	5.2	-
1200	10.5	13.7	1.7	2.9	-	7.4	5.6	-
1300	10.3	14.1	1.9	2.8	-	-	5.4	-
1350	10.7	14.9	1.9	2.8	-	-	6.2	-
1400	10.8	15.1	2.0	5.4	-	-	5.7	4.3
1450	10.6	14.3	1.8	5.2	-	-	6.3	3.9
1500	10.9	15.1	1.9	3.9	-	-	-	3.9
1550	10.5	14.5	1.9	2.8	-	-	-	4.5
1600	10.5	13.9	1.8	3.9	-	-	-	4.1

Table 4.8. Figures-of-merit from Rietveld refinement with HTND data for CA100 sample.

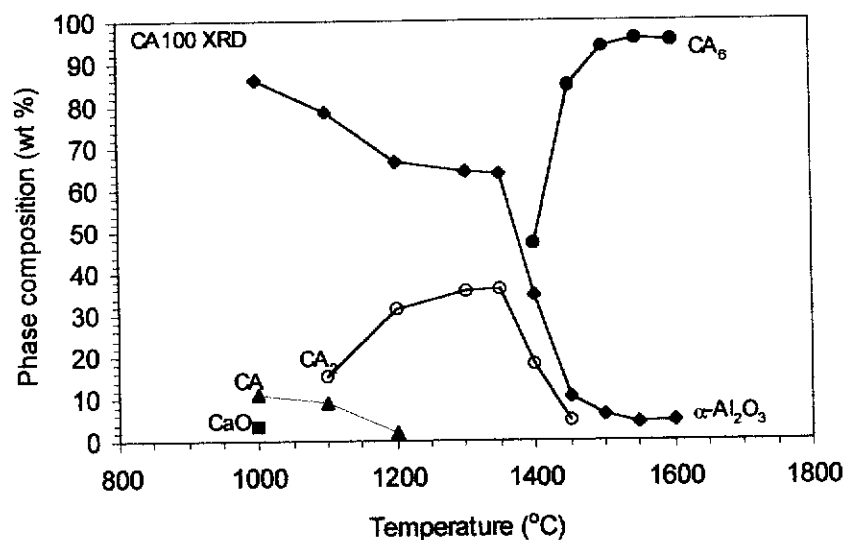
Temperature (°C)	R _{exp}	R _{wp}	GOF	R _B α -Al ₂ O ₃	R _B CaO	R _B CA	R _B CA ₂	R _B CA ₆
1000	5.3	6.4	1.5	1.2	3.6	3.9	-	-
1100	5.2	6.7	1.7	1.5	1.4	3.1	-	-
1200	5.1	6.9	1.8	1.9	-	-	3.8	-
1300	5.3	7.0	1.8	2.2	-	-	3.7	-
1350	5.3	6.9	1.6	1.9	-	-	3.3	-
1400	5.3	7.2	1.8	2.6	-	-	4.3	2.6
1450	5.3	6.7	1.6	1.9	-	-	3.0	3.2
1500	5.4	7.0	1.7	2.1	-	-	-	3.3
1550	5.5	7.1	1.7	1.8	-	-	-	3.2
1600	5.5	6.9	1.6	1.4	-	-	-	3.0

Table 4.9. Relative phase compositions determined from Rietveld refinement with XRD data for CA100 sample.

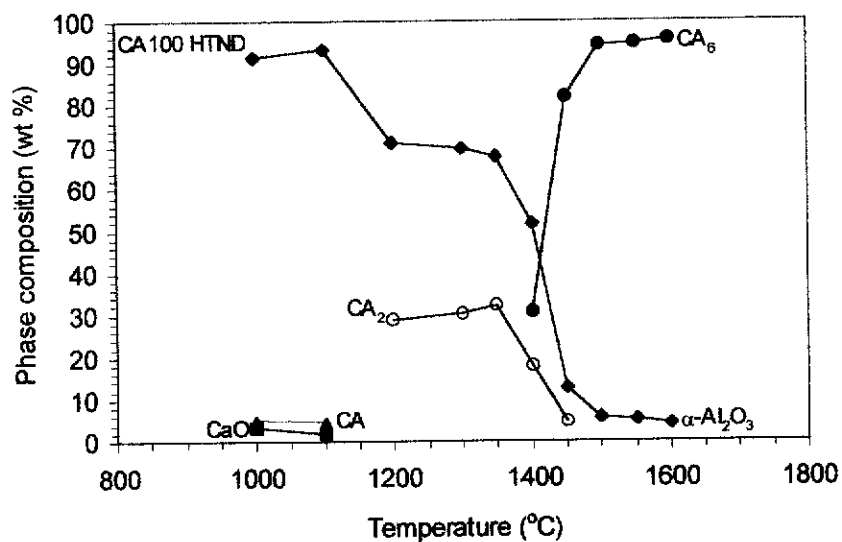
Temperature (°C)	α -Al ₂ O ₃ wt%	CaO wt%	CA wt%	CA ₂ wt%	CA ₆ wt%
1000	86.0 (1.1)	3.1 (0.1)	10.9 (0.3)	-	-
1100	78.8 (1.1)	-	9.0 (0.3)	15.2 (0.4)	-
1200	66.9 (0.9)	-	1.9 (0.2)	31.2 (0.4)	-
1300	64.5 (1.0)	-	-	35.5 (0.6)	-
1350	64.0 (1.0)	-	-	36.0 (0.7)	-
1400	34.7 (0.8)	-	-	18.0 (0.5)	47.3 (0.9)
1450	10.3 (0.6)	-	-	4.8 (0.4)	84.9 (1.2)
1500	6.3 (0.4)	-	-	-	93.7 (1.3)
1550	4.4 (0.3)	-	-	-	95.6 (1.2)
1600	4.7 (0.4)	-	-	-	95.3 (1.2)

Table 4.10. Relative phase compositions determined from Rietveld refinement with HTND data for CA100 sample.

Temperature (°C)	α -Al ₂ O ₃ wt%	CaO wt%	CA wt%	CA ₂ wt%	CA ₆ wt%
1000	91.4 (1.5)	3.2 (0.2)	5.5 (0.6)	-	-
1100	93.2 (1.8)	1.9 (0.2)	4.8 (0.8)	-	-
1200	70.9 (1.5)	-	-	29.1 (1.3)	-
1300	69.9 (1.5)	-	-	30.2 (1.3)	-
1350	68.0 (1.5)	-	-	32.0 (1.2)	-
1400	51.5 (1.4)	-	-	17.8 (0.9)	30.7 (1.2)
1450	13.0 (0.7)	-	-	4.9 (0.9)	82.2 (1.9)
1500	5.5 (0.6)	-	-	-	94.5 (2.1)
1550	5.0 (0.9)	-	-	-	95.0 (2.2)
1600	4.3 (0.8)	-	-	-	95.7 (2.3)



(a)

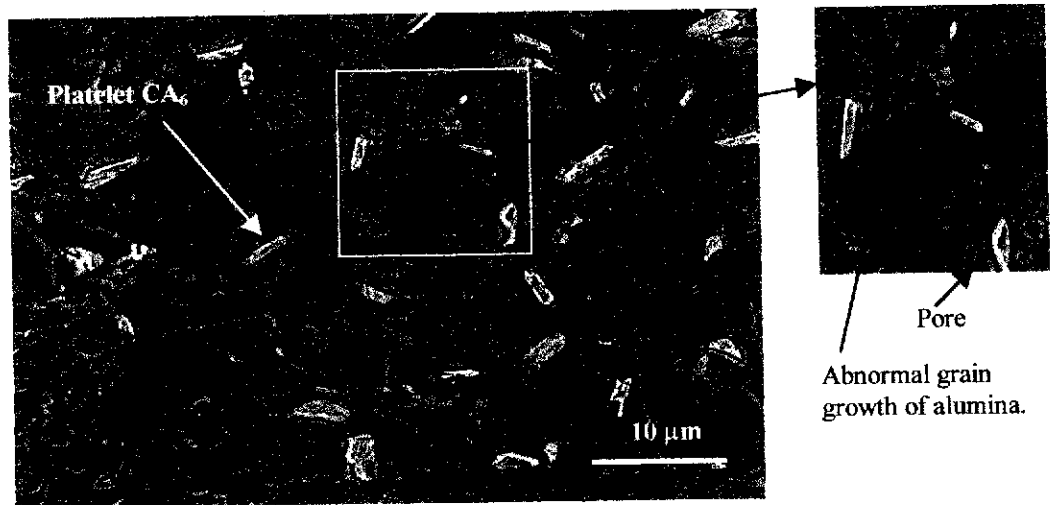


(b)

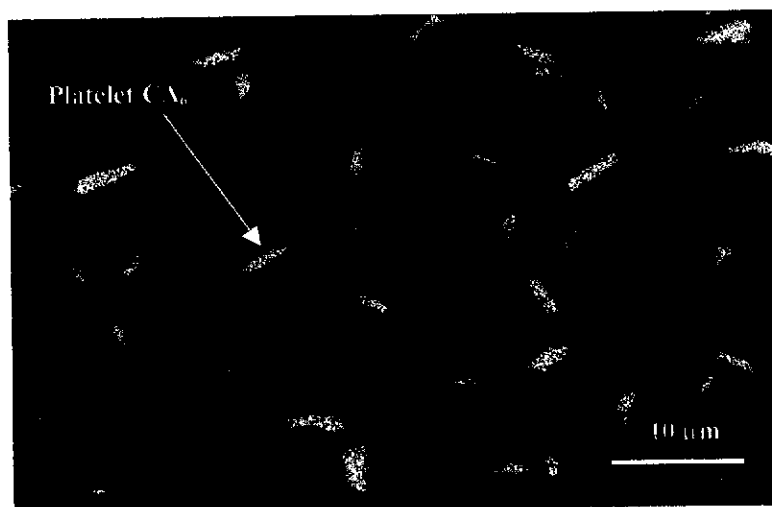
Figure 4.19. Variation in the Rietveld analysis values for the relative phase composition (wt%) of the CA100 sample obtained from XRD data in (a) and HTND data in (b) as a function of temperature. Error bars are too small to include.

4.2.3 Microstructural Analysis

SEM micrographs for CA5 and CA30 samples are reproduced in Figures 4.20, 4.21 and 4.22. Two phases can be clearly distinguished in these micrographs, one being characteristic hexagonal grains, which are attributed to α - Al_2O_3 , and the other exhibiting a plate-like morphology, which must therefore be CA_6 . The *plate-like* morphology of CA_6 grains in the A/ CA_6 composites is clearly revealed by the back-scattered imaging and confirmed by Ca x-ray map (see Figure 4.20b and 4.21b), whereas the alumina matrix dominates the Al x-ray map (see Figure 4.22). The grain size of alumina decreased with increasing CA_6 content. The size of Al_2O_3 grains in samples CA5 and CA30 ranged 1-10 and 1-7 μm , respectively. It is considered that the CA_6 grains act to reduce the matrix grain size and also to make composite matrix more uniformly structured. The *in-situ* formed CA_6 grains appear to be very strongly bonded within the matrix, and the pores formed at triple-point junctions. Abnormal grain growth of Al_2O_3 was found in the composite products (see Figure 4.20a). Abnormal grain growth in this sample was believed due to either inhomogeneous densification during sintering or the presence of glassy phase material at the grain boundaries. Inhomogeneous densification causes local regions of the microstructure to densify faster than the surrounding matrix (Harmer *et al.* 1983, Sharm and Brook 1986). Abnormal grain growth can also be promoted by the presence of a small quantity of liquid phase at the grain boundaries (Stuijts 1977). Further research needs to concentrate on investigating and clarifying the abnormal grain growth of alumina in this system.



(a)

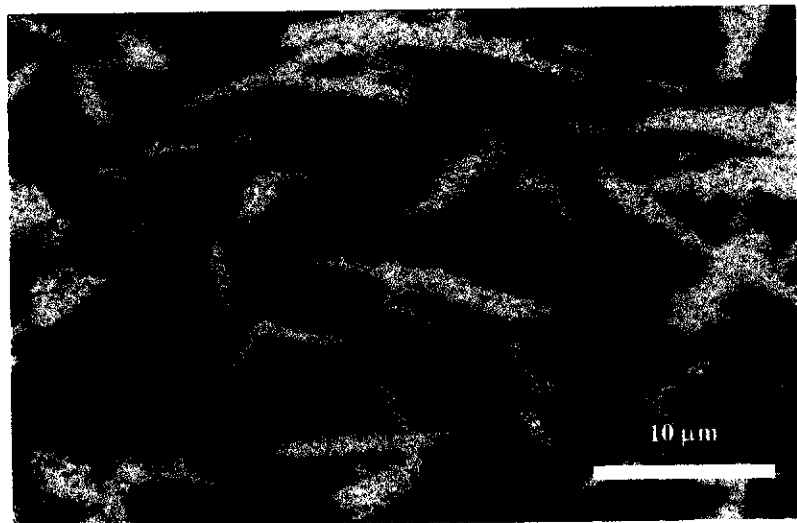


(b)

Figure 4.20. SEM micrograph for CA5 sample. Polished surface was thermally etched at 1350 °C for 30 minutes. Back scattered image in (a) and Ca x-ray map image in (b). (Inset: image of an area showing the presence of abnormal alumina grain growth in the A/CA₆ composite).

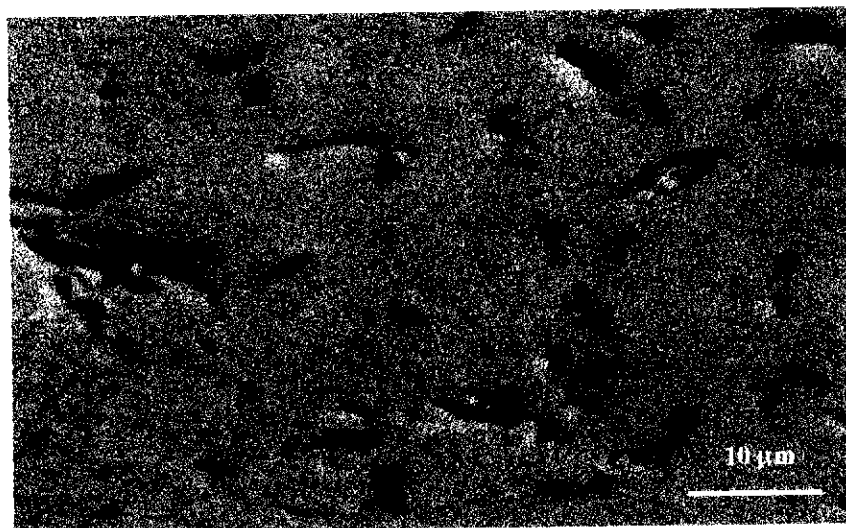


(a)

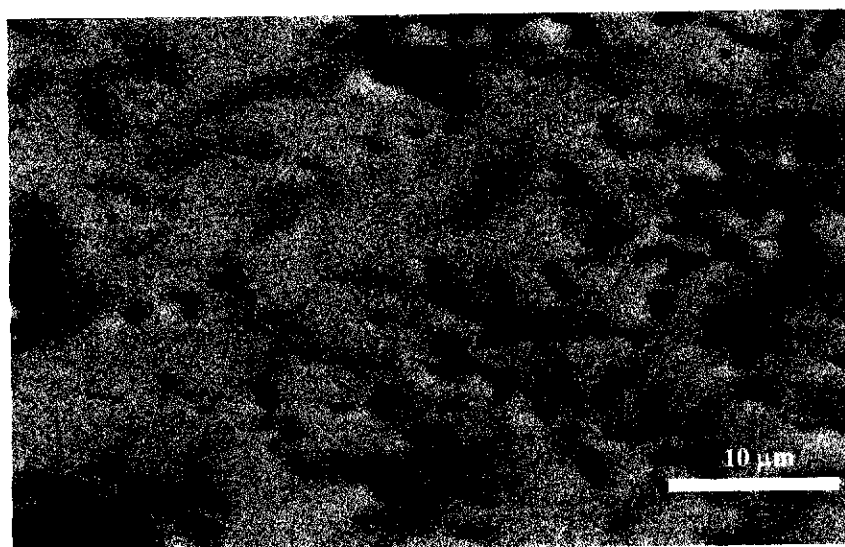


(b)

Figure 4.21. SEM micrograph for CA30 sample. Polished surface was thermally etched at 1350 °C for 30 minutes. Back-scattered image in (a) and Ca x-ray map image in (b).



(a)



(b)

Figure 4.22. Al x-ray map images for CA5 in (a) and CA30 in (b). Polished surface was thermally etched at 1350 °C for 30 minutes.

4.2.4 Physical and Thermal Properties

Shrinkage, Porosity and Density

The shrinkage ($\Delta D/D_0$) was determined as the relative reduction in diameter of the green body compact relative to the sintered sample according to Equation 3.12. The shrinkage results for the compositions CA0, CA5, CA15, CA50, and CA100 shown in Figure 4.23 indicate that the shrinkage decreased steadily with increase in the CA₆ content. The results suggest that the presence of >15 wt% CA₆ caused a significant retardation in the process of densification, possibly due to the formation of CA₆ at approximately 1400 °C as confirmed by XRD and ND results (see section 4.2.2).

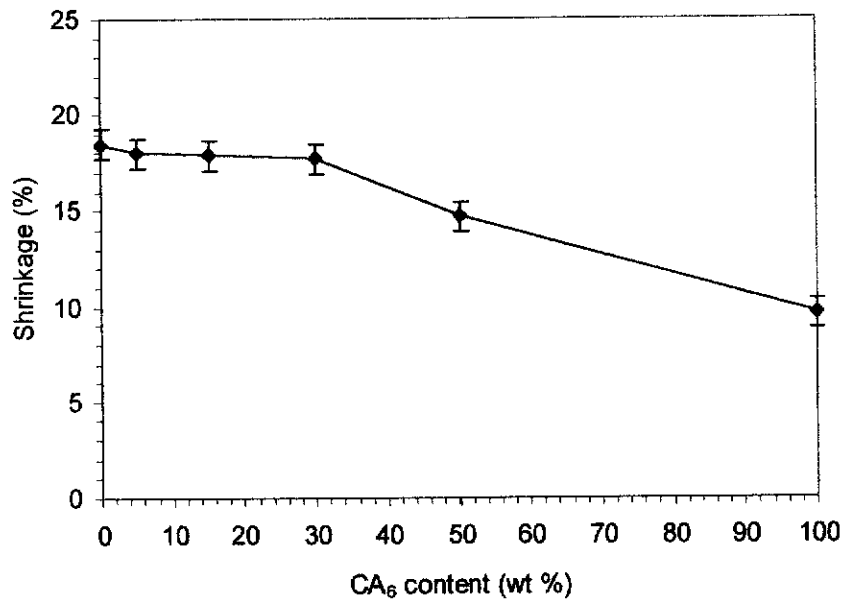


Figure 4.23. Shrinkage as a function of CA₆ content for CA0, CA5, CA15, CA30, and CA100 samples. Error bars indicate two estimated standard deviations (2σ).

The apparent porosity was determined using the Archimedes principle according to Australian Standard (AS 1774.5 – 1989) with water as the immersion medium. The apparent porosity results for the compositions CA0, CA5, CA15, CA50, and CA100 shown in Figure 4.24 indicate that dense samples with < 2 % porosity were obtained for CA₆ content 0 – 15 %. The porosity values increased rapidly for higher CA₆ contents to a value of 7 % for CA100. This can be attributed due to the interlocking of CA₆ grains as confirmed by SEM result (see Figure 4.21a). Therefore, in most cases, these composites must be hot-pressed or hot-isostatically pressed.

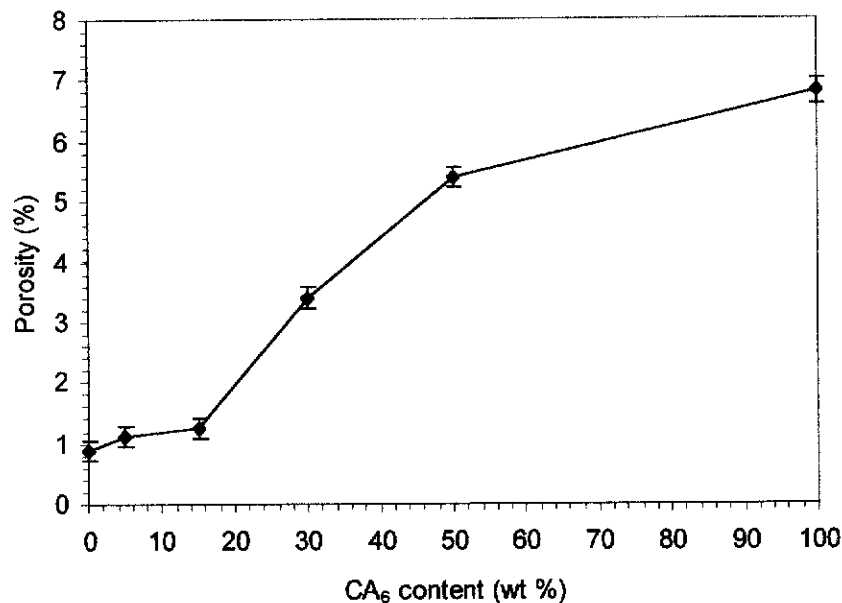


Figure 4.24. Porosity as a function of CA₆ content for CA0, CA5, CA15, CA30, and CA100 samples. Error bars indicate two estimated standard deviations (2σ).

The bulk density of a product usually follows a similar trend to the porosity results. The bulk density results for the compositions CA0, CA5, CA15, CA50, and CA100 samples are shown in Figure 4.25. Crystallographic density values of 3.986 g/cm³ for α -Al₂O₃ (PDF No. 43-1484, ICDD data base) and 3.786 g/cm³ for CA₆

(PDF No. 84-1613) were used to compute the theoretical densities of the A/CA₆ composites based on a rule of mixtures. The results were 3.976 g/cm³, 3.955 g/cm³, 3.924 g/cm³, and 3.883 g/cm³ for the samples CA5, CA15, CA30 and CA50, respectively. The sintered density of the unmodified sample (CA0) reached 99.22 % of theoretical density. The bulk density of the composite product decreased with CA₆ content. This can be attributed to poorer densification and the presence of a less dense CA₆ phase. In comparison with theoretical density of A/CA₆ composites, the density of product reached 98.87, 98.76, 96.60, 94.60, 93.20 % of theoretical density for the compositions CA5, CA15, CA30, CA50, and CA100, respectively. Therefore, it is possible to affirm that hexaluminate crystals act as rigid inclusions during the densification process and retard sintering (Schmid *et al.* 1999).

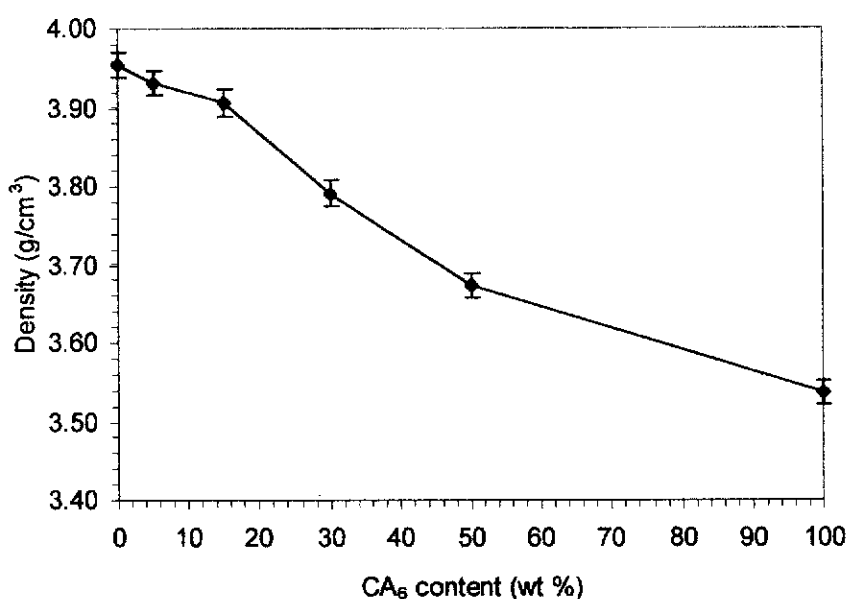


Figure 4.25. Density as a function of CA₆ content for CA0, CA5, CA15, CA30, and CA100 samples. Error bars indicate two estimated standard deviations (2σ).

Thermal Expansion and Shrinkage Behaviour

The thermal expansion and densification behaviour of materials were observed using a THETA 160 dilatometer calibrated with a NIST single crystal sapphire standard. A bar sample with dimensions of 4x4x10 mm³ was prepared for the measurements. The experiment was conducted at temperatures between 20 - 1500 °C. Figure 4.26 shows plots for the thermal expansion and densification versus temperature for α -Al₂O₃ (CA0) and A/CA₆ (CA30) samples. The α -Al₂O₃ commenced to densify at 1137 °C, whereas the A/CA₆ composite at 1194 °C. The thermal expansion of A/CA₆ composites between 20 and 1200 °C is the expansive process. The formation of CA₂ from CA and Al₂O₃, which starts at 1200 °C, and the formation of CA₆ from CA₂ and Al₂O₃ which starts at 1350 °C, are expansive (Criado and De Aza 1991). The maximum shrinkage for the A/CA₆ composites occurred at 1452 °C, which is higher than 1347 °C found for Al₂O₃. The large expansion at temperature 1450 °C in A/CA₆ composites is associated with the formation of CA₆ as a second phase. The presence of CA₆ phase hindered the processes of sintering and densification in alumina matrix. However, the expansion/shrinkage effects do not exceed 7 – 8 %. The average thermal expansion coefficient (TEC) of both green samples is shown in Table 4.11. The A/CA₆ composite has a slightly higher thermal expansion coefficient than Al₂O₃.

Table 4.11. Average thermal expansion coefficient for the A/CA₆ composite (CA30) and α -Al₂O₃ (CA0) at between 20 – 1000 °C.

Sample	Average TEC value (10 ⁻⁶ /°C)
Alumina (control)	8.63
A/CA ₆ (composite)	9.36

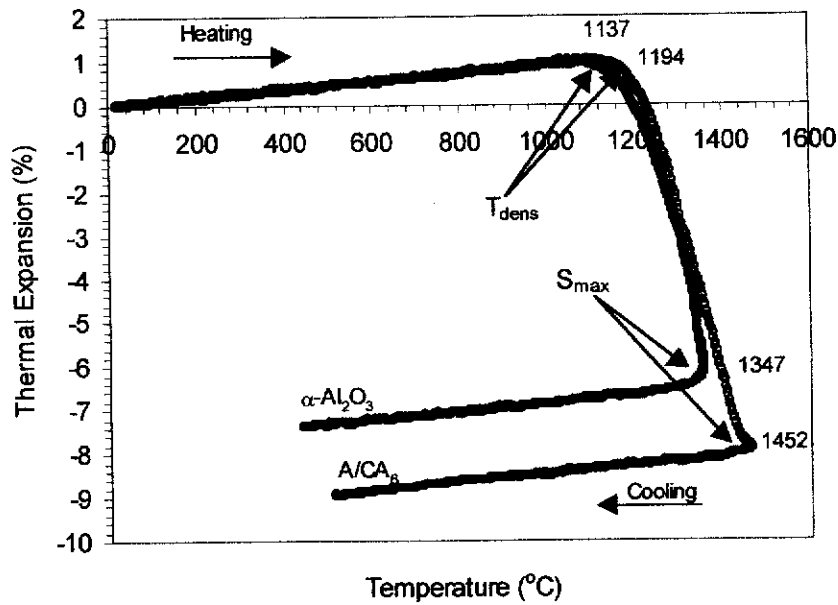


Figure 4.26. Thermal expansion and shrinkage behaviour for the α - Al_2O_3 (CA0) and A/CA₆ (CA30), between 20 - 1500 °C. T_{dens} indicates the temperature at which densification commences and S_{max} indicates the maximum shrinkage.

Young's Moduli

The Young's moduli for the A/CA₆ and Al_2O_3 control samples were determined at room temperature with a Grindo Sonic tester (see section 3.5.1). The results for the compositions CA0, CA5, CA15, CA50, and CA100 shown in Figure 4.27 indicate that the Young's moduli decreased with an increase in the CA₆ content. The results suggest that the presence of CA₆ platelets presumably caused the systematic reduction in Young's modulus from 428 GPa for CA0 to 351 GPa for CA100. Moreover, the presence of porosity in the samples may also contribute to a reduction in the Young's modulus.

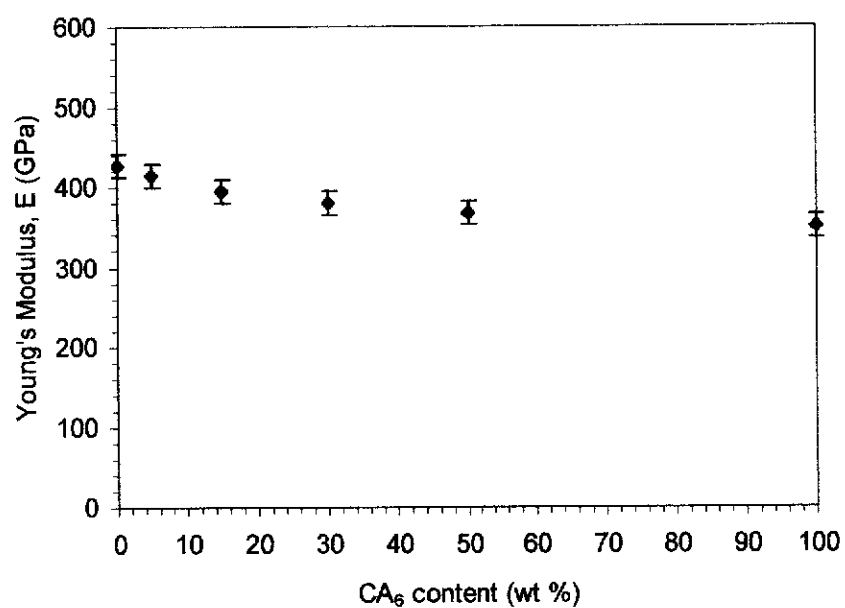
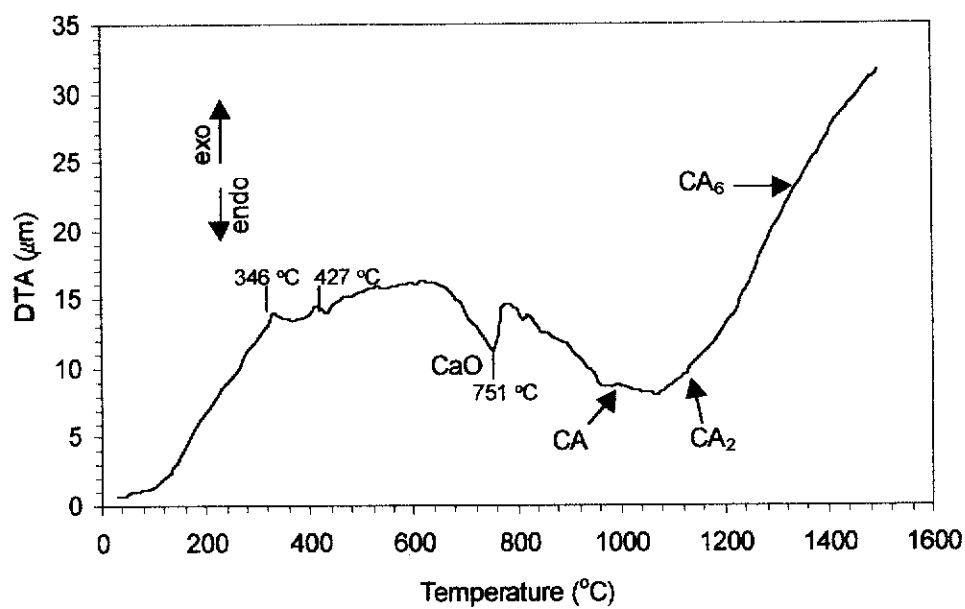


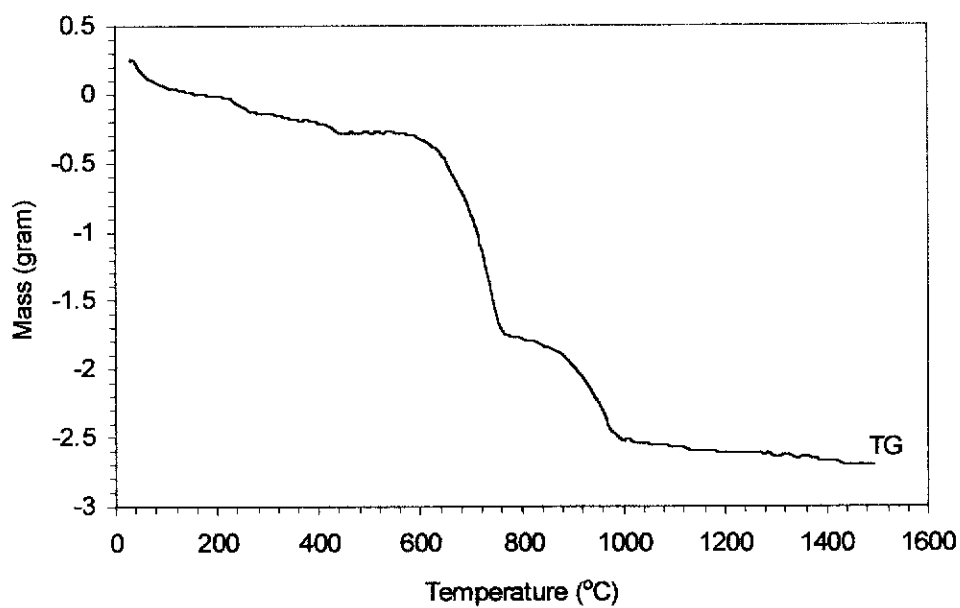
Figure 4.27. Young's modulus as a function of CA₆ content for the compositions CA0, CA5, CA15, CA30, CA50, and CA100. Error bars indicate two estimated standard deviations (2σ).

Differential Thermal and Gravimetric Analysis (DTA and TG)

To the best of the author's knowledge, there is no information in the literature on CA₆ formation by differential thermal and gravimetric analysis. The results of simultaneous DTA and TG analyses with the CA100 sample recorded in the temperature range 20 – 1500 °C are shown in Figure 4.28. A heating rate of 10°/min was chosen to carry out this analysis. Two small exothermic peaks at approximately 346 and 427 °C can be ascribed to the removal of organic additives (propylene glycol, PVA, and glycerol). The sharp endotherm at 751 °C can be associated with the substantial weight losses on the TG curve (Figure 4.28b), presumably due to the decomposition of calcium carbonate. This result is slightly lower (~ 100 °C) than that for the thermogram of pure CaCO₃ (Figure 4.29a) obtained at the same heating rate of 10°/minute, where the sharp endotherm associated with the substantial weight loss occurred at 859 °C. This difference can be attributed to the presence of Al₂O₃. There was no exotherm at 1350 °C, due to the formation of CA₆. The absence of any sharp exotherms or endotherms suggests that the rate formation for the CA, CA₂, and CA₆ phases is very sluggish and the growth of these aluminates is diffusion-controlled and strongly time-dependent. The alumina-rich CA₆ evolved from CA and CA₂, according to Equations 4.2, 4.3, 4.4, and 4.5. The formation temperatures of CA and CA₂ reported here are slightly higher than that of gel-derived calcium alumina powders calcined at 900 – 1000 °C (Gulgun, Popoola and Kriven 1994). This difference can be attributed to the different routes used to prepare the powders.

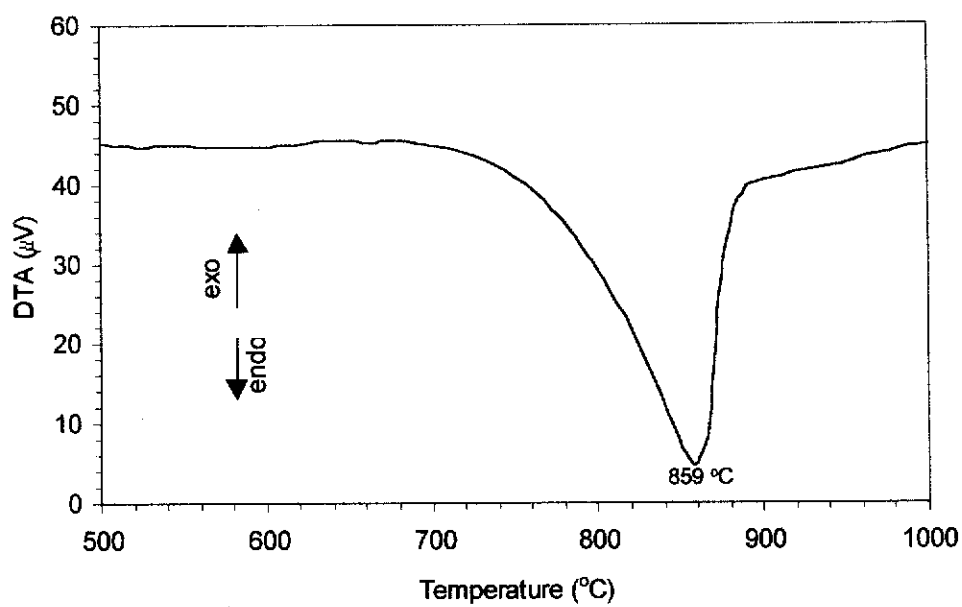


(a)

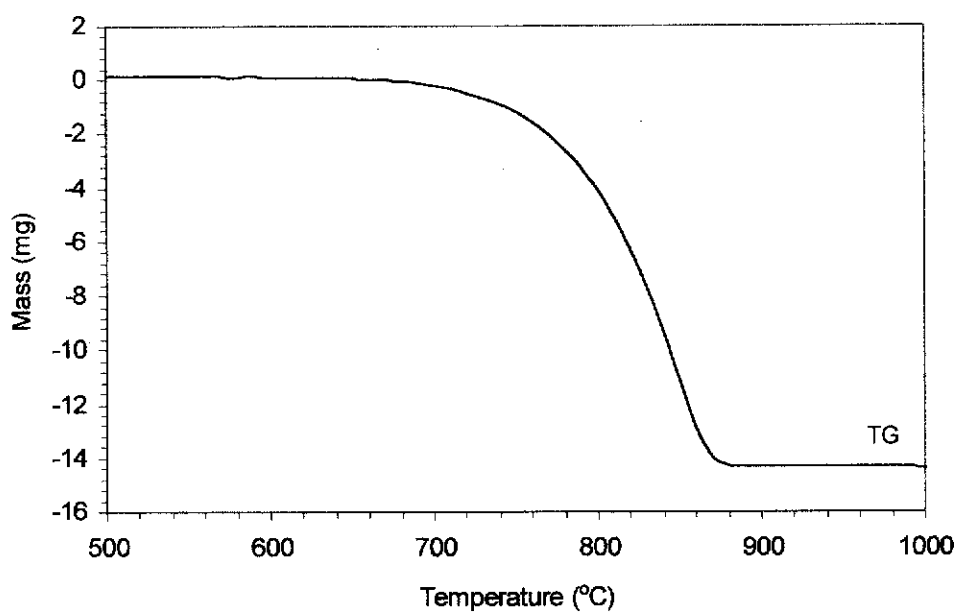


(b)

Figure 4.28. Thermal analysis for the CA100 sample from 20 to 1500 $^{\circ}\text{C}$: (a) DTA and (b) TG.



(a)



(b)

Figure 4.29. Thermal analysis for the as-received CaCO_3 powder from 20-1500 °C: (a) DTA and (b) TG.

4.2.5 Mechanical Properties

Vickers Hardness

The hardness and fracture toughness were measured according to the details outlined in section 3.5.2. The determination of hardness is one of the simplest and most convenient methods for the assessment of mechanical properties. The indentation by a rigid indenter allows determination not only hardness, but also plasticity (Milman, Galanov, and Chugunova 1993). The hardness as a function of CA₆ content, for a 98 N load, is shown in Figure 4.30 for CA0, CA5, CA15, CA30, CA50 and CA100 samples. Results show that the hardness decreased with an increase in the CA₆ content. The reduction in hardness with increasing CA₆ content can be attributed to an increased porosity. Porosity has a very strong effect on the mechanical properties of sintered materials. In general, increasing porosity leads to a monotonic decrease in strength and elastic modulus. However, the dependence of mechanical properties on porosity is more complicated if an increase in porosity leads to a change in the fracture mechanism (Ristich *et al.* 1992). The influence of porosity on hardness of ceramics has recently been investigated by Milman *et al.* (1999), Quinn and Quinn (1997) and Yurkov *et al.* (1997).

Selected samples (CA0, CA5, and CA15) were chosen to study the effect of loads on the Vickers hardness in view of their relatively low porosity values. Figure 4.31 shows the variation of Vickers hardness as a function of applied load in the low load range 4.9 – 48 N. Each of the data points obtained represents an average of measurements from at least three indentations. The results indicate that the dependence of hardness on load is quite evident for each composition where the hardness decreases with increasing load. Such phenomenon, also known as the indentation size effect (ISE), has been observed for ceramics by several researchers (Frohlich, Grau and Wrellmann 1977; Li and Bradt 1993; Gong, Wu and Guan 1999).

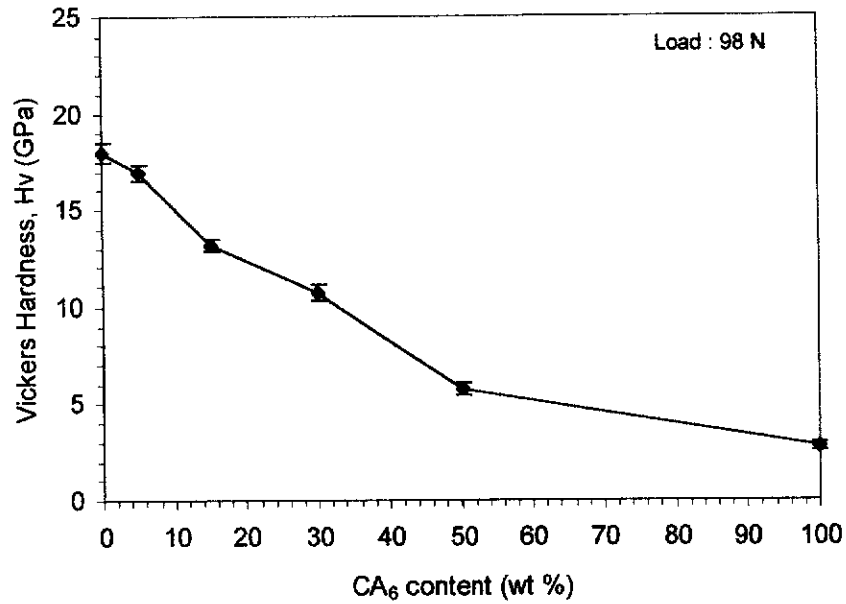


Figure 4.30. Variation of Vickers hardness as a function of CA₆ content for an applied load of 98 N. Error bars indicate two estimated standard deviations (2σ).

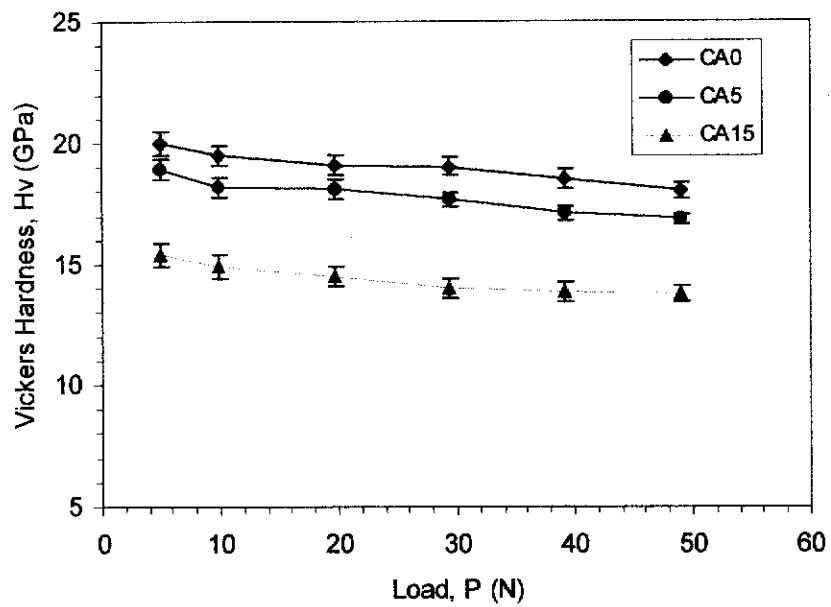


Figure 4.31. Variation of Vickers hardness versus applied load for CA0, CA5, and CA15 samples. Error bars indicate two estimated standard deviations (2σ).

Many attempts have been made to describe the relationship between the applied load and the resulting indentation size. The widely used model is the Meyer law (Quinn and Quinn 1997):

$$P = \beta d^n \quad (4.6)$$

where P is the applied load, d is the length of the diagonal indentation, β and n are constants which can be derived directly from curve fitting with the experimental data. The value of n , the Meyer index can be used to express the indentation size effect (ISE): (i) $n < 2$, the hardness is dependent of load (ISE) and (ii) $n = 2$, the hardness is independent of load (Sangwal 2000).

Recent reviews by Gong, Wu and Guan (1999a, 1999b) found many ceramics are not well modeled by the Meyer analysis. They have identified the energy-balance model (Frohlich, Grau and Wrellmann 1977; Quinn and Quinn 1997) and the proportional specimen resistant (PSR) model (Li and Bradt 1993) to explain the source of the ISE. The relationship between the applied test load and the indentation size is given by:

$$P = \kappa_1 d + \kappa_2 d^2 \quad (4.7)$$

where κ_1 and κ_2 are constants which relate to the proportional resistance of the test specimen and the load independence, respectively. This model has been successfully demonstrated to represent experimental data in some ceramic materials (Li and Bradt 1991, 1993). However, the PSR model proposed by Li and Bradt was only useful to describe the ISE in a very narrow range test loads, i. e. not exceeding 19.6 N, but insufficient if wider range of loads is used (Gong, Wu and Guan 1999a, 2000). Hence, they proposed a new approach based on empirical equation, which was originally proposed by Bückle (1965). This approach is called modified-PSR model given by (Gong, Wu and Guan, 1998):

$$P = \kappa_0 + \kappa_1 d + \kappa_2 d^2 \quad (4.8)$$

where κ_1 and κ_2 are constants which have the same physical meaning as Equation 4.7, κ_0 is a constant related to the effect of machining or polishing which induced plastically-deformed surface associated with the residual stresses for the test specimens. In a series of papers Gong, Wu and Guan (1998, 1999a, 1999b, 2000), have shown that the modified PSR model has wide applicability to describing the ISE, which has been observed in many materials.

The application of Equation 4.8 to the CA0, CA5, and CA15 samples is shown in Figure 4.32. The solid lines in these plots are derived from a conventional polynomial regression according to Equation 4.8. It can be seen that the modified-PSR has proven sufficiently suitable for the representation of the experimental data. The best-fit value of the κ_0 , κ_1 and κ_2 parameters for each material is shown in Table 4.12. The relatively low, negative values of κ_0 relate to the magnitudes of the residual surface stresses of the test materials, which have been subjected to a careful polishing after machining (Gong, Wu and Guan 1999b).

Table 4.12. Variation of κ_0 , κ_1 and κ_2 parameters derived from Equation 4.8 for CA0, CA5, and CA15 samples.

Sample	κ_0 (N)	κ_1 (N/mm)	κ_2 (N/mm ²)	Correlation
CA0	-2.4349	7883.8	167.82	0.9998
CA5	-2.1560	7412	152.98	0.9999
CA15	-0.5660	6725.1	62.85	0.9999

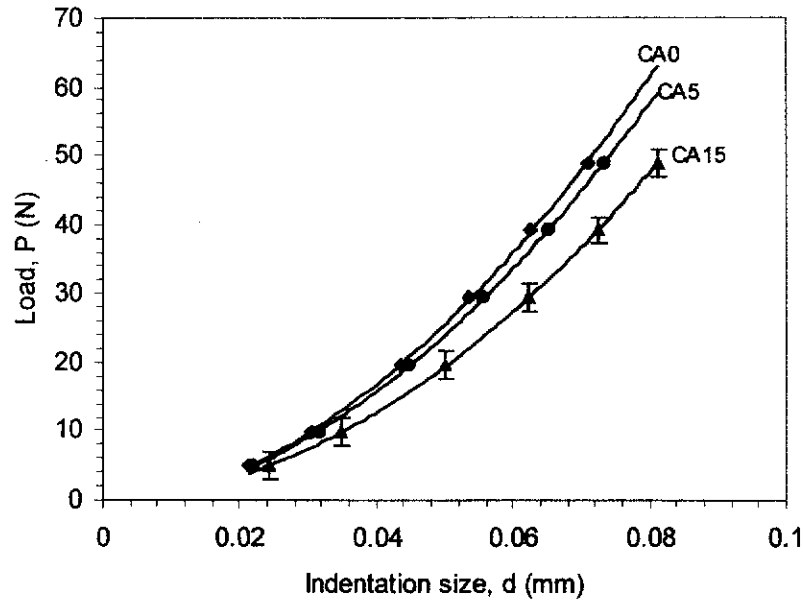


Figure 4.32 Variation of indentation size as a function of the applied load for the CA0, CA5, and CA15 samples. The solid line indicates the best fit satisfying Equation 4.8. Error bars (2σ) have only been shown for one of the data sets to aid clarity.

Fracture Toughness

The measurement of fracture toughness was made using a single-value toughness method. Despite their lower hardness, the composites have improved fracture toughness when compared to alumina, except for the CA50 and CA100 samples. The fracture toughness as a function of CA_6 content for the compositions CA0, CA5, CA15, CA30, CA50 and CA100 is shown in Figure 4.33. The results indicate that the fracture toughness initially increased with increasing CA_6 content and then decreased slightly. An optimum toughness of $7.12 \text{ MPa}\cdot\text{m}^{1/2}$ was obtained for the sample containing 5 wt% CA_6 (CA5 sample). The increase in toughness can be attributed principally to the crack bridging effect of the elongated CA_6 grains. The presence of these grains also helped to suppress the alumina grain growth. A similar trend in the improvement of fracture toughness due to the crack bridging effect has

been observed for the $\text{Al}_2\text{O}_3/\text{La}_2\text{Al}_{11}\text{O}_{18}$ by addition of 300 ppm SiO_2 (Kanzaki 1995). An and Chan (1996) have also attributed the improvement in fracture toughness of their $\text{Al}_2\text{O}_3/\text{CA}_6$ composites to a crack bridging effect. The formation of large elongated or plate-like grains was also reported to increase the fracture toughness of other ceramic systems (Padture and Chan 1992, Chen and Chen 1992). However, it is unclear at this stage why 5 wt% CA_6 gave the maximum K_{IC} value, and why more than 15 wt% CA_6 resulted in a lower fracture toughness. A closer examination of the microstructure and the crack-tip interactions with CA_6 would be necessary to address these issues.

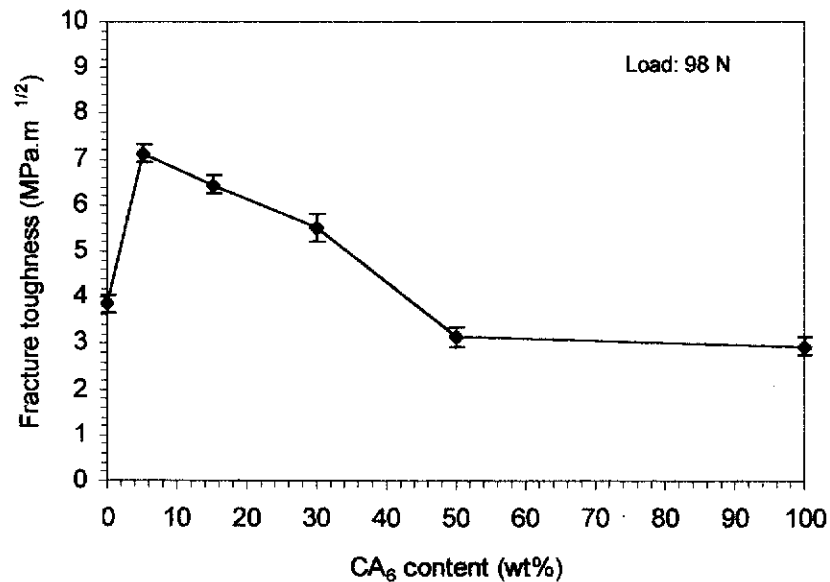


Figure 4.33. Variation of the fracture toughness as a function of CA_6 content for an applied load of 98 N. Error bars indicate two estimated standard deviations (2σ).

Figure 4.34 shows the variation of fracture toughness as a function of indentation load for CA_0 , CA_5 , and CA_{15} samples. Vickers indentation tests were conducted on each specimen in the load range from 29.4 to 196 N. The results show

that the fracture toughness for the CA5 and CA15 increased with increasing load, indicating the presence of a modest rising R-curve behaviour in the materials. However, the CA0 sample appeared to be independent of indentation load.

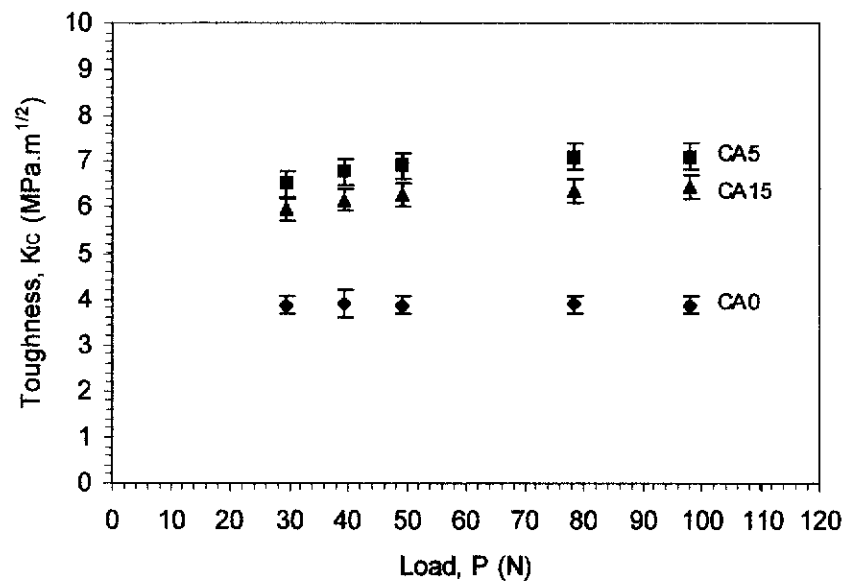


Figure 4.34. Variation of the fracture toughness as function of load for the CA0, CA5, and CA15 samples. Error bars indicate two estimated standard deviations (2σ).

4.3 Summary

The synthesis of alumina/calcium-hexaluminate (A/CA₆) composites through *in-situ* reaction sintering of alumina and CA₆ precursor has been successfully demonstrated.

Both room-temperature XRD and ND patterns revealed that α -Al₂O₃ was the only phase presence in the CA0 sample, whereas α -Al₂O₃ and CA₆ phases were found in CA5, CA15, CA30, and CA50 samples. The peak intensity of CA₆ in the A/CA₆ composites increased in proportion with an increase in CA₆ content. The diffraction patterns for CA100 sample showed mainly CA₆ with traces of α -Al₂O₃.

The formation of calcium aluminates (CA, CA₂, and CA₆) is temperature-dependent. XRD results revealed that CA, CA₂ and CA₆ phases formed at approximately 1000, 1100 and 1400°C respectively, which are very closed to the values of 1000, 1200 and 1400°C obtained from the *in-situ* HTND results. The formation of CA₆ phase is believed to occur via reactions between α -Al₂O₃ and CaO according to Equations 4.1 – 4.4.

Quantitative phase analysis of the A/CA₆ composites by the Rietveld method has provided useful information on the phase relations and development in this system. Both results from the XRD and ND data showed that the GOF values are relatively low and the fluctuations in the difference plots show a reasonable fit between the observed and the calculated plot.

The *plate-like* morphology of CA₆ grains in the A/CA₆ composites is clearly revealed by the back-scattered SEM imaging and confirmed by the Ca x-ray map. The presence of CA₆ caused a size reduction in alumina grains.

The presence of CA₆ phase in Al₂O₃ matrix has significant effects on the physical properties, i.e. shrinkage, porosity and density of the final products. The shrinkage of A/CA₆ composites decreased with an increase in CA₆ content, whereas the porosity values increased rapidly for higher CA₆ content. The bulk density of a composite also followed a similar trend with the porosity results. The bulk density of

composites reached 98.87, 98.76, 96.60, 94.60, and 93.40 % of theoretical density for CA5, CA15, CA30, CA50, and CA100 samples.

The thermal expansion and densification behaviour of A/CA₆ composites showed that the presence of CA₆ phase hinders the processes of sintering and densification of alumina matrix. An expansive process was observed to occur from 20 to 1200 °C, while at higher temperatures two process were observed, i.e. the expansion due to the formation of calcium aluminates (CA₂ and CA₆) and the shrinkage due to the sintering process. The thermal expansion coefficient of A/CA₆ composites was higher than pure Al₂O₃, by virtue of the high thermal expansion anisotropy of CA₆.

The presence of CA₆ caused the reduction of hardness in A/CA₆ composites. This reduction can be attributed to the increase in porosity and the presence of the softer CA₆ phase. In the test load range of 4.9 - 49 N, samples CA0, CA5, and CA15 samples exhibited a significant indentation size effect (ISE), making it impossible to conduct a comparison between materials based on a hardness number measured at only a single test load level. The modified PSR model (Equation 4.7) was proven to be suitable for describing the observed ISE.

Although the presence of CA₆ platelets caused the reduction of hardness, they served to improve the fracture toughness when compared to alumina. An improvement of 82 % in toughness was obtained in the CA5 sample. The increase in toughness can be attributed due to a crack bridging effect. In the test load range of 29.4 - 196 N, samples CA5 and CA15 showed an increase in fracture toughness with an increase in indentation load, indicating a display of a modest rising R-curve behaviour, which was not apparent in the CA0 sample.

CHAPTER 5

SYNTHESIS OF β -SPODUMENE MODIFIED ALUMINA/CALCIUM-HEXALUMINATE (A/CA₆) COMPOSITES

5.1 Introduction

Alumina ceramics reinforced with calcium hexaluminate (CA₆) can possess several advantages. Firstly, the CA₆ phase has a *plate-like* morphology, which can give rise to *self-toughening* by crack bridging of alumina grains (Chen and Chen 1992; An, Chan and Soni 1996). Secondly, CA₆ exhibits a very high refractory performance and high peritectic transformation at 1875 °C (Chatterjee and Zhmoidin 1972). Thirdly, The coefficient of thermal expansion and density of CA₆ are similar to those of alumina, and it has a high stability in reducing atmospheres (Chatterjee and Zhmoidin 1972). Finally, CA₆ has large primary crystallisation fields, which means low solubility in several multi-component systems (Task and Young 1982; Pena and de Aza 1984). However, it was found that the presence of > 15 wt% CA₆ in alumina matrix caused significant retardation in the process of densification (see section 4.2.4).

Recently, extensive work has been devoted to the study of β -spodumene (Li₂O.Al₂O₃.4SiO₂) as liquid-phase sintering aid for densification of alumina (Latella, Burton and O'Connor 1995; Bayuseno, Lattela and O'Connor 1999), mullite (Low *et al.* 1997; Low, Suherman and Phillips 1997) and aluminium titanate (Shi and Low 1998) ceramics. However, the effect of β -spodumene on the densification of A/CA₆ composites with the aim of achieving optimum mechanical performance has not been reported.

In this chapter, results on the synthesis, phase composition development and the physical and mechanical properties of β -spodumene modified alumina/calcium

hexaluminate (A/CA₆) composites are described. The characteristics and properties of these composites have been studied using room-temperature x-ray diffraction (XRD) and neutron diffraction (ND), scanning electron microscopy (SEM), differential thermal and gravimetric analysis (DTA and TG), dilatometry, and Vickers indentation. Quantitative phase analysis (QPA) of β -spodumene modified A/CA₆ composites was conducted using the Rietveld refinement with neutron diffraction patterns.

5.2 Results and Discussion

5.2.1 Raw Material Evaluation

The particle size distributions for the as-received β -spodumene, processed β -spodumene, CAS0, CAS2.5, CAS10, and CAS15 were determined using laser scattering method described in section 3.4.1. The particle size distribution results for the as-received and processed β -spodumene are shown in Figure 5.1. A summary of the particle size data is given in Table 5.1. The mean particle size (D_{50}) of as-received β -spodumene is 18.83 μm . This broad particle sizes represents a crystal size and no agglomeration of smaller particles. Therefore, to obtain finer particle size, the milling time of 8 h was employed before adding to the A/30 wt% CA₆ precursor. The results show that, after 8 h milling the D_{50} of particle size had decreased to near a micron size.

The particle size distributions for the milled CAS0, CAS2.5, CAS10 and CAS15 powders are shown in Figure 5.2. The results are presented in Table 5.2. The D_{50} measure of particle size was below 1 μm in size for all compositions. Particle size distribution is important, depending on which consolidation or shaping is to be used. In most cases the objective of the consolidation step is to achieve maximum particle packing and uniformity, so that minimum shrinkage and retained porosity will result during densification. Therefore, attaining a fine powder has a beneficial effect on sinterability and densification. In addition, high strength ceramics require

very fine particles (typically $< 1\ \mu\text{m}$) to achieve a fine-grained microstructure with minimum flaw size (Richerson 1992).

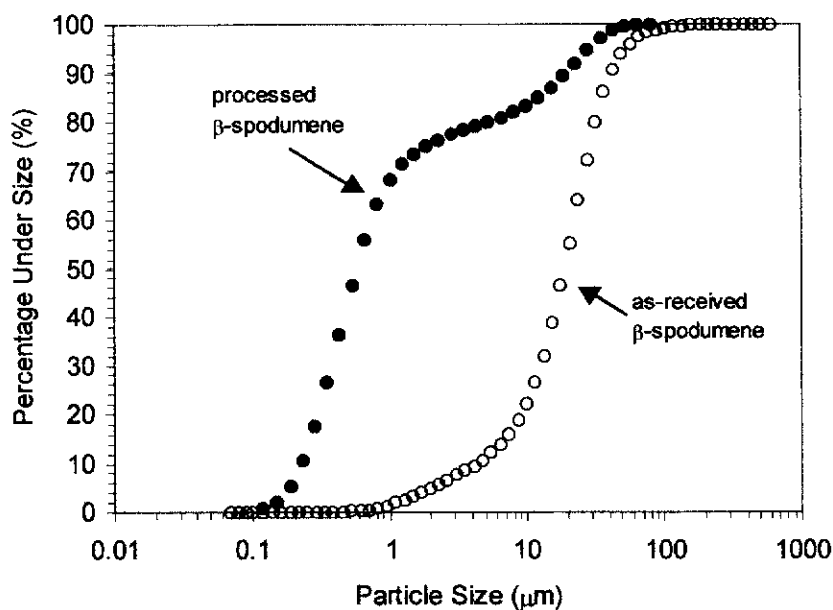


Figure 5.1. Particle size distributions for the as-received and processed β -spodumene powders.

Table 5.1. Milling time and particle size data for the as-received and processed β -spodumene powders.

Sample	Milling time (h)	D ₁₀ (μm)	D ₅₀ (μm)	D ₉₀ (μm)
β -spodumene (as-received)	0	4.3	18.8	41.4
β -spodumene (processed)	8	0.2	0.6	19.6

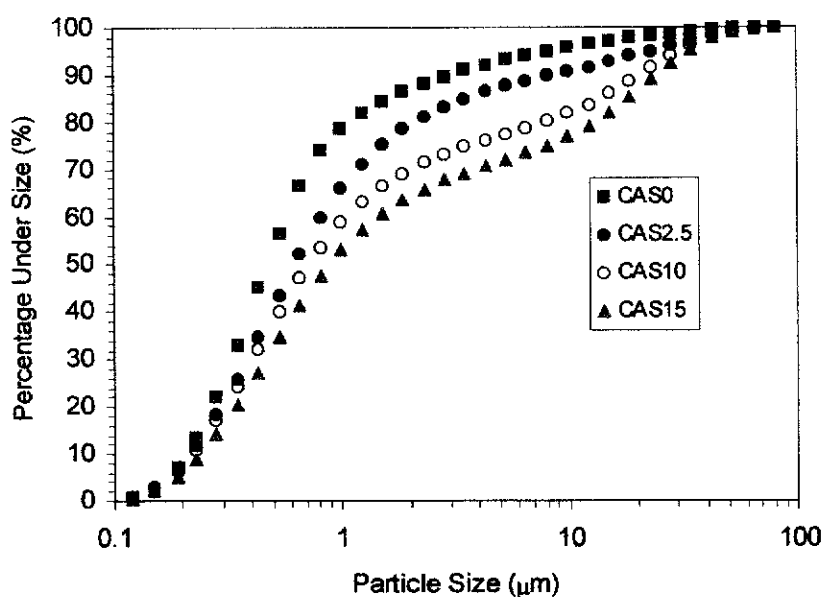


Figure 5.2. Particle size distributions for the milled CAS0, CAS2.5, CAS10 and CAS15 powders.

Table 5.2. Particle size data for the CAS0, CAS2.5, CAS10, and CAS15 processed powders after milling for 3 h.

Sample	β -spodumene content (wt%)	D ₁₀ (μm)	D ₅₀ (μm)	D ₉₀ (μm)
CAS0	0	0.2	0.5	3.0
CAS2.5	2.5	0.2	0.6	8.3
CAS10	10	0.2	0.7	20.4
CAS15	15	0.2	0.9	24.2

Laboratory x-ray powder diffraction patterns were used to examine the crystallographic form of the as-received β -spodumene. The result is shown in Figure 5.3a. The primary phase detected is β -spodumene (PDF 35-797). Rietveld analysis with x-ray powder diffraction data (XRPD) was performed for the as-received β -spodumene, using the procedure described in section 3.4.2. The crystal structure model used was taken from ICSD # 14235 – see Appendix A. Quality of refinements for the as-received β -spodumene powder may be assessed from the Rietveld refinement plots in Figure 5.3b. The relative phase compositions were determined from Equation 3.19 (see section 3.4.2) using the Rietveld scale factors. The refinement results showed that the material contained β -spodumene ($\text{Li}_2\text{O} \cdot \text{Al}_2\text{O}_3 \cdot 4\text{SiO}_2$) as the primary phase.

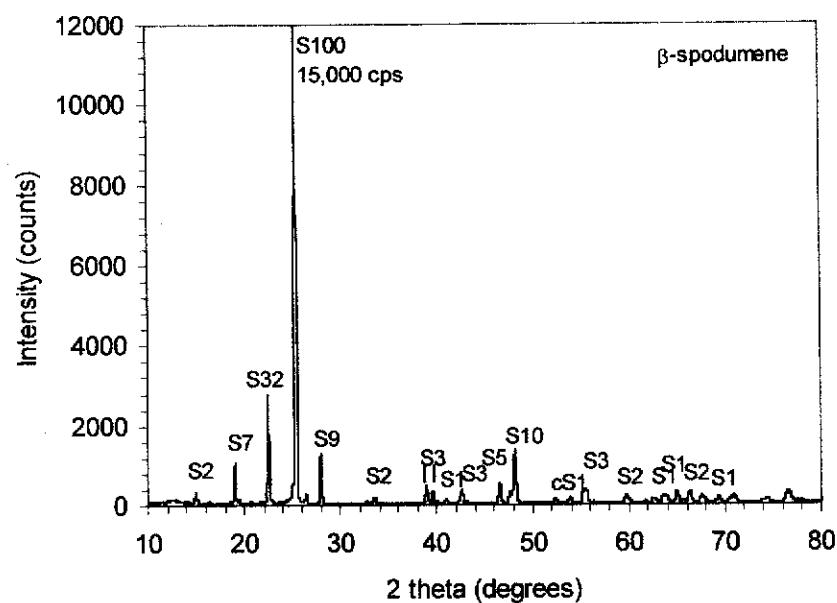


Figure 5.3a. Measured x-ray powder diffraction patterns for the as-received β -spodumene powders using $\text{CuK}\alpha$ radiation. The peaks are labeled S (β -spodumene). The associated number is the PDF file intensity.

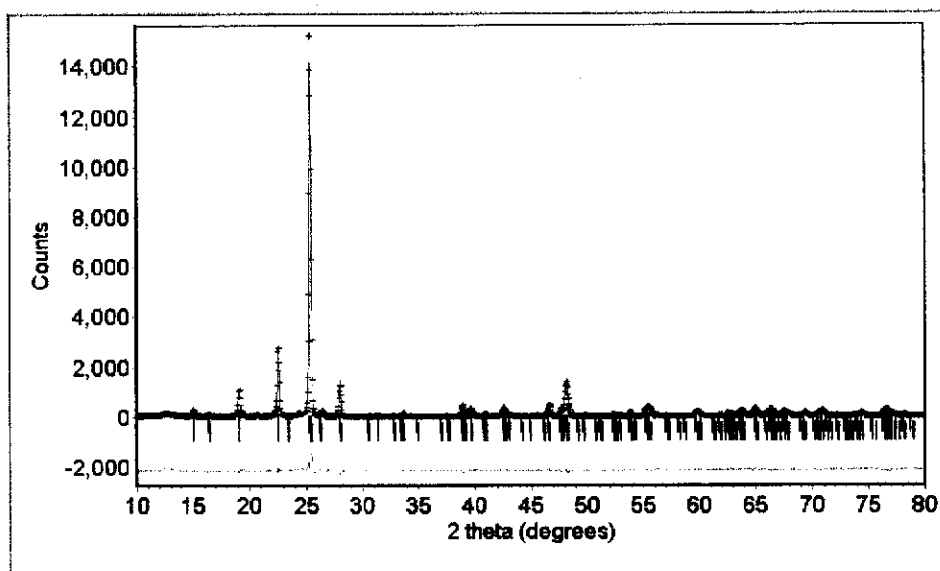


Figure 5.3b Quality of the Rietveld pattern-fitting results for the as-received β -spodumene. The observed data are shown by a (+) sign, and the calculated data by a solid line. Vertical line represents the positions of diffraction lines for $\text{Li}_2\text{O} \cdot \text{Al}_2\text{O}_3 \cdot 4\text{SiO}_2$. The green line below the vertical lines is the difference plot.

5.2.2 Phase Composition Analysis

Room temperature x-ray and neutron diffraction data were used to examine the phase compositions for the sintered β -spodumene modified A/CA₆ composites. Search/match identification analysis with the PDF file was employed to identify the phase presents in each sample prior to Rietveld phase composition analysis. The results of the phase abundance extracted from each pattern obtained are described in the following section.

X-ray Diffraction (XRD) Analysis

Figure 5.4 shows the room temperature x-ray diffraction patterns of β -spodumene modified A/CA₆ composite for CAS0, CAS2.5, CAS10 and CAS15 samples after sintering at 1650 °C for 2h. The phases α -Al₂O₃ (PDF 42-1268) and CA₆ (PDF 38-0470) accounted for all lines in the diffraction patterns the CAS0 and CAS2.5 samples. However, for CAS10 and CAS15 samples the phases present were α -Al₂O₃, CA₆, β -spodumene - Li₂O.Al₂O₃.4SiO₁₀ (PDF 35-797), and β -quartz solid solution - Li₂Al₂O₃O₁₀ (PDF 73-2336). The addition of β -spodumene played an important role in this system. In sample CAS2.5, it can be seen that the peak intensity of CA₆ phase decreased, while the peak intensity of α -Al₂O₃ increased as a result of β -spodumene added. This suggests that the expected reaction sintering of alumina and precursor CA₆ to form A/CA₆ composite did not occur completely. Of particular interest is the addition of 10 and 15 wt% β -spodumene an additional phase of β -quartz solid solution (Li₂Al₂O₃O₁₀) was found. The β -quartz solid solution is a solid solution based on the hexagonal β -quartz structure. It has a hexagonal cell (space group: P6₂22) with lattice parameters $a = 5.217(1)$ Å and $c = 5.464$ Å (ICSD # 24897). The β -quartz solid solution is generally metastable. It usually forms from heat-treating a glass of spodumene composition Li₂O.Al₂O₃.nSiO₂ with $n \geq 2$, and transforms into keatite solid solution at an elevated temperature (Li 1971). It was found that in the LAS (Li₂O-Al₂O₃-SiO₂) system the β -quartz solid solution transform completely to β -spodumene solid solutions at approximately 900 °C

(Nordmann *et al.* 1995). More recently Nordmann and Cheng (1997) studied the formation and stability of β -quartz solid solution in the Li-Si-Al-O-N system. The presence of nitrogen has been found to stabilise the crystalline metastable β -quartz solid solution phase up to 1200 °C, and it was proposed that the enhanced thermal stability of the β -quartz solid solution (prepared with AlN) was due to both the replacement of oxygen by nitrogen and the positioning of excess Al^{3+} ions into interstitial sites within the β -quartz solid solution lattice (Nordmann and Cheng 1997). Therefore, it is reasonable to assume that the presence of the β -quartz solid solution in sintered samples of CAS10 and CAS15 may be due to the presence of Ca^{2+} ions which promotes a similar structural stabilisation of crystalline phases in the $\text{Li}_2\text{O}-\text{Al}_2\text{O}_3-\text{SiO}_2$ system.

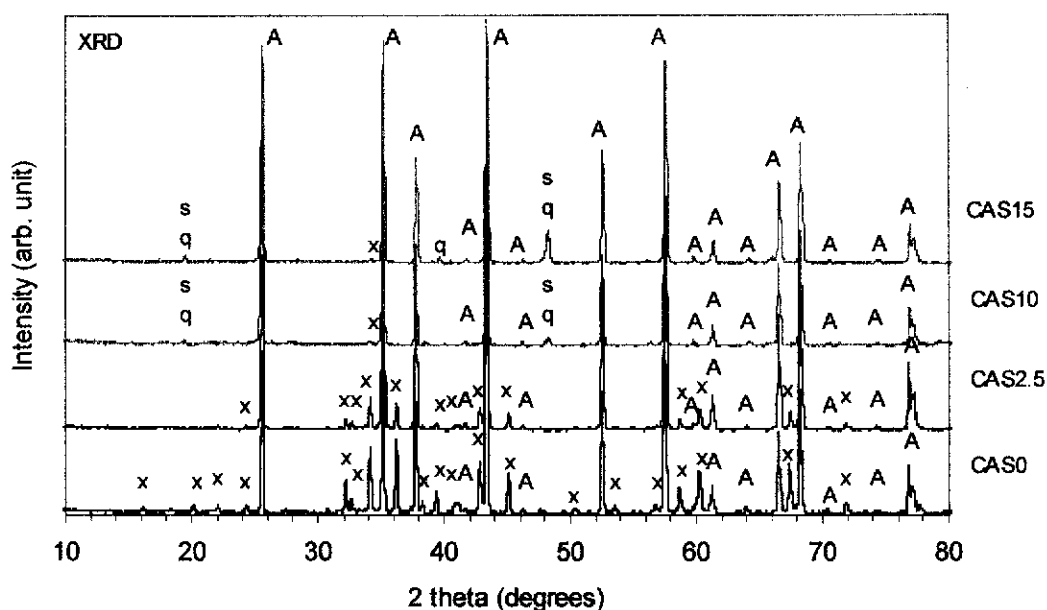


Figure 5.4. Room temperature x-ray diffraction (XRD) patterns for CAS0, CAS2.5, CAS10, and CAS15 samples. Legends A = $\alpha\text{-Al}_2\text{O}_3$, x = CA_6 , s = β -spodumene and q = β -quartz solid solution.

Neutron Diffraction (ND) Analysis

Figure 5.5 shows room temperature ND patterns of β -spodumene modified A/CA₆ samples for compositions CAS0, CAS2.5, CAS10, and CAS15. Samples were sintered at 1650 °C for 2h. As for the XRD search/match results, α -Al₂O₃ and CA₆ accounted for all lines in the ND patterns for CAS0 and CAS2.5; and for the composition CAS10 and CAS15 the phases present were β -spodumene and β -quartz solid solution. It can be seen from ND patterns of CAS2.5 the peak intensity of CA₆ phase decreased, but the peak intensity of α -Al₂O₃ increased when 2.5 wt% β -spodumene was added. This result is consistent with those of XRD obtained previously.

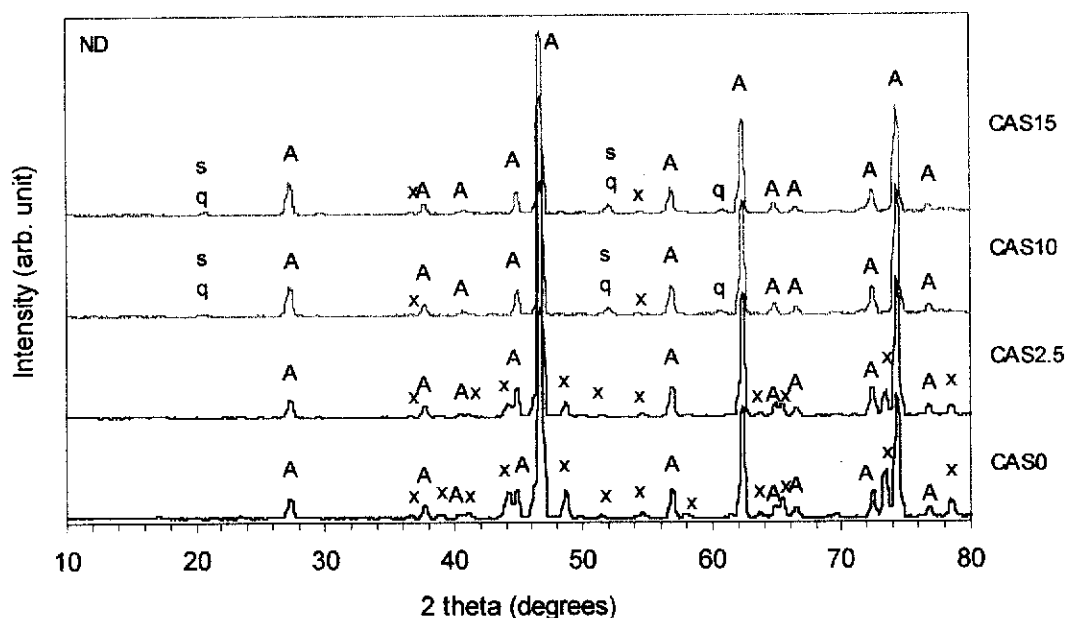


Figure 5.5. Room temperature neutron diffraction (ND) patterns for compositions CAS0, CAS2.5, CAS10, and CAS15. Legends A = α -Al₂O₃, x = CA₆, s = β -spodumene and q = β -quartz solid solution.

Rietveld Phase Composition Analysis

The XRD and ND relative phase composition values for compositions CAS0, CAS2.5, CAS10 and CAS15 were performed by the Rietveld method using the *Rietica* program for Windows 95/98/NT version 1.6.5 program which is derived from the Hill-Howard-Hunter LHPM program (Hill, Howard and Hunter 1995). The crystal structure models used in the calculation were taken from the Inorganic Crystal Structure Data Base (Fach Informations Zentrum and Gmelin Institut, Germany) – ICSD # 75725, 34394, 24897, 14235 for α -Al₂O₃, CA₆, beta-quartz solid solution- Li₂Al₂O₃O₁₀ and β -spodumene - Li₂O.Al₂O₃.4SiO₂, respectively (see Appendix A). The parameters refined were those controlling pattern intensity (scale factors), peak profile (width and shape), peak position (zero point and unit cell parameters), background polynomial parameters, and the individual atom thermal parameters. The final Rietveld scale factors were converted to phase compositions by weight using Equation 3.19 (see section 3.4.2).

The quality of the Rietveld calculations for all samples may be assessed from the Rietveld difference plots and the refinement figures-of-merit. Selected XRD and ND Rietveld refinement plots for CAS0 and CAS10 samples are shown in Figures 5.6 and 5.7, while for CAS2.5 and CAS15 are presented in Appendix B (Figures B13 and B14). The profile figures-of-merit values obtained by the Rietveld refinement analysis with XRD and ND data are shown in Tables 5.3 and 5.4. The R_B factor for the individual phase in each composition derived from ND is lower than that for the corresponding XRD patterns, i.e. 1.4 – 3.9 % for ND data and 3.6 – 8.2 % for the XRD data. The GOF values for both were relatively low, i.e. less than 3 %, indicating that the assumed crystal structure models are correct according to these low values.

The relative phase compositions (wt%) values for CAS0, CAS2.5, CAS10, and CAS15 samples obtained by the Rietveld refinement analysis with XRD and ND data are shown in Tables 5.5 and 5.6. The variations of phase composition (wt%) as a function of β -spodumene content (wt%) derived from XRD and ND data are

represented in Figure 5.8. The wt% of the α -Al₂O₃ phase from XRD data increased from 68.5 (0.8) to 87.5 (0.8) wt% and then 95.9 (1.3) wt% for addition of 0, 2.5 and 10 wt% β -spodumene, but decreased steadily to 93.9 (1.3) wt% for addition of 15 wt% β -spodumene. The wt% of the α -Al₂O₃ phase from ND data showed similar trend, i.e. increased from 69.7 (0.8) to 82.6 (8) wt%, then 96.1(1.2) wt% for addition of 0, 2.5, 10 wt% β -spodumene, but the α -Al₂O₃ concentration for addition of 15 wt%, viz. 95.6(1.4) wt% showed no significant increase. The wt% of the CA₆ phase from XRD and ND patterns were also represented similar behaviour, i.e. decreased steadily from 31.5(0.5) – 0.3(0.2) wt% for XRD and from 30.3(0.5) to 0.7(0.2) wt% for ND, respectively, when 0 – 15 wt% β -spodumene added. The wt% of β -spodumene increased from 1.5 (0.1) to 2.7 (0.2) wt% for XRD and from 1.1(0.2) to 1.4(0.2) wt% for ND, when 0 – 15 wt% β -spodumene added. The wt% of β -quartz increased from 2.4(0.1) to 3.1(0.2) wt% for XRD and from 1.5(0.1) to 2.3(0.1) wt% for ND, for the addition of 10 – 15 wt% β -spodumene. In general, the two sets of Rietveld refinement results (XRD and ND) were in reasonable agreement. Slightly different can be attributed due to different diffractometer used.

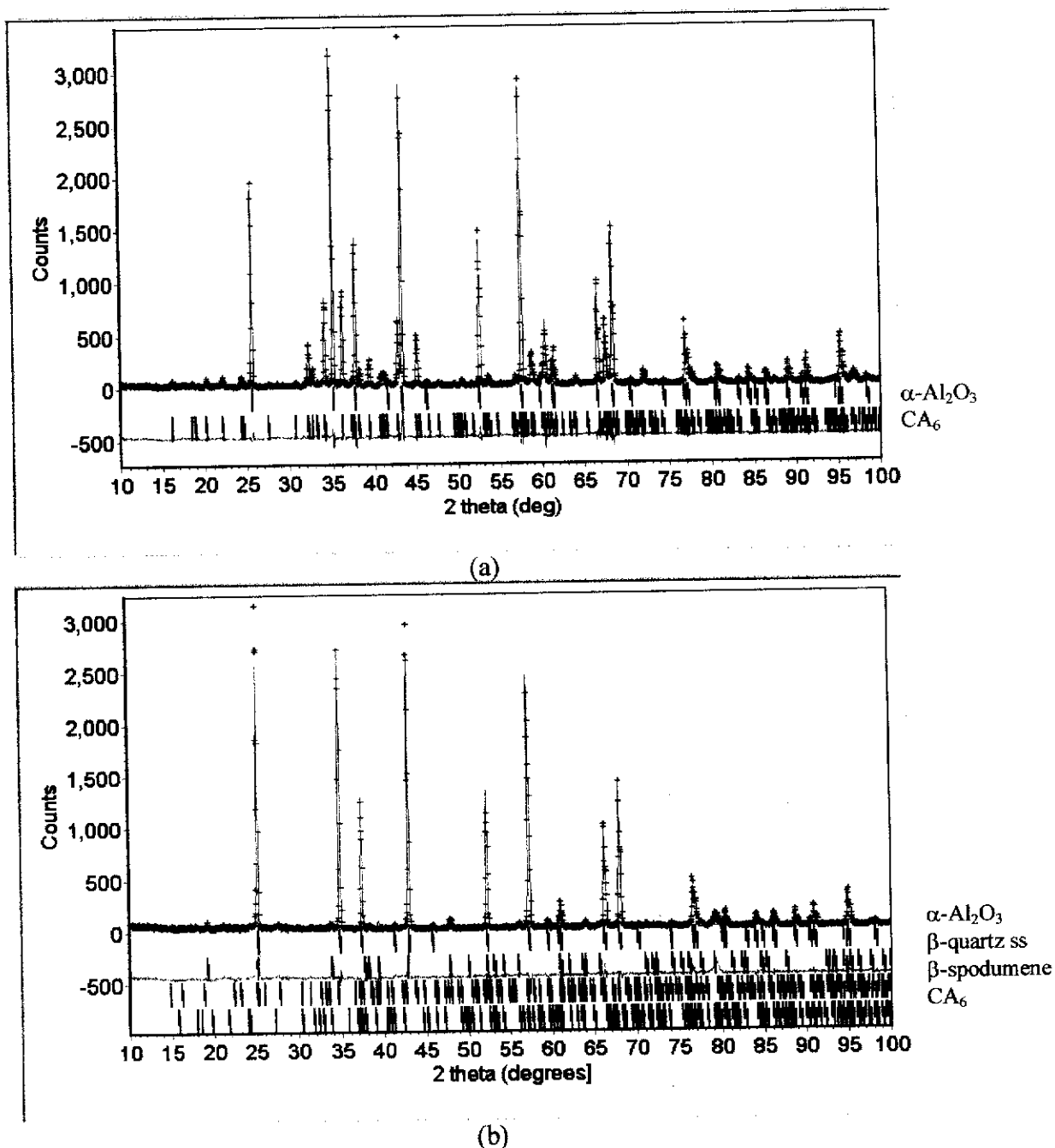


Figure 5.6. XRD Rietveld difference plots for β -spodumene modified A/CA₆ composite: (a) CAS0 and (b) CAS10. The observed data are shown by a (+) sign, and the calculated data by a solid line. Vertical line represents the positions of diffraction lines for α -Al₂O₃ and CA₆ in (a) and α -Al₂O₃, β -quartz, β -spodumene and CA₆ in (b). The green line below the vertical lines is the difference profile.

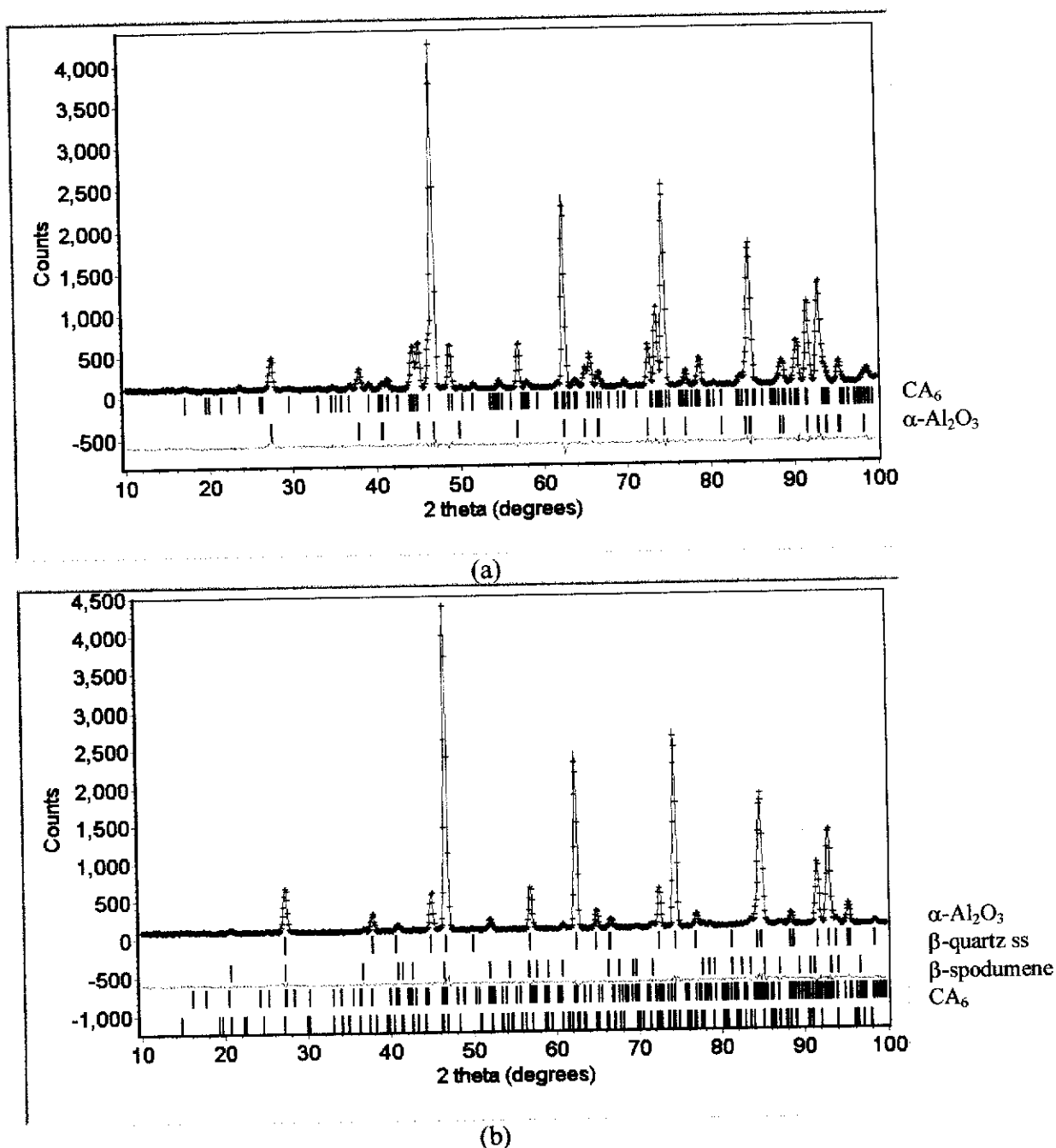


Figure 5.7. ND Rietveld difference plots for β -spodumene modified A/ CA_6 composite: (a) CAS0 and (b) CAS10. The observed data are shown by a (+) sign, and the calculated data by a solid line. Vertical line represents the positions of diffraction lines for CA_6 and $\alpha\text{-Al}_2\text{O}_3$ in (a) and $\alpha\text{-Al}_2\text{O}_3$, $\beta\text{-quartz ss}$, $\beta\text{-spodumene}$ and CA_6 in (b). The green line below the vertical lines is difference profile.

Table 5.3. Figures-of-merit from Rietveld refinement with XRD data for CA0, CAS2.5, CA10 and CA15 samples.

Sample	R _{exp}	R _{wp}	GOF	R _B α -Al ₂ O ₃	R _B CA ₆	R _B β -quartz	R _B β -spodumene
CAS0	10.9	14.4	1.8	3.8	4.2	-	-
CAS2.5	10.7	14.6	1.9	3.6	6.3	-	-
CAS10	11.1	15.2	2.9	3.8	6.5	6.3	5.5
CAS15	10.8	15.1	3.1	4.6	5.9	8.2	7.9

Table 5.4. Figures-of-merit from Rietveld refinement with ND data for CA0, CAS2.5, CA10 and CA15 samples.

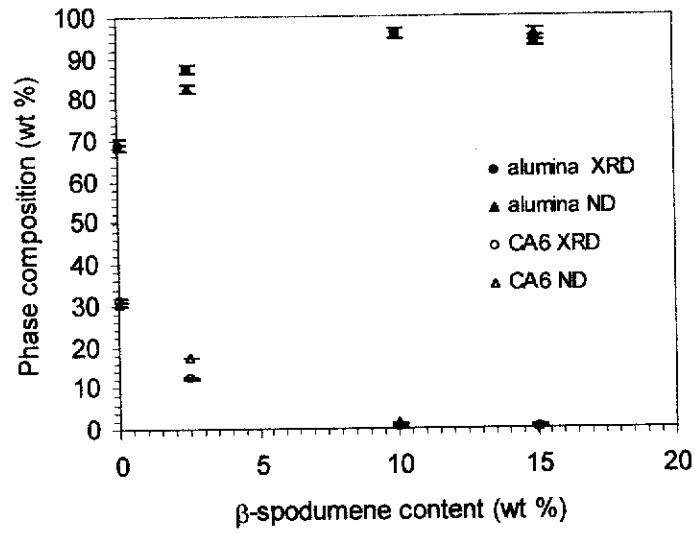
Sample	R _{exp}	R _{wp}	GOF	R _B α -Al ₂ O ₃	R _B CA ₆	R _B β -quartz	R _B β -spodumene
CAS0	3.1	5.1	2.7	1.4	2.1	-	-
CAS2.5	3.3	5.0	2.3	2.3	2.0	-	-
CAS10	3.3	5.6	2.8	2.1	2.5	3.4	3.6
CAS15	3.5	6.1	3.1	2.2	3.6	3.9	3.8

Table 5.5. Relative phase composition (wt%) from Rietveld refinement with XRD data for CAS0, CAS2.5, CAS10 and CAS15 samples.

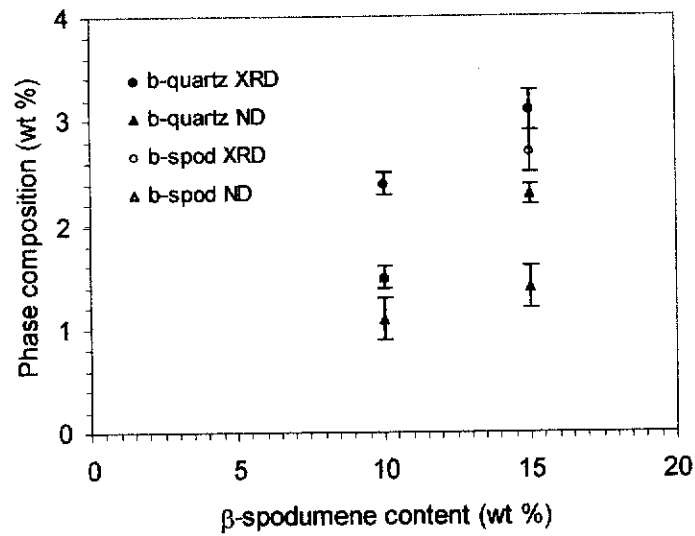
Sample	α -Al ₂ O ₃ (wt%)	CA ₆ (wt%)	β -quartz (wt%)	β -spodumene (wt%)
CAS0	68.5 (0.8)	31.5 (0.5)	-	-
CAS2.5	87.5 (0.8)	12.5 (0.3)	-	-
CAS10	95.9 (1.3)	0.5 (0.1)	2.4 (0.1)	1.5 (0.1)
CAS15	93.9 (1.3)	0.3 (0.1)	3.1 (0.2)	2.7 (0.2)

Table 5.6. Relative phase composition (wt%) from Rietveld refinement with ND data for CAS0, CAS2.5, CAS10 and CAS15 samples.

Sample	α -Al ₂ O ₃ (wt%)	CA ₆ (wt%)	β -quartz (wt%)	β -spodumene (wt%)
CAS0	69.7 (0.8)	30.3 (0.5)	-	-
CAS2.5	82.6 (0.8)	17.4 (0.2)	-	-
CAS10	96.1 (1.2)	1.3 (0.2)	1.5 (0.1)	1.1 (0.2)
CAS15	95.6 (1.4)	0.7 (0.2)	2.3 (0.1)	1.4 (0.2)



(a)



(b)

Figure 5.8. Variations of phase composition (wt%) of α - Al_2O_3 and CA_6 in (a) and β -quartz and β -spodumene in (b) obtained from XRD and ND data as a function of β -spodumene content (wt%).

5.2.3 Microstructural Analysis

Scanning Electron Microscopy (SEM)

The microstructures for the CAS2.5 and CAS10 samples were examined using SEM (see section 3.4.4). Back-scattered electron imaging together with Ca and Al x-ray maps were used to carry out these experiments. Polished samples were thermally etched, at 1350 °C for 30 minutes, prior to microstructural analysis to enhance grain structure and reveal grain boundaries.

Figure 5.9 shows the representative microstructures of the CAS0 sample. The alumina grains are recognisable by their equiaxed morphology and randomly oriented with grain size ranged 1 – 7 μm , whereas the CA_6 grains, in backscattered electron image mode appear bright because of their high atomic number. The Al x-ray image is shown in Figure 5.9c. CA_6 grains showed *plate-like* or elongated morphology with grain size ranged 8 – 13 μm . The elongated CA_6 grains were clearly revealed by Ca x-ray mapping in Figure 5.9b. The few small pores observed were predominantly at grain boundary triple points.

Figure 5.10 shows the representative microstructure of the CAS2.5 sample. The elongated CA_6 grains as confirmed by the Ca x-ray map are also clearly evident in these micrographs. The size of CA_6 grains is 6 – 10 μm . The large alumina grains appear more platy with the size ranged 2-12 μm , the Al x-ray map is presented in Figure 5.10c. SEM result shows no β -spodumene and β -quartz grains were observed in this sample, but residual glass concentrated at the grain boundaries was revealed. In the CAS2.5 sample, spherical pores ($\sim 12 \mu\text{m}$) were observed as shown in Figure 5.10d.

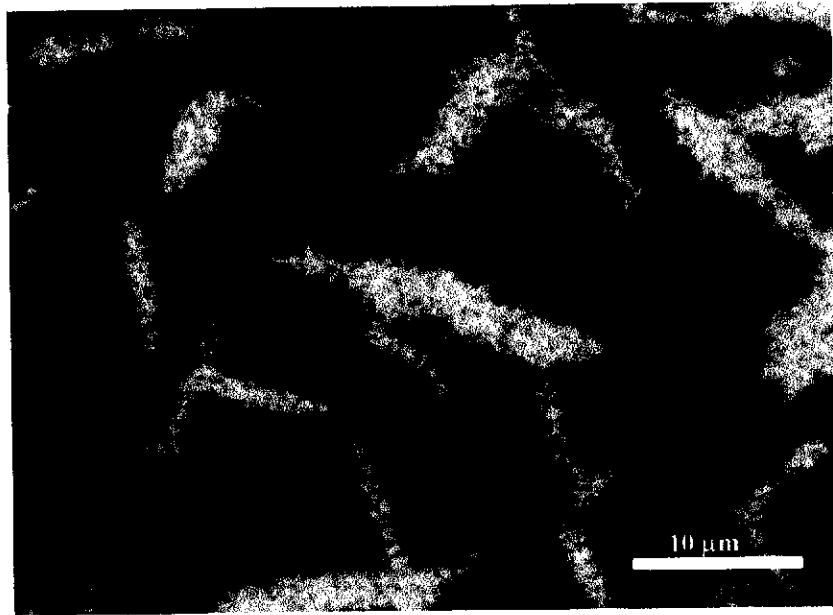
In the sample containing 10 wt% β -spodumene, no CA_6 , β -spodumene and β -quartz grains were observed (Figure 5.11). Here the large alumina grains ($\sim 15 \mu\text{m}$) appear more platy and some of the grains can be seen to be bonded with glassy phase. This glassy phase is formed predominantly at the triple points, grain

boundaries, and also as pockets. Some large spherical pores ($\sim 15 \mu\text{m}$) can also be observed. The Al x-ray image is shown in Figure 5.11b.

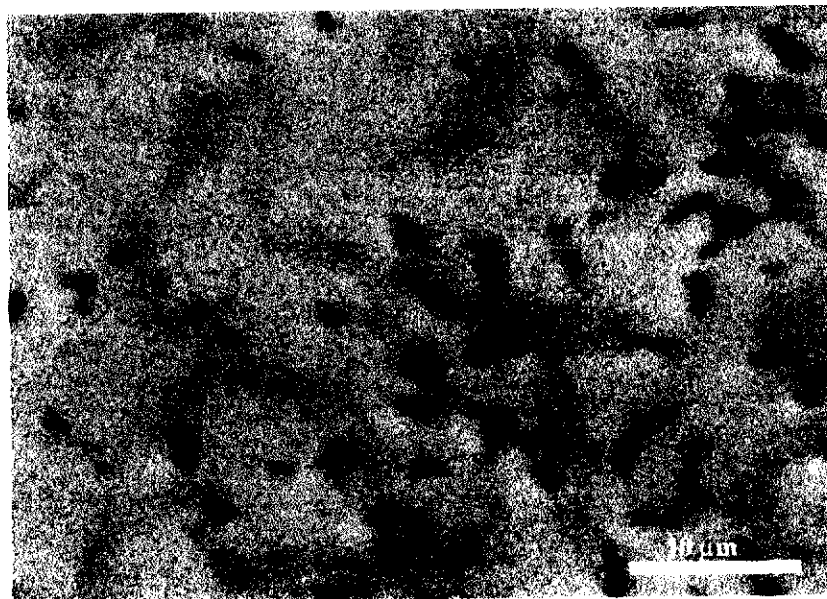


(a)

Figure 5.9. SEM micrograph for the CAS0 sample. Polished surface was thermally-etched at 1350 °C for 30 minutes. (a) Back-scattered electron image. Legends: A = alumina, CA₆ = calcium hexaluminate and P = porosity.

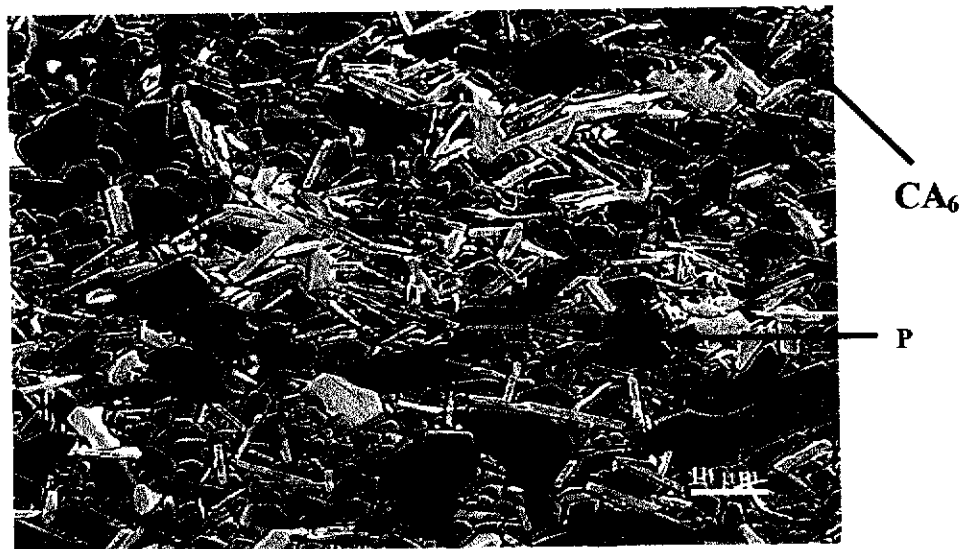


(b)

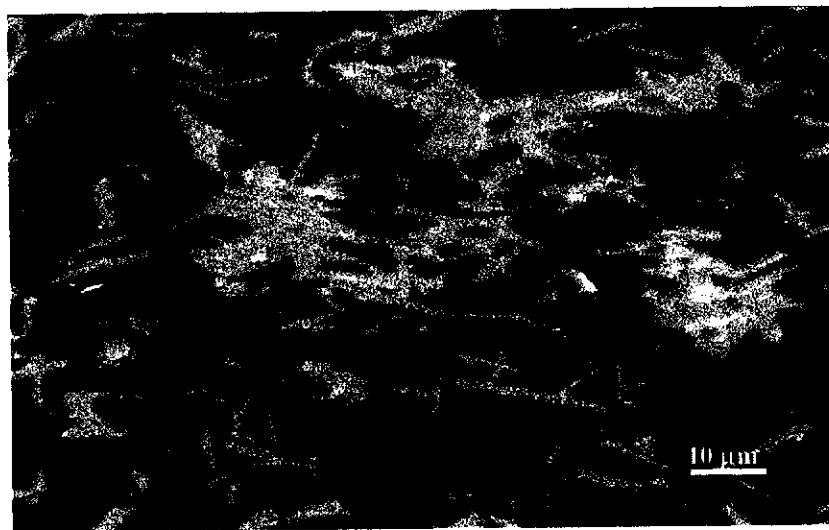


(c)

Figure 5.9. (Continued) SEM micrograph for the CAS0 sample. Polished surface was thermally-etched at 1350 °C for 30 minutes. (b) Ca x-ray image and (c) Al x-ray image.

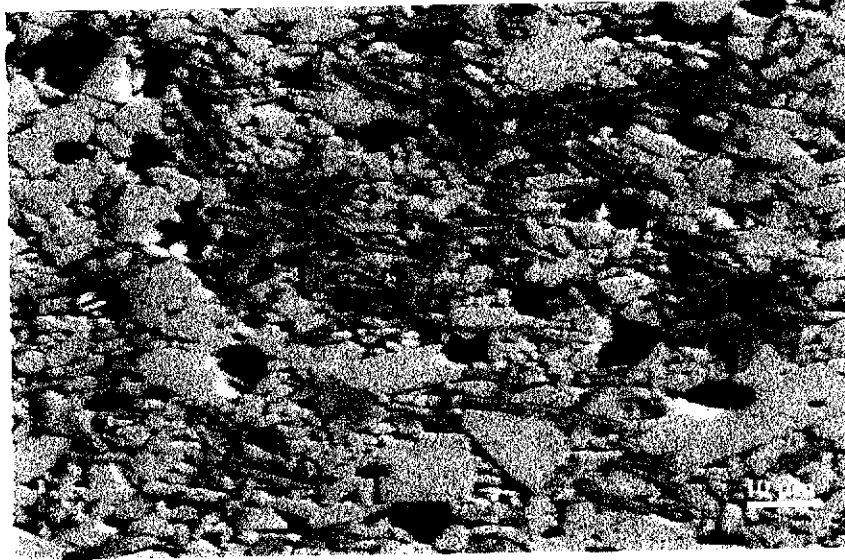


(a)



(b)

Figure 5.10. SEM micrograph for the CAS2.5 sample. Polished surface was thermally-etched at 1350 °C for 30 minutes. (a) Back-scattered electron image and (b) Ca x-ray image. Legends: A = alumina, CA_6 = calcium hexaluminate and P = Porosity.

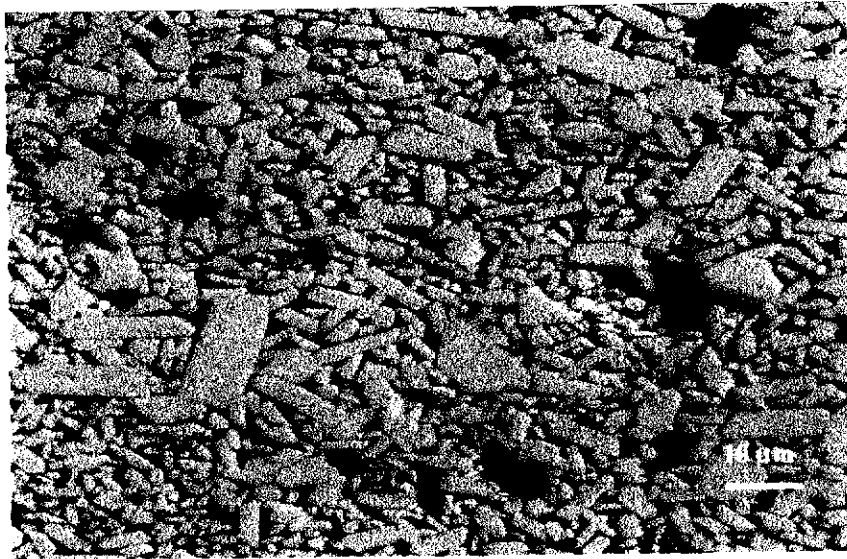


(c)

Figure 5.10. (Continued) SEM micrograph for the CAS2.5 sample. Polished surface was thermally-etched at 1350 °C for 30 minutes. (c) Al x-ray image.



(a)



(b)

Figure 5.11. SEM micrograph for the CAS10 sample. Polished surface was thermally-etched at 1350 °C for 30 minutes. (a) Back-scattered electron image and (b) Al x-ray image. Legends: A = alumina and P = Porosity.

5.2.4 Physical and Thermal Properties

Shrinkage, Porosity and Density

The shrinkage was determined using the relative reduction in diameter of the green body compact relative to the fired sample according to Equation 3.12. The results of shrinkage for CAS0, CAS2.5, CAS10, and CAS15 samples are shown in Figure 5.12. The shrinkage decreased steadily as the amount of β -spodumene increased. The behaviour can be attributed to the presence of β -quartz and β -spodumene in the CAS10 and CAS15 samples as confirmed by the XRD and ND results (see section 5.2.2).

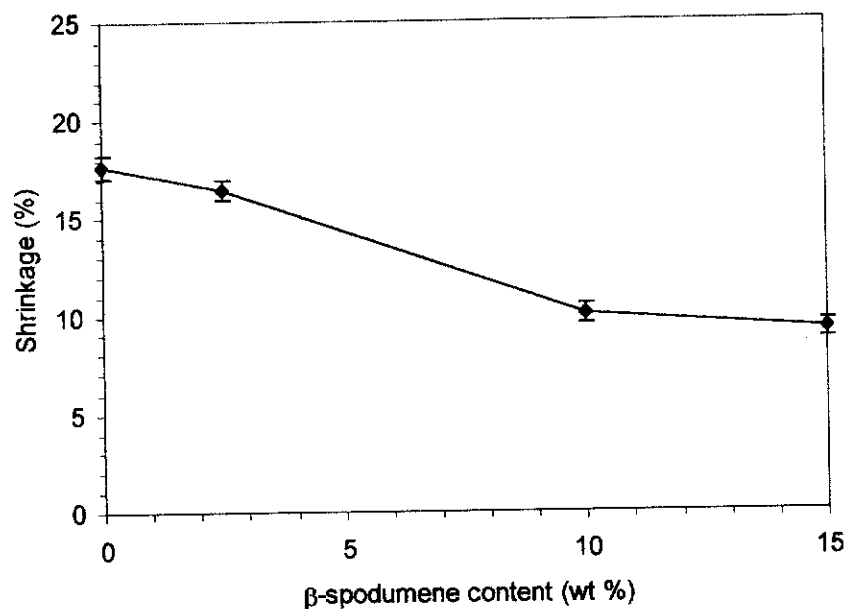


Figure 5.12. Shrinkage for compositions CAS0, CAS2.5, CAS10, and CAS15 samples. Error bars indicate two estimated standard deviations (2σ).

The apparent porosity was measured by the Archimedes principle using water as working liquid. The porosity for CAS0, CAS2.5, CAS10 and CAS15 is shown in Figure 4.13. The porosity decreased rapidly with the addition of β -spodumene, i.e.

from 3.4 to 0.2 % for 0 – 15 wt% β -spodumene added. This indicates that adding β -spodumene can be an effective method of improving the densification of A/CA₆ composites. Shi and Low (1998) also found that the presence of spodumene significantly reduced the porosity and enhanced the densification of aluminium titanate (AT). The porosity decreased from 32 to 8 % when 0 – 30 wt% of spodumene added.

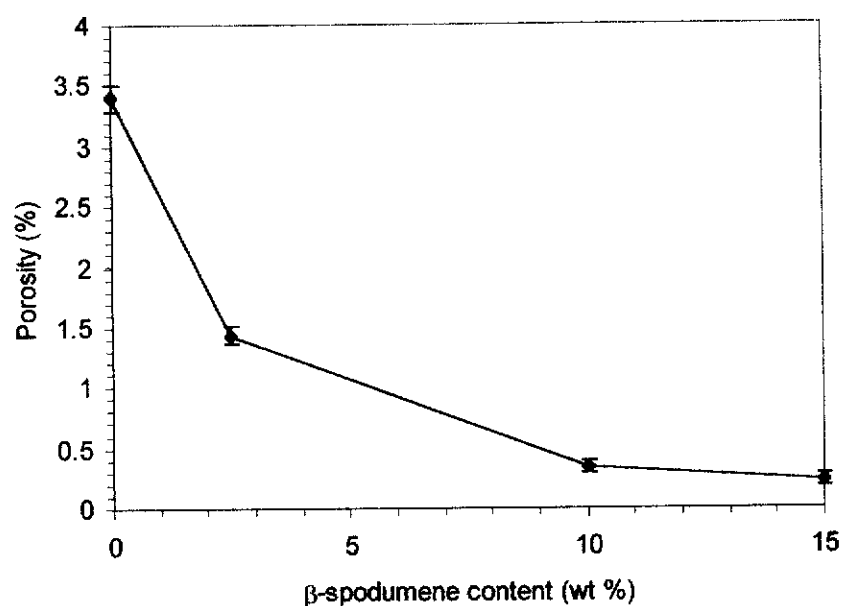


Figure 5.13. Porosity for compositions CAS0, CAS2.5, CAS10, and CAS15 samples. Error bars indicate two estimated standard deviations (2σ).

The bulk density was determined using the Archimedes method. The density for compositions CAS0, CAS2.5, CAS10 and CAS15 is shown in Figure 5.14. The density decreased with increasing β -spodumene additions can be attributed to the presence of less dense phase such as β -quartz solid solution and β -spodumene as confirmed by XRD and ND results (see section 5.2.2). This result is consistent with those obtained by Kobayashi *et al.* (1990). They found that addition of excess β -spodumene resulted in mullite with decreased density due to the formation of 5 – 10

μm pores caused by the excess liquid phase and the presence of less dense phase such as β -spodumene.

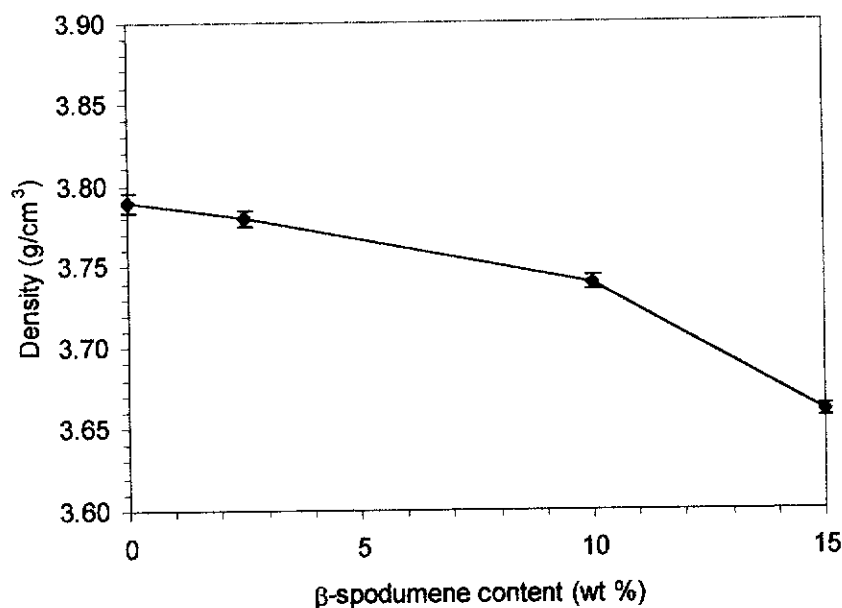


Figure 5.14. Density for compositions CAS0, CAS2.5, CAS10, and CAS15 samples. Error bars indicate two estimated standard deviations (2σ).

Thermal Expansion and Shrinkage Behaviour

The thermal expansion and shrinkage behaviour of materials measured using a THETA 160 dilatometer as a function of temperature for the CAS2.5 and CAS15 samples is shown in Figure 5.15. The CAS2.5 sample starts to densify at approximately 1142 °C, whereas the CAS15 sample starts to densify at 1177 °C. These temperatures for the onset of densification are lower than the 1194 °C found in sample without spodumene (see Figure 4.18b). The maximum shrinkage for the CAS2.5 and CAS15 samples occurred at approximately 1444 °C and 1458 °C, respectively, which is similar to the 1452 °C found in sample without spodumene.

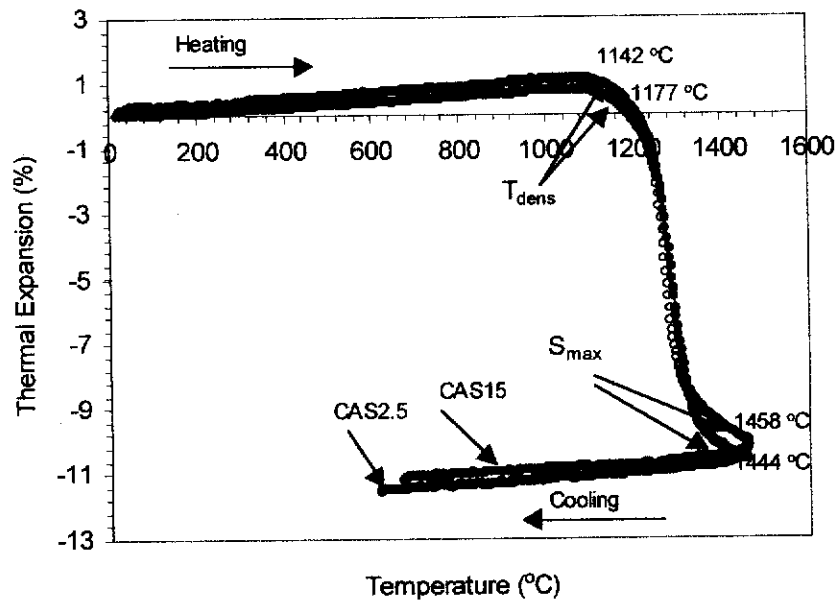


Figure 5.15. Thermal expansion and shrinkage behaviour for CAS2.5 and CAS15 samples. T_{dens} indicates the temperature at which densification commences and S_{max} indicates the maximum shrinkage.

The average thermal expansion coefficients (TEC) value for the CAS0, CAS2.5, CAS15 and alumina samples are shown in Table 5.5. The CAS15 sample has a lower TEC than that of CAS0, CAS2.5 and alumina. This can be attributed to the presence of glassy phase such β -spodumene, which has a relatively low TEC, i.e. $0.4 - 2.0 \times 10^{-6} \text{ K}^{-1}$ (Mchale 1991). When anisotropic materials are fabricated into polycrystalline ceramic body, the net thermal expansion can be very low, as shown for β -spodumene. Such a material has very little dimensional change as a function of temperature and can therefore withstand extreme thermal cycling or thermal shock without cracking (Richerson 1992).

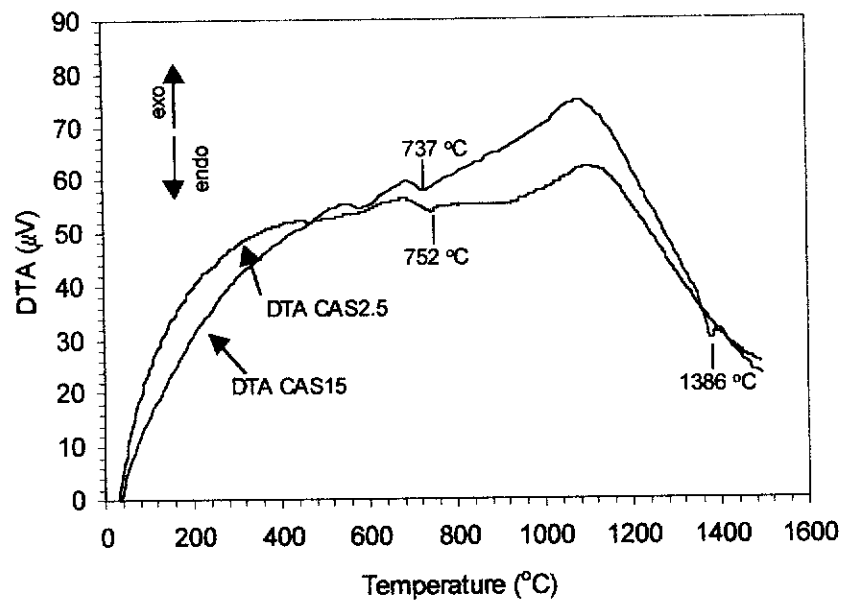
Table 5.7. Average thermal expansion coefficient for CAS0, CAS2.5, CAS15, and alumina samples, at 20 - 1000 °C.

Sample	Average thermal expansion coefficient value ($10^{-6} \text{ }^{\circ} \text{C}^{-1}$)
CAS0	9.4
CAS2.5	11.1
CAS15	7.6
Alumina	8.6

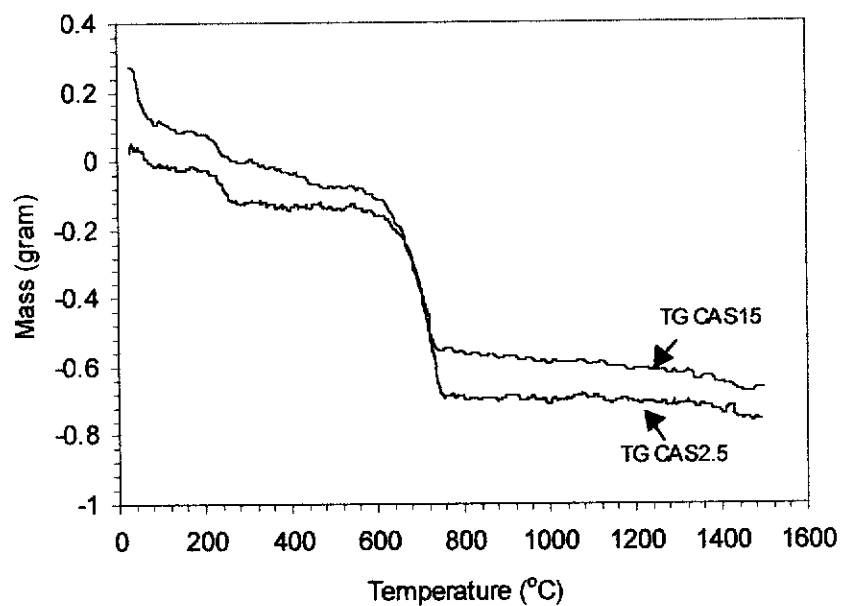
Differential Thermal and Gravimetric Analysis (DTA and TG)

The results of the simultaneous DTA and TG for the CAS2.5 and CAS15 samples recorded in the temperature range 20 – 1500 °C are shown in Figure 5.16. A heating rate of 10°/min was chosen to carry out this analysis.

The diffuse exothermic peaks at approximately 400 and 600 °C can be ascribed to the removal of organic additives. The small endotherms at ~ 752 °C in the CAS2.5 sample and at ~ 737 °C in the CAS2.5 sample are associated with a substantial weight losses on TG curve (Figure 5.16b), presumably due to the decomposition of calcium carbonate. These results are slightly lower (~ 100–120 °C) than the thermogram of pure CaCO₃ (Figure 4.29a) obtained at the same heating rate of 10°/minute where the sharp endotherm associated with the substantial weight loss occurred at 859 °C. This difference can be attributed to the presence of Al₂O₃. The small endotherm in the CAS15 sample at 1386 °C can be ascribed to the melting of β-spodumene.



(a)



(b)

Figure 5.16. Thermal analysis for the CAS2.5 and CAS15 samples between 20 and 1500 $^{\circ}C$: (a) DTA and (b) TG.

5.2.5 Mechanical Properties

Vickers Hardness

The hardness and fracture toughness were measured according to the details outlined in section 3.5.2. Each of the data points obtained represents an average of measurements from at least three indentations. Figure 5.17 shows hardness for CA0, CAS2.5, CAS10, and CAS15 samples as a function of β -spodumene content for a 98 N load. The plot shows the hardness decreased with increasing β -spodumene content. The reduction in hardness with an increase in β -spodumene content can be attributed to the presence of the glassy phase such as β -spodumene and β -quartz solid solution as revealed by the XRD and ND results.

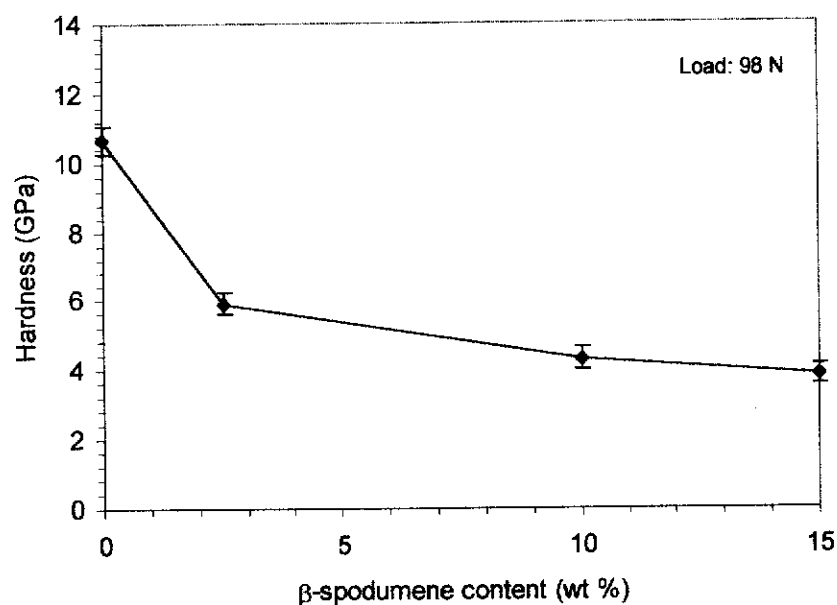


Figure 5.17. Variation of hardness as a function of β -spodumene content for an applied load of 98 N. Error bars indicate two estimated standard deviations (2σ).

Fracture Toughness

Figure 5.18 shows the fracture toughness for CA0, CAS2.5, CAS10, and CAS15 samples as a function of β -spodumene content for a 98 N load. The plot shows the fracture toughness decreased with increasing β -spodumene content. The reduction in fracture toughness with an increase in β -spodumene content can be attributed to the presence of the glassy phase, β -spodumene and β -quartz solid solution as revealed by the XRD and ND results.

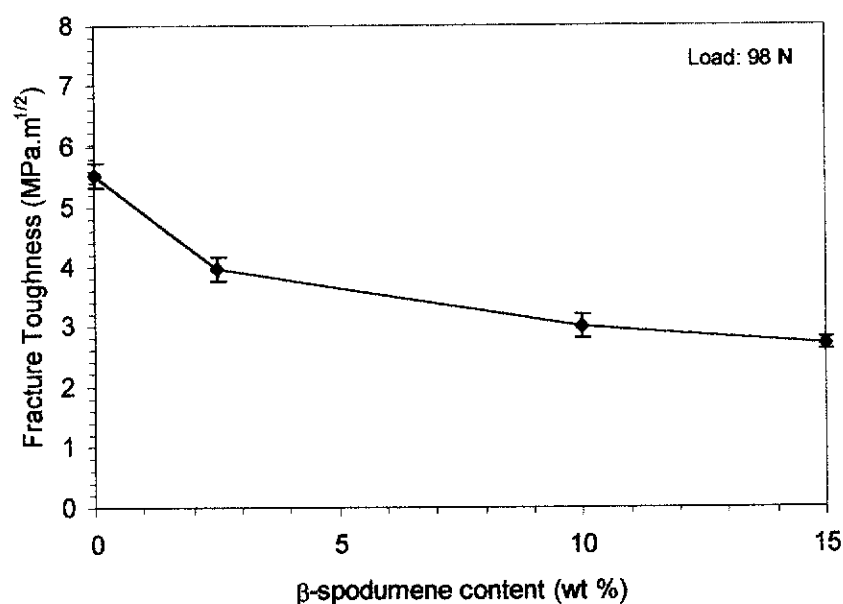


Figure 5.18. Variation of fracture toughness as a function of β -spodumene content for an applied load of 98 N. Error bars indicate two estimated standard deviations (2σ).

5.3 Summary

β -spodumene modified A/CA₆ composites have been successfully synthesised through reaction sintering of A/CA₆ precursor and β -spodumene. The influence of β -spodumene on the phase relations, microstructure, densification, hardness and fracture toughness has been investigated.

The addition of β -spodumene has a significant effect on the phase composition of the A/CA₆ composites as confirmed by XRD and ND Rietveld refinement analysis. The addition of > 2.5 wt% β -spodumene caused the decomposition of CA₆ and the formation of β -quartz solid solution.

The microstructural examination of the β -spodumene modified A/CA₆ composites revealed the presence of elongated CA₆ grains in samples containing 0-2.5 wt% β -spodumene but not in samples with 10 wt% or more additive. In the latter, a significant amount of residual glass was observed to concentrate along the grain boundaries and triple-point pockets.

The addition of β -spodumene in A/CA₆ matrix has significant influence on the physical and mechanical properties. The shrinkage, porosity and density of composites decreased as the amount of β -spodumene increased. The reduction in porosity shows that β -spodumene can be an effective sintering aid for the densification of A/CA₆ composites. However, the presence of β -spodumene resulted in both hardness and fracture toughness to decrease, probably due to the formation of glassy phase, recrystallised β -spodumene and β -quartz solid solution.

CHAPTER 6

FUNCTIONALLY-GRADED ALUMINA/CALCIUM- HEXALUMINATE ($\text{Al}_2\text{O}_3/\text{CA}_6$) COMPOSITES

6.1 Introduction

Recent advances in materials processing and engineering have led to a new class of materials called functionally-graded materials (FGMs). They are distinguished from conventional (ie. macroscopically uniform) materials by gradients of composition, phase distribution, porosity, and related properties such as hardness, density, Young's modulus etc. The most important aspect in designing FGMs is the gradual variation in the composition profile, because it effectively bridges the gap between the properties of two different materials in a continuous manner. Two desirable properties can be combined with gradual change in properties from one face to the other by simply controlling the phase distribution. Therefore, the accurate characterisation of the phase composition distribution throughout the FGMs becomes an important aspect in the understanding of the properties of these materials.

This chapter presents results of a study to produce a novel A/ CA_6 system which has a graded dispersion of CA_6 within the alumina matrix through an infiltration process to yield a heterogeneous CA_6 /alumina layer for toughness and crack dispersion, and also a homogeneous alumina layer for hardness and wear resistance. The results of infiltration characteristics and the effects of graded composition on the physical and mechanical properties are also presented. The functionally-graded A/ CA_6 system has been characterised using x-ray diffraction (XRD), synchrotron radiation diffraction (SRD), high temperature neutron diffraction (HTND), scanning electron microscopy (SEM), transmission electron microscopy (TEM), differential thermal and gravimetric analysis (DTA/TG), dilatometry and Vickers indentation.

6.2 Results and Discussion

6.2.1 Infiltration kinetics

Alumina preforms, with dimensions (5 x 12 x 60) mm³, were pre-sintered at temperatures 900, 1000, 1100 and 1200 °C for 2 h. The apparent porosity and bulk density of the preforms were measured by the Archimedes method (see section 3.5.1). The variations of apparent porosity and bulk density of the alumina preforms as a function of sintering temperatures are shown in Figures 6.1 and 6.2. A summary of the apparent porosity and bulk density data is given in Table 6.1. As expected the apparent porosity decreased with an increase in temperature, whereas the bulk density decreased with an increase in temperature.

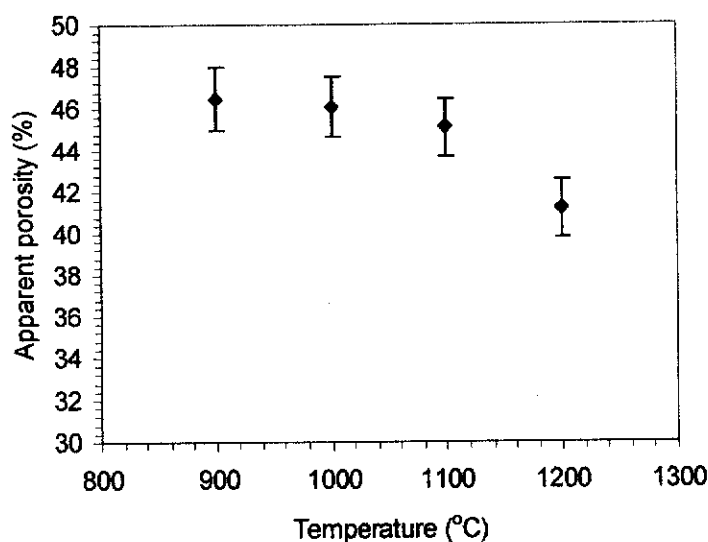


Figure 6.1. Variations of apparent porosity of the alumina preforms as a function of temperature. Error bars indicate two estimated standard deviations (2σ).

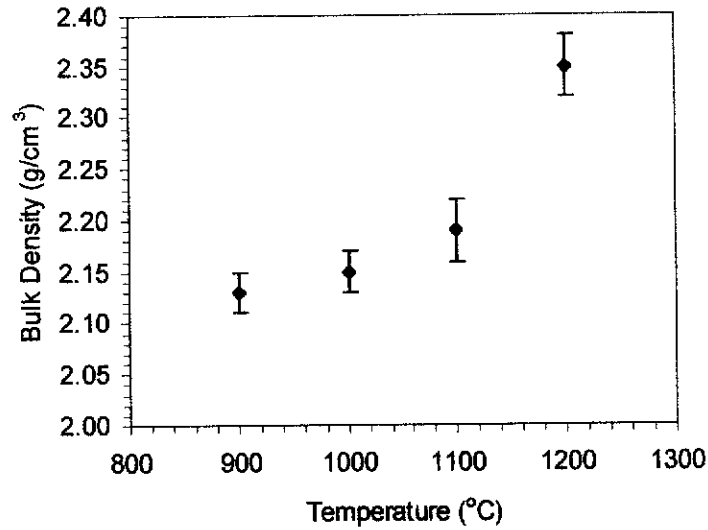


Figure 6.2. Variation of bulk density of the alumina preforms as a function of temperature. Error bars indicate two estimated standard deviations (2σ).

Table 6.1. Apparent porosity and bulk density of the alumina preform pre-sintered at 900, 1000, 1100, and 1200 °C.

Pre-sintering temperature (°C)	Apparent Porosity (%)	Bulk density (g/cm ³)
900	46.5 ± 1.5	2.13 ± 0.02
1000	46.1 ± 1.4	2.15 ± 0.02
1100	45.1 ± 1.4	2.19 ± 0.03
1200	41.2 ± 1.4	2.35 ± 0.03

For applications where the aim is to maximise the amount of second phase incorporated into a body, it is desirable that the alumina preforms have as high a volume fraction of porosity as possible. As can be seen from Table 6.1, the high volume fraction of porosity obtained for the alumina preform pre-sintering at 900 °C,

resulted in a low density of 2.13 g/cm^3 . However, attempts to conduct such an infiltration were not successful because the alumina preform cracked easily. Resistance against infiltration cracking by the various preforms at 900, 1000, 1100 and 1200 °C are summarised in Table 6.2. The result indicates that, pre-sintering at 1100 and 1200 °C for 2h yielded suitable alumina preforms, were strong enough to withstand the subsequent processing steps.

Table 6.2. Resistance against infiltration cracking by the various preforms at 900, 1000, 1100 and 1200 °C

Pre-sintering temperature (°C)	Conditions of infiltrated preform
900	Cracked during infiltration
1000	Cracked during drying
1100	No cracks
1200	No cracks

The physical properties of liquids considered in this experiment were viscosity and surface tension. The viscosity of water and calcium acetate was measured using an Oswald Viscometer. Water was used as a standard solution. The surface tension of liquid was measured using the torsion balance method. Values of viscosity and surface tension for water and calcium acetate solution are summarised in Table 6.3. The results show that calcium acetate solution has a higher viscosity and surface tension than water.

Table 6.3. Viscosity and surface tension of water and calcium acetate solution.

Liquid (20 °C)	Viscosity, η (N.s/m ²)	Surface tension, γ (N/m)
Water	$(0.9 \pm 0.1) \times 10^{-3}$	$(72.2 \pm 0.3) \times 10^{-3}$
Calcium acetate	$(2.7 \pm 0.5) \times 10^{-3}$	$(73.2 \pm 0.4) \times 10^{-3}$

The alumina preforms sintered at 1100 and 1200 °C with dimensions of 5 x 12 x 60 mm³ were used to study the kinetics of infiltration because of their relatively high strength, which resulted in no cracks during infiltration in the solution of calcium acetate (see Table 6.2). The preform was scaled (in mm) and the bottom of preform was immersed in liquid. The red ink (Scarlet drawing ink, product of Australia) was added to water and calcium acetate solution. The colouring of the liquid was intended to facilitate the monitoring of liquid rise. The height of liquid rise into alumina preform was recorded every 60 second and the infiltrated height squared h^2 (m²) as a function of time, t (second) was plotted. The influences of preform sintering temperature, liquid type, vacuum and non-vacuum and multiple infiltrations on the infiltration behaviour are described in the following section.

The effect of preform sintering temperature on the liquid infiltration rate at room temperature was studied using water. The infiltrated height squared as a function of infiltration time is shown in Figure 6.3. The result shows that the rate of infiltration decreased with an increase in pre-sintering temperature. The decrease in infiltration rate can be attributed principally to the reduction in porosity with the increased alumina preform pre-sintering temperature (see Table 6.1).

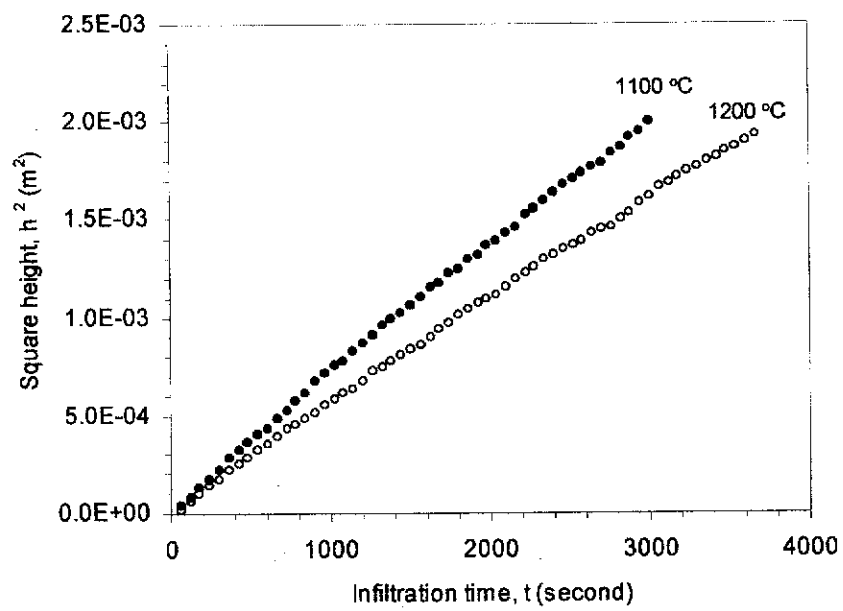


Figure 6.3. Square height (h^2) as a function of infiltration time (t) for the infiltration of water into alumina preform.

The effect of surface tension and viscosity on infiltration behaviour was studied using water and calcium acetate solution. The alumina preform sintered at 1100 °C was infiltrated with water under atmospheric pressure. The height squared, h^2 as a function of infiltration time, t is shown in Figure 6.4. The result shows that the infiltration rate of the calcium acetate was slower than that of water into alumina preform. This behaviour can be attributed to the viscosity of the calcium acetate solution which is higher than water (see Table 6.2). This result is consistent with the Washburn model in Equation 2.7 as would be expected because the rate of infiltration is proportional to the surface tension and inversely proportional to the viscosity of liquid.

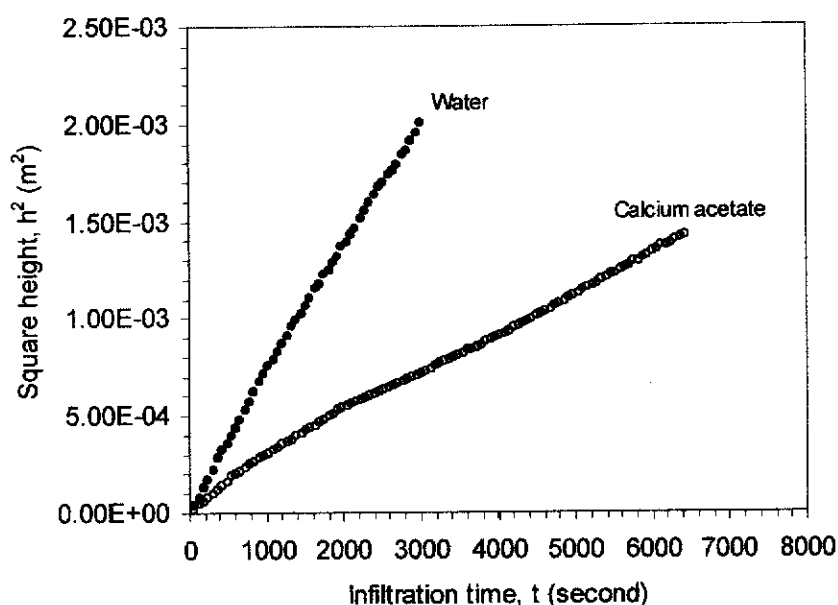


Figure 6.4. Square height (h^2) as a function of infiltration time (t) for the infiltration of water and calcium acetate into alumina preform.

A very important factor is the atmospheric condition under which the infiltration of the preform takes place. The experimental set-up considered is vacuum and non-vacuum. The effect of vacuum and non-vacuum on infiltration behaviour of water into alumina preform is shown in Figure 6.5. The alumina preform pre-sintered at 1100 °C was used in this experiment. The result shows that the rate of infiltration increased when experiment was conducted under vacuum. This result can be explained by the Darcy's law in Equation 2.3, where external pressure P_a plays an important role in the process of the infiltration behaviour. In general increasing the applied pressure will enhance the infiltration rate.

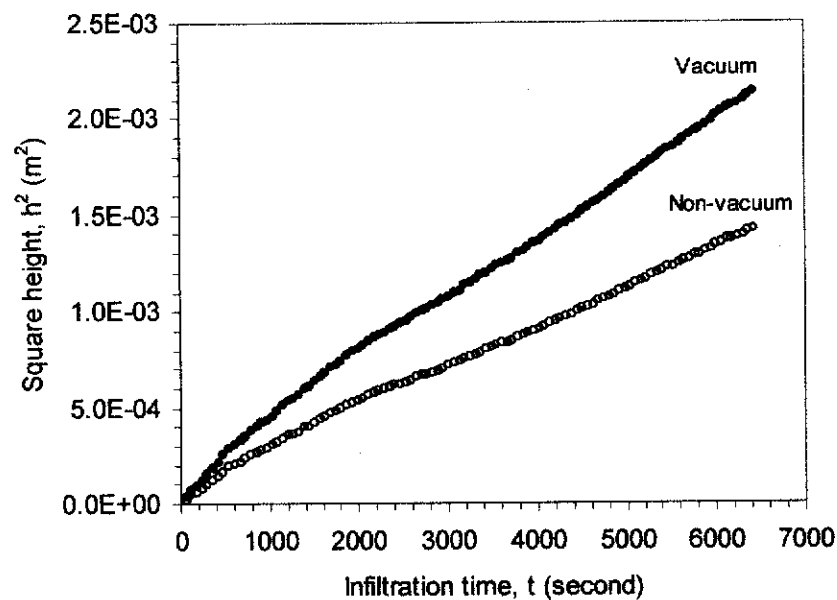


Figure 6.5. Square height (h^2) as a function of infiltration time (t) for the infiltration of water into alumina preform under vacuum and non-vacuum.

Pre-sintered alumina preform at 1100 °C and calcium acetate solution were used to study the effect of multiple infiltrations on infiltration behaviour. Experiment was conducted under vacuum. After the first infiltration, the infiltrated sample was dried at room temperature for 24 h followed by drying in oven at 70 °C for 12 h then fired in furnace at 450 °C for 30 minutes to decompose the infiltrant prior to continuing the next cycle. The results are shown in Figure 6.6. The rate of infiltration for the first cycle was higher than the second cycle. This indicates that after first infiltration the effective pore radius within the alumina preform decreased, therefore reduced the infiltration rate for the subsequent cycle.

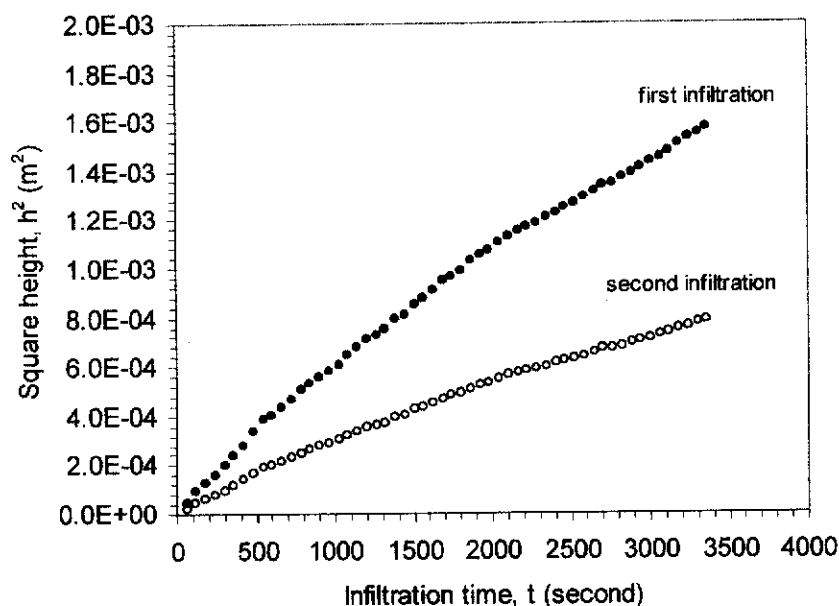


Figure 6.6. Square height (h^2) as a function of infiltration time (t) for the first and second infiltrations of calcium acetate solution into alumina preform under vacuum.

6.2.2 Analysis of Phase Composition and Development

X-ray Diffraction (XRD) Analysis

Room temperature x-ray diffraction (XRD) was used to construct composition profiles and to monitor the formation of calcium aluminates CA , CA_2 , and CA_6 in functionally-graded A/CA_6 composites. The *partially-infiltrated* sample was used to study the graded composition profile and the *fully-infiltrated* sample was used to study the formation temperature of calcium aluminates. Two methods were used to obtain the composition profiles: a *gradual polishing* method and a *slicing* method (see section 3.4.2). An alumina sintered at 1650 °C for 2 h was used as a control sample. The phase composition profiles for the functionally-graded A/CA_6 composites obtained from XRD data, obtained by Rietveld analysis, are described below.

Figure 6.7 shows the room-temperature XRD patterns for the alumina control sample and for the functionally-graded A/CA_6 composites obtained by the *gradual polishing* method. The sintered sample was polished with emery paper to depths of 0.0, 0.1, 0.2, 0.4, 0.5, 0.6, and 0.8 mm. Expanded XRD patterns are shown in Figures 6.8a and 6.8b. $\alpha\text{-Al}_2\text{O}_3$ was the only phase observed for the alumina control sample. The phases observed for the graded A/CA_6 sample were $\alpha\text{-Al}_2\text{O}_3$ and CA_6 phase. The peak intensities for alumina increased with depth, whereas the peaks for CA_6 decreased with depth. These changes in intensity with depth indicate that the functionally-graded A/CA_6 composite has a graded composition.

Figure 6.9 shows the room-temperature XRD patterns for the functionally graded A/CA_6 composite at various depths obtained by *slicing*. The partially-infiltrated sample was cut using diamond blade into consecutive slices thickness of 2 mm. Each of these slices was then crushed into powder using mortar and pestle followed by heat-treatment at 1400 °C for 12 h and 1650 °C for 2 h. The sintered powder was then milled with high-purity zirconia ring mill for 2 min to obtain a sufficiently fine particle size. The patterns were collected using Bragg Brentano diffractometry (see section 3.4.2). It can be seen from Figure 6.8, that only $\alpha\text{-Al}_2\text{O}_3$

and CA_6 were observed. The peak intensities of alumina increased with the depth, whereas the peak intensity of CA_6 decreased with depth. These results show that the functionally graded A/ CA_6 composite has a graded composition as expected, which is consistent with the XRD results obtained by gradual polishing method.

Room-temperature XRD was used to study the temperatures of formation for the calcium aluminate phases CA, CA_2 and CA_6 in the functionally-graded A/ CA_6 composites. A fully-infiltrated sample was used in this experiment. The dried sample was crushed into powder and placed in high-purity α - Al_2O_3 crucibles for firing at selected temperatures in the range 1000 – 1650 °C for 0.5h. The fired powder was then milled in a high-purity zirconia ring mill for 2 min to obtain particle sizes sufficiently small for phase analysis. Figure 6.10 shows the room-temperature XRD patterns. Expanded views of XRD patterns in Figure 6.10 are shown in Figures 6.11a and 6.11b. The phases observed between 1000 and 1200 °C are α - Al_2O_3 and CA. Residual CaO phase was not observed at this temperature indicating that the reaction of α - Al_2O_3 and CaO to form the CA phase was complete. The CA_2 phase was detected at 1300 °C. The temperature formation of CA_2 in the functionally graded A/CA composites was 100 °C higher than the XRD results of the sample processed by *in-situ* reaction sintering method (see section 4.2.2). However, both CA and CA_2 phases remained at 1400 °C before fully transformed to CA_6 at 1650 °C. The formation of CA_6 occurred at approximately 1400 °C. This agrees well with the results of XRD and HTND (see section 4.2.2). The *in-situ* formation of CA, CA_2 and CA_6 are believed to occur via exothermic reactions between α - Al_2O_3 and CaO from 1000 – 1400 °C according to Equations 4.1, 4.2, 4.3 and 4.4.

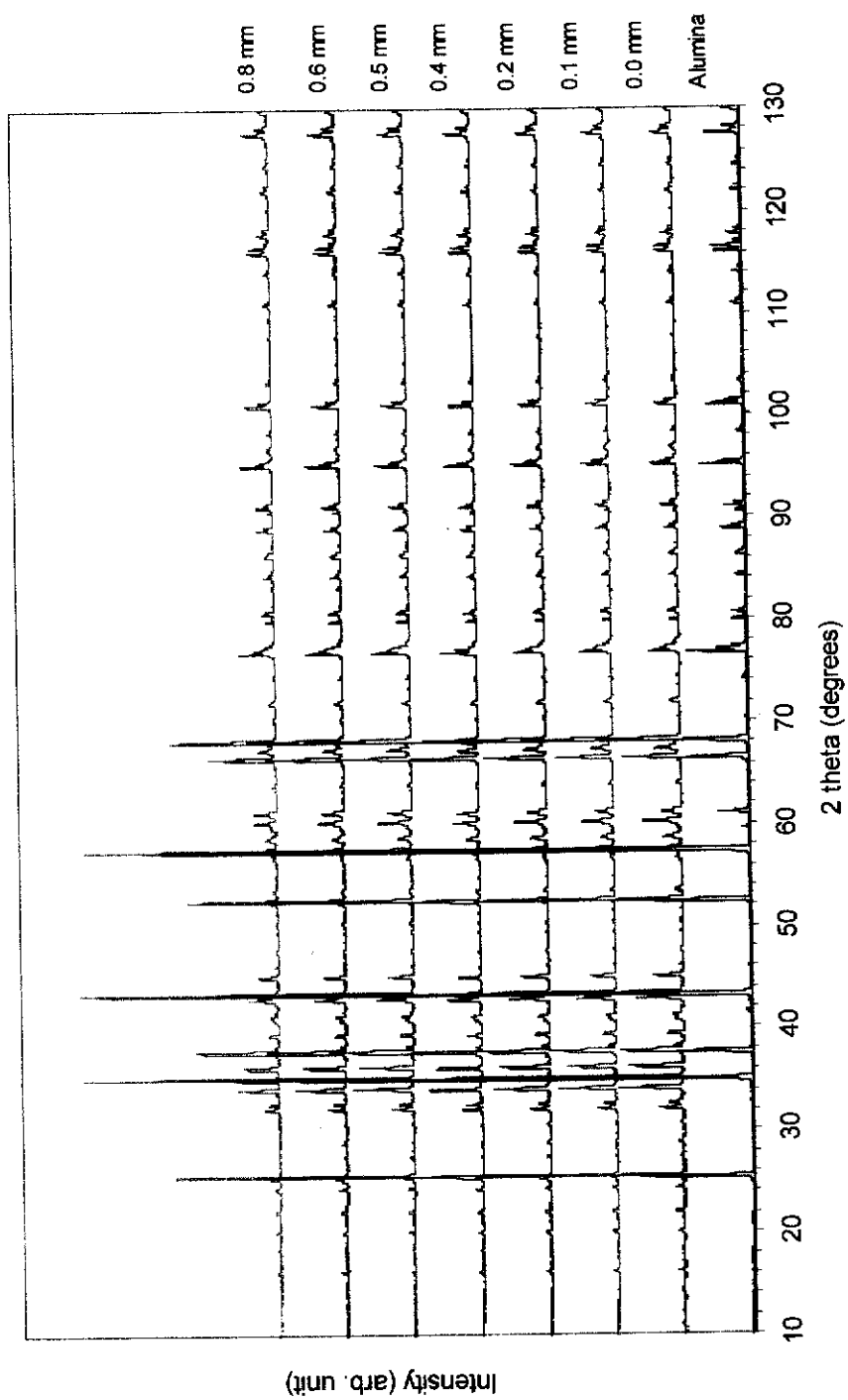
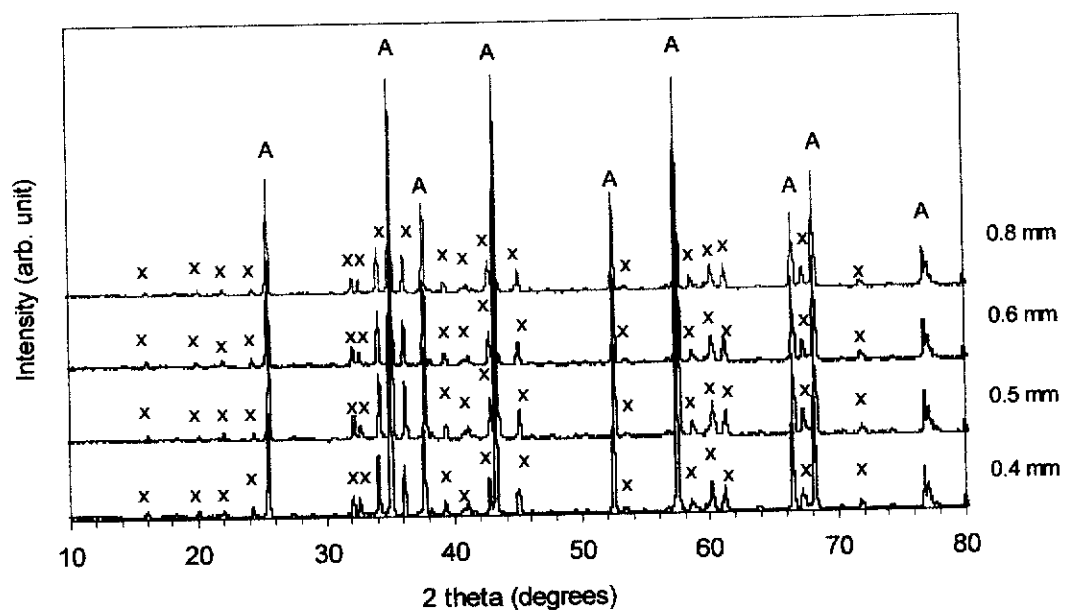
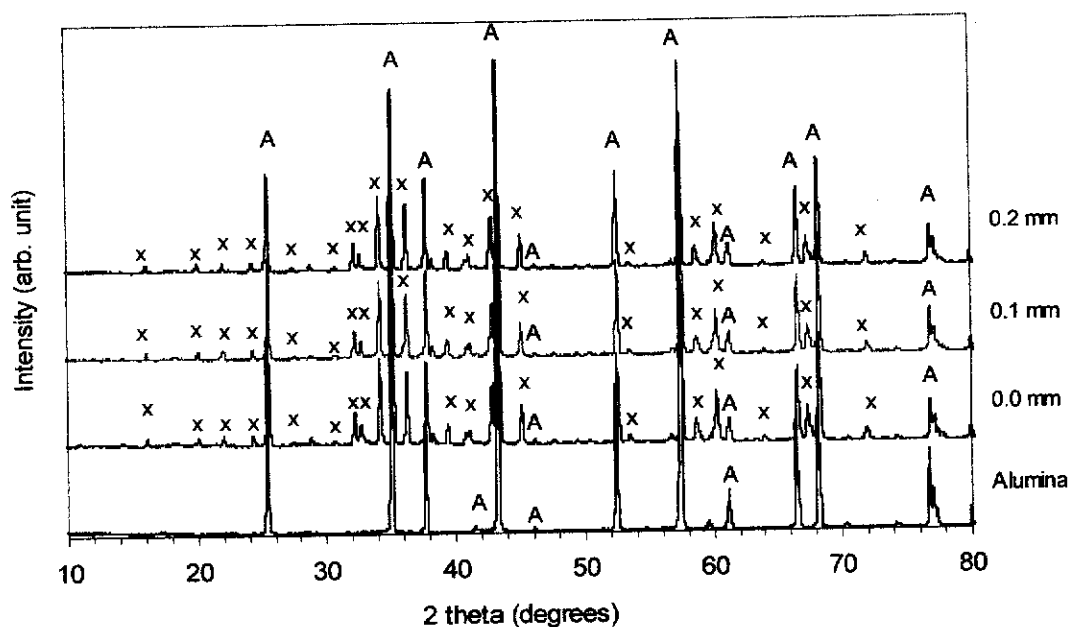


Figure 6.7. Room-temperature XRD patterns for the alumina control sample and the functionally-graded A/CA₆ composites obtained by the gradual polishing method.



(a)



(b)

Figure 6.8. Expanded views of the XRD patterns in Figure 6.7 for alumina and functionally-graded A/CA₆ composites obtained by the gradual polishing method at depths of 0 – 0.2 mm in (b) and 0.4 – 0.8 in (a). Legends: A = α-Al₂O₃ and x = CA₆.

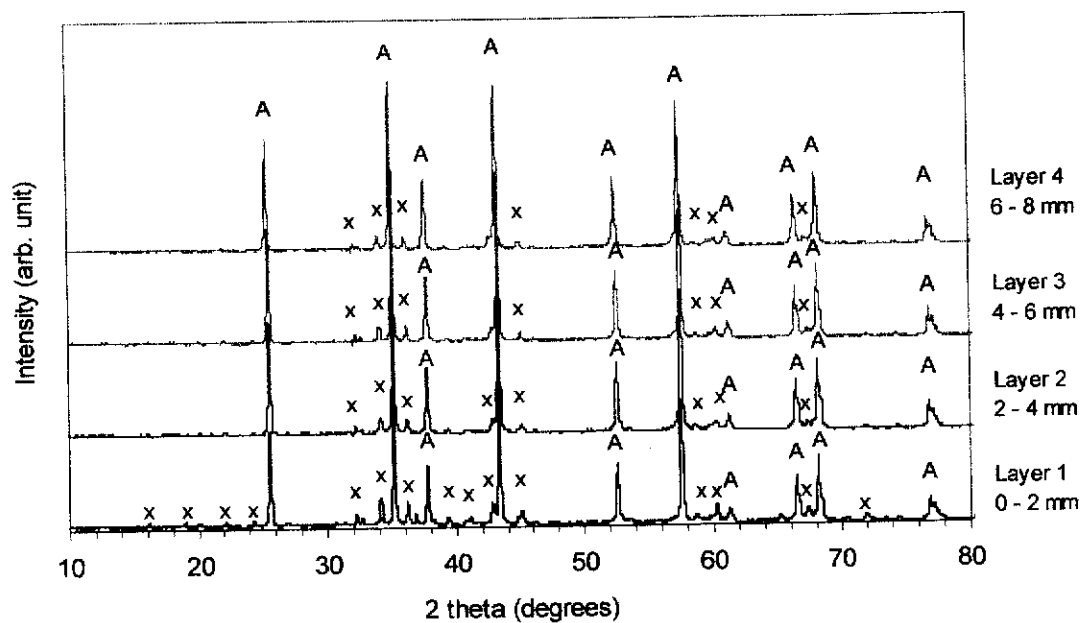


Figure 6.9. Room-temperature XRD patterns for functionally-graded A/CA₆ composites obtained by the slicing method at various depths (Layers 1 – 4).

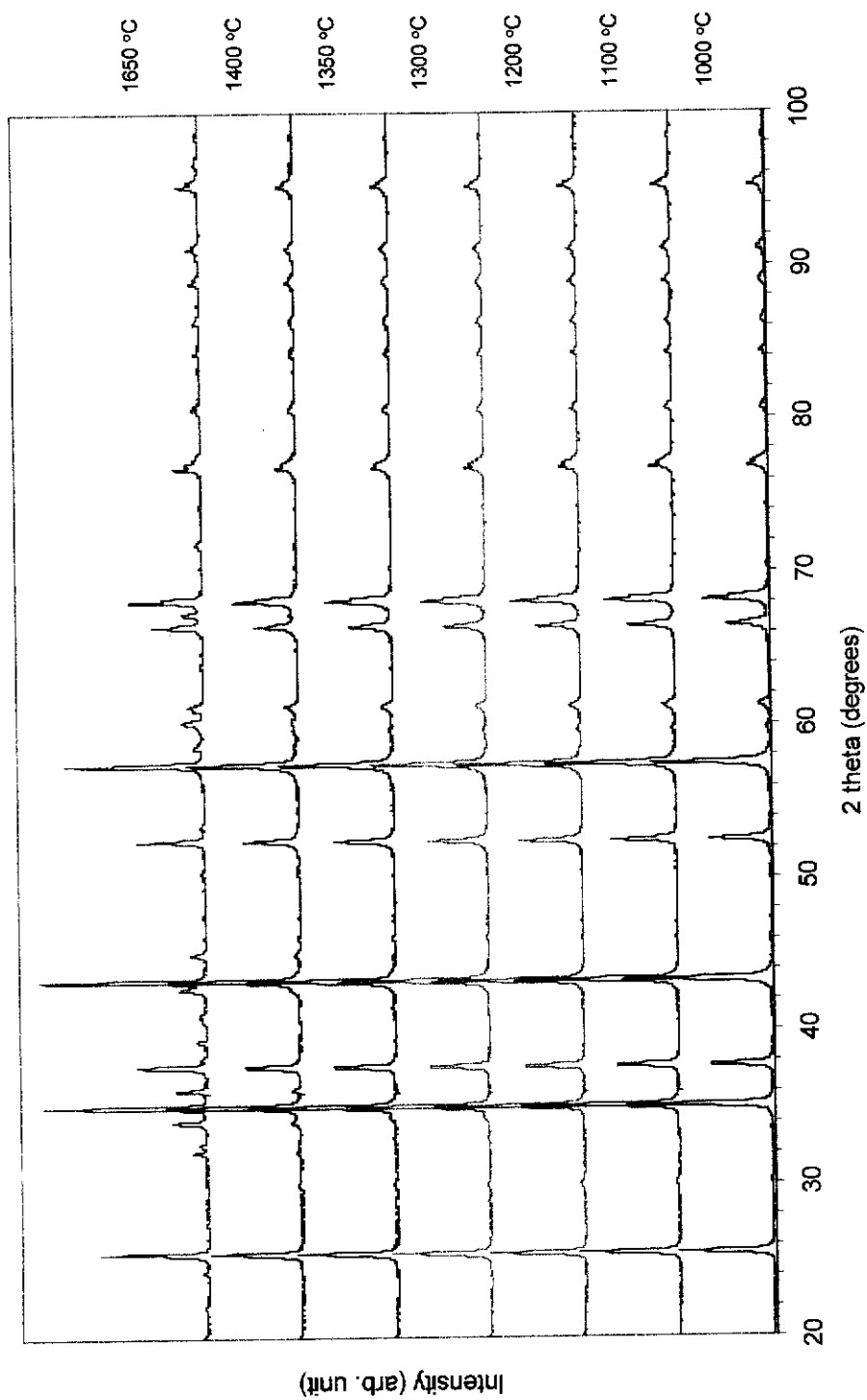
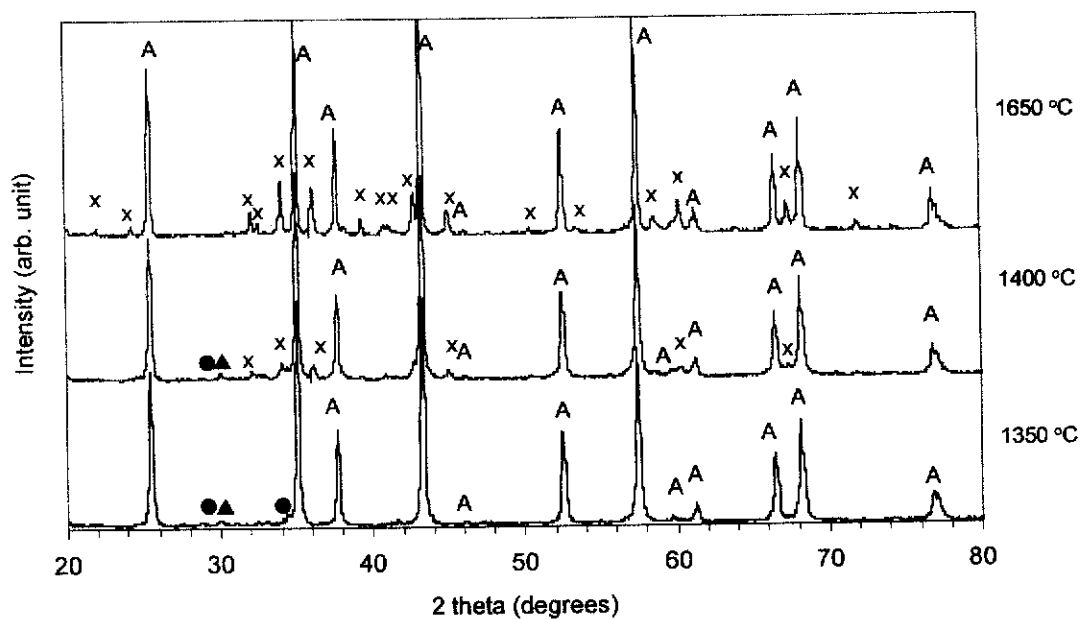
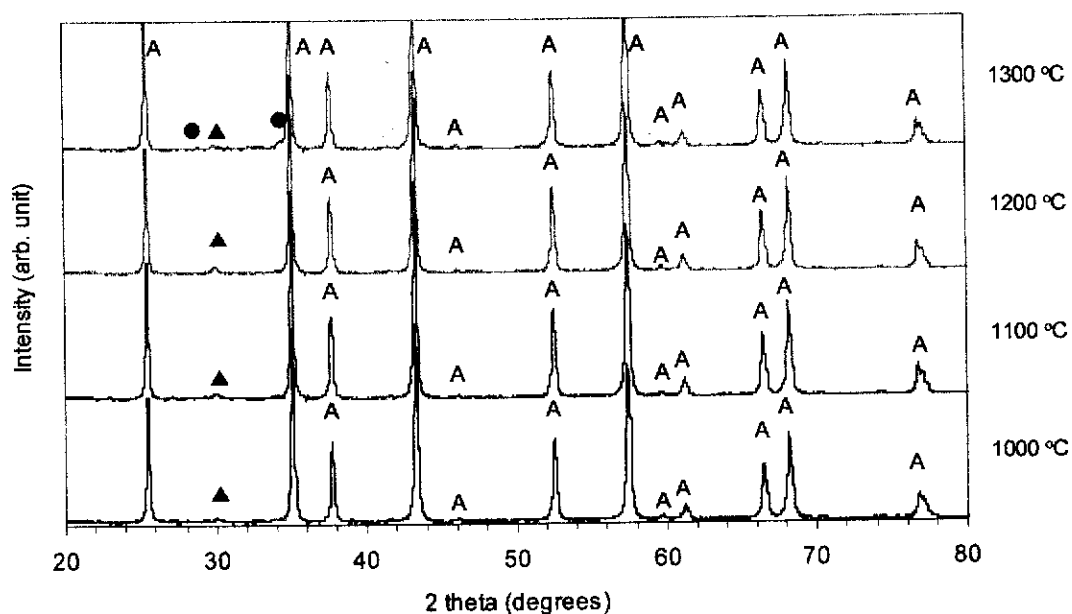


Figure 6.10. Room-temperature XRD patterns for the functionally-graded A/CA₆ composites heat-treated at various temperatures as obtained by the slicing method.



(a)



(b)

Figure 6.11. Expanded views of the XRD patterns for the functionally-graded A/CA₆ composites heat-treated at 1000 – 1300 °C in (b) and 1350 – 1650 °C in (a). Legends A = α-Al₂O₃, ▲ = CA, ● = CA₂, and x = CA₆.

Rietveld analysis with XRD data was performed for the functionally-graded A/CA₆ and alumina control samples, using the procedure described in section 3.4.2, to obtain a quantitative estimate of the phase concentrations. Selected representative Rietveld difference plots for the alumina control and A/CA₆ samples obtained by both gradual polishing and slicing methods and A/CA₆ composite at 1000 °C and 1400 °C are shown in Figures 6.12, 6.13 and 6.14. The corresponding plots for the other refinements are shown in Appendix B Figures B15-B23. The results show no unassigned Bragg reflections, thus indicating that correct models were used in the Rietveld calculations. The fluctuations in the difference plots show reasonable fit between the observed and the calculated patterns.

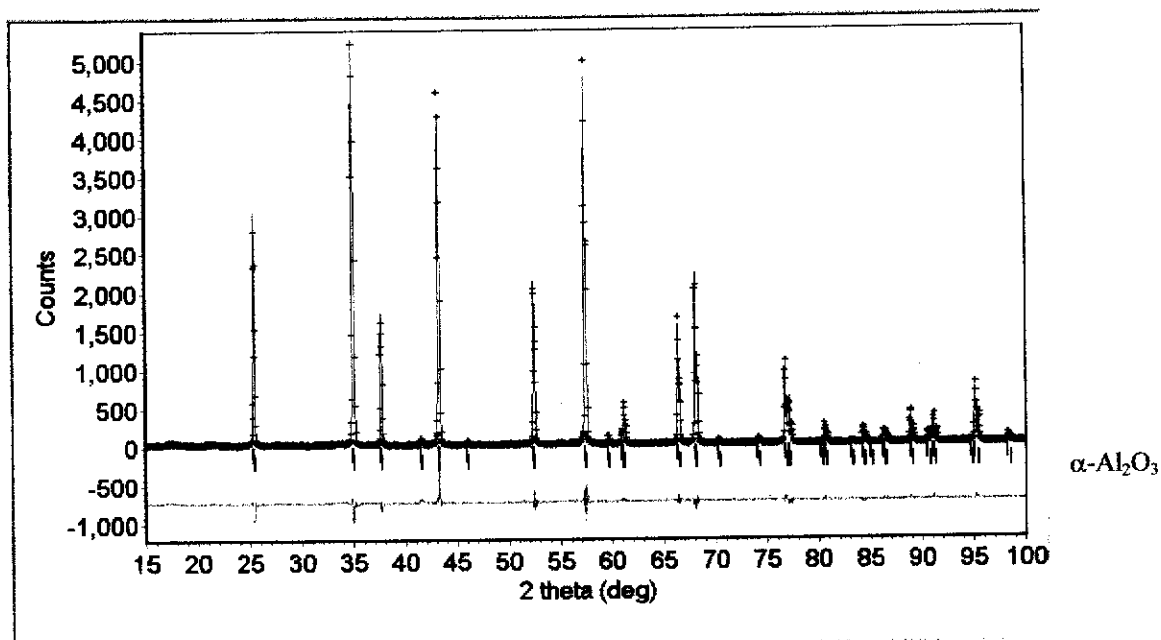
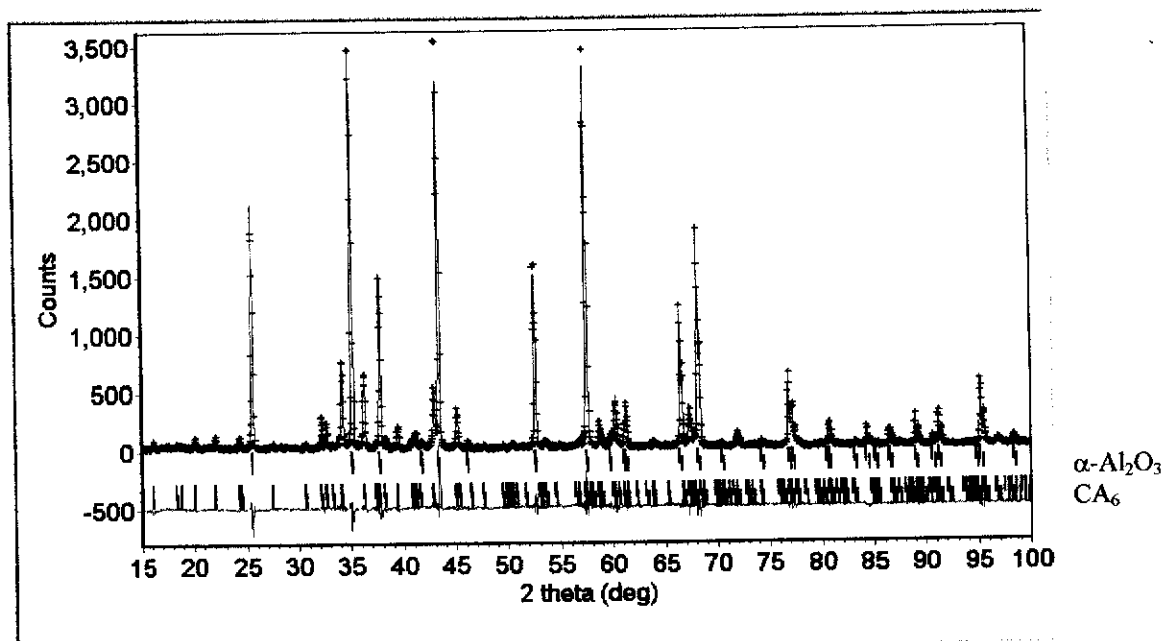
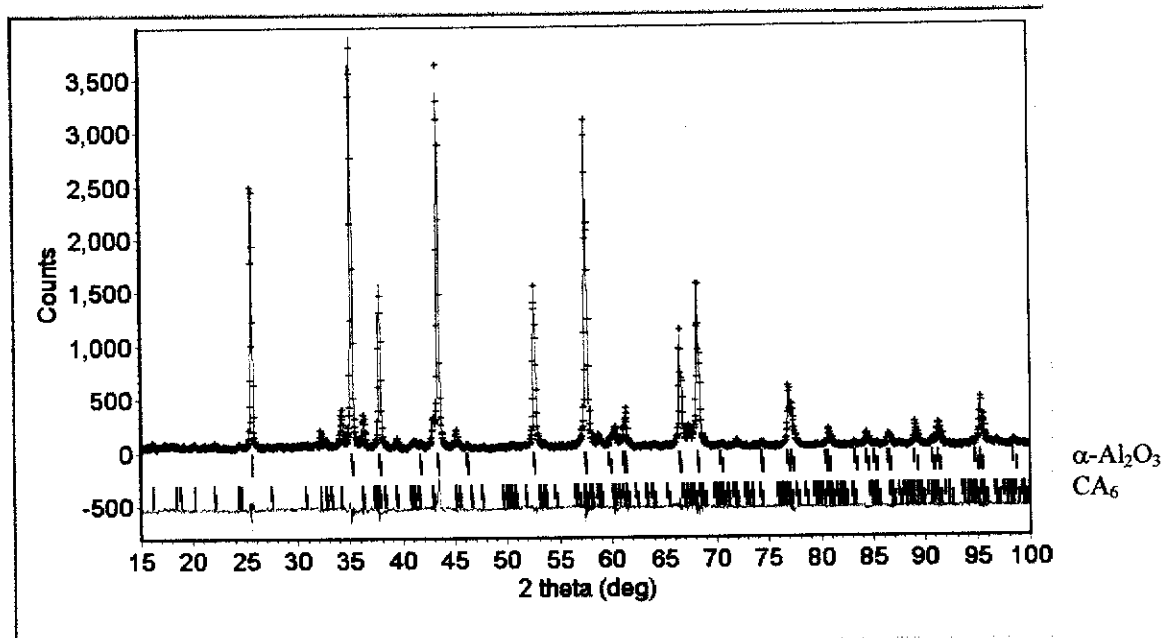


Figure 6.12. XRD Rietveld difference plots for the alumina control sample. The observed data are shown by a (+) sign, and the calculated data by the solid line. Vertical lines represent the positions of diffraction lines for $\alpha\text{-Al}_2\text{O}_3$. The green line below the vertical line is the difference profile.

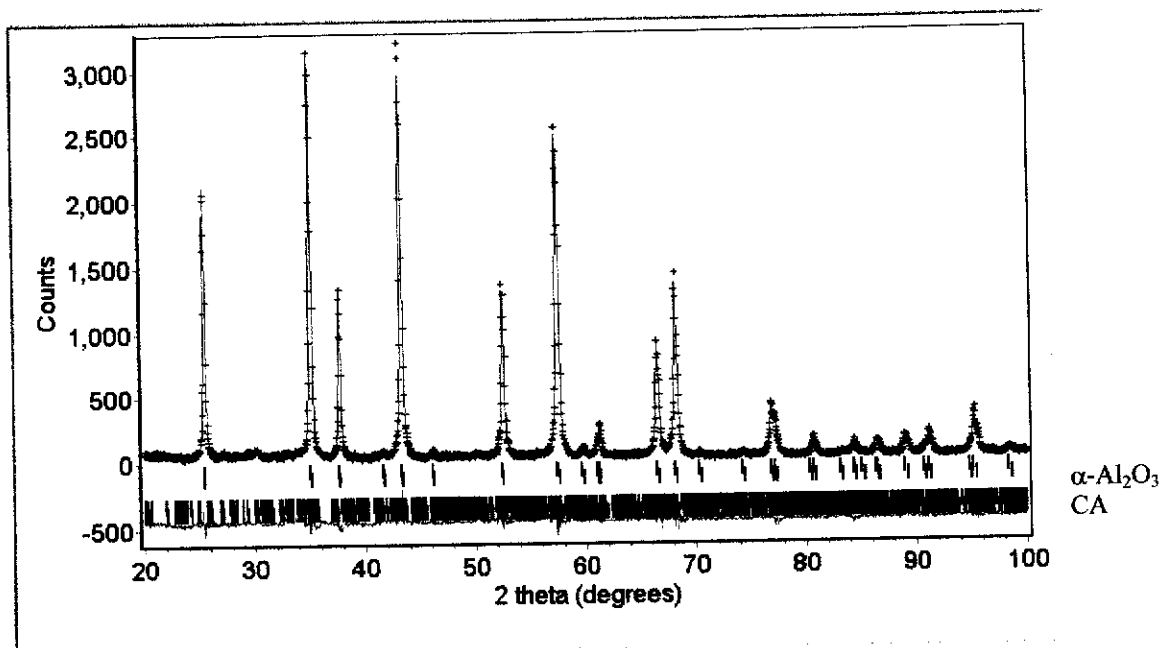


(a)

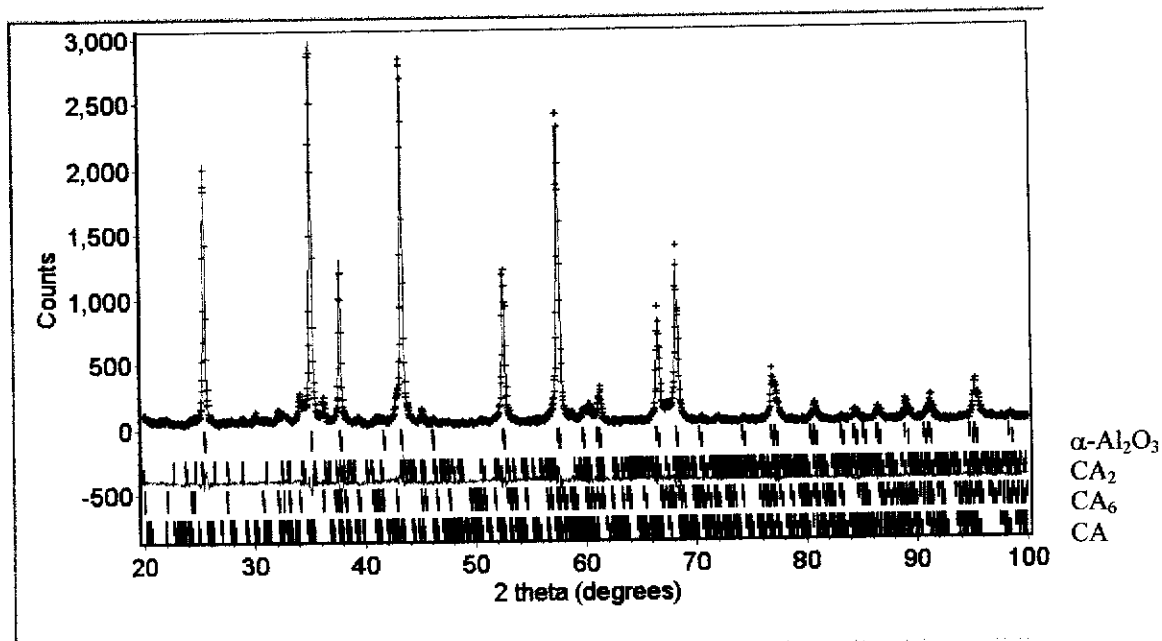


(b)

Figure 6.13. XRD Rietveld difference plots for the functionally-graded A/CA₆ composite obtained by gradual polishing at the depth of 0.5 mm in (a) and slicing method at layer 2 (2 – 4 mm) in (b). The observed data are shown by a (+) sign, and the calculated data by the solid line. Vertical line represents the positions of diffraction lines for α -Al₂O₃ and CA₆. The green line below the vertical line is the difference profile.



(a)



(b)

Figure 6.14. XRD Rietveld difference plots for the functionally-graded A/CA₆ composite at 1000 °C in (a) and 1400 in (b). The observed data are shown by a (+) sign, and the calculated data by the solid line. Vertical line represents the positions of diffraction lines for α -Al₂O₃ and CA in (a) and α -Al₂O₃, CA₂, CA₆ and CA in (b). The green line between the vertical line is the difference profile.

The figures-of-merit values for the alumina and functionally-graded A/CA₆ samples obtained by gradual polishing and slicing are shown in Table 6.4. The R_{wp} values for the graded A/CA₆ sample obtained by gradual polishing, ranged between 10.0 – 10.7 %, whereas the corresponding values obtained by slicing were slightly lower, i.e. 9.1 – 9.3 %. The R_B values ranged between 4.8 – 6.6 % for α -Al₂O₃ phase and 4.9 – 5.7 % for CA₆ phase were observed for the A/CA₆ sample obtained by gradual polishing. The corresponding values ranged between 2.8 – 3.4 % for α -Al₂O₃ were lower as obtained by slicing, but the R_B values ranged between 4.7 – 6.7 % for CA₆ were slightly higher. The R_{wp} value should be ideally close to R_{exp} if the model is basically correct, i.e. GOF = 1 (Prince 1993). But for phase composition GOF < 4 is acceptable (Kisi 1994). The GOF for all refinements were less than 2.5 % suggesting that the quality of refinement is acceptable.

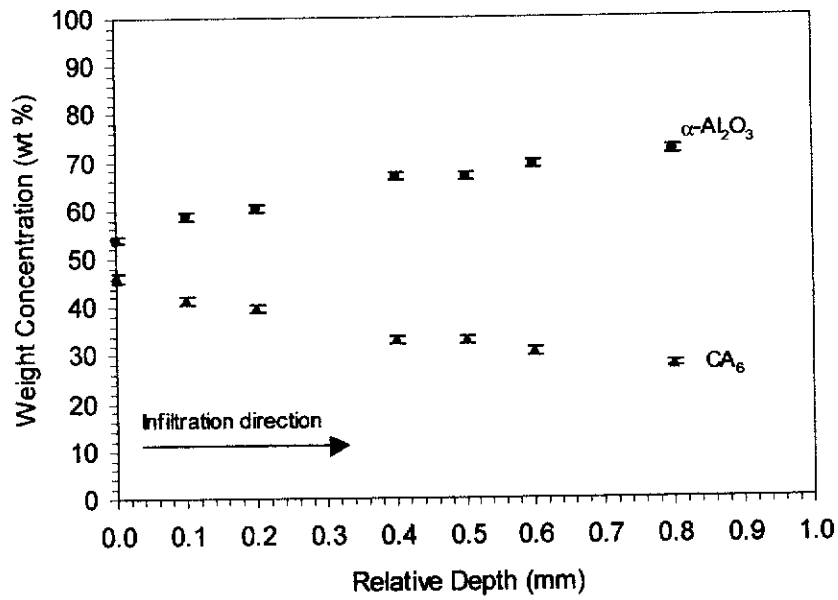
Variations in weight for α -Al₂O₃ and CA₆ phases in functionally-graded A/CA₆ composites obtained by gradual polishing and slicing are shown in Figure 6.15. Summaries of the data are presented in Tables 6.5. The relative weight fraction for CA₆ in functionally-graded A/CA₆ composites obtained by gradual polishing method is 46.1(0.9) wt% on the surface and reduces with depth to 33.0(0.7) wt% at 0.5 mm, and then to 27.8(0.6) wt% at 0.8 mm. In contrast, the alumina content increases with depth from 53.9(0.8) wt% at the surface to 67.0(0.8) wt% at 0.5 mm, and then to 72.2(0.8) wt% at 0.8 mm. The relative weight fraction for the CA₆ phase obtained by the slicing method is 25.7(0.7) wt% for layer 1 and reduces progressively with depth to 12.4(0.5) wt% in layer 4 (see Table 6.4). In contrast, the weight fraction for alumina increases with depth from 74.3(0.5) wt% for layer 1 to 87.6(1.0) wt% in layer 4.

Table 6.4. Figures-of-merit from Rietveld refinement with XRD data for the alumina and graded A/CA₆ composite obtained by gradual polishing and slicing methods.

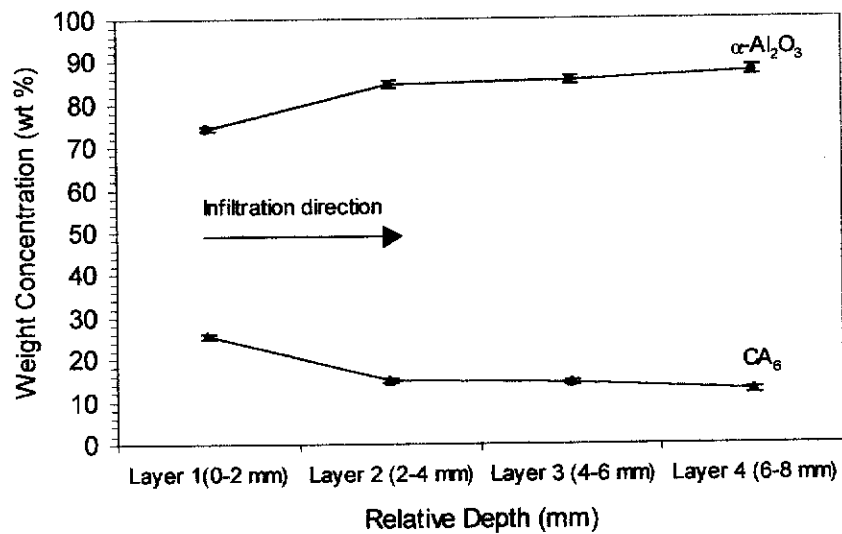
Sample/ Depth	R _{exp}	R _{wp}	GOF	R _B α-Al ₂ O ₃	R _B CA ₆
Alumina	10.8	16.4	2.3	5.0	-
Graded A/CA ₆ composite:					
- <i>Gradual polishing method</i>					
0.0 mm	10.0	15.1	2.3	6.1	5.3
0.1 mm	10.6	15.1	2.0	6.6	4.5
0.2 mm	10.7	16.1	2.4	5.4	5.2
0.4 mm	10.7	15.3	2.0	5.6	5.8
0.5 mm	10.7	14.9	2.3	5.6	5.3
0.6 mm	10.0	15.1	2.3	5.4	4.9
0.8 mm	10.5	14.9	2.0	4.8	5.7
- <i>Slicing method</i>					
Layer 1 (0-2 mm)	9.1	14.4	2.5	3.2	4.7
Layer 2 (2-4 mm)	9.2	12.8	1.9	2.9	5.5
Layer 3 (4-6 mm)	9.2	12.7	1.9	2.8	6.1
Layer 4 (6-8 mm)	9.3	13.4	2.1	3.4	6.7

Table 6.5. Relative phase compositions from Rietveld refinements with XRD data for the sintered alumina and graded A/CA₆ samples obtained by gradual polishing and slicing methods.

Sample/Depth	α -Al ₂ O ₃ (wt%)	CA ₆ (wt%)
Alumina	100.0 (0.5)	0
Graded A/CA ₆ composite:		
- <i>Gradual polishing method</i>		
0.0 mm	53.9 (0.8)	46.1 (0.9)
0.1 mm	58.6 (0.7)	41.4 (0.7)
0.2 mm	60.3 (0.8)	39.7 (0.8)
0.4 mm	66.9 (0.8)	33.1 (0.7)
0.5 mm	67.0 (0.8)	33.0 (0.7)
0.6 mm	69.4 (0.8)	30.6 (0.7)
0.8 mm	72.2 (0.8)	27.8 (0.6)
- <i>Slicing method</i>		
Layer 1 (0 – 2 mm)	74.3 (0.5)	25.7 (0.7)
Layer 2 (2 – 4 mm)	85.0 (0.9)	15.0 (0.5)
Layer 3 (4 – 6 mm)	85.4 (0.9)	14.6 (0.5)
Layer 4 (6 – 8 mm)	87.6 (1.0)	12.4 (0.5)



(a)



(b)

Figure 6.15. Variations of weight concentrations (wt%) for $\alpha\text{-Al}_2\text{O}_3$ and CA_6 in functionally graded A/ CA_6 composites obtained by the gradual polishing method in (a) and the slicing method in (b). Error bars indicate two estimated standard deviations (2σ).

The figures-of-merit from Rietveld refinement with XRD data for the graded A/CA₆ composites at selected temperature in the range 1000 – 1650 °C are shown in Table 6.6. The R_B factors for each phase in each refinement are 2.6 – 3.1 % for α-Al₂O₃, 5.6 – 8.6 % for CA, 4.9 – 5.3 % for CA₂ and 4.6 % for CA₆. The GOF values were relatively low, i.e. all approximately less than 2 % indicating that the quality of refinements is acceptable.

Table 6.6. Figures-of-merit from Rietveld refinement with XRD data for the functionally graded A/CA₆ composite, sintered at 1000 – 1650 °C for 0.5h.

Temperature (°C)	R _{exp}	R _{wp}	GOF	R _B α-Al ₂ O ₃	R _B CA	R _B CA ₂	R _B CA ₆
1000	8.9	13.0	2.2	2.6	8.6	-	-
1100	9.0	12.6	2.0	3.1	6.7	-	-
1200	9.1	12.5	1.9	2.5	6.0	-	-
1300	8.9	11.7	1.7	3.1	7.3	5.3	-
1350	9.0	11.9	1.8	3.0	7.5	5.2	-
1400	8.8	11.2	1.6	2.7	5.6	4.9	4.6
1650	8.7	12.4	2.0	3.0	-	-	4.6

Table 6.7 shows the relative phase composition (wt%) for the functionally-graded A/CA₆ composite at selected temperature in the range 1000 – 1650 °C. The variations of relative phase composition (wt%) as a function of temperature are presented in Figure 6.16. The wt% of the α-Al₂O₃ phase decreased with increasing temperature, i.e. from 99.0(1.3) wt% at 1000 °C to 72.9(0.9) wt% at 1650 °C. The wt% of CA increased from 1.0(0.2) – 1.9(0.3) wt% at 1000 – 1200 °C, while from 1300 to 1400 °C decreased slightly. The wt% of CA₂ decreased from 5.5(0.3) wt% at 1300 °C to 4.2(0.3) wt% at 1400 °C. The wt% CA₆ phase increased markedly from 10.3(0.3) wt% at 1400 °C to 27.1(0.6) wt% at 1650 °C.

Table 6.7. Relative phase compositions from Rietveld refinements with XRD data for the functionally-graded A/CA₆ composites, sintered at 1000 – 1650 °C for 0.5h.

Temperature (°C)	α -Al ₂ O ₃ (wt%)	CA (wt%)	CA ₂ (wt%)	CA ₆ (wt%)
1000	99.0 (1.3)	1.0 (0.2)	-	-
1100	98.1 (1.2)	1.9 (0.3)	-	-
1200	98.1 (1.2)	1.9 (0.2)	-	-
1300	93.2 (1.1)	1.3 (0.2)	5.5 (0.3)	-
1350	92.3 (1.1)	1.3 (0.2)	5.8 (0.3)	-
1400	84.0 (1.0)	1.5 (0.2)	4.2 (0.3)	10.3 (0.3)
1650	72.9 (0.9)	-	-	27.1 (0.6)

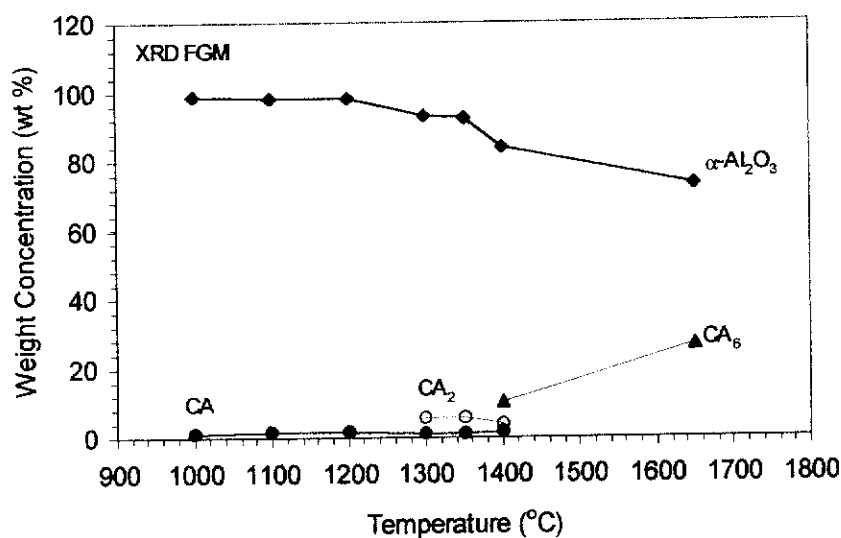


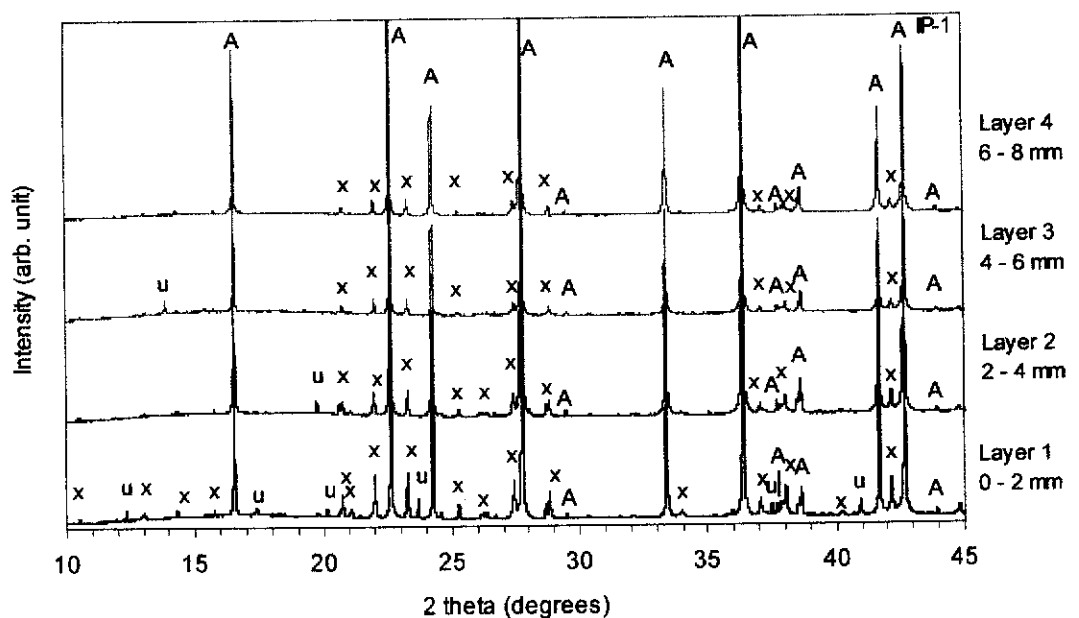
Figure 6.16. Variation of weight concentrations (wt%) from Rietveld refinement with XRD data for the functionally-graded A/CA₆ composites as a function of temperature. Error bars too small to include.

Synchrotron Radiation Diffraction (SRD) Analysis

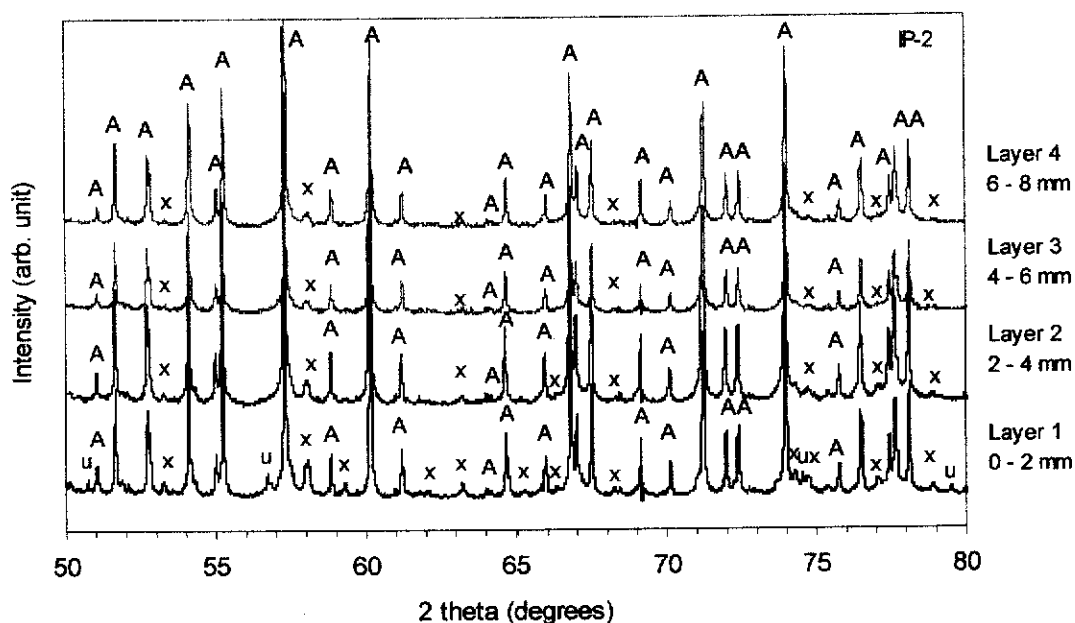
SRD patterns for the functionally-graded A/CA₆ composites were acquired with the BIGDIFF instrument at the Australian National Beamline Facility (ANBF) at Tsukuba, Japan, using the procedure described in section 3.4.2. The powdered sample used in the XRD work was also employed in this experiment. The powders were packed in low absorption lithium borate glass capillaries of diameter of 0.3 mm. Four imaging plates with dimensions of (400 x 200 mm²) were used to obtain the diffraction patterns. A search/match procedure using PDF file was also employed to identify the individual peak in each pattern prior to Rietveld analysis.

Figures 6.17a and 6.17b show the synchrotron radiation diffraction patterns for the imaging plate 1, $2\theta = 10 - 45^\circ$ and imaging plate 2, $2\theta = 50 - 80^\circ$ for layers 1 – 4 in functionally-graded A/CA₆ composite. The phases observed in layer 1 – 3 are α -Al₂O₃, CA₆ and unknown phases. However, the unknown peak was not observed in layer 4. The peak intensity of CA₆ decreased with depth whereas the peak intensity of α -Al₂O₃ increased with depth. The graded nature of this system is clearly revealed. When compared with laboratory x-ray powder diffraction results obtained previously, the superiority of synchrotron radiation diffraction data is evident in terms of sharper peaks, shorter collection time (~ 20 minutes), and better detection of unknown peaks.

The relative phase compositions (wt%) of the SRD patterns for the layers 1 - 4 were computed by the Rietveld refinement method using the procedure described in section 3.4.2. Four imaging plates in each layer were used in the SRD Rietveld refinement. Selected representative Rietveld difference plots for layer 4, imaging plates 1 – 4 of the functionally graded A/CA₆ composites are shown in Figure 6.18. The fluctuation in the difference plots in each imaging plate show reasonable fit between the observed and the calculated patterns. The Rietveld difference plots for layers 1, 2 and 3 are shown in Appendix B (Figures B24-26).

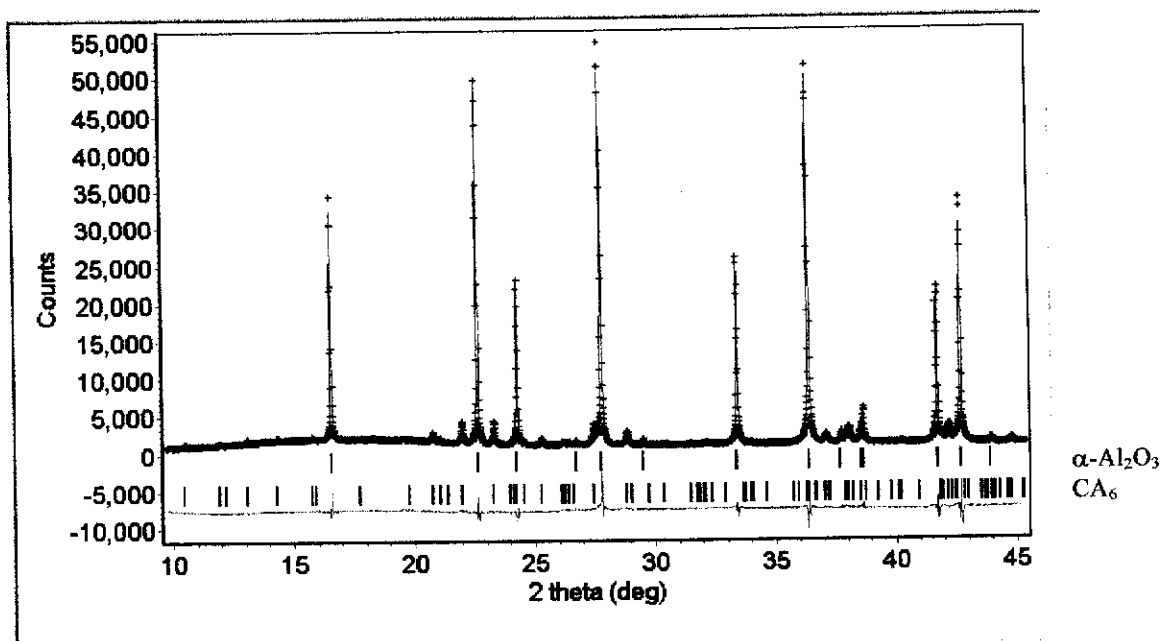


(a)

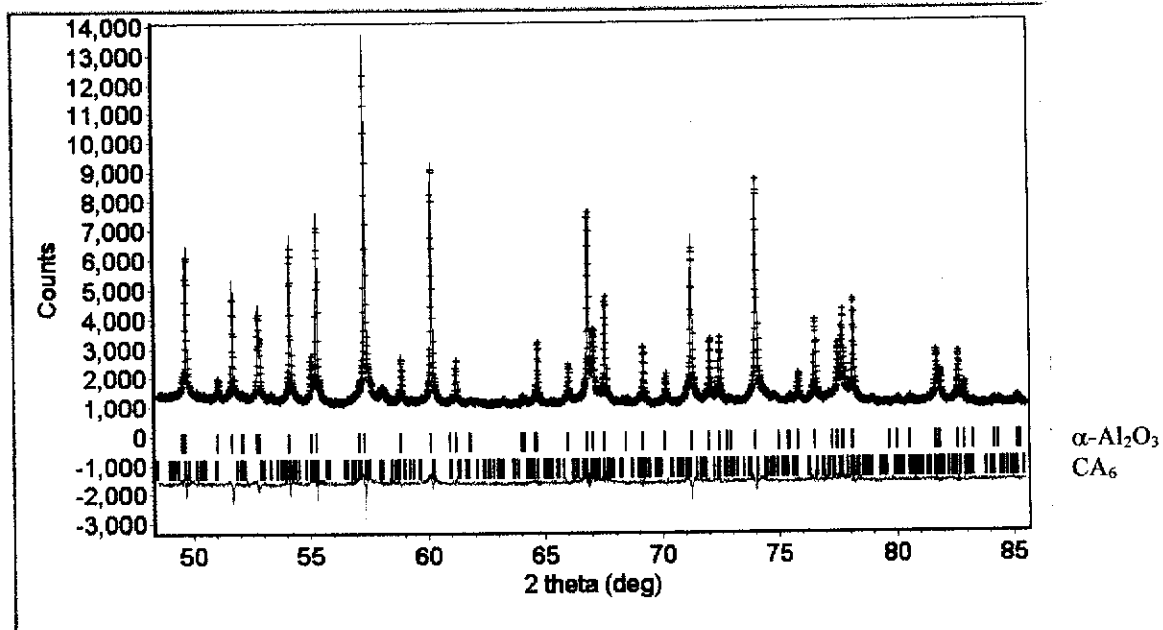


(b)

Figure 6.17. SRD patterns for the functionally-graded A/CA₆ composites for layers 1 – 4 (a) imaging plate 1, $2\theta = 10 - 45^\circ$ and (b) imaging plate 2, $2\theta = 50 - 80^\circ$. The graded composition samples were obtained by *slicing method*. Legends: A = α -Al₂O₃, x = CA₆, and u = unknown.



(a)



(b)

Figure 6.18. SRD Rietveld difference plots for layer 4 of the functionally-graded A/CA₆ composites: (a) imaging plate 1 and (b) imaging plate 2. The observed data are shown by a (+) sign, and the calculated data by the solid line. Vertical lines represent the positions of diffraction lines of α -Al₂O₃ and CA₆. The green line below the vertical line is the difference profile.

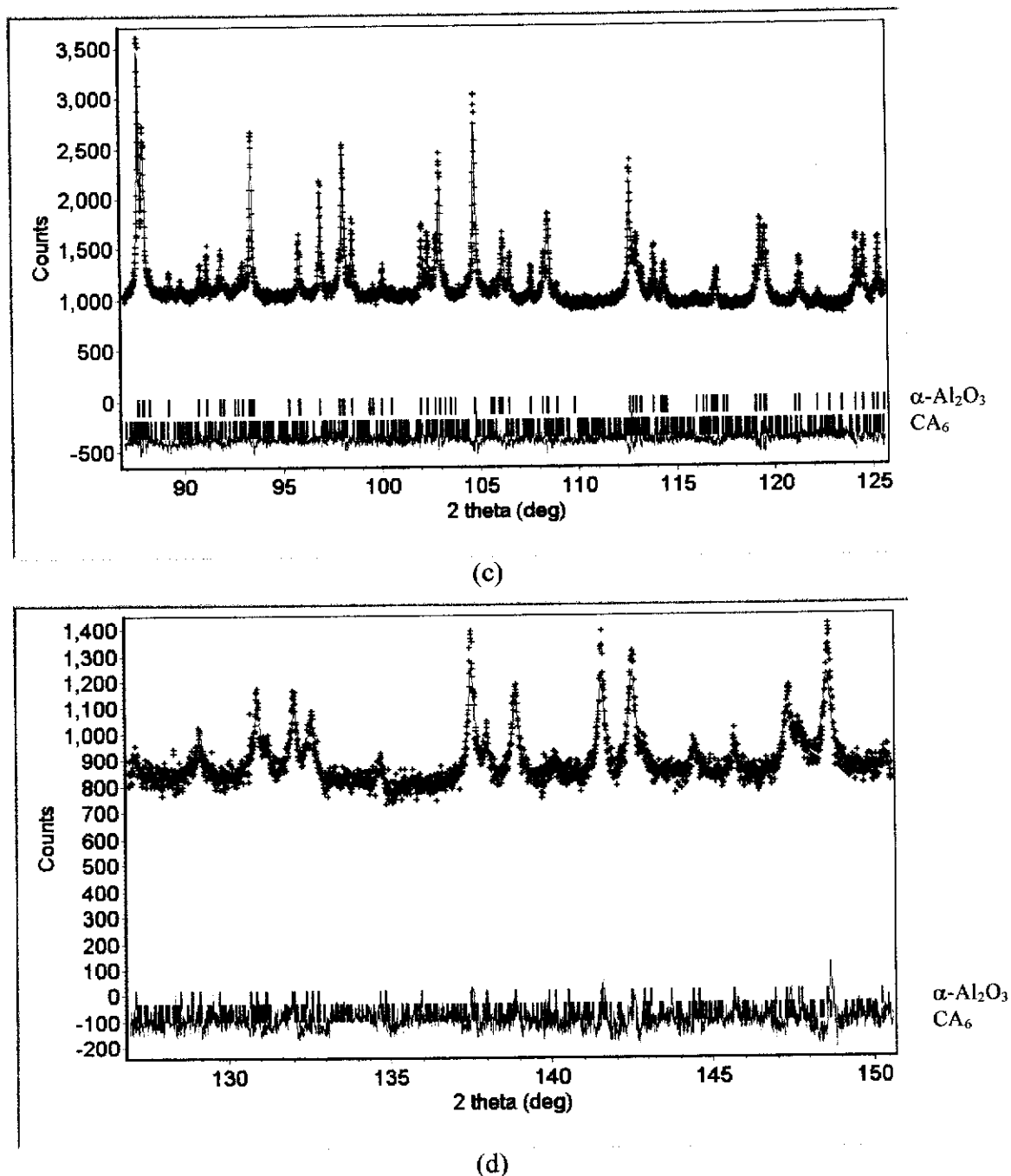


Figure 6.18. (Continued) SRD Rietveld difference plots for layer 4 of the functionally-graded A/CA₆ composites: (c) imaging plate 3 and (d) imaging plate 4. The observed data are shown by a (+) sign, and the calculated data by the solid line. Vertical lines represent the positions of diffraction lines of α -Al₂O₃ and CA₆. The green line below the vertical line is the difference profile.

The figures-of-merit values from Rietveld refinement with SRD data for the functionally-graded A/CA₆ composites are presented in Table 6.8. Variations of weight concentrations (wt %) for the α -Al₂O₃ and CA₆ phases obtained from SRD data for layer 1 to layer 4 are shown in Figure 6.19. A summary of weight concentration data is presented in Table 6.9. The result shows the wt% CA₆ phase decreased with increase in depth, but the α -Al₂O₃ phase increased with increase in depth. The weight concentration for the α -Al₂O₃ obtained by SRD data is slightly higher than that for XRD data, i.e. 78.5(0.4), 88.0(0.3), 89.0(0.4) and 90.0(0.3) wt% for layers 1 – 4 for SRD data and 74.3(0.5), 85.0(0.9), 85.4(0.9) and 87.6(1.0) wt% for XRD data. In contrast, the wt % for the CA₆ obtained by SRD is slightly lower than that for XRD, i.e. 21.5(0.2), 12.0(0.1), 11.0(0.2) and 10.0(0.1) wt% for SRD and 25.7(0.7), 15.0(0.5), 14.6(0.5) and 12.4(0.5) for XRD data. Slight differences arising from different methods used (XRD and SRD) may be attributed to the presence of the unknown phase as found in SRD patterns. However, the two sets of results are in reasonable agreement and the graded composition profiles in functionally graded A/CA₆ composite is clearly evident.

Table 6.9. Relative phase compositions (wt%) from Rietveld refinements with SRD data for the functionally-graded A/CA₆ composites obtained by slicing method.

Sample/ Depth	α -Al ₂ O ₃ (wt%)	CA ₆ (wt%)
Layer 1 (0 – 2 mm)	78.5(0.4)	21.5(0.2)
Layer 2 (2 – 4 mm)	88.0(0.3)	12.0(0.1)
Layer 3 (4 – 6 mm)	89.0(0.4)	11.0(0.2)
Layer 4 (6 – 8 mm)	90.0(0.3)	10.0(0.1)

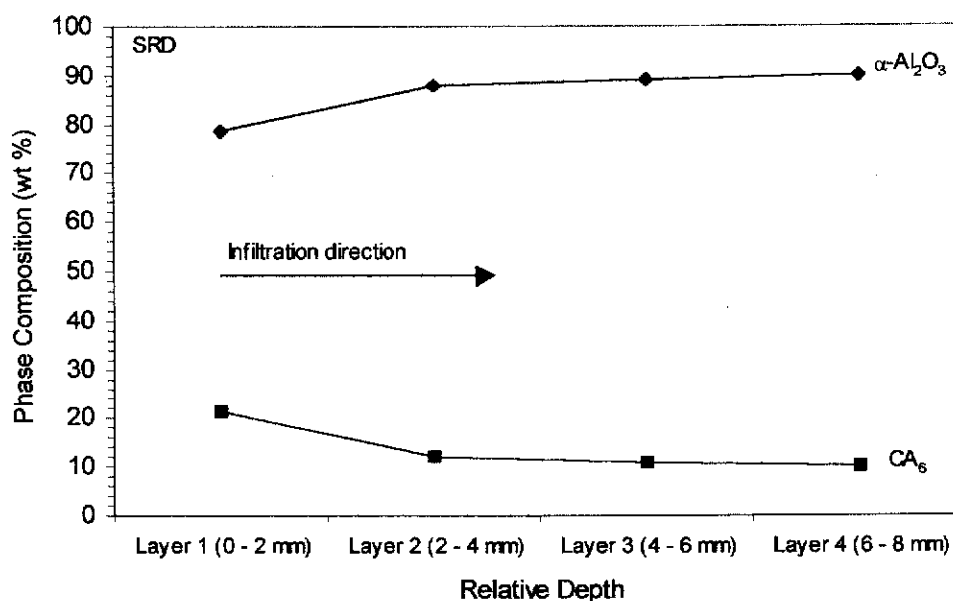
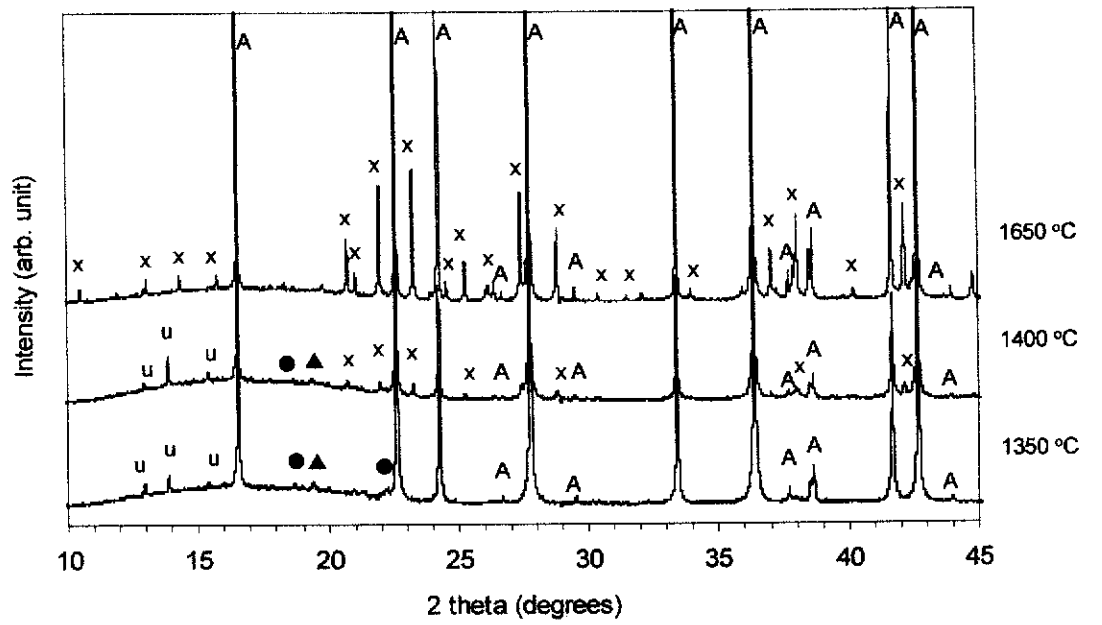
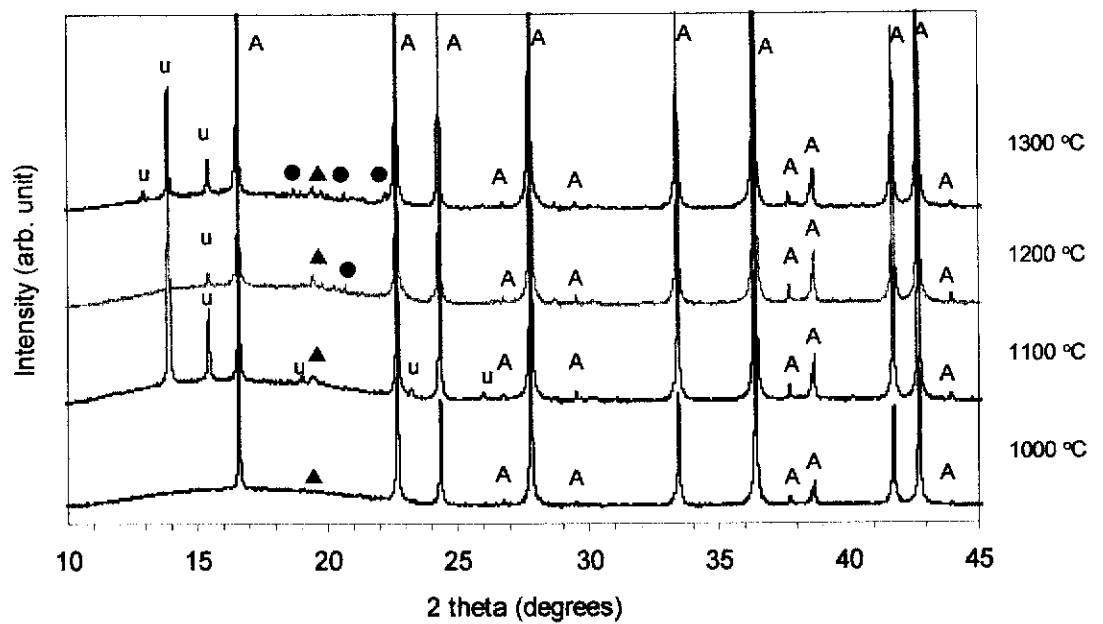


Figure 6.19. Variation of weight concentrations (wt%) for the α -Al₂O₃ and CA₆ phases in the functionally-graded A/CA₆ composites for layers 1 – 4 obtained by SRD data. Error bars too small to include.

SRD was also used to monitor the formation temperature of calcium aluminates (CA, CA₂ and CA₆) in functionally graded A/CA₆ composites. The analysis of the synchrotron data at this stage was done in a qualitative manner. The same powdered material previously employed in the XRD work was used in this experiment. Figures 6.20a and 6.20b show SRD patterns for the functionally-graded A/CA₆ composite heat-treated at temperatures 1000 – 1650 °C for 0.5 h for imaging plate 1. The phases observed at 1000 °C are α -Al₂O₃ and CA. The CA phase remained at 1400 °C. Residual CaO phase was not detected at 1000 °C because of the complete reaction between α -Al₂O₃ and CaO to form CA phase. The CA₂ phase was observed at temperature between 1200 - 1400 °C. The unknown peaks were observed between 1100 – 1600 °C. The formation temperature of CA₆ occurred at approximately 1400 °C. This agrees well with the results obtained from XRD described previously. The formation of *in-situ* CA, CA₂ and CA₆ are believed to occur via exothermic reaction between α -Al₂O₃ and CaO, at 1000 – 1400 °C according to Equations 4.1, 4.2, 4.3, 4.4, respectively.



(a)



(b)

Figure 6.20. SRD patterns for the functionally-graded A/CA₆ composites at 1000 – 1300 °C in (b) and 1350 – 1650 °C in (a). Legends: A = α-Al₂O₃, ▲ = CA, ● = CA₂, x = CA₆ and u = unknown.

High Temperature Neutron Diffraction (HTND) Analysis

High temperature neutron diffraction (HTND) was used to monitor the formation of calcium aluminates (CA, CA₂ and CA₆) in functionally-graded A/CA₆ composites. The fully-infiltrated sample was used in this experiment. Figure 6.21 shows HTND patterns of functionally graded A/CA₆ composites at RT (room temperature), 1000, 1100, 1200, 1300, 1350 and 1400 °C. Expanded views of HTND patterns in Figure 6.21 are shown in Figures 6.22a and 6.22b. The phases observed at RT and between 1000 and 1100 °C are α -Al₂O₃ and CA. Residual CaO phase was also not observed at this temperature indicating that the reaction between α -Al₂O₃ and CaO to form CA was complete. The CA phase disappeared at 1200 °C followed by the appearance of CA₂ phase, which remained at temperature 1400 °C. This agrees well with the HTND results described previously for CA100 sample obtained by reaction sintered method (see section 4.2.2). The formation temperature of CA₆ occurred at approximately 1400 °C. The formation of CA, CA₂ and CA₆ phases are believed to occur via exothermic reaction between α -Al₂O₃ and CaO, at 1000 – 1400 °C according to the Equations 4.1, 4.2, 4.3 and 4.4.

Phase abundance for the sintered functionally graded A/CA₆ composites in each temperature obtained from HTND data was performed by Rietveld refinement method, using the procedure described in section 3.4.2. Selected representative HTND Rietveld difference plots at 1000 and 1400 °C are shown in Figure 6.23. The results show no unassigned Bragg reflections, thus indicating that the correct models were used in the Rietveld calculations. The fluctuation in the difference plots show reasonable fit between the observed and the calculated patterns. The Rietveld difference plots at RT, 1100, 1200, 1300 and 1350 °C are presented in Appendix B (Figures B27-B29).

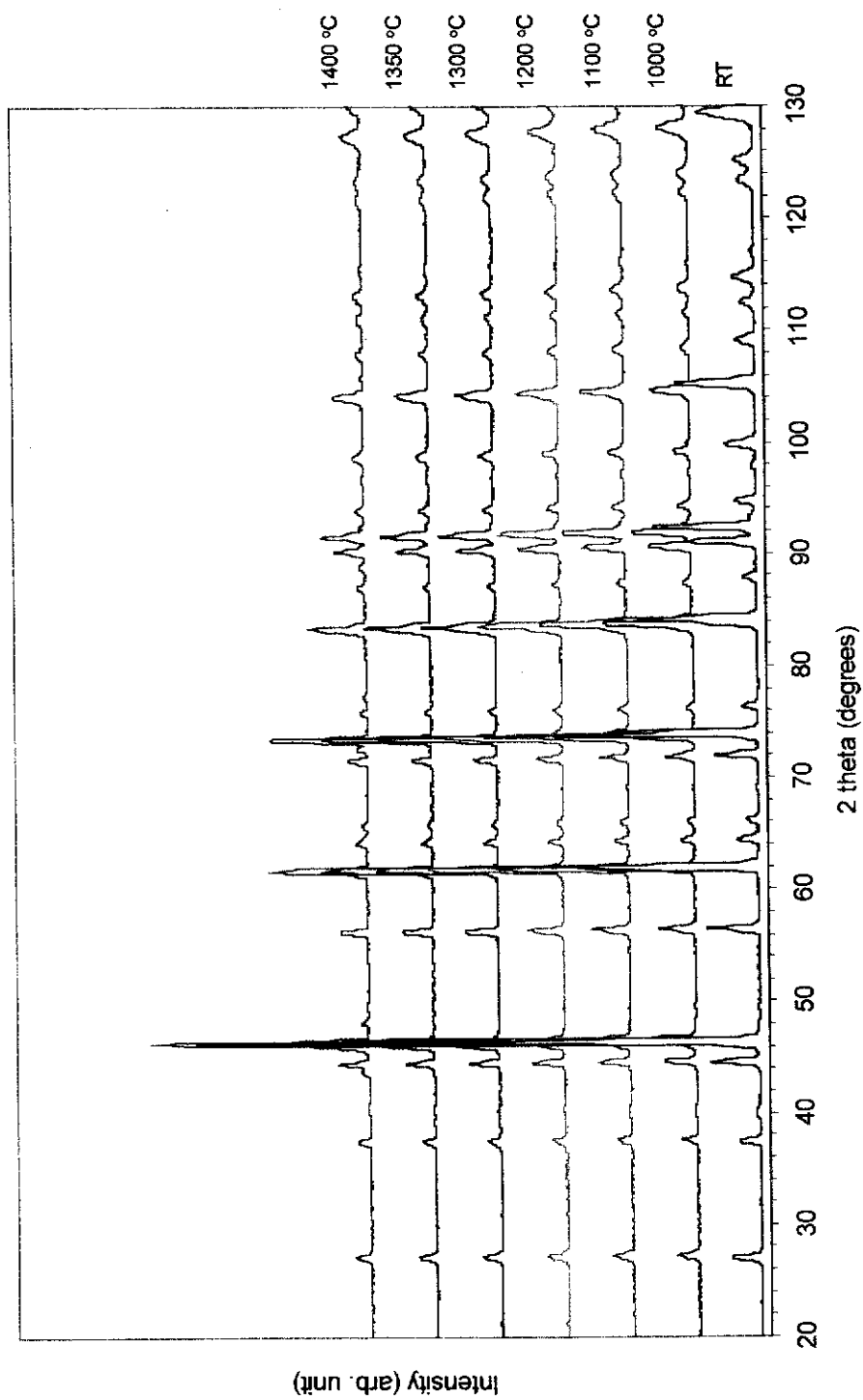
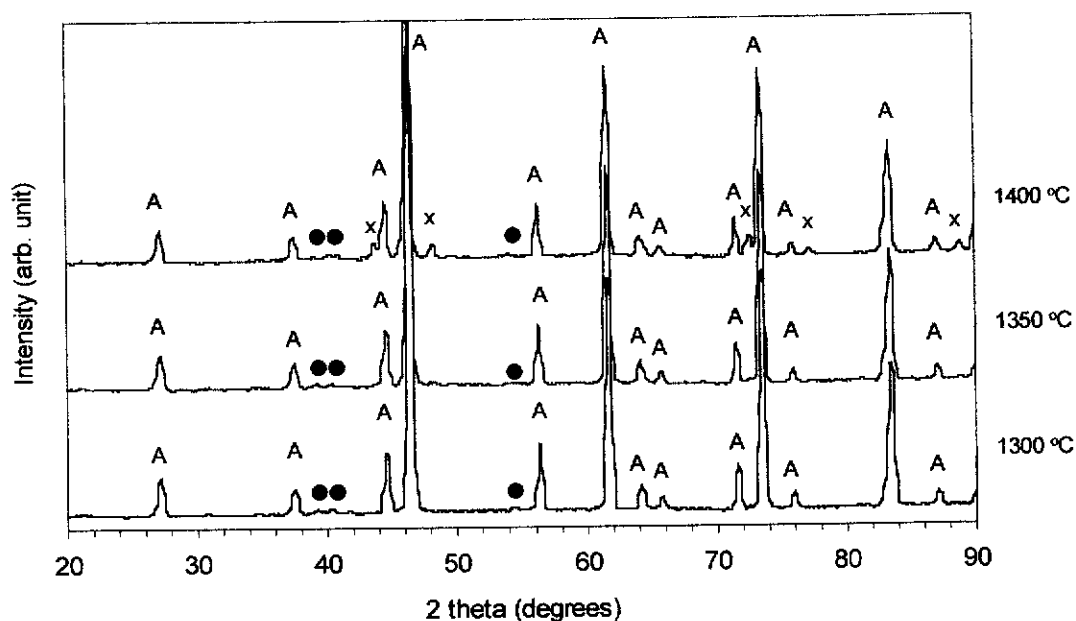
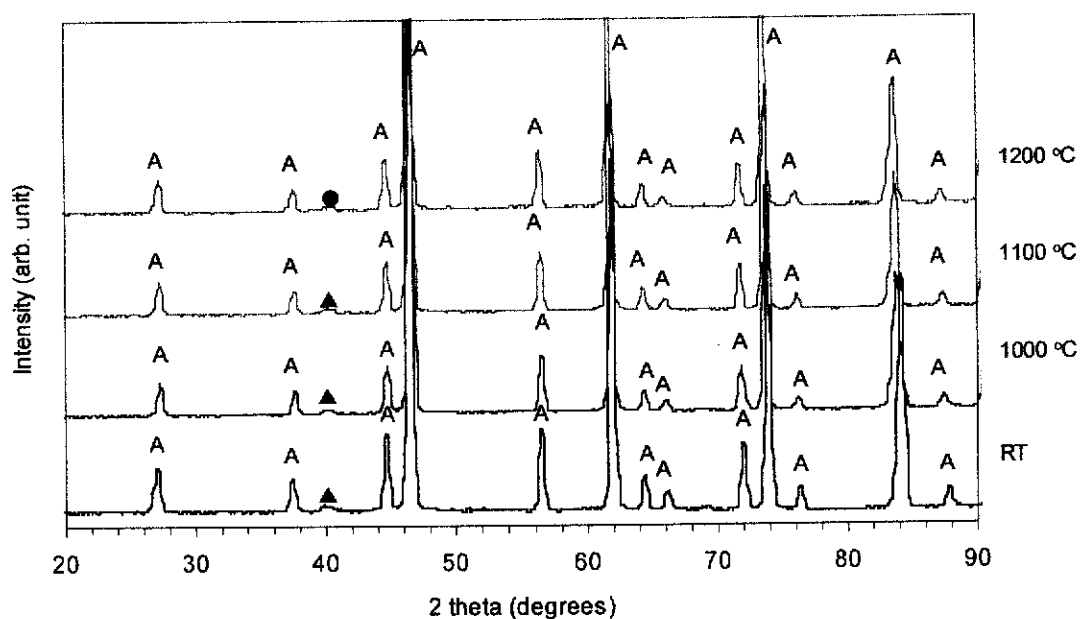


Figure 6.21. HTND patterns for the functionally-graded A/CA₆ composites heat-treated at various temperatures.

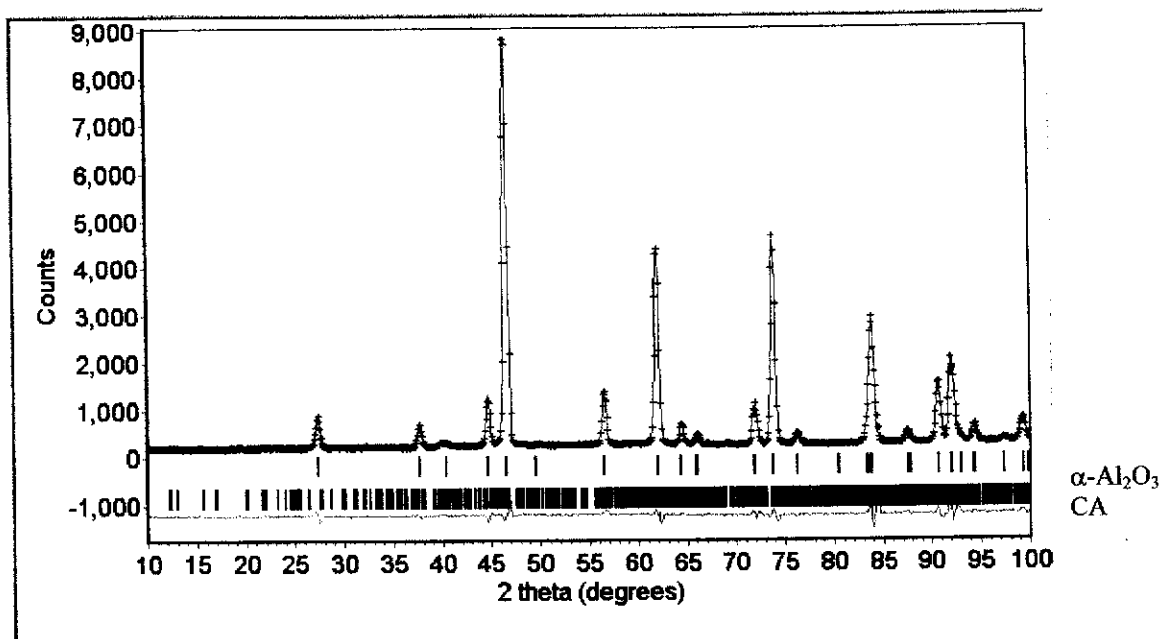


(a)

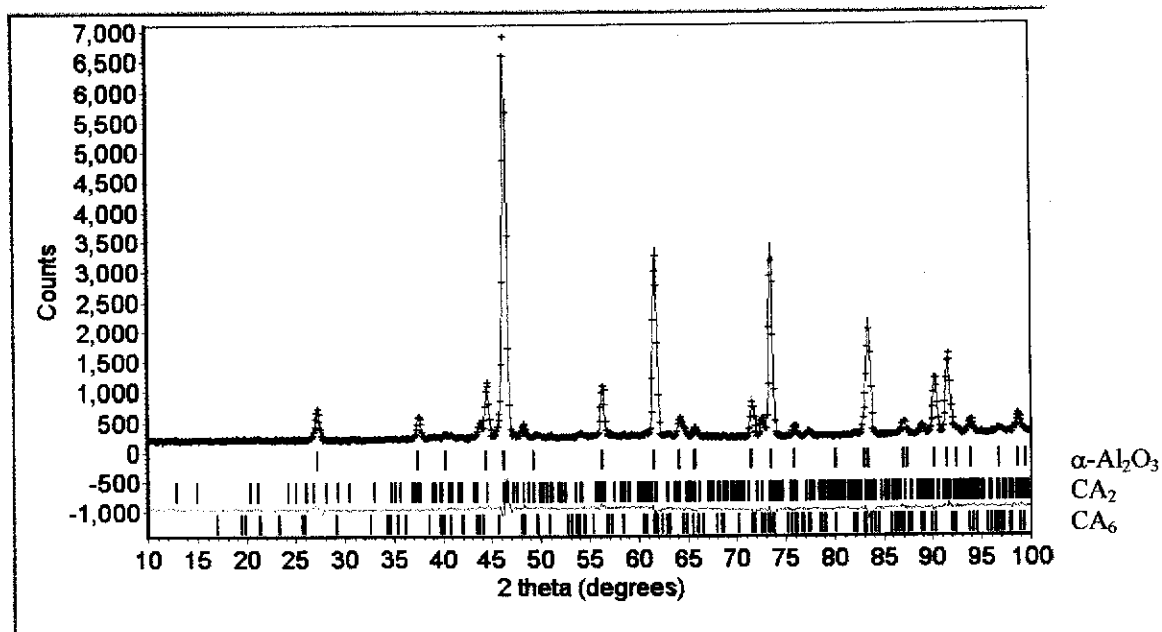


(b)

Figure 6.22. Expanded views of the HTND views patterns for the functionally-graded A/CA₆ composites at RT, 1000, 1100 and 1200 °C in (b) and at 1300, 1350 and 1400 °C in (a). Legends: A = α -Al₂O₃, ▲ = CA, ● = CA₂ and x = CA₆.



(a)



(b)

Figure 6.23. HTND Rietveld difference plots for the functionally-graded A/CA₆ composite at 1000 °C in (a) and 1400 in (b). The observed data are shown by a (+) sign, and the calculated data by the solid line. Vertical line represents the positions of diffraction lines for $\alpha\text{-Al}_2\text{O}_3$ and CA in (a) and $\alpha\text{-Al}_2\text{O}_3$, CA₂ and CA₆ in (b). The green line between the vertical line is the difference profile.

The figures-of-merit from Rietveld refinement with HTND data for the functionally graded A/CA₆ composites at selected temperature in the range 1000 – 1400 °C are shown in Table 6.10. The R_B factors for each phase in each refinement are 1.7 – 4.1 % for α -Al₂O₃, 2.7 – 3.0 % for CA, 3.6 – 4.7 % for CA₂ and 5.2 % for the CA₆ phase. The GOF values were relatively low, i.e. less than 3 % indicating that the quality of refinement is acceptable.

Table 6.10. Figures-of-merit from Rietveld refinement with HTND data for the functionally-graded A/CA₆ composite.

Temperature (°C)	R _{exp}	R _{wp}	GOF	R _B α -Al ₂ O ₃	R _B CA	R _B CA ₂	R _B CA ₆
1000 (RT)	2.2	4.5	3.2	1.7	2.7	-	-
1000	2.3	6.6	3.0	2.3	3.7	-	-
1100	2.3	5.1	2.9	1.9	3.4	-	-
1200	2.3	5.0	3.7	2.0	3.0	3.6	-
1300	2.4	5.5	2.8	3.4	-	3.7	-
1350	2.4	5.8	2.6	3.4	-	4.0	-
1400	2.5	6.6	3.0	4.1	-	4.7	5.2

Table 6.11 shows the relative phase composition (wt%) for the functionally graded A/CA₆ composite obtained by HTND data at selected temperature in the range 1000 – 1400 °C. Variations of relative phase composition (wt%) as a function of temperature are presented in Figure 6.24. The wt% of the α -Al₂O₃ phase decreased with increasing temperature, i.e. from 97.0(0.9) wt% at 1000 °C to 92.2(1.3) wt% at 1400 °C. The wt% of CA decreased from 2.1.0(0.2) – 0.6(0.3) wt% at 1000 – 1200 °C. The wt% of CA₂ increased from 2.7(0.3) wt% at 1200 °C to 10.1(1.6) wt% at 1400 °C, then decreased to 1.7(0.5) wt% at 1400 °C due to the presence of 6.1(0.3) wt% CA₆ phase at this temperature.

Table 6.11. Relative phase compositions from Rietveld refinements with HTND data for the functionally-graded A/CA₆ composites.

Temperature (°C)	α -Al ₂ O ₃ (wt%)	CA (wt%)	CA ₂ (wt%)	CA ₆ (wt%)
1000 (RT)	97.9 (0.9)	2.1 (0.2)	-	-
1000	98.2 (1.2)	1.8 (0.3)	-	-
1100	98.3 (0.9)	1.7 (0.2)	-	-
1200	96.7 (1.0)	0.6 (0.2)	2.7 (0.3)	-
1300	89.9 (1.7)	-	10.1 (1.6)	-
1350	90.0 (1.8)	-	10.0 (1.6)	-
1400	92.2 (1.3)	-	1.7 (0.5)	6.1 (0.3)

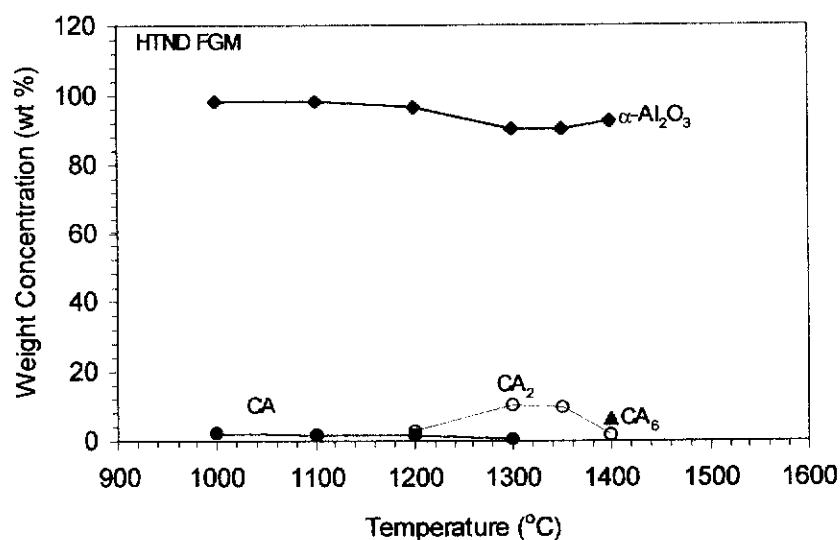


Figure 6.24. Variation of weight concentrations (wt%) from Rietveld refinement with HTND data for the functionally-graded A/CA₆ composites as a function of temperature. Error bars too small to include.

6.2.3 Microstructural Analysis

Scanning Electron Microscopy (SEM)

The microstructure of the functionally-graded A/CA₆ composite was examined by scanning electron microscopy (SEM), using procedure described in section 3.4.3. A cross-section of the sample was polished using a Struers Pedamat polisher beginning with 40 μm , 15 μm , 9 μm , 6 μm , 3 μm , and finally 1 μm diamond paste. Polished samples were thermally etched at 1350 °C for 30 minutes, prior to microstructural analysis to enhance grain structure and reveal grain boundaries.

Figure 6.25 shows a typical graded microstructure of the functionally graded A/CA₆ composites. The CA₆ grains are readily recognisable by their elongated morphology with grain size ranged 4 – 8 μm , where in the back-scattered electron image mode appear bright because of their high atomic number, whereas the alumina grains with grain size ranged 2 – 7 μm are seen to be in dark grey. The content of CA₆ is most abundant near the surface and decreases with increasing depth. This observation, essentially, supports those made earlier with respect to the XRD and SRD results (see section 6.2.2) regarding a graded or continuously varying phase composition through the cross-section.

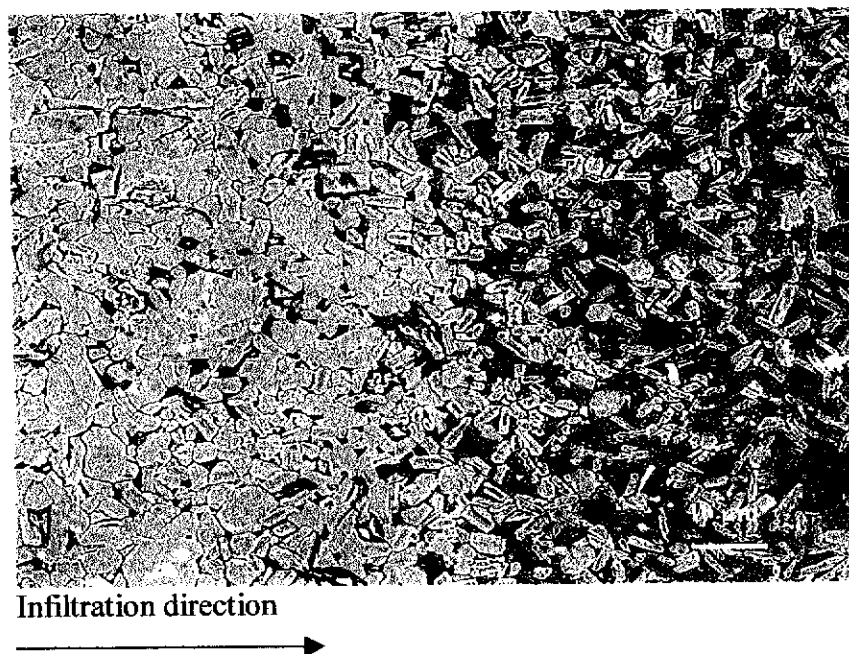
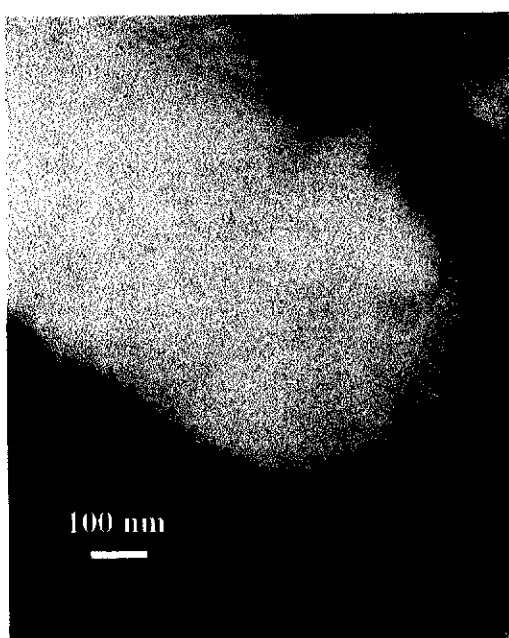


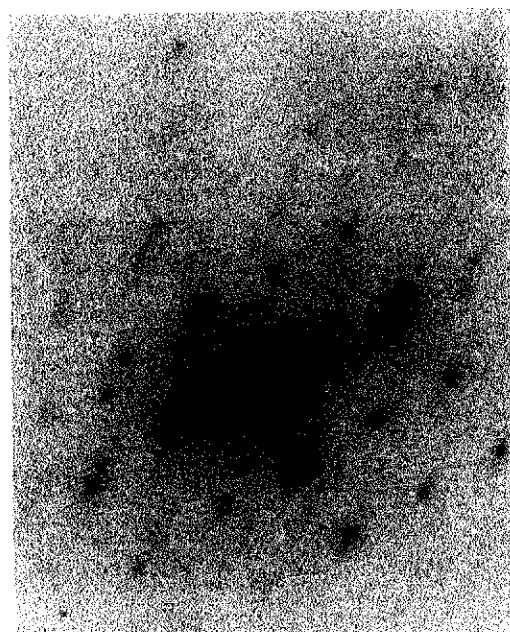
Figure 6.25. Typical microstructure of functionally-graded A/CA₆ composite as viewed in the SEM. The lighter grains are CA₆.

Transmission Electron Microscopy (TEM)

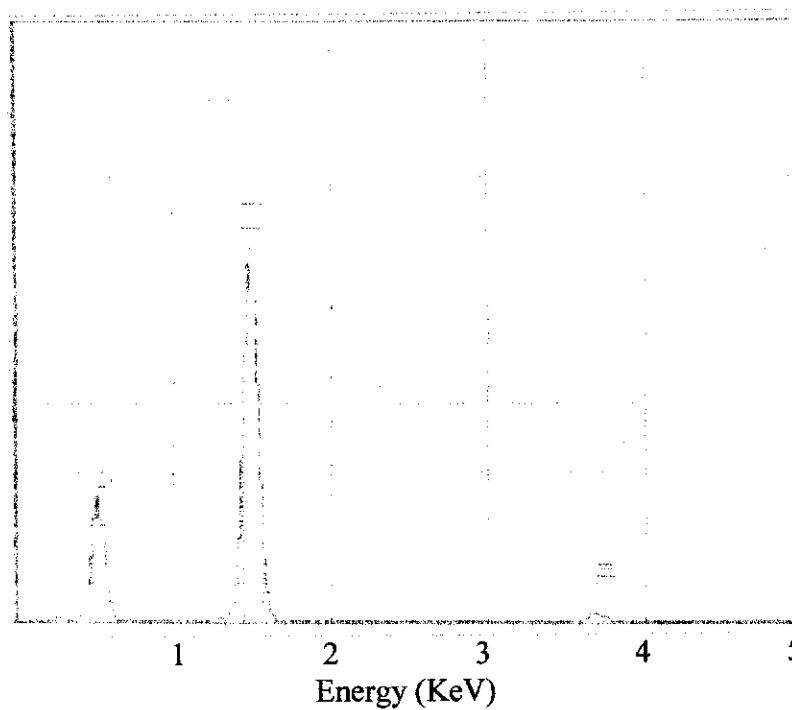
The transmission electron microscopy (TEM) – JEOL operating at 200 kV acceleration voltage, coupled with the selected area diffraction (SAD) and energy dispersive spectroscopy (EDS) were used to observe and confirm the microstructure of calcium aluminates (CA, CA₂, and CA₆) in functionally-graded A/CA₆ composite. Figure 6.26 shows the TEM bright-field image, selected-area diffraction (SAD) pattern and the energy dispersive spectroscopy (EDS) chart for the functionally graded A/CA₆ composites calcined at 1400 °C for 0.5h. The presence of CA₆ is clearly evident in this micrograph as confirmed by the energy-dispersive spectroscopy (EDS) and selected-area diffraction (SAD) during the preliminary TEM analysis.



(a)



(b)



(c)

Figure 6.26. TEM micrograph of CA_6 in functionally-graded A/ CA_6 composite calcined at 1400 °C for 0.5h as revealed by (a) bright field imaging, (b) SAD and (c) the corresponding EDS chart.

6.2.4 Physical and Thermal Properties

Weight Gain, Density, Porosity and Shrinkage

The porosity of alumina preform after pre-sintering at 1100 °C was 45.1 ± 1.5 % (see Table 6.2). Samples with similar porosity values were used for the fabrication of mullite/ZTA (Low *et al.* 1996), mullite-AT/ZTA (Pratapa and Low 1996), and AT/A (Skala 2000) using an infiltration route. The mass change due to infiltration after sintering, bulk density, apparent porosity and bulk shrinkage for both the sintered A/CA₆ (FGM) and alumina (control) samples is presented in Table 6.12.

Table 6.12. Weight gain, density, porosity, and shrinkage for the A/CA₆ (FGM) and alumina (control) samples.

Sample	Δm (%)	Density (ρ) (g/cm ³)	Porosity (P) (%)	Shrinkage (S_v)* (%)
A/CA ₆ (FGM)	8.7(4)	3.86(4)	3.6(3)	38.2(17)
Alumina (Control)	-0.8(2)	3.92(3)	1.7(2)	45.3(15)

Δm = weight difference before infiltration and after sintering.

* = volume shrinkage.

Values in parentheses are the estimated standard deviation of the values to the left.

The weight gain measurement method (Marple and Green 1990) was used to estimate the amount of CA₆ incorporated into alumina preform. This method is based on the weight difference between the alumina preform prior to infiltration and the composite body after sintering. Note that the CA₆ contents calculated using this method yield a bulk concentration and therefore provide no information on the distribution of the CA₆ within the composite body. As expected, the infiltrated sample (FGM) increased in mass after sintering. A mass increase of 8.7 % for the FGM sample was achieved. This result suggests that a new phase had been introduced into alumina preform, i.e. the formation of CA₆ phase. Assuming that CaO had reacted completely with alumina in the matrix to form CA₆, the mass

increase can be related to the average amount of CA₆ (9.1 vol%) present in the bulk. The mass of the sintered control sample was slightly lower than the green body. This reduction is due to the removal of organic binder (polyethylene glycol) present which occurs during the initial sintering stage.

The bulk density of sintered samples was determined using the Archimedes method with water as the immersion medium. The bulk density results for the FGM and control samples are shown in Table 6.12. Crystallographic density values of 3.786 g/cm³ for CA₆ (PDF No. 84-1613, ICDD data base) and 3.986 g/cm³ for α-Al₂O₃ (PDF No. 43-1484) were used to compute the theoretical density of the FGM sample based on a rule of mixtures. The result was 3.97 g/cm³. The measured densities for the sintered FGM and control samples were 3.86 ± 0.04 and 3.92 ± 0.03 g/cm³, which represent 97.5 % and 98.3 % theoretical densities. The result suggests that both the FGM and control samples sintered well and achieved near full density. The slightly lower value for the sintered FGM when compared to the control sample can be attributed to the presence of CA₆ phase, which may hinder the densification process (see section 4.2.3).

The apparent porosity for the FGM and control samples is shown in Table 6.12. The result indicates that dense samples with porosity < 4 % was obtained for FGM sample and < 2 % for control sample. This residual porosity can be attributed to incomplete densification in some sections of material.

The volumetric shrinkage of the samples was determined by measuring their volume before infiltration (V_i) and after sintering (V_f). The volume shrinkage (S_v) was calculated using following equation:

$$S_v = \frac{(V_i - V_f)}{V_i} \quad (6.1)$$

The volumes of the A/CA₆ (FGM) and control samples were reduced by as much as 38.2(17) % and 45.3(15) % respectively after sintering. The lower shrinkage of the FGM sample can be attributed to the presence of CA₆ phase. It was found that the

shrinkage of the A/CA₆ composite produced by *in-situ* reaction sintering decreased with increase in the CA₆ content (see 4.2.3).

Thermal Expansion and Shrinkage Behaviour

The thermal expansion and densification behaviour for the functionally graded A/CA₆ composites were observed using a THETA 160 dilatometer calibrated with a NIST single crystal sapphire standard. A bar-shaped sample with dimensions of 4x4x10 mm³ was prepared for measurement. The experiment was conducted at temperature between 20 - 1500 °C. The alumina ceramic was chosen as the control sample to provide a comparison of thermal expansion and densification behaviour for the FGM sample. Figure 6.27 shows the thermal expansion and densification versus temperature for both α -Al₂O₃ and FGM A/CA₆ samples. When compared to α -Al₂O₃ that commenced to densify at approximately 1137 °C, the graded A/CA₆ raised that temperature to approximately 1206 °C. This result is higher by 25 °C when compared with the A/CA₆ composites produced by *in-situ* reaction sintering process (see 4.2.3). The maximum shrinkage of functionally-graded A/CA₆ composites occurred at approximately 1352 °C which is slightly higher than Al₂O₃ of 1347 °C but lower by 100 °C when compared to A/CA₆ composites produced by the *in-situ* reaction sintering process. The presence of CA₆ phase appeared to hinder the processes of sintering and densification in alumina matrix. However, the values of expansion/shrinkage do not exceed 6 – 7 %. The average values of thermal expansion coefficient (TEC) for the A/CA₆ (FGM), A/CA₆ (*in-situ* reaction sintered) and alumina control samples are shown in Table 6.13. The functionally graded A/CA₆ composite has higher thermal expansion coefficient than α -Al₂O₃ but slightly lower than A/CA₆ composites produced by reaction sintering.

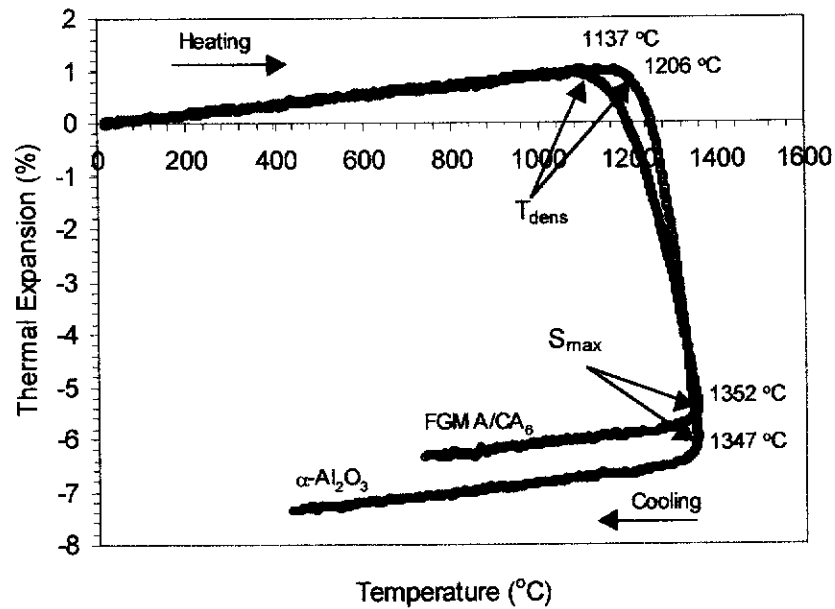


Figure 6.27. Thermal expansion and shrinkage behaviour for the functionally-graded A/CA₆ composites and alumina for the temperature range 20-1500°C. T_{dens} indicates the temperature at which densification commences and S_{max} indicates the maximum shrinkage.

Table 6.13. Average thermal expansion coefficient for the functionally-graded A/CA₆ composites, A/CA₆ composites produced by *in-situ* reaction sintering method and alumina control sample, between 20 – 1000 °C.

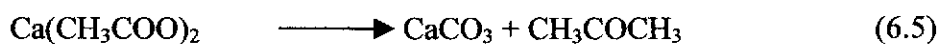
Sample	Average thermal expansion coefficient value ($\times 10^{-6}/^{\circ}\text{C}$)
A/CA ₆ (FGM)	9.11
A/CA ₆ (Reaction-Sintered)	9.36
Alumina (control)	8.63

Differential Thermal and Gravimetric Analysis (DTA and TG)

Simultaneous DTA and TG analysis for the calcium acetate and functionally graded A/CA₆ composites were carried out on a Netzsch STA-409C instrument in nitrogen atmosphere (see section 3.5.1). Figure 6.28 shows the simultaneous DTA and TG results for calcium acetate recorded in the range 20 – 1500 °C. A heating rate of 10 °C/min was used to carry out this analysis. Two small endothermic peaks at 162 and 206 °C in the DTA curve associated with the first step weight lost in the TG curve can be related to the two-step dehydration process (Ollova, Fralov, and Evstaf'eva (1993). First, one molecule of H₂O is lost, forming Ca(CH₃COO)₂.H₂O, and its subsequent formation of semihydrate Ca(CH₃COO)₂.0.5H₂O that becomes anhydrous at 180 – 220 °C given by:



By further heating calcium acetate decompose at temperatures between 340 - 480 °C with release of acetone in an oxidising and forms CaCO₃:



The acetone, CH₃COCH₃ further decomposes at high temperatures to allene, CH₂=C=CH₂ and this compound can be burnt with oxygen (Adáñez, de Diego, and García-Labiano 1999). The endothermic peak at 803 °C corresponds to the decomposition of the residual carbonate CaCO₃ to form calcium oxide CaO and carbon dioxide CO₂ as follows:

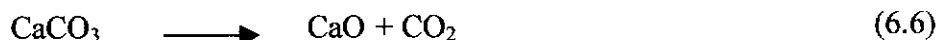
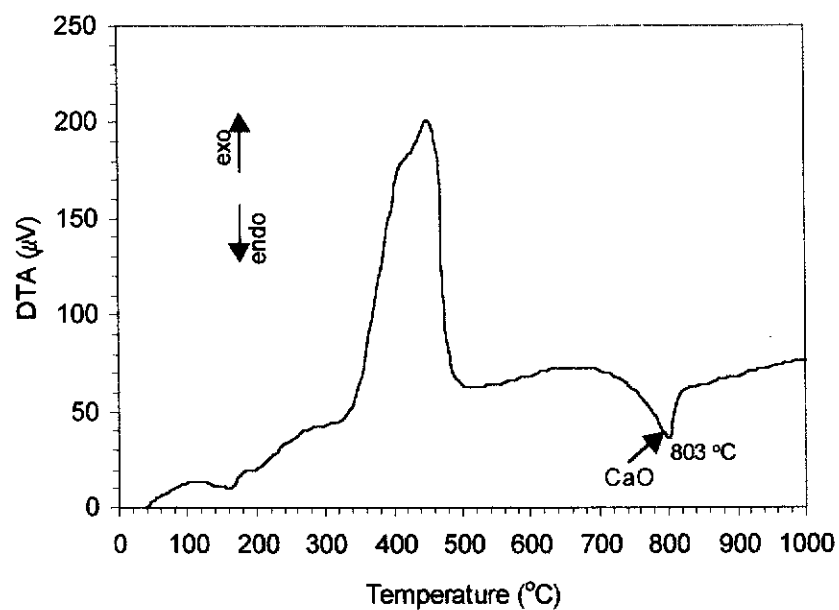
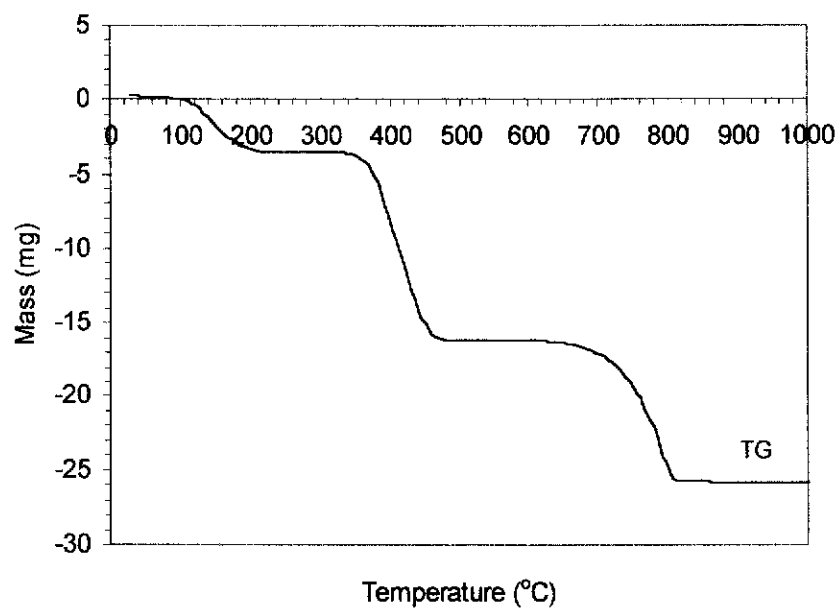


Figure 6.29 shows the simultaneous DTA and TG results for the functionally graded A/CA₆ composite recorded in the temperature range 20 – 1500 °C. A heating rate of 10 °C/min was also used to carry out this work. An exothermic peak appears at approximately 435 °C can be related to the removal of absorbed water, residual hydroxyl groups and organic materials and decomposition of calcium acetate. The endothermic peak at approximately 763 °C correlates well with the substantial weight losses on the TG curve (Figure 6.29b), indicates the decomposition of calcium carbonate to form calcium oxide. This result is slightly higher (~ 12 °C) than that for reaction sintered A/CA₆ (i.e. ~ 751 °C – see section 4.2.4). This difference can be attributed to the different routes used to synthesis the composites. There was no endothermic or exothermic peaks observed at approximately 1350 °C due to the formation of CA₆ phase in this system. Similar results were also found for the A/CA₆ sample produced from reaction sintering (see section 4.2.4). This suggests that the rate formations for the calcium aluminates (CA, CA₂, and CA₆) phases are very sluggish and their growth is diffusion-controlled and strongly time-dependent.

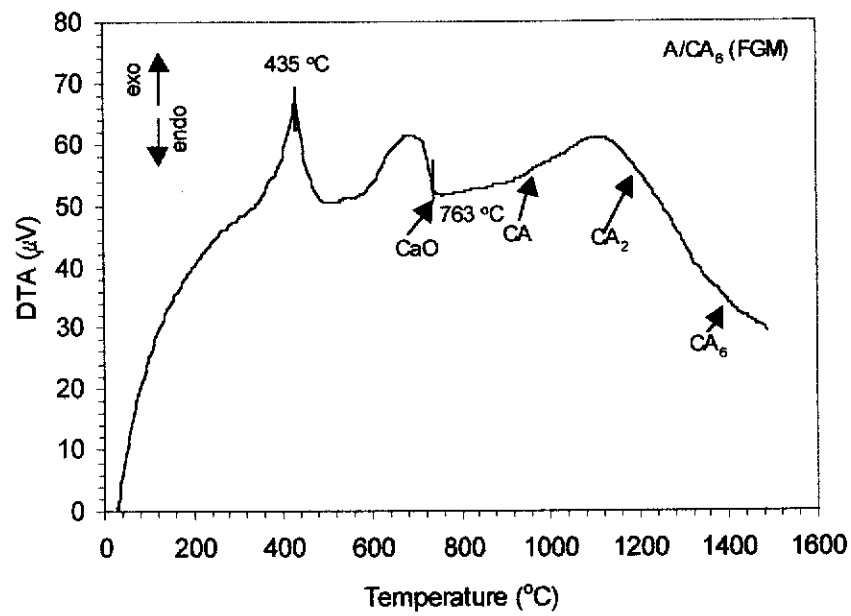


(a)

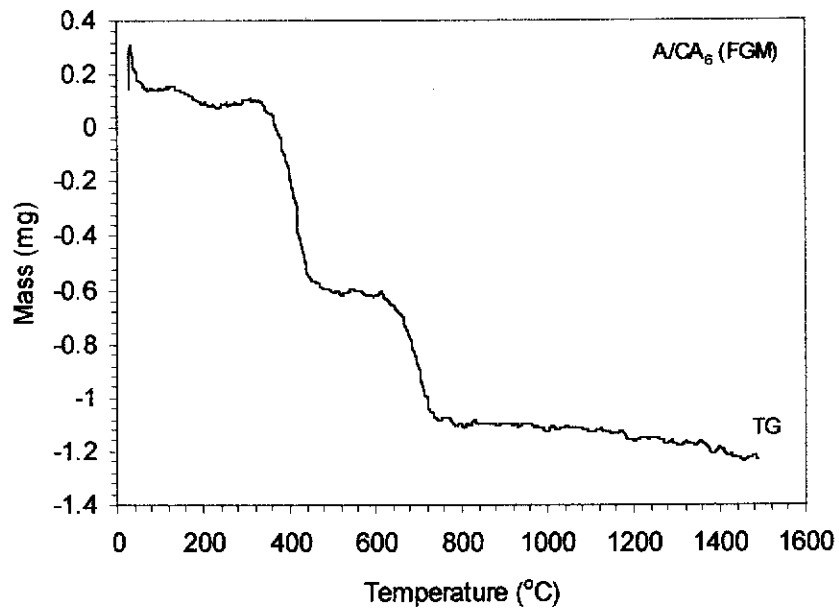


(b)

Figure 6.28. Thermal analysis for the calcium acetate from 20 to 1000 $^{\circ}C$: (a) DTA and (b) TG.



(a)



(b)

Figure 6.29. Thermal analysis for the functionally-graded A/CA composites from 20 to 1000 °C: (a) DTA and (b) TG.

6.2.5 Mechanical Properties

Vickers Hardness

The Vickers hardness as a function of depth for the FGM sample from the graded A/CA₆ layer to the homogeneous alumina layer was performed on the surface of the polished sample using a Vickers indenter. Indentation was made at the distances approximately 1, 2.9, 4.2, 5.9, 7.6, 9.9, 12.3, 15.1, 17, and 18 mm from the infiltrated surface. A load of 98 N was used to carry out this experiment. Figure 6.30 shows the variation of Vickers hardness as a function of distance for the FGM sample, i.e. from infiltrated part (graded region – A/CA₆) to non-infiltrated part (non-graded region – Al₂O₃) and the average hardness for the control sample. The plot illustrates the hardness markedly increased with increasing distance in the graded region and leveled-out in the non-grade region. For example, at approximately 1 mm distance, the hardness of material was 10.6 GPa but increased to 17.2 GPa at approximately 9.9 mm. Thereafter the values tended to plateau out. This graded change in hardness is not unexpected because the concentration of relatively soft CA₆ decreases with an increase distance as confirmed by the XRD results (see section 6.2.2). The average hardness in the non-graded region of 17.5 GPa is slightly lower than that of 17.8 GPa found for the control sample.

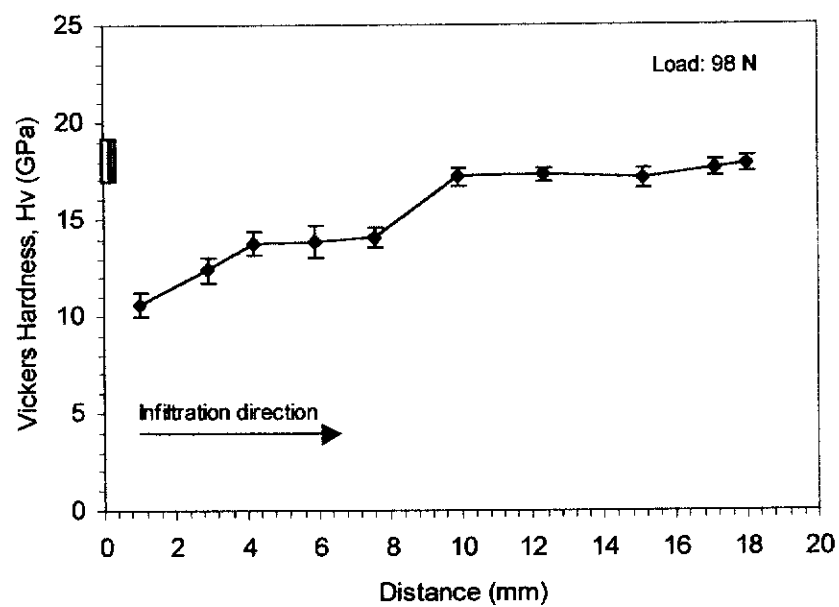


Figure 6.30. Variation of Vickers hardness as a function of distance for the FGM sample at an applied load of 98 N. Shaded box at the left represents the average Vickers hardness for the control sample. Error bars indicate two estimated standard deviations (2σ).

Selected areas of the FGM, i.e. at approximately 0 – 5 mm distance for graded-region was chosen to study the effect of loads on the Vickers hardness. Figure 6.31 shows the variation of Vickers hardness as a function of applied load in the range 29.4 – 294 N. The results indicate that the dependence of hardness on load is quite evident for FGM sample, where the hardness decreases with an increasing load. The decrease in hardness with load was also found in the reaction sintered of A/CA₆ composite (see section 4.2.6).

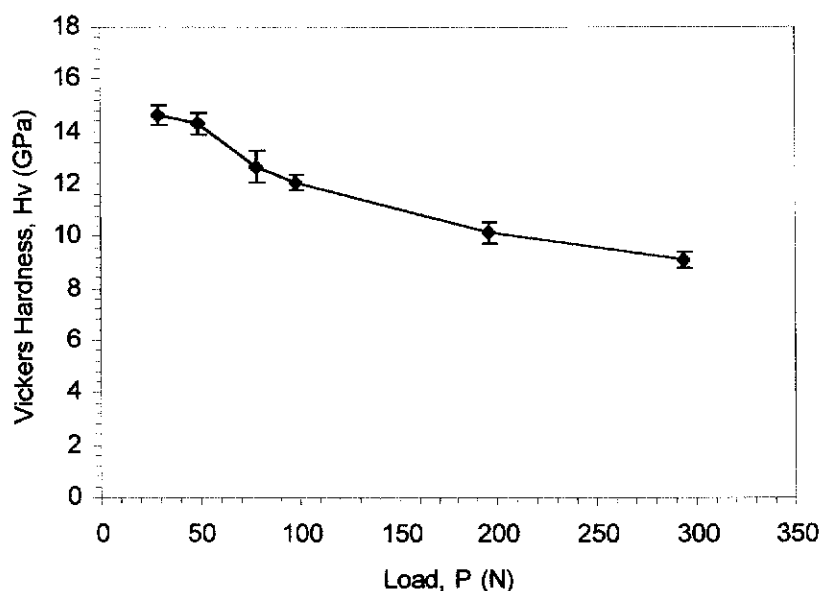


Figure 6.31. Variation of Vickers hardness as a function of applied load for the FGM at 0 – 5 mm distance. Error bars indicate two estimated standard deviations (2σ).

Fracture Toughness

Figure 6.32 shows the variation of fracture toughness as a function of distance for the FGM sample, i.e. from the infiltrated part (graded region – A/CA₆) to the non-infiltrated part (non-graded region – Al₂O₃) and the average fracture toughness for the alumina control sample. An applied load of 98 N was used in this experiment. The results show that fracture toughness decreased gradually with increasing distance in the graded region and leveled-out in the non-grade region. For example, at approximately 1 mm distance, the fracture toughness of material was 6 MPa.m^{1/2}, but decreased to 3.9 MPa.m^{1/2} at approximately 9.9 mm distance and leveled-out there after. This graded change in fracture toughness is not unexpected since the concentration of CA₆ platelets decreases with distance as confirmed by the XRDs result (see section 6.2.2). The average fracture toughness in the non-graded region of 3.9 MPa.m^{1/2} is slightly higher than that of 3.8 MPa.m^{1/2} found for the alumina control sample. The display of higher fracture toughness in the graded region can be attributed to the presence of the elongated CA₆ phase. This behavior is consistent with the reaction sintered A/CA₆ composites where the presence of 5 wt% CA₆ gave rise to 82 % improvement in fracture toughness when compared with pure alumina. It is believed that both the crack deflection and grain-bridging mechanisms were responsible for the improved fracture toughness as confirmed by the back-scattered SEM image in Figure 6.33.

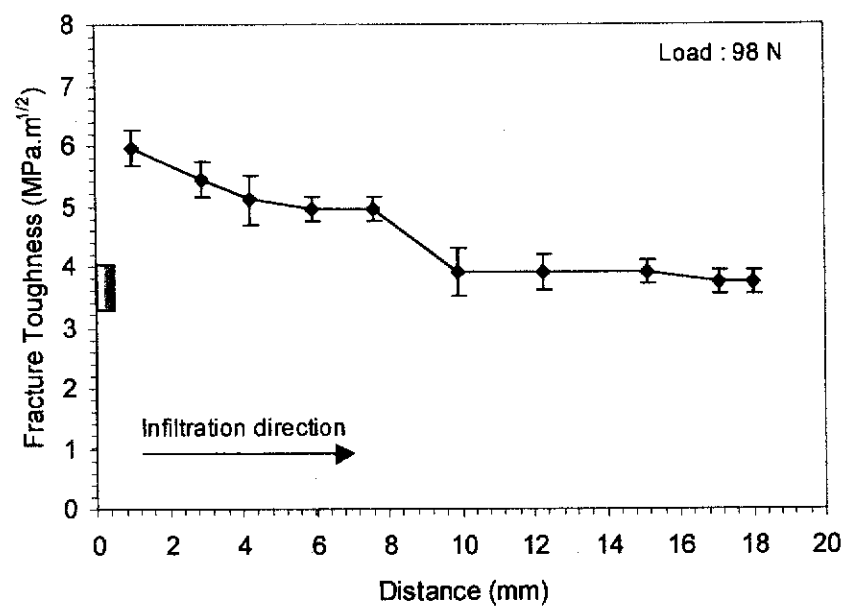


Figure 6.32. Variation of fracture toughness as a function of distance for the FGM sample at an applied load of 98 N. Shaded box at the left represents the average fracture toughness for the control sample. Error bars indicate two estimated standard deviations (2σ).

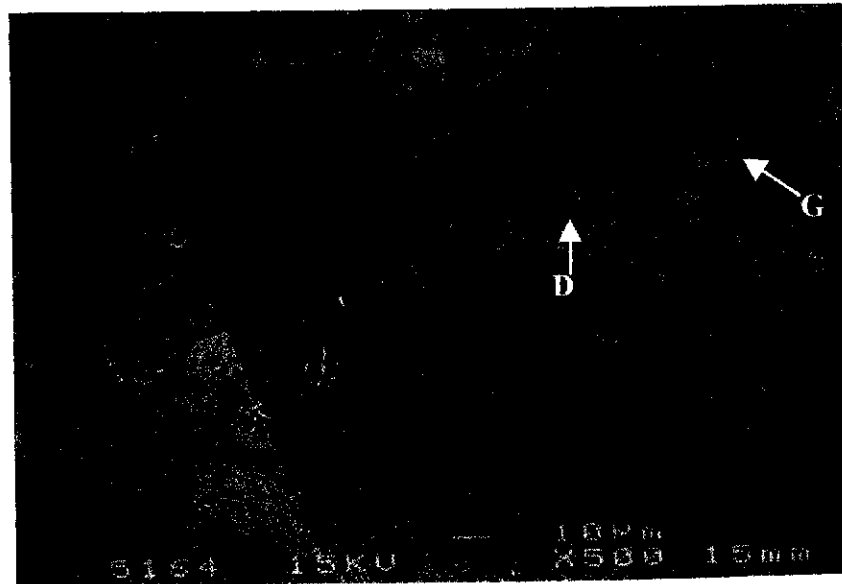


Figure 6.33. Back-scattered SEM micrographs of Vickers indentation for the functionally graded Al/CA₆ composites showing crack deflection (labelled as 'D') and grain-bridging (labelled as 'G').

6.3 Summary

A functionally-graded alumina/calcium-hexaluminate (A/CA₆) composite has been successfully synthesised through infiltration of porous alumina preform with a solution containing calcium acetate. The infiltration kinetics of liquids into porous alumina preform was investigated. The variables that control the infiltration process such as preform sintering temperature, liquid type, vacuum versus non-vacuum, and multiple infiltrations were studied. It was found that, the pre-sintering at 1100 and 1200 °C for 2h resulted in most suitable alumina preforms, were strong enough to withstand the subsequent processing steps. The influence of preform sintering temperature, liquid type and multiple infiltration on the rate of infiltration was observed to obey the Washburn model (i.e. Equation 2.7). In contrast, the effect of applied pressure (vacuum) was more consistent with the model proposed by Darcy (see Equation 2.8) where the external pressure enhances the infiltration rate.

The mass change in the sintered functionally graded A/CA₆ composite shows that an average amount of 8.7 wt% CA₆ formed within the bulk. Two processing methods were employed to obtain graded composition profiles in the composites, i.e. gradual polishing and slicing methods. The weight concentration (wt%) computed from the XRD data showed that the concentration of CA₆ in the FGM sample obtained by gradual polishing decreased from 46.1(0.9) wt% on the surface and reduced with depth to 33.0(0.7) wt% at 0.5 mm, then to 27.8(0.6) wt% at 0.8 mm. In contrast, the concentration of α -Al₂O₃ increased with depth from 53.9(0.8) wt% at the surface to 67.0(0.8) wt% at 0.5 mm, then to 72.2(0.8) wt% at 0.8 mm. The graded composition profiles obtained by the slicing method showed similar behaviour, i.e. the concentration of CA₆ reduced progressively from 25.7(0.7) wt% at layer 1 (0 – 2 mm) to 12.4(0.5) wt% at layer 4 (6 – 8 mm). Similarly the corresponding values for α -Al₂O₃ increased with depth from 74.3(0.5) wt% at layer 1 to 87.6(1.0) at layer 4. These graded concentrations were consistent with SRD results, i.e. the concentration of CA₆ decreased from 78.5(0.5) wt% at layer 1 to 90.0(0.3) wt% at layer 4, and the α -Al₂O₃ increased from 21.5(0.2) wt% at layer 1 to 10.0(0.1) wt % at layer 4. Slight differences arising from XRD and SRD data can be

attributed to the presence of an unknown phase found in SRD patterns. However, the two sets of results are in reasonable agreement. This result emphasizes that the infiltration process can be a useful technique to produce ceramic-ceramic functionally graded materials.

The development of calcium aluminates CA , CA_2 and CA_6 in the functionally-graded A/CA_6 composite studied with XRD, SRD and HTND data showed the formation of calcium aluminates is temperature-dependent. The XRD results showed that the CA phase formed at 1000 °C, the CA_2 phase at 1300 °C and CA_6 at 1400 °C. These results were consistent with the SRD and HTND results. It is believed that the formations of calcium aluminates in the functionally-graded A/CA_6 composite occurred via exothermic reactions between $\alpha\text{-Al}_2\text{O}_3$ and CaO at 1000 – 1400 °C according to the Equations 4.1, 4.2, 4.3 and 4.4.

The microstructural study by back-scattered SEM showed that graded microstructure was found in the material. The concentration of CA_6 is most abundant near the surface and decreases with increasing depth. This observation agrees well with the evidence obtained from the phase composition analysis.

The thermal expansion and densification behaviour for the functionally-graded A/CA_6 composite are significantly different from those of the alumina control sample. The presence of CA_6 phase appears to hinder the process of sintering and densification in alumina matrix, but the expansion or shrinkage effects do not exceed 6 – 7 %. The thermal expansion coefficient of the functionally-graded A/CA_6 composite was higher than pure Al_2O_3 .

Vickers hardness results showed that the functionally graded A/CA_6 composites exhibits a graded-region (A/CA_6) which is softer than the non-graded-region ($\alpha\text{-Al}_2\text{O}_3$). The hardness at approximately 1 mm distance is 10.6 GPa, then increased markedly to 17.2 GPa at 9.9 mm and leveled-out there after. The lower hardness in the graded region is believed to be due to the presence of a large amount of relatively soft CA_6 as confirmed by XRD and SRD results. Since, the amount of CA_6 gradually reduces with depth the hardness increases toward the non-graded-region. The load

dependence of Vickers hardness for the functionally-graded A/CA₆ composite is also evident from Figure 6.28, where the hardness decreases with increasing load.

It was found that, the fracture toughness decreased gradually with increasing distance in the graded region and leveled-out in the non-graded region. These results are expected, since the presence of the elongated CA₆ grains in the graded-region would serve to enhance fracture toughness. The fracture toughness at approximately 1 mm distance (graded region) achieved 6 MPa.m^{1/2} and decreased to 3.9 MPa.m^{1/2} at 9.9 mm (non-graded region) and leveled-out then after. It was also found that crack deflection and grain bridging were the major toughening processes in the graded region as confirmed by the SEM imaging in Figure 6.23.

CHAPTER 7

CONCLUSIONS AND FUTURE WORK

7.1 Conclusions

This research was conducted with the general aim of producing a novel A/CA₆ composite with both highly mechanical performance and microstructural control. Two processing routes were investigated, *in-situ* reaction sintering and infiltration. In relation to the specific objectives of the research, the following conclusions have been made:

7.1.1 Synthesis and Properties of *In-situ* Reaction Sintered Alumina/Calcium-Hexaluminate (A/CA₆) Composites.

The A/CA₆ composites in this experiment were synthesised by *in-situ* reaction sintering of alumina powder and (0, 5, 15, 30, 50 and 100 wt %) CA₆ precursors. The major findings and conclusions from the synthesis of *in-situ* reaction sintered alumina/calcium-hexaluminate (A/CA₆) composites can be summarised as follows:

- The phase compositions of the A/CA₆ composites were confirmed using quantitative XRD and ND Rietveld analysis. The results showed that the CA₆ content in the A/CA₆ composites increased in proportion with the amount of CA₆ precursor added.
- The phase developments of various calcium aluminates (i.e. CA, CA₂ and CA₆) in A/CA₆ composites at 1000 – 1600 °C have been systematically studied by XRD and HTND. The XRD study revealed that the CA and CA₂ phases start to develop at approximately 1000 and 1100 °C and transform to the CA₆ phase at 1400 °C. Whereas the dynamic HTND study showed that the corresponding

calcium aluminates phases commence to develop at 1000 and 1200 °C and then eventually transform to CA₆ at 1400 °C.

- The presence of the *plate-like* CA₆ grains in the composite has been observed by the back-scattered SEM imaging and confirmed by the Ca x-ray map, whereas the alumina matrix dominates in the Al-map. It was found that CA₆ hinders the grain growth of alumina in the A/CA composites.
- The A/CA₆ composites demonstrated pronounced mechanical properties over the alumina control sample and these include (a) much improved fracture toughness, as indicated by improvement of 82 % in toughness for the sample containing 5 wt% of CA₆, and (b) exhibited R-curve behaviour, as indicated by its load-dependent toughness. It is believed that the crack bridging mechanism was responsible for the increase in toughness.

7.1.2 Synthesis and Properties of β -spodumene Modified Alumina/Calcium-Hexaluminate (A/CA₆) Composites.

The A/CA₆ composites examined in this study were synthesised by *in-situ* reaction sintering of alumina/30 wt% CA₆ precursor with 0, 2.5, 10 and 15 wt% β -spodumene. The major findings and conclusions from the synthesis of β -spodumene modified alumina/calcium-hexaluminate (A/CA₆) composites are as follows:

- The phase relations of the β -spodumene modified alumina/calcium-hexaluminate (A/CA₆) composites were studied using quantitative XRD and ND Rietveld analysis which indicated the addition of > 2.5 wt% β -spodumene caused the reduction of CA₆ content and the formation of β -quartz solid solution
- The presence of CA₆ *platelets* in the composites was observed in the CAS0 and CAS2.5 samples but not in the CAS10 sample. The presence of β -spodumene caused the decomposition of CA₆ and the formation of large spherical pores within the microstructure.

- The addition of β -spodumene in the A/CA₆ composite has significant effects on the physical and mechanical properties. The reduction of porosity indicates that adding β -spodumene can be effective for improving densification of the composite. However improvements in hardness and fracture toughness were not achieved, which can be attributed due to the presence of large spherical pores as confirmed by SEM and the presence of β -spodumene and β -quartz solid solution as revealed by XRD and ND.

7.1.3 Synthesis and Properties of Functionally-Graded Alumina/Calcium-Hexaluminate (A/CA₆) Composites.

The functionally-graded A/CA₆ composite in this experiment was synthesised by infiltrating an alumina preform in a calcium-acetate solution. Subsequent heat-treatment led to decomposition of infiltrant, solid state reactions between alumina and calcium oxide (CaO) to form CA₆ and finally densification. The kinetics of liquid infiltration in porous alumina preform has also been investigated. The major findings and conclusions from the synthesis of functionally graded A/CA₆ composites can be summarised as follows:

- The infiltration kinetics was characterised by measuring the infiltration height with respect to time. It was found that the infiltration-rate equation proposed by Washburn was proven to be suitable for describing the effects of preform sintering temperature, viscosity and multiple infiltration on the infiltration behaviour. The influence of applied pressure was consistent with the model proposed by Darcy, where the applied pressure enhanced the infiltration rate behaviour. Key parameters in the processing route were also identified and these include (i) pre-sintering at 1100 °C and 1200 °C for 2 h for best alumina preforms, (ii) decomposition temperature of infiltrant at 450 °C, (iii) CA₆ formation at 1400 °C and (iv) sintering temperature of 1650 °C for 2 h for composite bodies to achieve a theoretical density of 97.5 %. The weight gain

after infiltration has been used to estimate the amount of CA_6 phase introduced into the alumina matrix.

- The graded composition character of the functionally-graded A/ CA_6 composite has been determined by x-ray diffraction (XRD) and synchrotron radiation diffraction (SRD). Graded compositions with XRD and SRD Rietveld refinement analysis showed that the concentration of CA_6 decreases with depth, whereas the $\alpha-Al_2O_3$ content increases with depth.
- The formation temperature of calcium aluminates CA , CA_2 and CA_6 in functionally graded A/ CA_6 composites at temperatures ranging 1000 – 1650 °C have been systematically analysed by XRD, SRD and HTND. Results showed that the formation of calcium aluminates is temperature-dependent. The XRD and SRD results showed that CA and CA_2 phases formed at 1000 °C and 1300 °C, respectively. They remained stable even at 1400 °C, but eventually transform to CA_6 at 1650 °C. These results were consistent with HTND data.
- A graded microstructural study using SEM revealed that the content of CA_6 platelets was most abundant near the surface and decreased with increasing depth. The presence of CA_6 in the composite fired at 1400 °C was confirmed by TEM in conjunction with the energy dispersive spectroscopy (EDS).
- The hardness results of FGM showed a softer material in the graded-region (A/ CA_6) but harder in non-graded region. The lower hardness in the graded region can be attributed due to the presence of the softer CA_6 phase. However, the fracture toughness in the graded region is higher than the non-graded region. The crack deflection and grain bridging mechanism were found to be responsible for the enhancement of fracture toughness.

7.2 Future Work

This thesis has dealt with an investigation of the structure-property relationships for reaction-sintered A/CA₆, β -spodumene modified A/CA₆ and functionally-graded A/CA₆ composites. Much information regarding the characters and properties of these materials has been elucidated from the study, but a number of issues could not be addressed due to equipment and time constraints. Therefore, the future work should be undertaken to fully elucidate the complex interplay between the composition, microstructure and mechanical properties in this system. This is essential before the full potential of these materials can be fully realized in the commercial applications. For future study, it recommended that the following aspects be considered:

1. The effects of grain size and aspect ratio of CA₆ platelets on the fracture toughness of alumina deserves an in-depth study. It is well-known that these platelets can impart self-toughening to the matrix material. However, it is still unknown what is the ideal grain size and aspect ratio of these platelets for imparting the optimum fracture toughness. For instance, are large CA₆ grains with a high aspect ratio the best? Thus, future research should focus on the heat-treatment A/CA₆ system at various temperatures and dwelling times to obtain CA₆ of various sizes and aspect-ratios.
2. Successful microstructural designs of ceramic composites are those that yield good mechanical properties from the ambient to service temperature. Therefore the complete measurement and evaluation of mechanical and fracture properties in the A/CA₆ system should be undertaken both at ambient and elevated temperatures.
3. The development of a hybrid system based on A/CA₆/AT warrants serious considerations. The presence of AT (10-30 wt%) is well-known to provide considerable improvements in the flaw-tolerance of alumina (Harmer et al. 1992; Low 1998; Skala 2000). Thus the addition of 10-30 wt% AT to the A/CA₆

system could provide further enhancement in the fracture properties. A similar approach has recently been attempted by Low and co-workers at Curtin University where both acicular AT and elongated mullite grains are dispersed within the alumina to provide toughening contributions from both phases.

REFERENCES

- Adánez, J., de Diego, L.F. and Gracia-Labiano, F. (1999). Calcination of Calcium Acetate and Calcium Magnesium Acetate: Effect of the Reacting Atmosphere. *Fuel*, **78**, p583-592.
- Aghajania, M.K. and Nagelberg, A. (1996). Method of Forming a Metal Matrix Composite Body by a Spontaneous Infiltration Technique. *Composites Part A: Applied Science and Manufacturing*, **27**(4), p341.
- An, L., Chan, H. M. and Soni, K. K. (1996). Control of Calcium Hexaluminate Grain Morphology in In-situ Toughened Ceramic Composites. *Journal of Materials Science*, **31**, p3223-3229.
- An, L. and Chan, H.M. (1996). R-curve Behaviour of In-situ Toughened $\text{Al}_2\text{O}_3/\text{CaAl}_2\text{O}_9$ Ceramic Composites. *Journal of the American Ceramic Society*, **79**(12), p3142-3148.
- An, L., Chan, H.H. and Chan, H.M. (1998). High-strength Alumina/Alumina Calcium Hexaluminate Layer Composites. *Journal of the American Ceramic Society*, **81**, p3321-3324.
- Asmi, D., Low, I.M. and Sitepu, H. (1997). Characteristic of Layered and Graded Alumina-Calcium Hexaluminate Composites. *Proc. of AXAA WASEM Conference*, 20-21 September 1997, Elcavallo Resort, Perth, Australia, p45-46.
- Asmi, D. and Low, I.M. (1998). Processing of In-situ Layered and Graded Alumina/Calcium-Hexaluminate Composite: I, Physical Characteristics. *Journal of the European Ceramic Society*, **18**, p2019-2024.

Asmi, D., Low, I.M., Kennedy, S. and Day, R.A. (1999). Characteristics of a Layered and Graded Alumina/Calcium Hexaluminate Composites. *Journal of Materials Science Letters*, **40**, p96-102.

Asthana, R., Rohatgi, P.K. and Tewari, S.N. (1992). Infiltration Processing of Metal-Matrix Composites: A Review. *Processing of Advanced Materials*, **2**, p1-17.

Australian Standard 1774.5. (1989). Refractories and Refractory Materials-Physical Test Methods. *Method 5: The Determination of Density, porosity and water Absorption* p1-4. Standards Australia, Sydney.

Babini, G. N. Bellosi, A. and Galassi, C. (1987). Characterisation of Hot-pressed Silicon Nitride Based Materials by Microhardness Measurements. *Journal of Materials Science*, **22**, p1687-1693.

Bacon, G.E. (1962). *Neutron Diffraction*, 2nd edition, Oxford, Great Britain.

Bateman, C.A. Bennison, S.J. and Harmer, M.P. (1989). Mechanism for the Role of Magnesia in the Sintering of Alumina Containing Small Amounts of a liquid Phase. *Journal of the American Ceramic Society*, **72**(7), p1241-1244.

Bayuseno, A. P., Latella, B.A. and O'Connor, B. H. (1999). Resistance of Alumina-Spodumene Ceramics to Thermal Shock. *Journal of the American Ceramic Society*, **82** (4), 819-824.

Becher, P.F. (1991). Microstructural Design of Toughened Ceramics. *Journal of the American Ceramic Society*, **74**(2), p255-269.

- Bennison, S.J. and Harmer, M.P. (1983). Effect of MgO Solute on the Kinetics of Grain Growth in Al_2O_3 . *Journal of the American Ceramic Society*. **66(5)**, pC90-C92.
- Bennison, S.J. and Lawn, B.R. (1989). Flaw Tolerance in Ceramics with Rising Crack-Resistance Characteristic. *Journal of Materials Science*, **24**, p3169.
- Birchall, J.D., Howard, A.J. and Kendall, K. (1981). Flexural Strength and Porosity of Cements. *Nature* (London), **289**, p388-389.
- Boch, P., Chartier, T. and Giry, J.P. (1990). Zirconia-Toughened Mullite: the Role of Zircon Dissociation. *Ceramic Transactions*, **6** (Mullite, Mullite Matrix Composites), p 473-494.
- Brooksbank, D. (1970). Thermal Expansion of Calcium-aluminate Inclusions and Relation to Tessellated Stresses. *Journal of the Iron and Steel Institute*. p495-499.
- Bückle (1965). *Mikrohartefrung*. Berliner Union, Verlag, Stuttgart.
- Carman, P.C. (1956). *Flow of Gaseous through Porous Media*. Butterworths Scientific Publications, London.
- Chantikul, P. Bennison, S.J. and Lawn, B.R. (1990). Role of Grain Size in the Strength and R-curve Properties of Alumina. *Journal of the American Ceramic Society*, **73**, p 2419.
- Cardinal, S., R'Mili, M. and Merle, P. (1998). Improvement of High Pressure Infiltration Behaviour of Alumina Platelet Preforms: Manufacture and Characterization of Hybrid Preforms. *Composites Part A: Applied Science and Manufacturing*, **29(11)**, p1433-1444.
- Carter J. (1995). *The Development of Reaction-Sintered Alumina-Matrix Ceramics*. PhD Thesis. Curtin Technology of University.

- Chatterjee, A.K. and Zhmoidin, G.I. (1972). The Phase Equilibrium Diagram of the System $\text{CaO-Al}_2\text{O}_3\text{-CaF}_2$. *Journal of Materials Science*, **7**, p93-97.
- Chen, P.L. and Chen, I.W. (1992). In-situ Alumina/Aluminate Platelet Composites. *Journal of the American Ceramic Society*, **75**(9), p2610-2612.
- Chevalier, J. Olagnon, C. Fantozzi, G. and Gros, H. (1997). Creep Behaviour of Alumina, Zirconia-Toughened Alumina. *Journal of the European Ceramic Society*, **17**, p859-864.
- Chung, W.S. and Lin, S.J. (1996). Ni-coated SiC Reinforced Aluminium Composites Processed by Vacuum Infiltration. *Materials Research Bulletin*, **31**, p1437-1447.
- Chung, W.S., Chang, S.Y and Lin, S.J. (1999). Low Volume Fraction $\text{SiC}_p/\text{AA 380.0}$ Composites Fabricated by Vacuum Infiltration. *Journal of Materials Research*, **14**(3), p803-810.
- Cinibulk, M.K.(1994). Magnetoplumbite Compounds as a Fiber Coating in Oxide/Oxide Composites. *Ceramic Engineering and Science Proceedings*, **15**, p721-729.
- Cinibulk, M.K. (1995). Microstructure and Mechanical Behaviour of an Hibonite Interphase in Alumina-based Composites. *Ceramic Engineering and Science Proceedings*, **16**, p633-641.
- Cinibulk, M. K. and Hay, R. S. (1996). Textured Magnetoplumbite Fibre-Matrix Interphase Derived from Sol-gel Fiber Coatings. *Journal of the American Ceramic Society*, **79**, p1233-1246.
- Clarke, P.T. and Spink, J.M. (1969). The Crystal Structure of β -Spodumene, $\text{LiAlSi}_2\text{O}_6$ -II. *Zeitschrift fuer Kristallographie*, **130**, p420-426.

Claussen, N. and Jahn, J. (1980). Mechanical Properties of Sintered, In-situ-reacted Mullite-zirconia Composites. *Journal of the American Ceramic Society*, **63**(2-3), p228-229.

Cook, R.B. (1997). Spodumene. *Rocks and Minerals*, p340-344.

Cowan, C.A., Bole, G. A. and Stone, R. L. (1950). Spodumene as a Flux Component in Sanitary Chinaware Bodies. *Journal of the American Ceramic Society*, **33**(6), p193-197.

Coy, K.L. (1994). Functionally Graded Materials, In *The Encyclopedia of Advanced Materials* (ed. Bloor, D., Brook, R.J., Flemings, M.C., Mahajan, S. and Chan, R.W.). Elsevier Science, Oxford, England.

Criado, E. Caballero, A. and Pena, P. (1987). Microstructural and Mechanical Properties of Alumina-calcium Hexaluminate Composites. In *High Technology Ceramics*, ed. P. Vicenzini. Elsevier Science, Amsterdam, p2279-2289.

Criado, E. Pena, P. and Caballero, A. (1988). Influence of Processing Method on Microstructural and Mechanical Properties of Calcium Hexaluminate Compacts. *Science of Ceramic*, p193-198.

Criado, E. and De Aza, S. (1991). Calcium Hexaluminate as Refractory Material. In *Unified International Technical Conference on Refractories Proceedings*, Aachen, Stahl, Eisen, Germany, p566-574.

Culter, R.A., Mayhew, R.J., Prettyman, K.M. and Virkar, A.V. (1991). High Toughness Ce-TZP/ Al_2O_3 Ceramics with Improved Hardness and Strength. *Journal of the American Ceramic Society*, **71**(1), p179-186.

- De Jonghe, L. C., Schmid, H. and Chang, M. (1984). Inter-reaction between Al_2O_3 and $\text{CaO-Al}_2\text{O}_3$ Melt. *Journal of the American Ceramic Society*, **67**(1), p27-30.
- Dougill, M.W. (1957). Crystal Structure of Calcium Monoaluminate. *Nature* (London), **180**, p292-293.
- Dörre, E. and Hübner, H. (1984). *Alumina: Processing, Properties, and Applications*. Springer-Verlag, Berlin, Heidelberg.
- Dollase, W.A. (1986). Correction of intensities for preferred orientation in powder diffractometry: application of the March Model. *Journal of Applied Crystallography*, **19**, p267-272.
- Dullien, F.A., El-Sayed, M.S. and Batra, V.K. (1977). Rate of Capillary Rise in Porous Media with Non-uniform Porous. *Journal of Colloids and Interface Science*, **60**, p497-506.
- Einset, E.O. (1996). Capillary Infiltration Rate into Porous Media with Application of Silicon Composite Processing. *Journal of the American Ceramic Society*, **79**(2), p333-338.
- Eriksson, G. and Pelton, A.D. (1993). Critical Evaluation and Optimization of the Thermodynamic Properties and Phase Diagrams of the $\text{CaO-Al}_2\text{O}_3$, $\text{Al}_2\text{O}_3\text{-SiO}_2$ and $\text{CaO-Al}_2\text{O}_3\text{-SiO}_2$ Systems. *Metallurgical Transactions B*, **24B**, p807-816.
- Evans, A.G. and Charles, E.A. (1980). Fracture Toughness Determinations by Indentations. *Journal of the American Ceramic Society*. **59**(7-8), p371-372.
- Evans, A.G. (1990) Perspective on the Development of High-Toughness Ceramics. *Journal of the American Ceramic Society*. **73**(2), p187-206.

Faber, K.T. Iwagoshi, T. and Ghosh, A. (1988). Toughening by Stress-Induced Microcracking in Two-Phase Ceramics. *Journal of the American Ceramic Society*, **71**(9), pC399-C401.

Filonenko, N.E. and Lavrov, I.V. (1949). Calcium Hexaluminate in the System CaO-Al₂O₃-SiO₂. *Dokl. Akad. Nauk SSSR*. **66**, p673-676.

Fishwick, J. H. (1974). *Application of Lithium in Ceramics*. Cahners, Boston. M.A.

Floyd, J.R. (1964). *Journal of the American Ceramic Society*, **47**, p539.

Frohlich, F., Grau, P., Wrellmann, W. (1977). Performance and Analysis of Recording Microhardness Tests. *Physica Status Solidi*, **42**, p79-89.

Galusek, D. and Majling, J. (1995). Preparation of Al₂O₃-ZrO₂ Ceramics by Infiltration Processing. *Ceramics International*, **21**, p101-107.

Garret, R.F., Cookson, D.J., Foran, G.J., Sabine, T.M., Kennedy, B.J. and Wilkins, S.W. (1995). Powder Diffraction Using Imaging Plates at the Australian National Beamline Facility at the Photon Factory. *Review of Scientific Instruments*, **66**(2), p1351-1353.

Geiger, G.H. and Poirier, D.R. (1980). *Transport Phenomena in Metallurgy*. Addison Wesley, New York.

Glass, S.J. and Green, D.J. (1987). Surface Modification of Ceramics by Partial Infiltration, *Advanced Ceramic Materials*, **2**(2), p129-131.

Gong, J., Wu, J. and Guan, Z. (1998). Load Dependence of the Apparent Hardness of Silicon Nitride in a Wide Range of Loads. *Materials Letters*, **35**, p58-61.

Gong, J. Wu, J. and Guan, Z. (1999a), Examination of the Indentation Size Effect in Low-load Vickers Hardness Testing of Ceramics, *Journal of the European Ceramic Society*, **19**, p2625 – 2631.

Gong, J. Wu, J. and Guan, Z. (1999b). Analysis of the Indentation Size Effect on the Apparent Hardness for Ceramics. *Materials Letters*, **38**, p197-201.

Gong, J., Zhao, Z., Guan, Z. and Miao, H. (2000). Load-dependence of Knoop Hardness of Al_2O_3 -TiC Composites. *Journal of the European Ceramic Society*. **20**, p1895-1900.

Gulgun, M.A., Popoola, O.O. and Kriven, W.A. (1994). Chemical Synthesis and Characterization of Calcium Aluminate Powders. *Journal of the American Ceramic Society*. **77(2)**, p531-539.

Haldsted, B. (1990). Assessment of the $\text{CaO-Al}_2\text{O}_3$ system. *Journal of the American Ceramic Society*, **73(1)**, p15-23.

Hill, R.J. and Howard, C.J. (1987). Quantitative Phase Analysis from Neutron Powder Diffraction Data using the Rietveld Method. *Journal of Applied Crystallography*, **20**, p467-474.

Hill, R.J., Howard, C.J. and Hunter, B.A. (1995). Computer Program for Rietveld Analysis of Fixed Wavelength X-ray and Neutron Powder Diffraction Patterns, Australian Atomic Energy Commission (now ANSTO). Rept. No. M112, Lucas Heights Research Laboratories, New South Wales, Australia.

Hirai, T. (1996). Functional Gradient Materials. In *Material Science and Technology: A Comprehensive Treatment* (Edited by Chan, R.W., Haasen, P. and

Kramer, E.J., Processing of Ceramics: Part II (Ed. Brook, R.J), Volume 17B, p293-341, VCH Verlagsgesellschaft mbH, Weinheim.

Hirosaki, N., Akimune, Y. and Mitomo, M. (1993). Effect of Grain Growth of β -Silicon Nitride on Strength, Weibull Modulus, and Fracture Toughness. *Journal of the American Ceramic Society*, **74**(7), p1892-1894.

Hofmann, M.J. (1994). *In-Situ* Development of Ceramic Composites. In *The Encyclopedia of Advanced Materials* (ed. Bloor, D., Brook, R.J., Flemings, M.C., Mahajan, S. and Chan, R.W.) Elsevier Science, Oxford, England.

Imlach, J.A. and Glasser, F.P. (1968). Phase Equilibria in the System $\text{CaO-Al}_2\text{O}_3\text{-TiO}_2$. *Transactions of the British Ceramic Society*, **67**, p581-609.

Iyi, N., Takekawa, S. and Kimura, S. (1989). Crystal Chemistry of Hexaluminates: β - Al_2O_3 and Magnetoplumbite Structure. *Journal Solid State Chemistry*, **83**(1), p8-19.

Jang, B.K. and Kishi, T. (1988). Fabrication and Microstructure of Al_2O_3 Matrix Composites by In-situ Reaction in the $\text{Al}_2\text{O}_3\text{-La}_2\text{O}_3$ System. *Journal of the Ceramic Society of Japan*, **106**(8), p739-743.

Kato, K. and Saalfeld, H. (1968). Verfeinerung der Kristallstruktur von $\text{CaO} \cdot 6\text{Al}_2\text{O}_3$. *Neues Jahrbuch fuer Mineralogie*, **109**, p192-200.

Kawasaki, A. and Watanabe, R. (1997). Concept and P/M Fabrication of Functionally Gradient Materials. *Ceramics International*, p73-83.

Kawase, M., Tago, T., Kurosawa, M., Utsumi, H. and Hashimoto, K. (1999). Chemical Vapor Infiltration and Deposition to Produce a Silicon Carbide-Carbon Functionally Gradient Material. *Chemical Engineering Science*, **54**(15-16), p3327-3334.

- Kisi, E.H. (1994). Rietveld Analysis of Powder Diffraction Patterns. *Materials Forum*, **18**, p135-153.
- Kobayashi, H., Ishibashi, N., Akiba, T. and Mitamura, T. (1990). Preparation and Thermal Expansion of Mullite-Beta-Spodumene Composite. *Journal of the Ceramic Society of Japan*, **98(9)**, p1023-1028.
- Koizumi, M. (1992). The Concept of FGM. In *Second International Symposium on Functionally Gradient Materials* (ed. Holt, J.B., Koizumi, M., Hirai, T. and Munir, Z.A.) p3-10. The American Ceramic Society, Westerville, Ohio, San Fransisco, CA.
- Koizumi, M. and Niino, M. (1995). Overview of FGM Research in Japan. *Materials Research Society Bulletin*, p19-21.
- Koizumi, M. (1997). FGM Activities in Japan. *Composites Part B*, **28B**, p1-4.
- Kopanda, J. E. and Maczura, G. (1990). Production Processes, Properties, and Applications for Calcium Aluminate Cements. In *Alumina Chemical Science and Technology Hanbook*, ed. Hart, L. D. American Ceramic Society , Westerville. OH. p171-184.
- Kraus, W. and Nolze, G. (1999). *Powder Cell for Windows Version 2.3*. Federal Institute for Materials Research Testing, Berlin, Germany.
- Kubo, E., Mizuwatari, Y. and Nakagawa, D. (1972). *Powders*. Maruzen, p161.
- Kusnik, J. and Terry, K. W. (1988). Physical Properties of Spodumene-Kaolin Mixtures in the Firing Range 1270 – 1300 °C. *Materials Science Forum*, **34-36**, p931-935.
- Lagerqvist, K. Wallmark, S. and Westgren, A. (1937). X-Ray Study of the Systems CaO-Al₂O₃ and SrO-Al₂O₃. *Z. Anorg. Allg. Chem*, **234**, p1-16.

- Lange, F.F. (1989). Powder Processing Science and Technology for Increased Reliability. *Journal of the American Ceramic Society*, **72**(1), p3-15.
- Lange, F.F., Tu, W.C. and Evans, A.G. (1995). Processing of Damage-tolerant, Oxidation-resistant Ceramic Matrix Composites by a Precursor Infiltration and Pyrolysis Method. *Materials Science and Engineering*, **A195**, p145-150.
- Latella, B. A. Burton, G. R. and O'Connor, B. H. (1995). Use of Spodumene in the Processing of Alumina-Matrix Ceramics: Influence on Microstructure and Mechanical Properties. *Journal of the American Ceramic Society*, **78**(7), p1895-1899.
- Lawn, B.R., Padture, N.P., Braun, L.M. and Bennison, S.J. (1993). Model for Toughness Curves in Two-Phase Ceramics: I, Basic Fracture Mechanics. *Journal of the American Ceramic Society*, **76**, p2335-2340.
- Lee, W.E. and Rainforth, W.M. (1994). *Ceramic Microstructures: Property Control by Processing*, Chapman and Hall, London, UK.
- Lee, S.K., Kim, Y.C. and Kim, C.H. (1994). Microstructural Development and Mechanical Properties of Pressureless Sintered SiC with Platelike Grains using Al₂O₃-Y₂O₃ Additives. *Journal of Materials Science*, **29**, p5321-5326.
- Li, H. and Bradt, R.C. (1991). Knoop Microhardness Anisotropy of Single Crystal Cassiterite (SnO₂). *Journal of the American Ceramic Society*, **74**, p1053-1060.
- Li, H. and Bradt, R.C. (1993), The Microhardness Indentation Load/Size Effect in Rutile and Cassiterite Single Crystals, *Journal of Materials Science*, **28**, p917-926.

- Li, C.T. (1971). Transformation Mechanism between High-Quartz and Keatite Phases of $\text{LiAlSi}_2\text{O}_6$ Composition, *Acta Crystallographica*, **B27**, p1132-1140.
- Li, C.W. and Yamanis, J. (1989). Super-Tough Silicon Nitride with R-curve Behaviour. *Ceramic Engineering and Science Proceedings*, **10(7-8)**, p632-645.
- Liu, J. and Ownby, P.D. (1991). Enhanced Mechanical Properties of Alumina by Dispersed Titanium Diboride Particulate Inclusions. *Journal of the American Ceramic Society*, **74(1)**, p241-243.
- Liu, H.K. (1996). Investigation on the Pressure Infiltration of Sol-gel Processed Textile Ceramic Matrix Composites. *Journal of Materials Science*, **31**, p5093-5099.
- Lutz, H.E., Laussen, N. and Swan, M.V. (1991). K^R -curve Behaviour of Duplex Ceramics. *Journal of the American Ceramic Society*, **74(1)**, p11-18.
- Low, I. M., Skala, R., Richards, R. and Perera, D. S. (1993). Synthesis and Properties of Novel Mullite-Zirconia-Toughened Alumina Composites. *Journal of Materials Science Letters*, **12**, p1585-1587.
- Low, I. M., Skala, R. and Li, D. Y. (1993). Assessment of Residual Strains in Mullite/ZTA Composites using XRD. *Journal of Materials Science Letters*, **13**, p1354-1356.
- Low, I. M., Skala, R. and Perera, D.S. (1994). Fracture Properties of Layered Mullite/ZTA Composites. *Journal of Materials Science Letters*, **13**, p1334-1336.
- Low, I.M. Skala, R.D. and Zhou, D. (1995). Synthesis of Functionally-gradient Aluminium Titanate/Alumina Composites. *Journal of Materials Science Letters*, **15**, p345-347.

- Low, I. M., Skala, R. and Zhou, D. (1996). Synthesis and Properties of Gel-derived Functionally Graded Ceramics. *Key note Paper at The International Workshop on Sol-Gel Processing of Advanced Ceramics*, Oxford and IBH Publisher, New Delhi, ed. Guanam, F. D., p143-158.
- Low, I. M., Garrod, T.D., Zhou, D., Phillips, D.N. and Pillai, Z. (1997). Processing of Spodumene Modified Mullite Ceramics. *Journal of Materials Science*, **32**, p3807-3812.
- Low, I.M., Suherman, P.M. and Phillips, D.N. (1997). Synthesis and Properties of Spodumene Modified Mullite Ceramics formed by Sol-Gel Processing. *Journal of Materials Science Letters*, **16**, p982.
- Low, I.M. (1998). Processing of an In-situ Layered and Graded Aluminium Titanate/Alumina Composites. *Materials Research Bulletin*. **33**, p1475.
- Marple, B.R. and Green, D.J. (1990). Mullite/Alumina Particulate Composites by Infiltration Processing: II, Infiltration and Characterization. *Journal of the American Ceramic Society*, **73(12)**, p3611-3616.
- Marple, B.R. and Green, D. J. (1991). Mullite/Alumina Particulate Composites by Infiltration Processing: III, Mechanical Properties. *Journal of the American Ceramic Society*, **74(10)**, p2453-2459.
- Marple, B.R. and Green, D. J. (1993). Graded Composition and Microstructures by Infiltration Processing. *Journal of Materials Science*, **28**, p4637-4643.
- Maschio, S. and Pezzotti, G. (1999). Microstruktural Development and Mechanical Properties of Alumina Hexaluminate composites As-sintered and after Aging in Aqueous and Physiological Solituion. *Journal of the Ceramic Society of Japan*, **107(3)**, p270-274.

- Maslen, E. N. Streltsov, V. A. Streltsova, N. R. Ishizawa, N. Satow, Y. (1993). Synchrotron X-ray Study of the Electron Density in α -Al₂O₃. *Acta Crystallographica*. **49B**, p973-980.
- Mendoza, J. L., Freese, A. and Moore, R. E. (1988). Thermomechanical Behaviour of Calcium Aluminate Composites. *Advanced Refractory Technology Ceramic Transactions*, **4**, p294-311.
- Milman, Yu.V., Galanov, B.A. and Chugunova, S.I. (1993), Plasticity Characteristic Obtained through Hardness Measurement. *Acta Metalurgica et Materialia*. **41(9)** Overview 107, p2523-2531.
- Milman, Yu.V., Chugunova, S.I., Goncharova, I.V., Chudoba, T., Lojkowski, W. and Gooch, W. (1999). Temperature Dependence of Hardness in Silicon-Carbide Ceramics with Different Porosity. *International Journal of Refractory Metal and Hard Materials*, **17**, p361-368.
- Misra, C. (1986). *Industrial Alumina Chemicals*. American Chemical Society Monograph. p184.
- Munro, R.G. (1997). Evaluated Material Properties for a Sintered α -alumina. *Journal of the American Ceramic Society*, **80(8)**, p1919-1928.
- Nordmann, A., Cheng, Y.B., Bastov, T.J. and Hill, A.J. (1995). Structural Characterization of Lithium Aluminosilicate Glass and Glass Ceramics Derived from Spodumene Mineral. *Journal of Physics Condensed Matter*, **7**, p3115-3128.
- Nordmann, A. and Cheng, Y.B. (1997). Formation and Stability of β -Quartz Solid-Solution Phase in the Li-Si-Al-O-N System. *Journal of the American Ceramic Society*, **80(12)**, p3045-3053.

- Nurse, R.W. Welch, J.H. and Majumdar, A.J. (1965). The CaO-Al₂O₃ System in a Moisture-Free Atmosphere. *Transactions of the British Ceramic Society*, **64**, p409-418.
- Obuchi, T. and Watanabe, T. (1970). On the Factors of Infiltration. *Journal of the Japan Society Powder and Powder Metallurgical*, **16**, p351-355.
- Ofori, J. Y. and Sotirchos, S.V. (1997). Multidimensional Modeling of Chemical Vapour Infiltration. *Industry and Engineering Chemistry Research*, **36**, p357-367.
- Orlova, V.T., Frolov, A.A. and Evstaffeva, O.N. (1993). Interaction in the system Mg(CH₃COO)₂-Ca(CH₃COO)₂-H₂O. *Russian Journal of Inorganic Chemistry*, **38(12)**, p1914-1917.
- Padture, N. and Chan, H.M. (1992). Improved Flaw Tolerance in Alumina-1 vol % Anorthite via Crystallization of the Intergranular Glass. *Journal of the American Ceramic Society*, **75(7)**, p1870-1875.
- Padture, N.P., Bennison, S.J. and Chan, H.M. (1993). Flaw Tolerance and Crack Resistance Properties of Alumina-Aluminium Titanate Composites with Tailored Microstructures. *Journal of the American Ceramic Society*, **76**, p2312-2320.
- Padture, N.P., Runyan, J.L., Bennison, S.J., Braun, L.M. and Lawn, B.R. (1993). Model for Toughness Curves in Two-Phase Ceramics: II, Microstructural Variables. *Journal of the American Ceramic Society*, **76**, p2341-2347.
- Padture, N.P. (1994). In-situ Toughened Silicon Carbide. *Journal of the American Ceramic Society*, **77(2)**, p519-523.

Padtare, N.P. and Lawn, B.R. (1994). Toughness Properties of a Silicon Carbide with an In-situ Induced Heterogeneous Grain Structure. *Journal of the American Ceramic Society*, **77**(10), p2518-2522.

Parker, K.M. and Sharp, J.H. (1982). Refractory Calcium Aluminate Cements. *Journal British Ceramic Society*, **8**(2), p35-42.

Pezzotti, G. (1993). Si₃N₄/SiC-Plated Composite without Sintering Aids: A Candidate for Gas Turbine Engines. *Journal of the American Ceramic Society*, **76**(5), p1313-1320.

Pezzotti, G., Okamoto, Y., Nishida, T. and Sakai, M. (1996). On the Near-Tip Toughening by Crack-Face Bridging in Particulate and Platelet-Reinforced Ceramics. *Acta Metallurgica et Materialia*, **44**(3), p899-914.

Ponomarev, V.I., Kheiker, D.M. and Belov, N.V. (1970). Crystal Structure of Calcium Dialuminate -CA₂. *Kristallografiya*, **15**, p1140-1143.

Pratapa, S. and Low, I. M. (1996). Synthesis and Properties of Functionally Graded AT/ZTA Composites. *Journal of Materials Science Letters*, **15**, p800-802.

Pratapa, S., O'Connor, B.H. and Low, I.M. (1997). Phase Composition Profile Character of a Functionally Graded AT/ZTA Composites, *Proc. 4th Int. Symp. on Functionally Graded Materials*; AIST Tsukuba Research Centre, Tsukuba, Japan, October 21-24, 1996. Edited by Shiota, I. and Miyamoto, Y., Elsevier, Tokyo, p367-372.

Pratapa, S. (1997). *Synthesis and Character of a Functionally-Graded Aluminium Titanate/Zirconia-Alumina Composite*. MSc Thesis, Curtin University of Technology, Perth, Australia.

- Pratapa, S. and Low, I.M. (1998). Infiltration-processed Functionally-graded AT/alumina-zirconia Composites: II, Mechanical Properties. *Journal Material Science*, **33**, p3047-3053.
- Prince, E. (1993). *Mathematical aspects of Rietveld refinements*, in Young, R.A. (ed) The Reitveld Method, Oxford University Press, Great Britain, p43-54.
- Quinn, J. B. and Quinn, G. D. (1997). Indentation Brittleness of Ceramics: A Fresh Approach. *Journal of Materials Science*. **32**, p4431-4346.
- Rahaman, M.N. (1995). *Ceramic Processing and Sintering*. Marcel Dekker, Inc. New York. USA.
- Rankin, G.A. and Wright, F.E. (1915). The Ternary System $\text{CaO-Al}_2\text{O}_3\text{-SiO}_2$. *American Journal of Science*, **39**, p1-79.
- Ricciello, S. and Marshall, M.K. (1994). 3-D Ceramic Matrix Composite Development. *Journal Advanced Material*, **25**, p22-28.
- Richerson, D.W. (1992). *Modern Ceramic Engineering: Properties, Processing and Use in Design*. M. Dekker, New York.
- Rietveld, H.M. (1967). Line profiles of neutron powder-diffraction peaks for structure refinement. *Acta Crystallographica*, **22**, p151-152.
- Rietveld, H.M. (1969). A profile refinement method for nuclear and magnetic structures. *Journal of Applied Crystallography*, **2**, p65-71.

- Sabine, T.M., Kennedy, B.J., Garret, R.F., Foran, G.J. and Cookson, D.J. (1995). The Performance of the Australian Powder Diffractometer at the Photon Factory, Japan, *Journal of Applied Crystallography*, **28**, p513-517.
- Sangwal, K. (2000). On the Reverse Indentation Size Effect and Microhardness Measurement of Solids. *Materials Chemistry and Physics*, **63**, p145-152.
- Sasaki, M. and Hirai, T. (1991). Fabrication and Properties of Functionally Gradient Materials. *Nippon Seramikkusu Kyokai Gakujutsu Ronbunshi (Journal of the Ceramic Society of Japan)*, **99(10)**, p1002-1013.
- Scheidegger, A.E. (1974). *The Physics of Flow through Porous Media*. 3rd ed. University of Toronto Press. Toronto. Canada.
- Scheildler, H. and Rodek, E. (1989). $\text{Li}_2\text{Al}_2\text{O}_3\cdot 4\text{SiO}_2$ Glass Ceramics. *American Ceramic Society Bulletin*, **68(11)**, p1926-1930.
- Schmid, C., Lucchini, E., Sbaizero, O. and Maschio, S. (1999). The Synthesis of Calcium or Strontium Hexaluminate Added ZTA Composite Ceramics. *Journal of the European Ceramic Society*, **19**, p1741-1746.
- Semlak, R.A. and Rhines, F.N. (1958). The rate of Infiltration of Metals. *Transaction of the Metallurgical Society of AIME*, **212(6)**, p325-331.
- Shaw, N.J. and Brook, R.J.(1986). Structure and Grain Coarsening during the Sintering of Alumina. *Journal of the American Ceramic Society*, **69(2)**, p107-110.
- Shepherd, E.S. Rankin, G.A. and Wright, F.E. (1909). The Binary Systems of Alumina with Silica, Lime and Magnesia. *American Journal Science*, **28**, p293-333.

- Shyu, J. J. and Lee, H. H. (1995). Sintering, Crystallization, and Properties of B_2O_3/P_2O_5 -Doped $Li_2Al_2O_3.4SiO_2$ Glass Ceramics. *Journal of the American Ceramic Society*, **78**(8), p2161-2167.
- Skala, R.D. (2000). Development of a Functionally-Graded Alumina/ Aluminium-Titanate Composite. *Ph.D Thesis*, Curtin University of Technology.
- Stujits, A.L. (1977). In *Ceramic Microstructures '76*. Ed. Fulrath, R. M. Pask, J. A. Boulder, CO, Westwood Press.
- Tani, E., Umebayashi, S., Kishi, K., Kobayashi, K. and Nishijima. (1986). Gas-Pressure Sintering of Si_3N_4 with Concurrent Addition of Al_2O_3 and 5 wt% Rare-Earth Oxide High Fracture Toughness Si_3N_4 with Fiberlike Structure. *American Ceramic Society Bulletin*, **65**(9), p1311.
- Tas, A.C. (1998). Chemical Preparation of the Binary Compounds in the Calcia-Alumina System by Self-Propagating Combustion Synthesis. *Journal of the American Ceramic Society*, **81**(11), p2853-2863.
- Taya, M., Hayashi, S., Kobayashi, A.S. and Yoon, H.S. (1990). Toughening of Particulate-Reinforced Ceramic-Matrix Composite by Thermal Residual Stress. *Journal of the American Ceramic Society*, **73**(5), p1382-1391.
- Trumble, K.P. (1998). Spontaneous Infiltration of Non-Cylindrical Porosity: Close-Packed Spheres. *Acta Materialia*, **46**(7), p2363-2367.
- Utsunomiya, A., Tanaka, K., Morikawa, H., Marumo, F. and Kojima, H. (1988). Structure refinement of $CaO.6Al_2O_3$. *Journal of Solid State Chemistry*, **75**, p197-200.
- Von Misses, R. and Fredricks, K.O. (1971). *Fluid Dynamics*. Springer-Verlag, New York.

Wallace, J.S. Petzow, G. and Claussen, N. (1984). Microstructure and Property Developments of In-situ Reacted Mullite-ZrO₂ Composites. Science and Technology of Zirconia II. *Advances in Ceramics*, **12**, p436-442.

Wallenberg, F. T. Weston, N. E. and Brown. (1991). Melt Processed Calcium Aluminate Fibres: Structural and Optical Properties: in *Proceeding of the Society of Photo-optical Instrumentation Engineers*. Vol. 1840, Growth and Characterisation of Material for Infrared Detectors. SPIE – The International Society for Optical Engineering, Bellingham, WA. p16-124.

Warren, B.E. (1969). *X-ray Diffraction*. Addison-Wesley Publishing Company Inc., United States of America.

Wei, G.C. and Becher, P.F. (1984). Improvements in Mechanical Properties in SiC by the Addition of TiC Particles. *Journal of the American Ceramic Society*, **67**(8), p571-574.

Xi, X. M., Xiao, L.M. and Yang, X.F. (1996). The Mechanism of Spontaneous Infiltration of AlSi Alloy into SiC Preform in Air. *Journal Materials Research*, **11**, p1037-1044.

Yasuoka, M., Hirao, K., Brito, M.E. and Kanzaki, S. (1995). High Strength and High Fracture Toughness Ceramics in the Al₂O₃/LaAl₁₁O₁₈ Systems. *Journal of the American Ceramic Society*, **78**(7), p1853-1856.

Yokota, M. Hara, A, Ohata, M. and Mitani, H. (1980). Infiltration of Liquids into Porous Bodies. *Transactions of the Japan Institute of Metals*, **21**(10), p652-659.

Young, R.A. (Ed). (1993). *The Rietveld Method*, International Union of Crystallography, Oxford University Press, Great Britain.

Yurkov, A.L., Sarkisyan, T.A., Ivanov, D.A. and Bradt, R.C. (1997). Final Stages of Sintering of Ceramic Materials: Effect of Residual Porosity and Microstructure on Mechanical Characteristics of Surface. *Ceramics International*, **23**, p389-399.

LIST OF PUBLICATIONS ARISING FROM THESIS

Refereed Publications

Asmi, D. and Low, I.M. (1998). Physical and Mechanical Characteristics of *In-situ* Alumina /Calcium-Hexaluminate Composites. *Journal of Materials Science Letters*, **17**, p1735-1738.

Asmi, D. and Low, I.M. (1998). Characteristics of Layered and Graded Alumina /Calcium-Hexaluminate Composites. *Journal of the Australasian Ceramic Society*, **34(2)**, p152-154.

Asmi, D., Shi, C.G., Low, I.M. and Day, R.A. (1998). Physical and Microstructural Characteristics of Spodumene-modified Alumina/ Calcium-Hexaluminate Composites. *Journal of the Australasian Ceramic Society*, **34(2)**, p155-160.

Asmi, D., Low, I.M. and Day, R.A. (1998). Physical and Microstructural Characteristics of HIPed Alumina /Calcium-Hexaluminate Composites. *Journal of the Australasian Ceramic Society*, **34(2)**, p108-113.

Asmi, D. and Low, I.M. (1998). Processing of In-situ Layered and Graded Alumina /Calcium-Hexaluminate Composite: I, Physical Characteristics. *Journal of the European Ceramic Society*, **18**, p2019-2024.

Asmi, D., Low, I.M., Kennedy, S. and Day, R.A. (1999). Characteristics of a Layered and Graded Alumina /Calcium-Hexaluminate Composite. *Materials Letters*, **40**, p96-102.

Asmi, D. and Low, I.M. (In Press). Infiltration and Physical Characteristics of Functionally-Graded Alumina /Calcium-Hexaluminate Composites. *Journal of Materials Processing Technology*.

Low, I.M., Skala, R.D., Asmi, D., Manurung, P. and Singh, M. (In Press). Infiltration Processing Novel Graded Ceramic Materials. *Proc. Int. Conf. on Powder Metallurgy (PM2000)*, 12-16 Nov. 2000, Kyoto, Japan.

Conference Proceedings

Asmi, D., Low, I.M. and Sitepu, H. (1997). Microstructural Design of Layered and Graded Alumina /Calcium-Hexaluminate Composites. *Proceeding 1997 State Conference and Workshop AXAA and WASEM*, 19 – 21 Sept., El Caballo Resort, WA. p45-46.

Asmi, D., Low, I.M. and Sitepu, H. (1997). Characteristics of Layered and Graded Alumina /Calcium-Hexaluminate Composites. *Proceeding Sixth Australian Institute of Physics (AIP) Postgraduate Research Conference*, 24 – 26 Sept., Jarahdale, WA. p16-17.

Asmi, D., Low, I.M. and Kennedy, S. (1998). Phase Compositions and Developments of Calcium Aluminates in Alumina/CA₆ Composites. *Proceeding 13th Australian Institute of Physics National Congress*, 28 Sept. – 2 Oct, Fremantle, WA. p316.

Asmi, D., Low, I.M., Day, A.R. and Shi, C. (1998). Phase Compositions and Developments of Calcium Aluminates in Alumina/CA₆ Composites. *Proceeding 13th Australian Institute of Physics National Congress*, 28 Sept. – 2 Oct, Fremantle, WA. p316.

Asmi, D., Low, I.M., O'Connor, B.H. and Buckley, C.E. (1999). Phase Compositions and Depth-Profiling of Calcium-Aluminates in a Functionally-Graded Alumina/Calcium-Hexaluminate Composite. *Proceeding International Conference on Advances in Materials and Processing Technologies (AMPT'99)* (Eds. M.S.J. Hashmi and L. Looney), August 3-6, Dublin, Ireland, p37-45.

Asmi, D. and Low, I.M. (1999). Infiltration and Physical Characteristics of Functionally-Graded Alumina /Calcium-Hexaluminate Composites. *Proceeding International Conference on Advances in Materials and Processing Technologies (AMPT'99)* (Eds. M.S.J. Hashmi and L. Looney), August 3-6, Dublin, Ireland, p1271-1279.

Asmi, D. Low, I.M., O'Connor, B.H. and Buckley, C.E. (1999). A Novel Route to Synthesise a Functionally-Graded Material Based on Alumina /Calcium-Hexaluminate. *Proceeding 1999 Joint WASEM and AXAA Conference* (Ed. B.J. Griffin), September 17-19, Mandurah, WA. p18.

Asmi, D., Skala, R., Manurung, P., Low, I.M., O'Connor, B. and Buckley, C. (2000). Depth-Profiling of Phase Compositions in Functionally-Graded Alumina-Based Composites Using Synchrotron Radiation Diffraction. *AUSTCERAM 2000 Transaction*, p273.

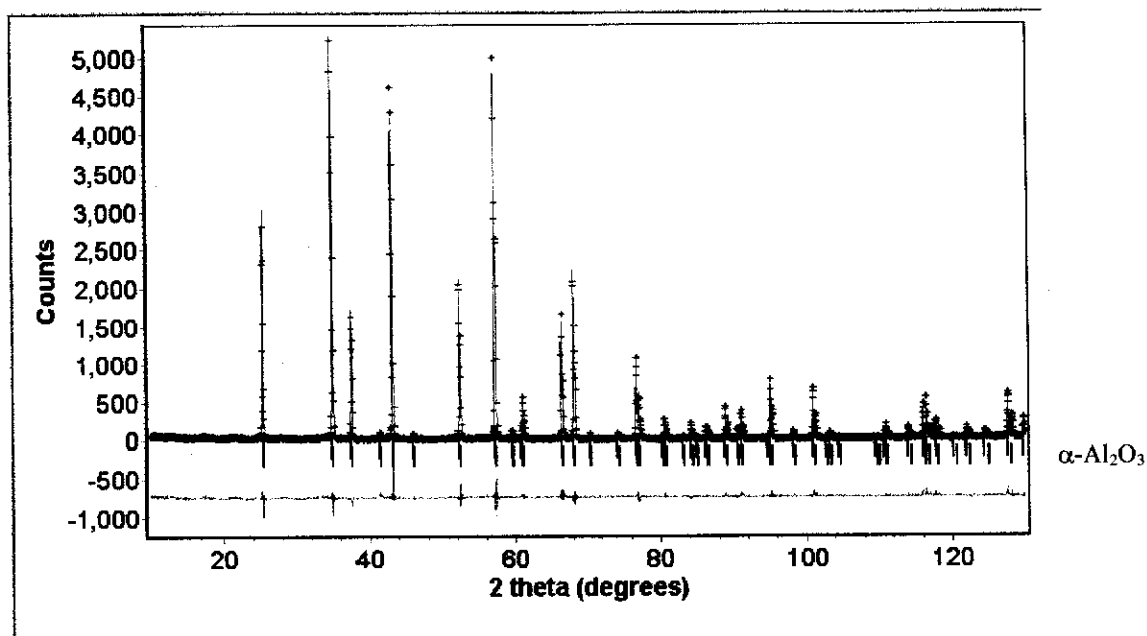
Asmi, D., Low, I.M., Kennedy, S.J. and O'Connor, B.H. (2000). Quantitative Phase Analysis of Alumina/Calcium-Hexaluminate Composites Using Neutron Diffraction Data and the Rietveld Method. *Proceeding 2nd AINSE Symposium on Neutron Scattering Powder Diffraction*, 22 June 2000, AINSE, p17.

APPENDICES

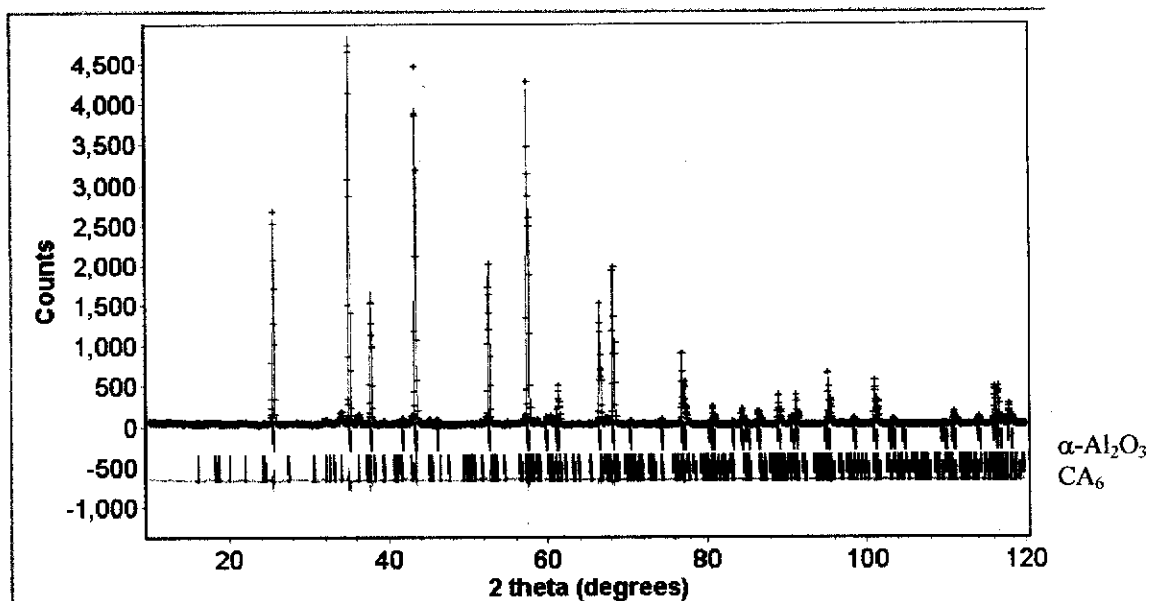
Note: For copyright reasons Appendix A has not been reproduced.

**(Co-ordinator, ADT Project (Retrospective), Curtin University of Technology,
9.7.03)**

Appendix B - Rietveld Refinement Patterns

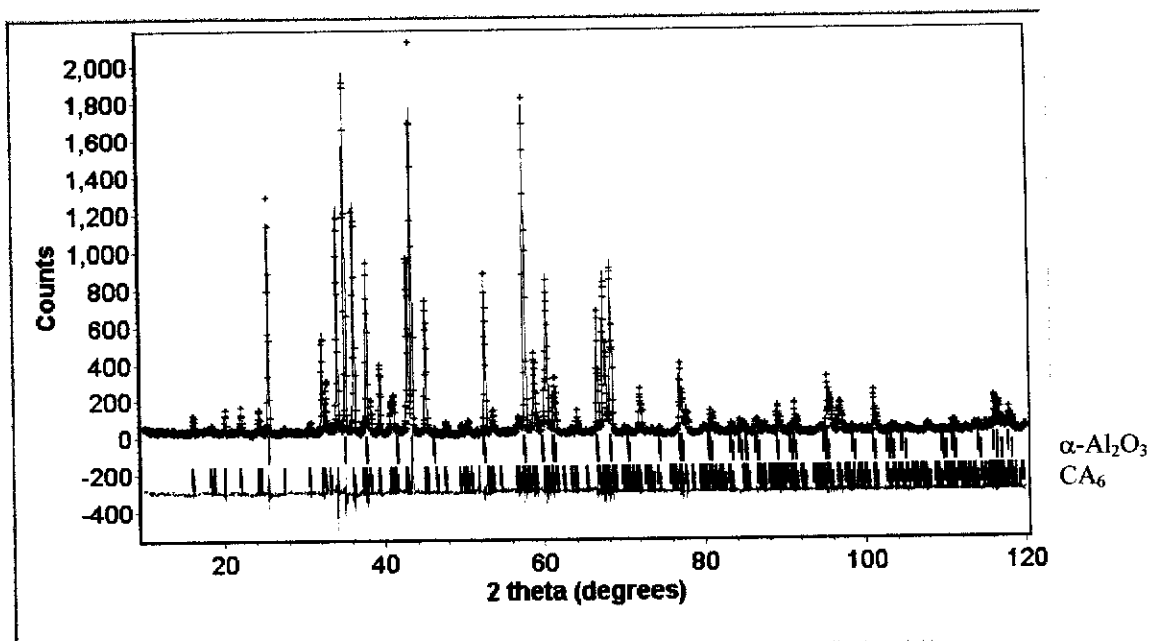


(a)

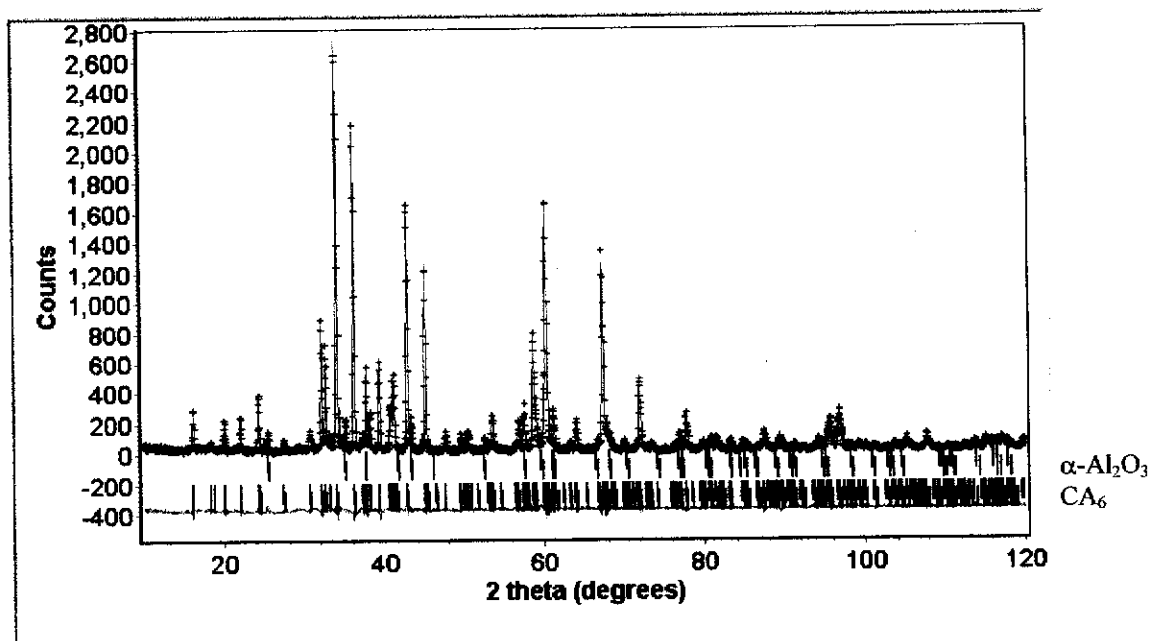


(b)

Figure B.1. XRD Rietveld difference plots for A/CA₆ composites: (a) CA0 and (b) CA5. The observed data are shown by a (+) sign, and the calculated data by a solid line. Vertical line represents the positions of diffraction lines for $\alpha\text{-Al}_2\text{O}_3$ in (a) and $\alpha\text{-Al}_2\text{O}_3$ and CA₆ in (b). The green line below the vertical lines is the difference profile.

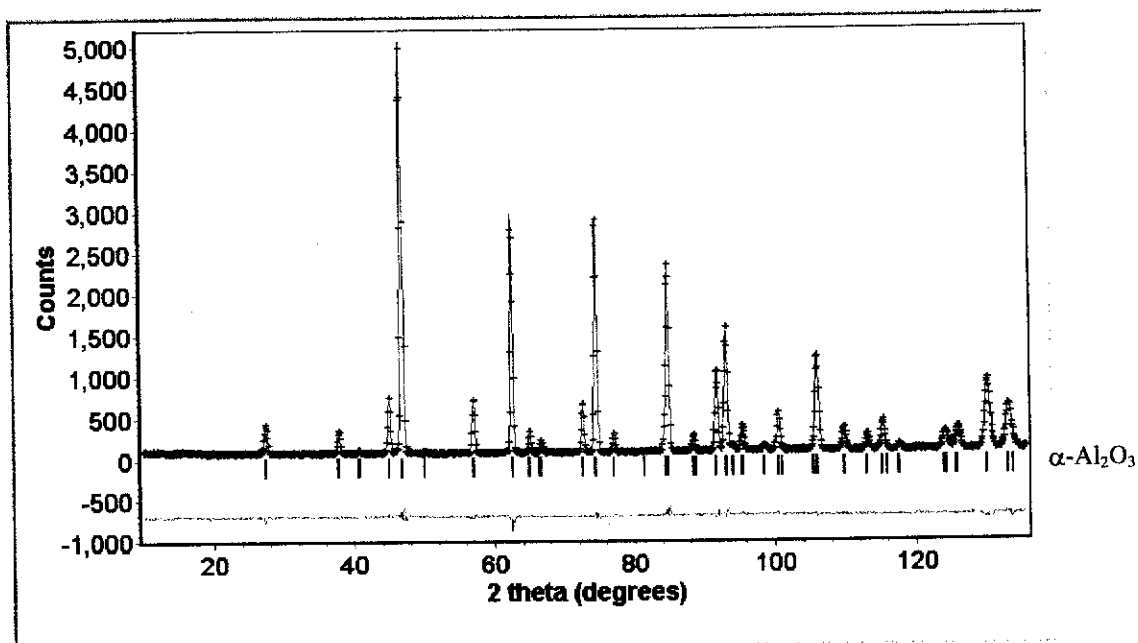


(a)

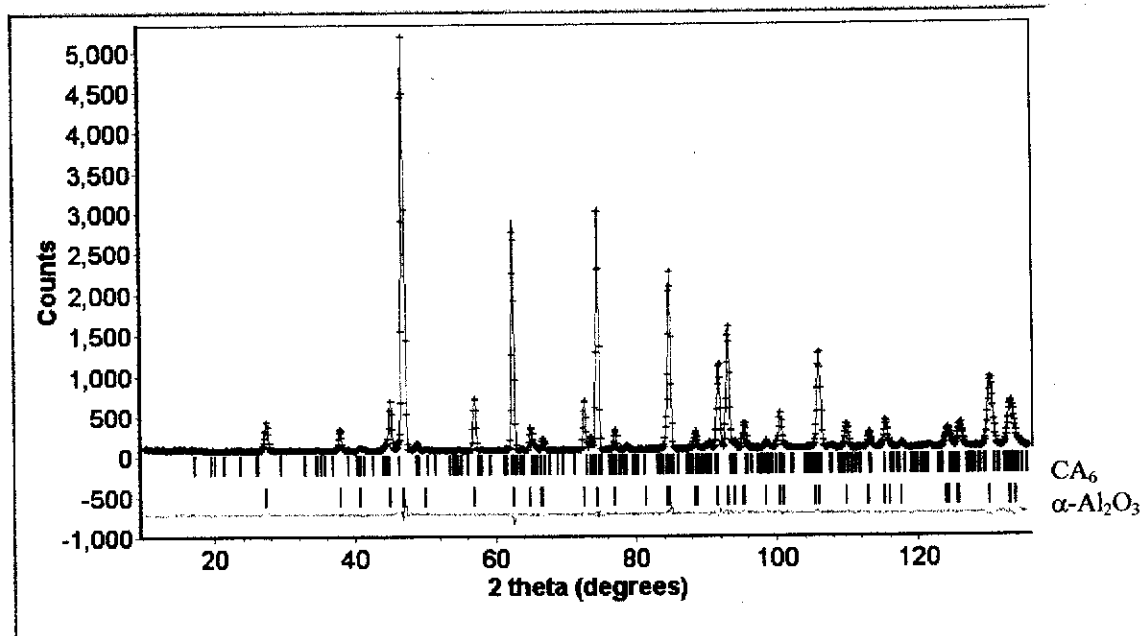


(b)

Figure B.2. XRD Rietveld difference plots for A/CA₆ composites: (a) CA50 and (b) CA100. The observed data are shown by a (+) sign, and the calculated data by a solid line. Vertical line represents the positions of diffraction lines for α -Al₂O₃ and CA₆ in (b). The green line below the vertical lines is the difference profile.

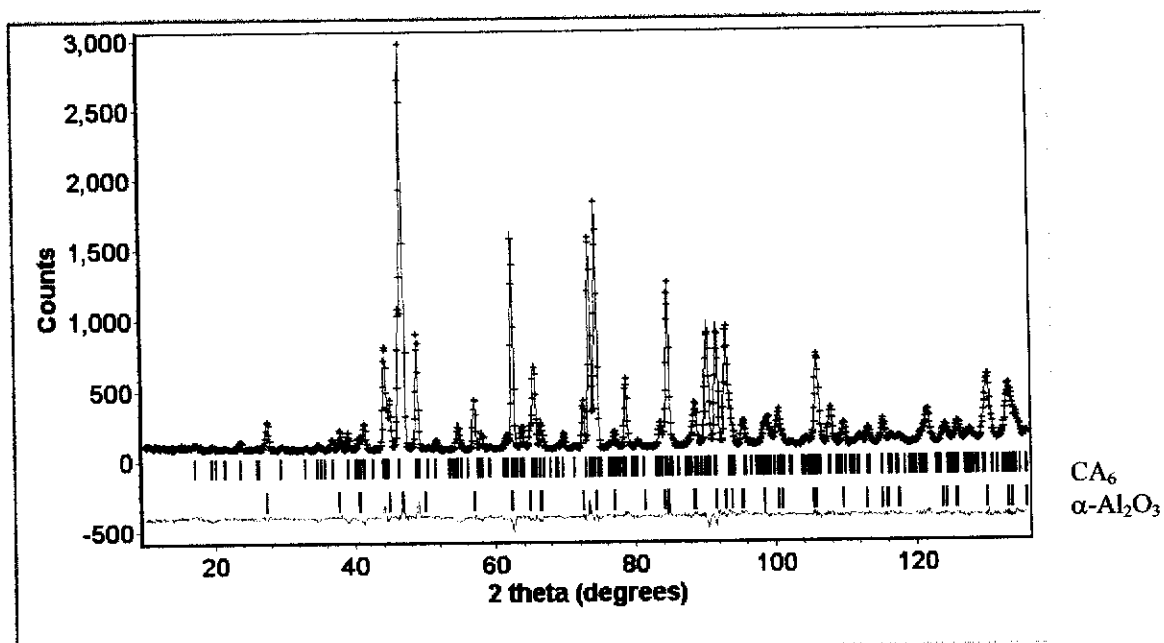


(a)

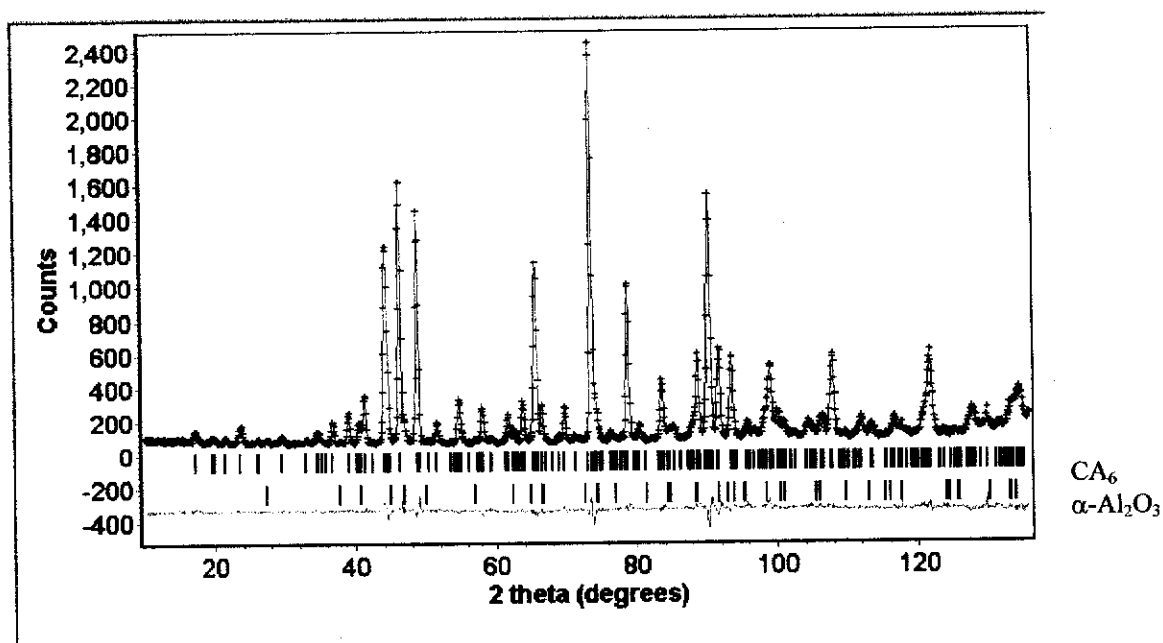


(b)

Figure B.3. ND Rietveld difference plots for A/ CA_6 composites: (a) CA0 and (b) CA5. The observed data are shown by a (+) sign, and the calculated data by a solid line. Vertical line represents the positions of diffraction lines for $\alpha\text{-Al}_2\text{O}_3$ in (a), and CA_6 and $\alpha\text{-Al}_2\text{O}_3$ in (b). The green line below the vertical lines is the difference profile.

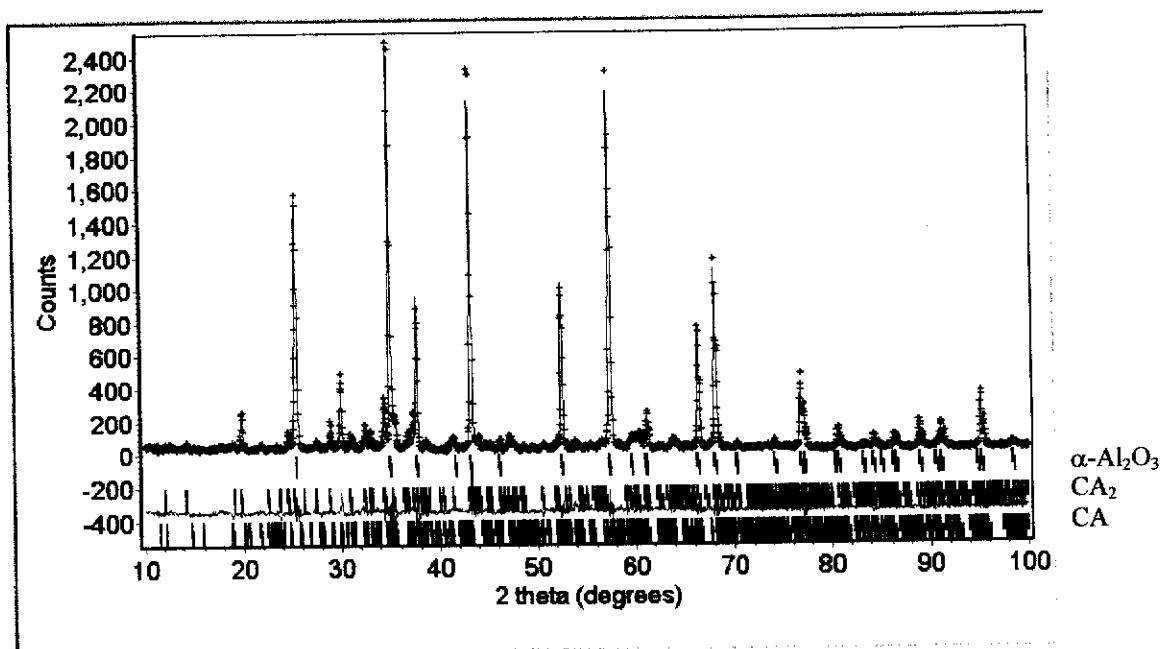


(a)

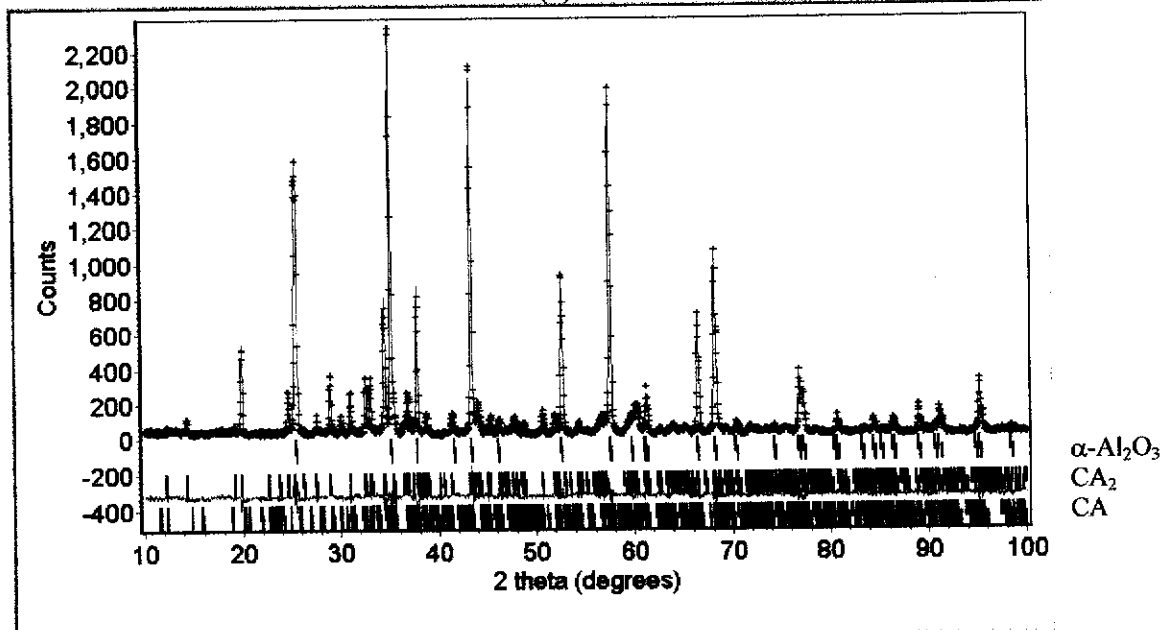


(b)

Figure B.4. ND Rietveld difference plots for A/CA₆ composites: (a) CA50 and (b) CA100. The observed data are shown by a (+) sign, and the calculated data by a solid line. Vertical line represents the positions of diffraction lines for CA₆ and α -Al₂O₃. The green line below the vertical lines is the difference profile.

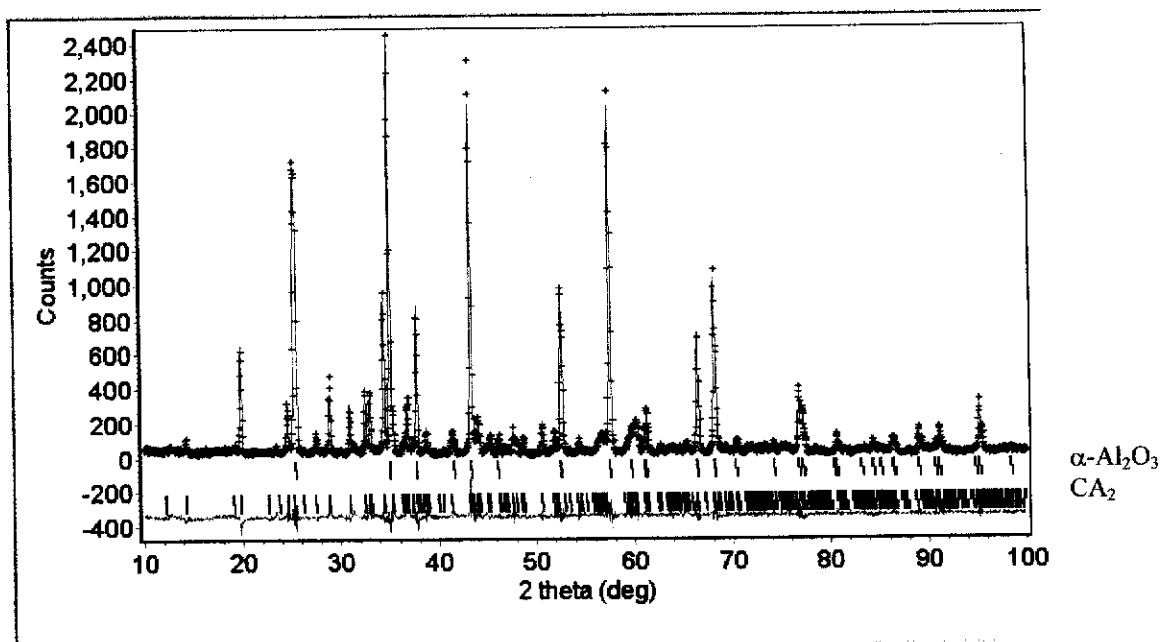


(a)

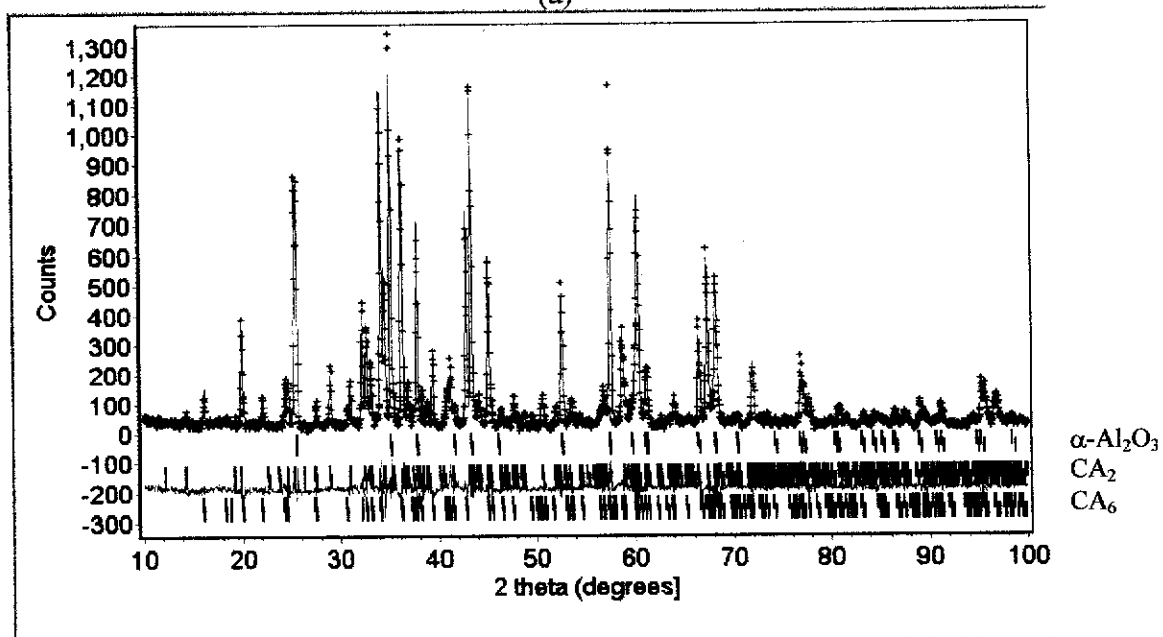


(b)

Figure B.5. XRD Rietveld difference plots for CA100 sample fired at (a) 1100 °C and (b) 1200 °C. The observed data are shown by a (+) sign, and the calculated data by a solid line. Vertical line represents the positions of diffraction lines for α -Al₂O₃, CA₂ and CA. The green line below the vertical lines is the difference profile.

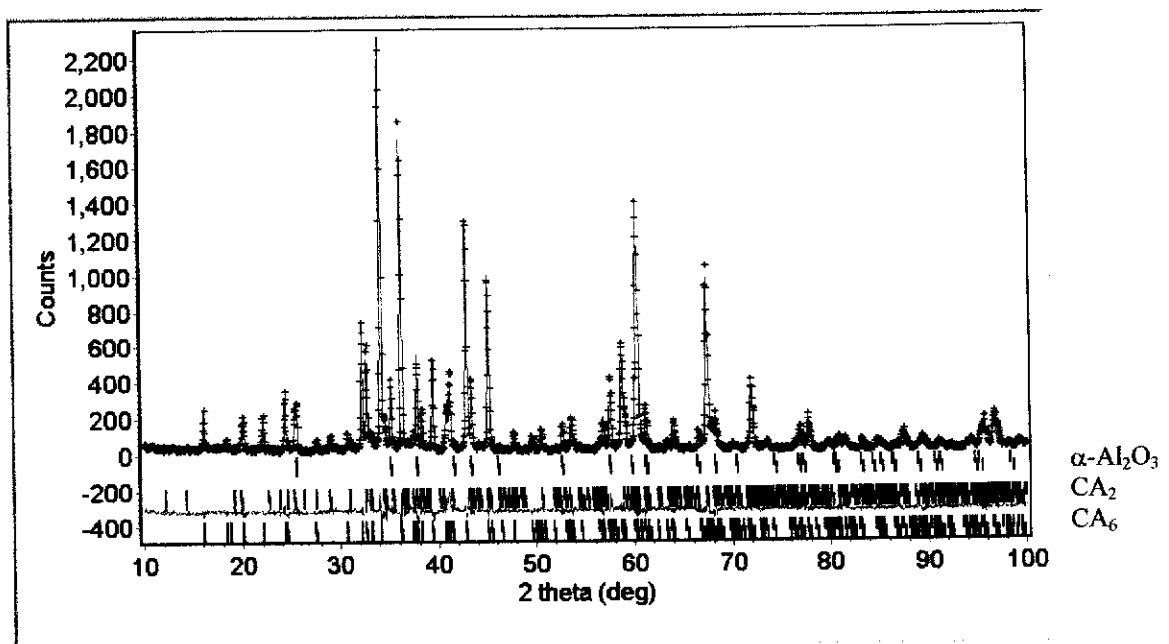


(a)

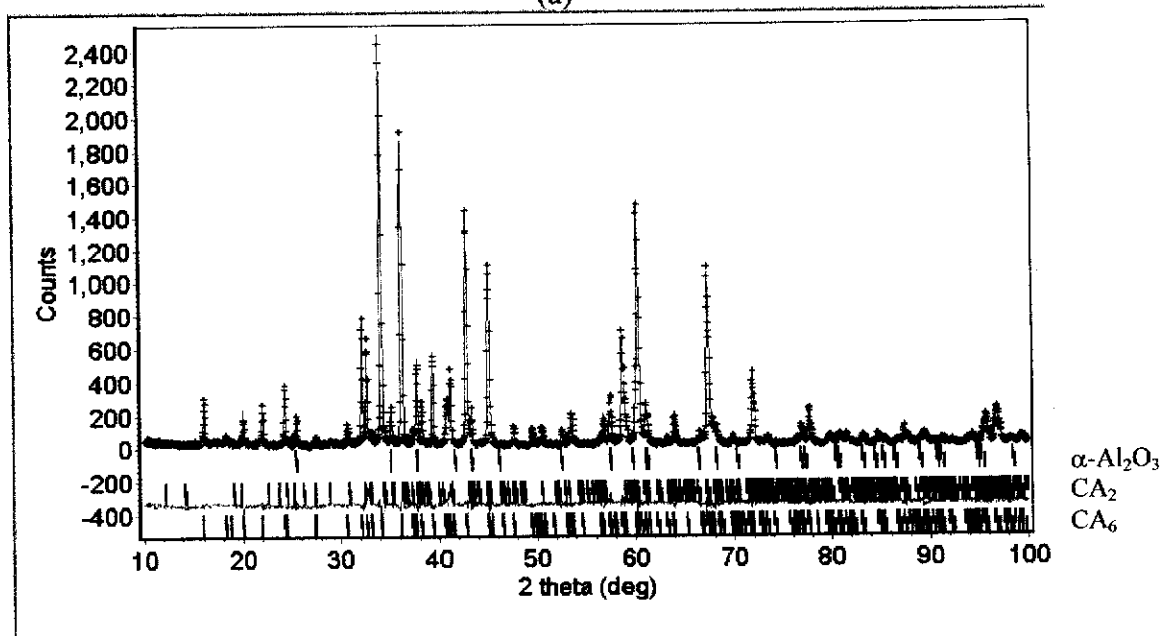


(b)

Figure B.6. XRD Rietveld difference plots for CA100 sample fired at (a) 1300 °C and (b) 1400 °C. The observed data are shown by a (+) sign, and the calculated data by a solid line. Vertical line represents the positions of diffraction lines for α -Al₂O₃, CA₂ in (a), and α -Al₂O₃, CA₂ and CA₆ in (b). The green line below the vertical lines is the difference profile.

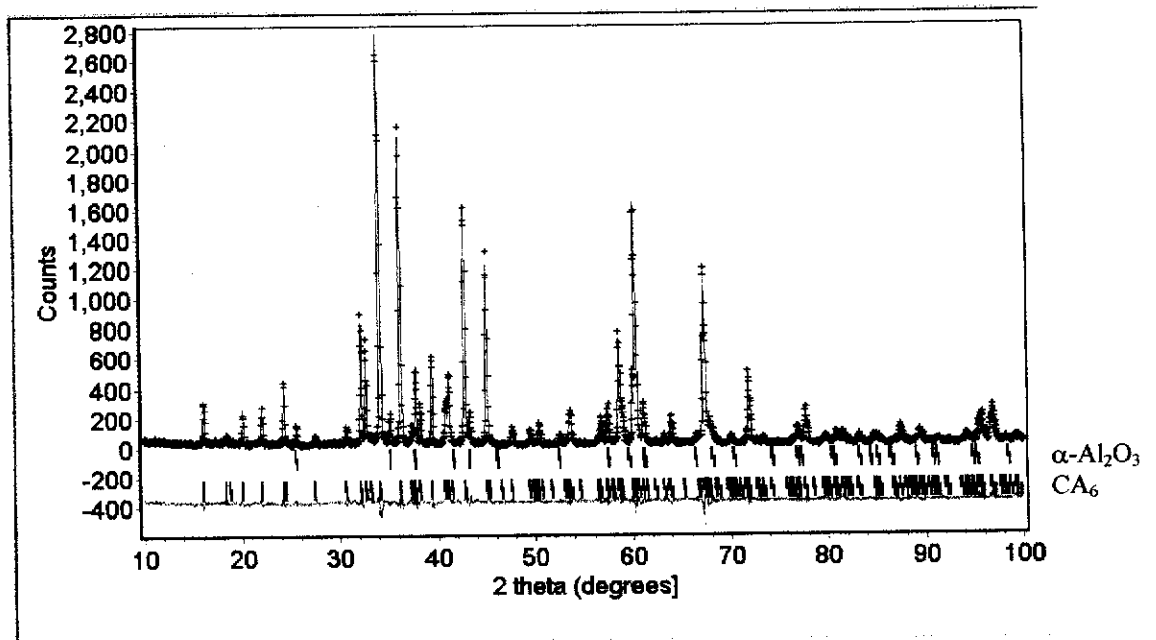


(a)

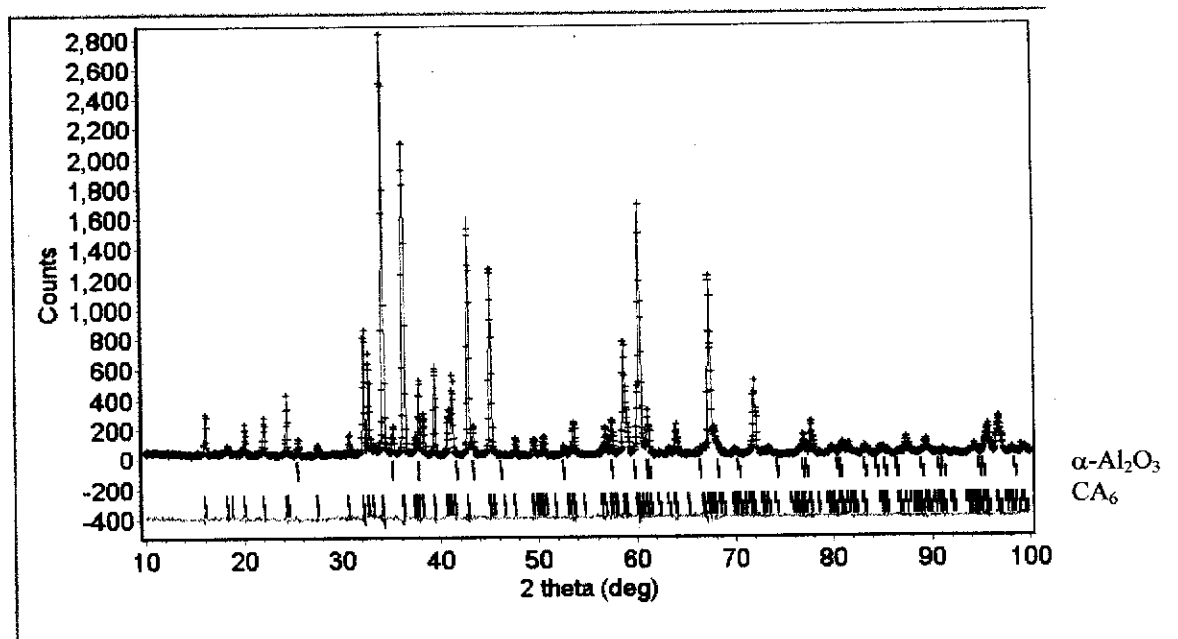


(b)

Figure B.7. XRD Rietveld refinement plot for CA100 sample fired at (a) 1450 °C and (b) 1500 °C. The observed data are shown by a (+) sign, and the calculated data by a solid line. Vertical line represents the positions of diffraction lines for α -Al₂O₃, CA₂ and CA₆. The green line below the vertical lines is the difference profile.



(a)



(b)

Figure B.8. XRD Rietveld difference plots for CA100 sample at (a) 1550 °C and (b) 1600 °C. The observed data are shown by a (+) sign, and the calculated data by a solid line. Vertical line represents the positions of diffraction lines of α -Al₂O₃ and CA₆. The green line below the vertical lines is the difference profile.

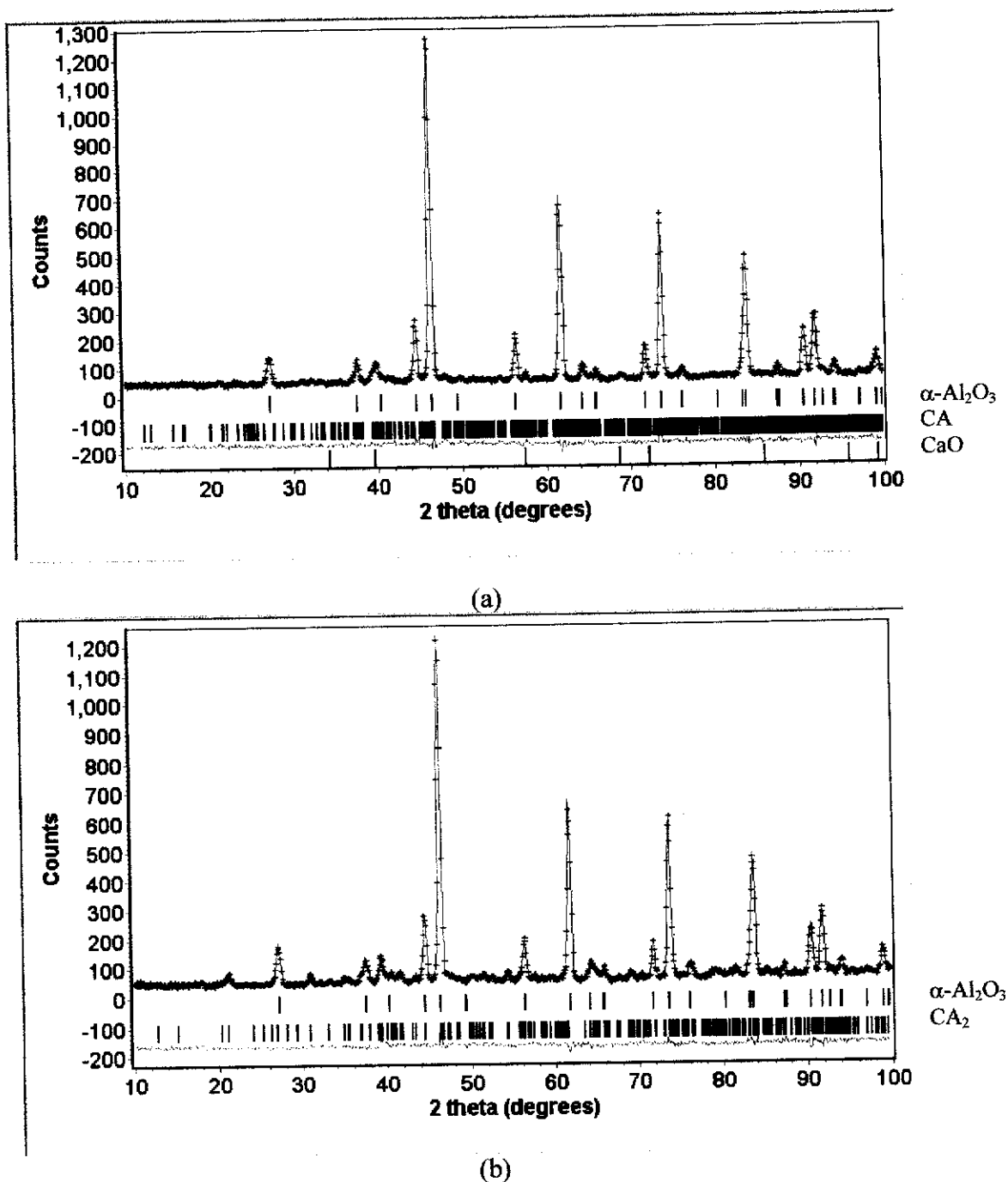
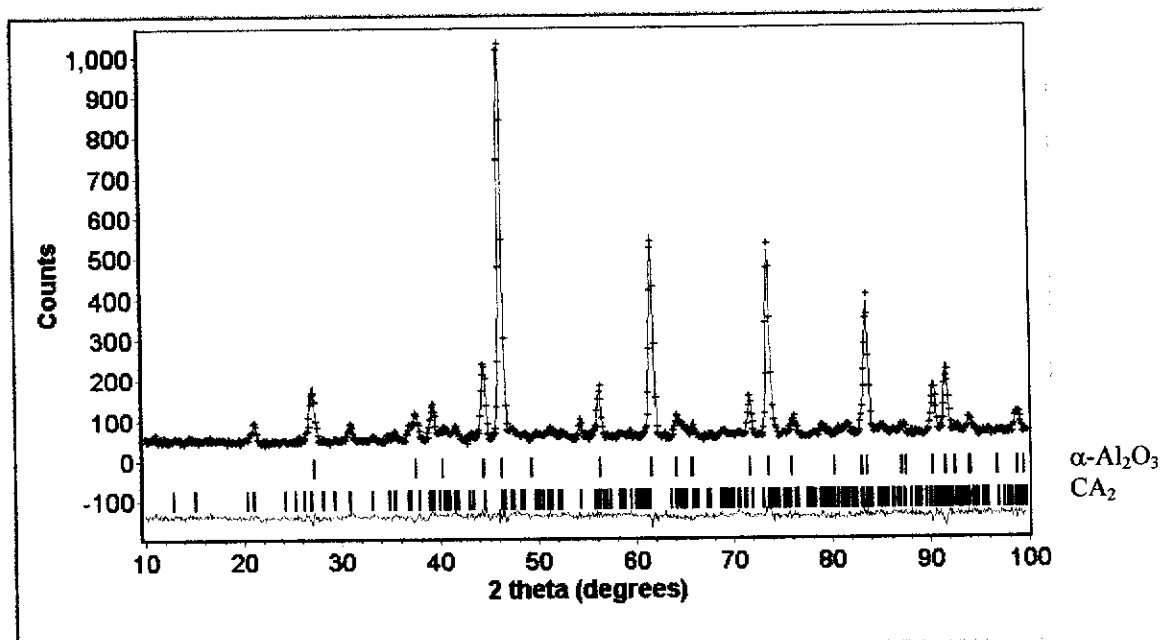
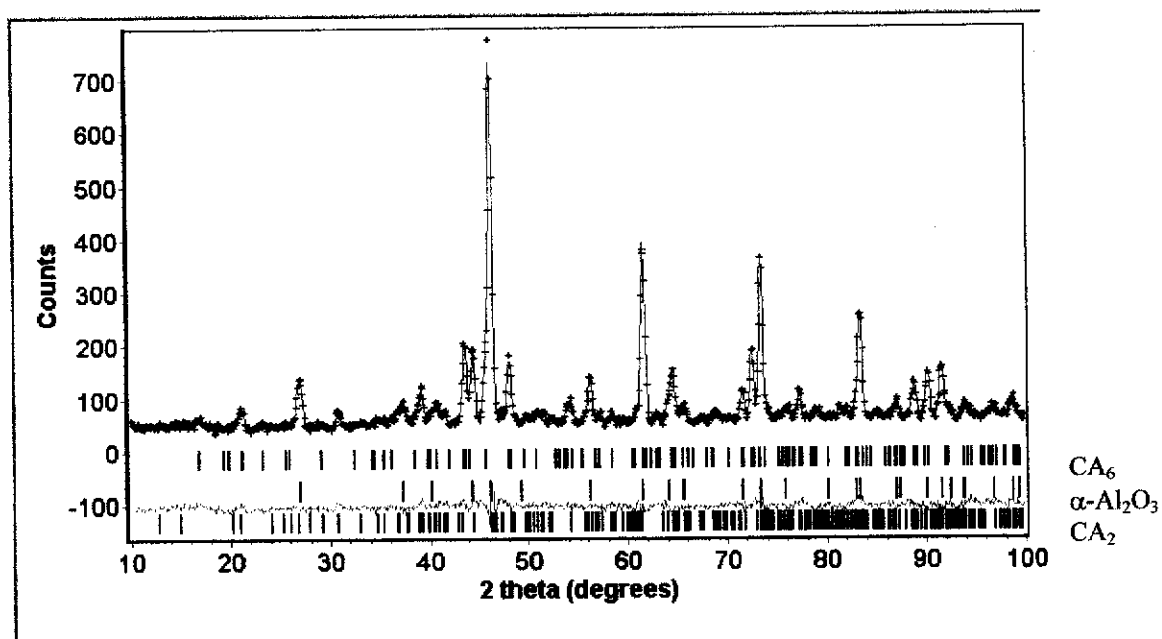


Figure B.9. HTND Rietveld difference plots for CA100 sample at (a) 1100 °C and (b) 1200 °C. The observed data are shown by a (+) sign, and the calculated data by a solid line. Vertical line represents the positions of diffraction lines of $\alpha\text{-Al}_2\text{O}_3$, CA and CaO in (a) and $\alpha\text{-Al}_2\text{O}_3$, and CA_2 in (b). The green line below the vertical lines is the difference profile.

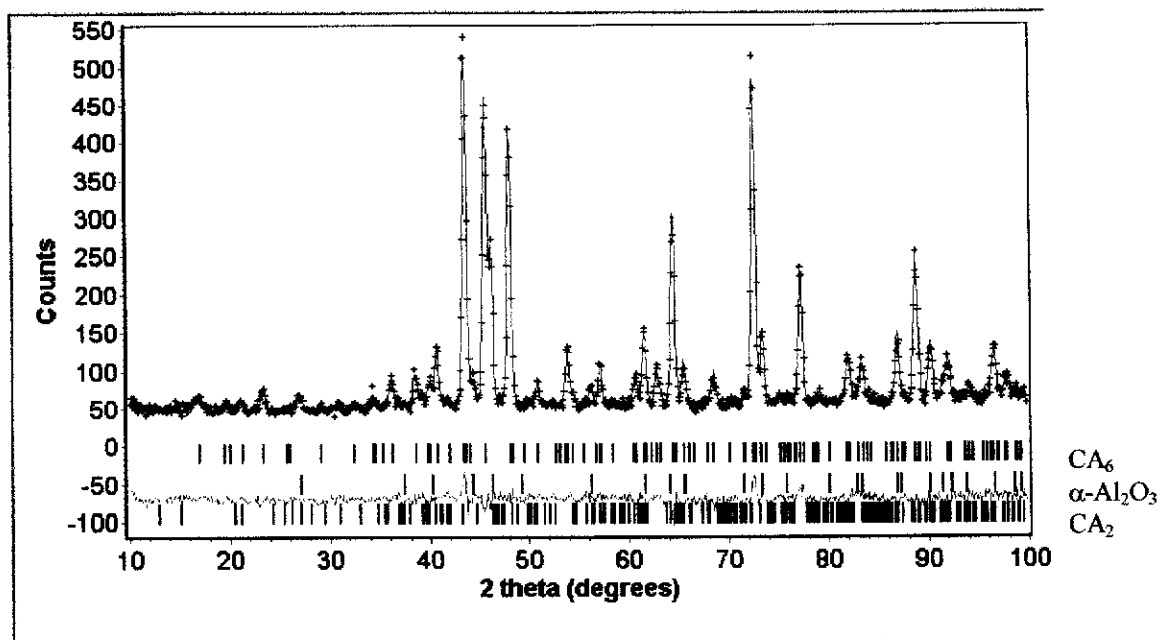


(a)

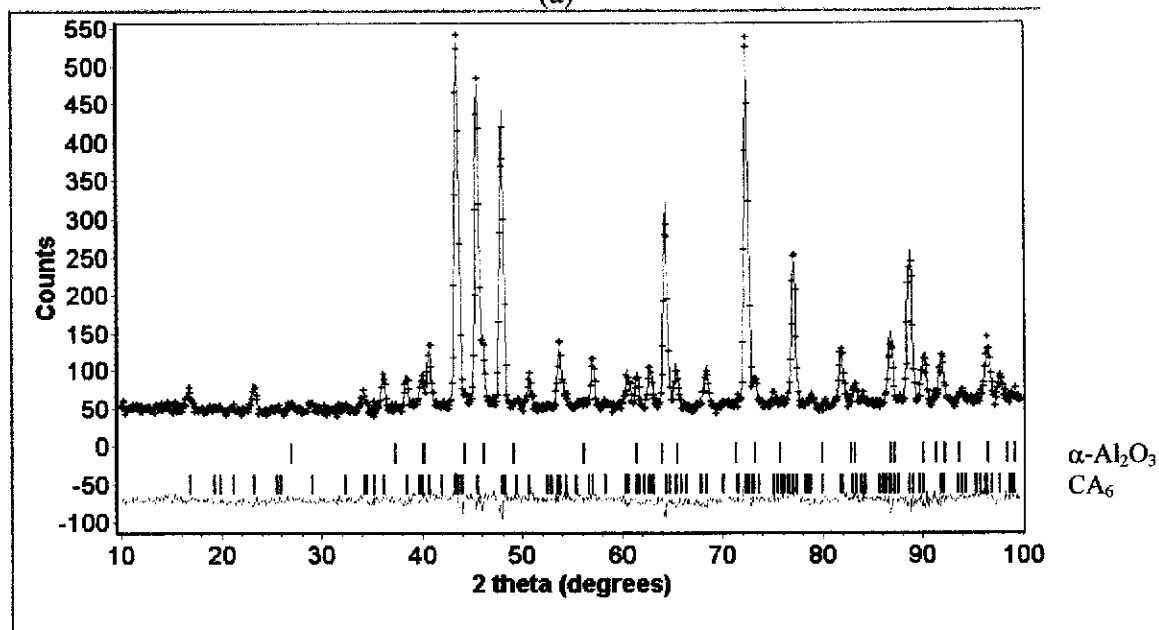


(b)

Figure B.10. HTND Rietveld difference plots for CA100 sample at (a) 1300 °C and (b) 1400 °C. The observed data are shown by a (+) sign, and the calculated data by a solid line. Vertical line represents the positions of diffraction lines of $\alpha\text{-Al}_2\text{O}_3$, CA_2 , in (a) CA_6 , $\alpha\text{-Al}_2\text{O}_3$ and CA_2 in (b). The green line below the vertical line is the difference profile.

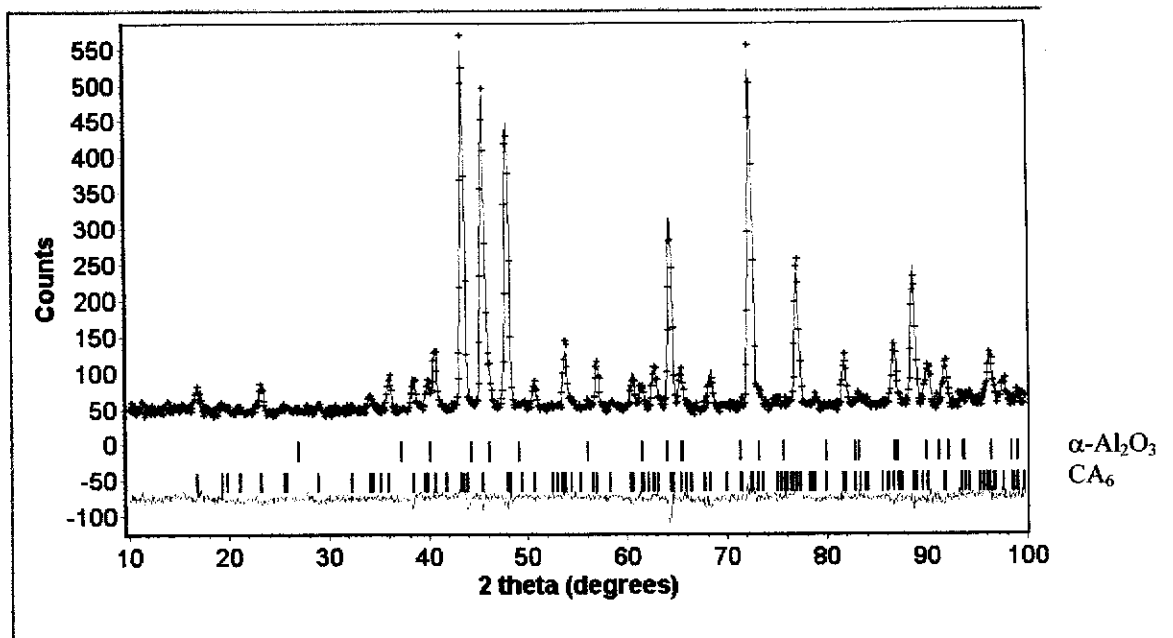


(a)

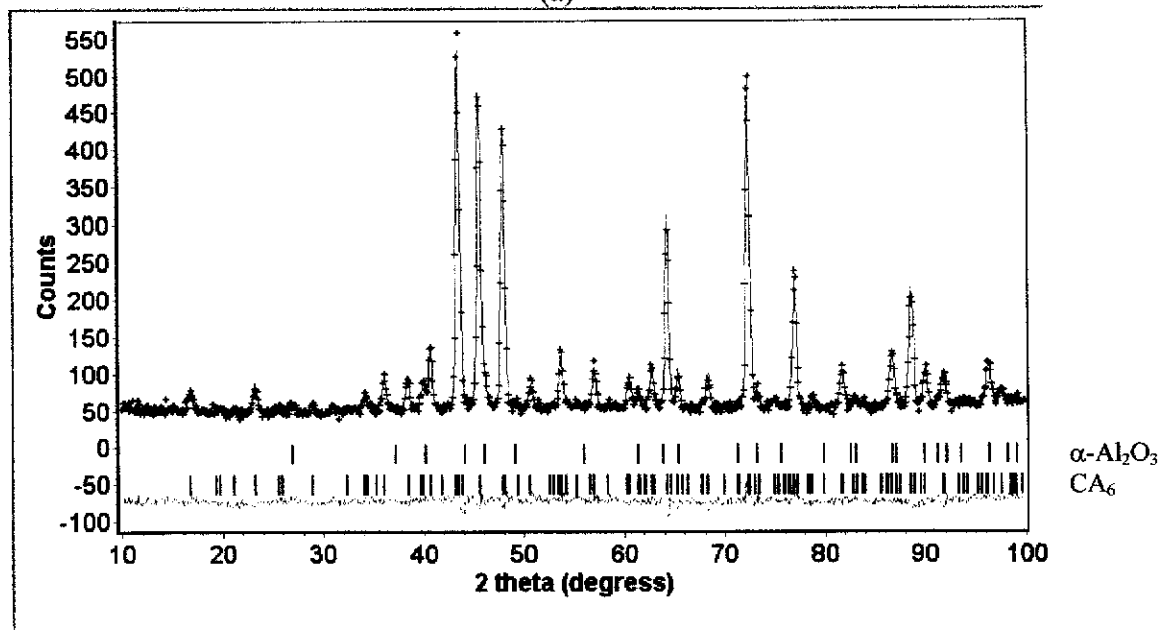


(b)

Figure B.11. HTND Rietveld difference plots for CA100 sample at (a) 1450 °C and (b) 1500 °C. The observed data are shown by a (+) sign, and the calculated data by a solid line. Vertical line represents the positions of diffraction lines of CA₆, α -Al₂O₃ and CA₂ in (a) and CA₆ and α -Al₂O₃ in (b). The green line below the vertical line is the difference profile.



(a)



(b)

Figure B.12. HTND Rietveld difference plots for CA100 sample at (a) 1550 °C and (b) 1600 °C. The observed data are shown by a (+) sign, and the calculated data by a solid line. Vertical line represents the positions of diffraction lines of α -Al₂O₃ and CA₆. The green line below the vertical line is the difference profile.

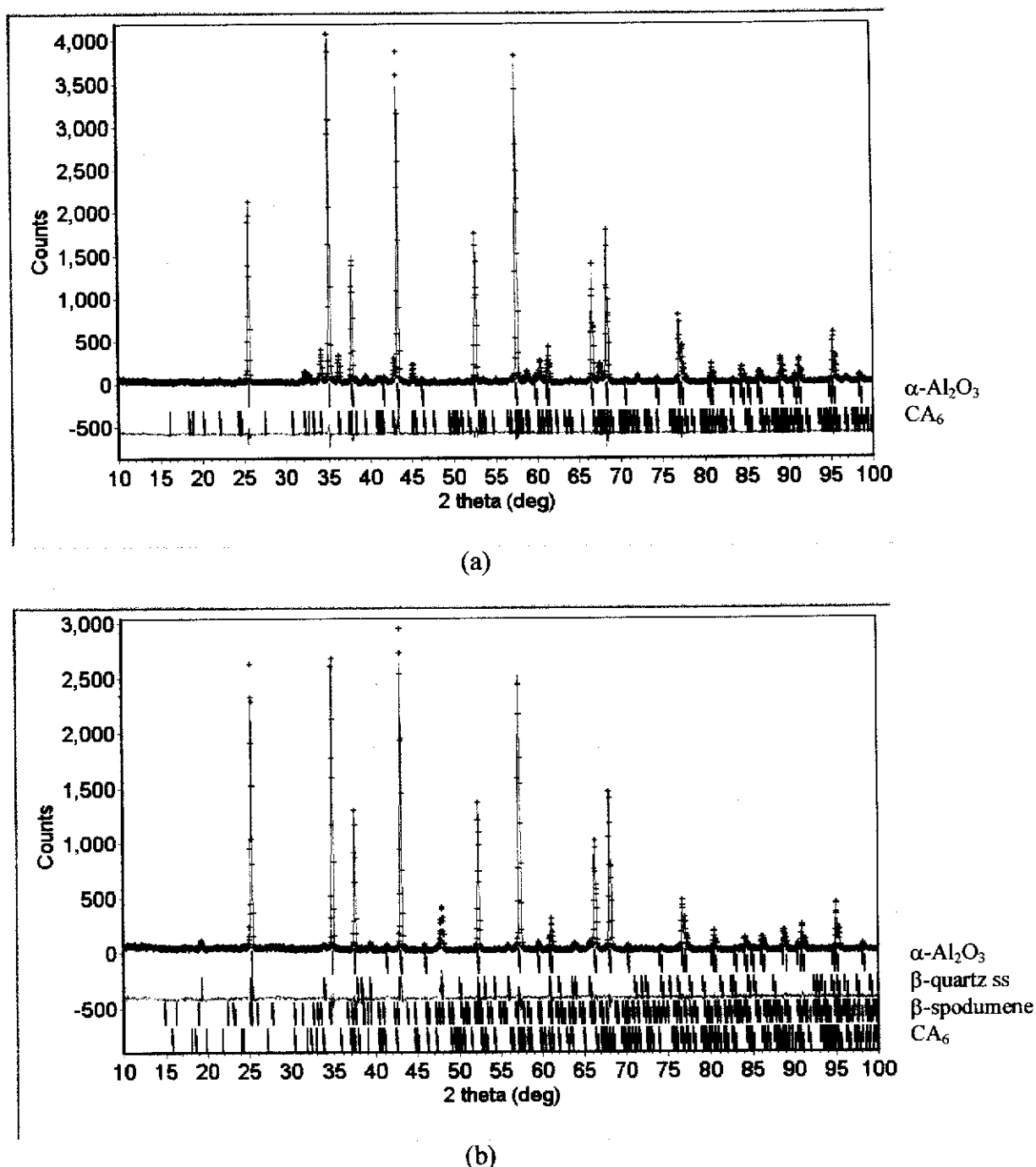


Figure B.13. XRD Rietveld difference plots for β -spodumene modified A/CA₆ composite: (a) CAS2.5 and (b) CAS15. The observed data are shown by a (+) sign, and the calculated data by a solid line. Vertical line represents the positions of diffraction lines of α -Al₂O₃ and CA₆ in (a) and α -Al₂O₃, β -quartz ss, β -spodumene and CA₆ in (b). The green line below the vertical line is the difference profile.

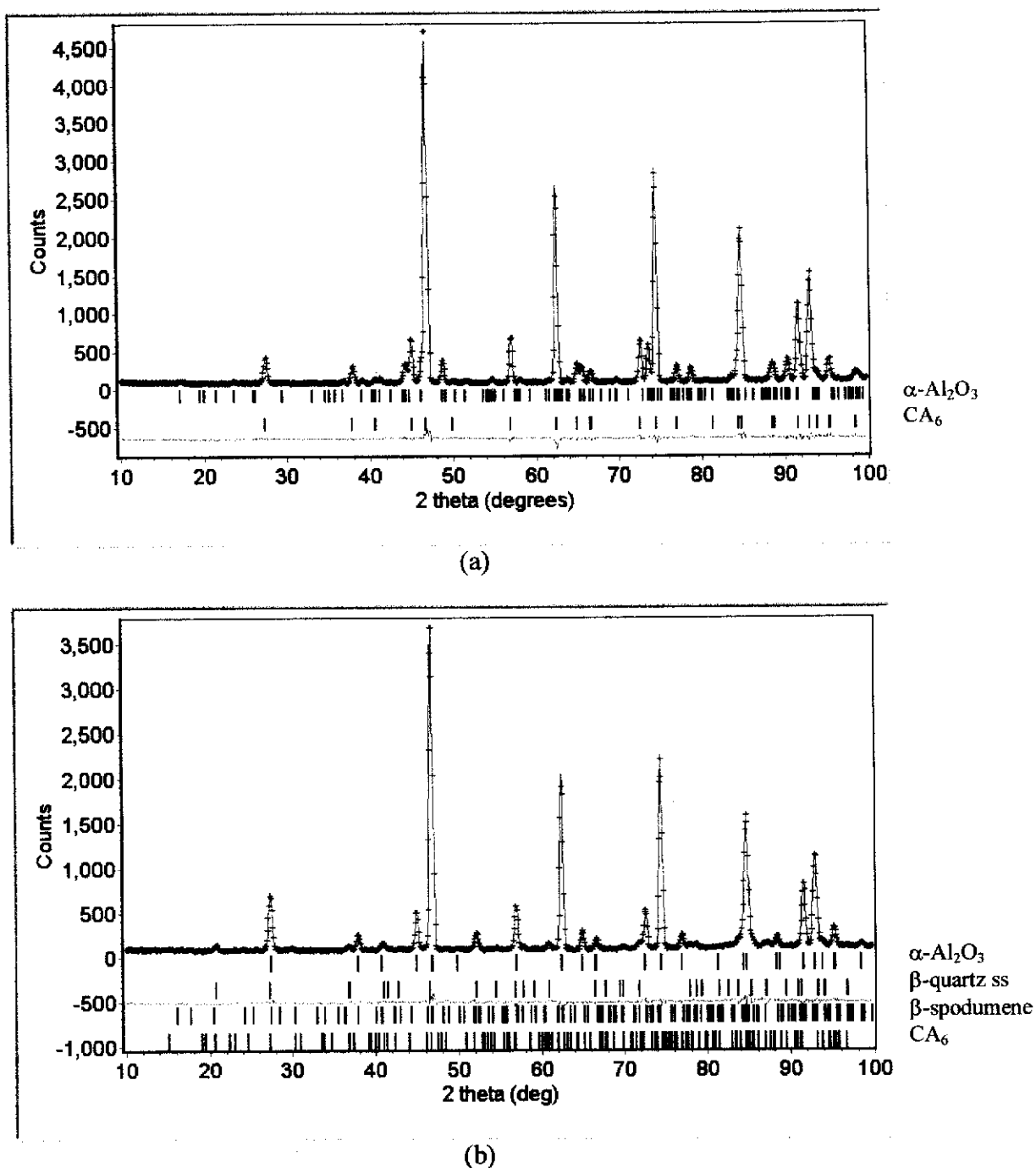
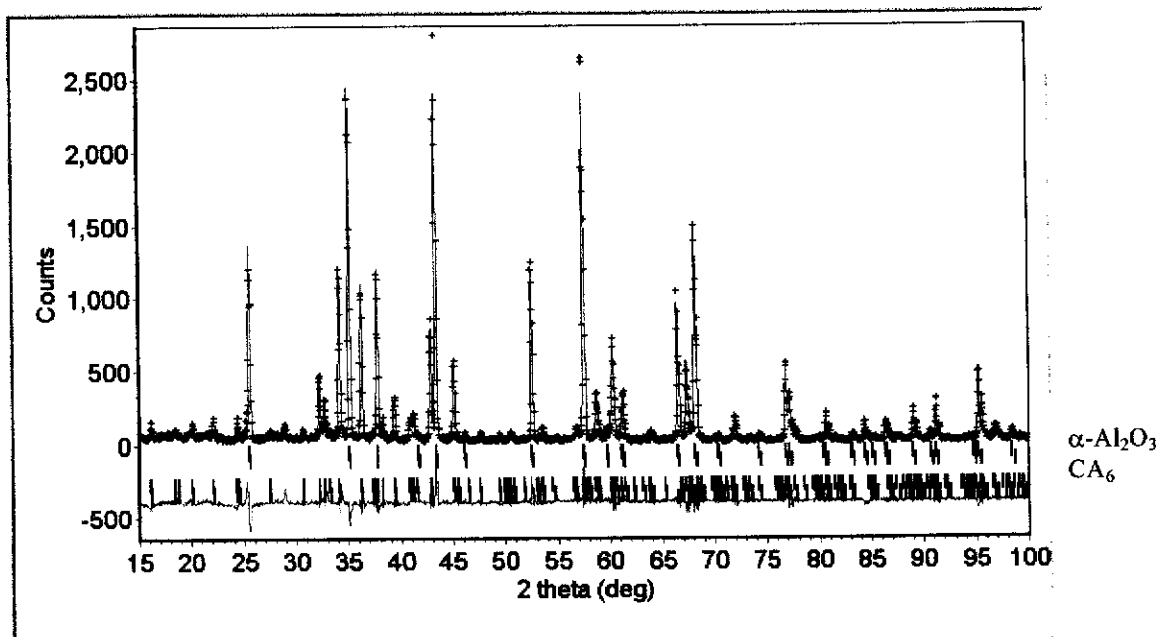
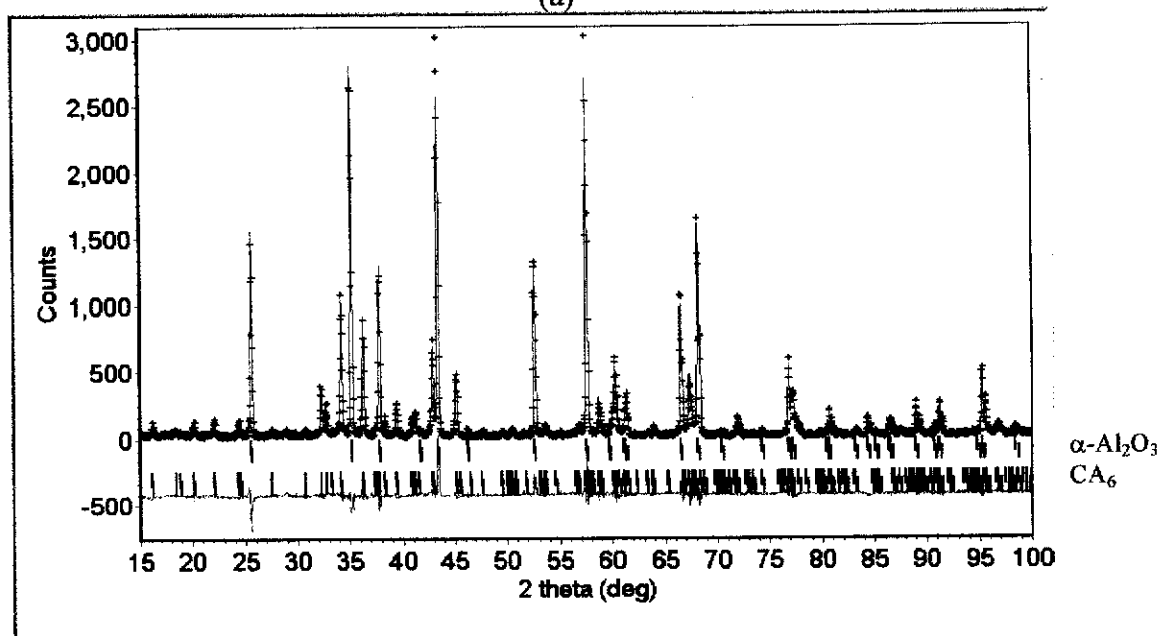


Figure B.14. ND Rietveld difference plots for β -spodumene modified A/ CA_6 composite: (a) CAS2.5 and (b) CAS15. The observed data are shown by a (+) sign, and the calculated data by a solid line. Vertical line represents the positions of diffraction lines of $\alpha\text{-Al}_2\text{O}_3$ and CA_6 in (a) and $\alpha\text{-Al}_2\text{O}_3$, $\beta\text{-quartz}$, $\beta\text{-spodumene}$ and CA_6 in (b). The green line below the vertical line is the difference profile.

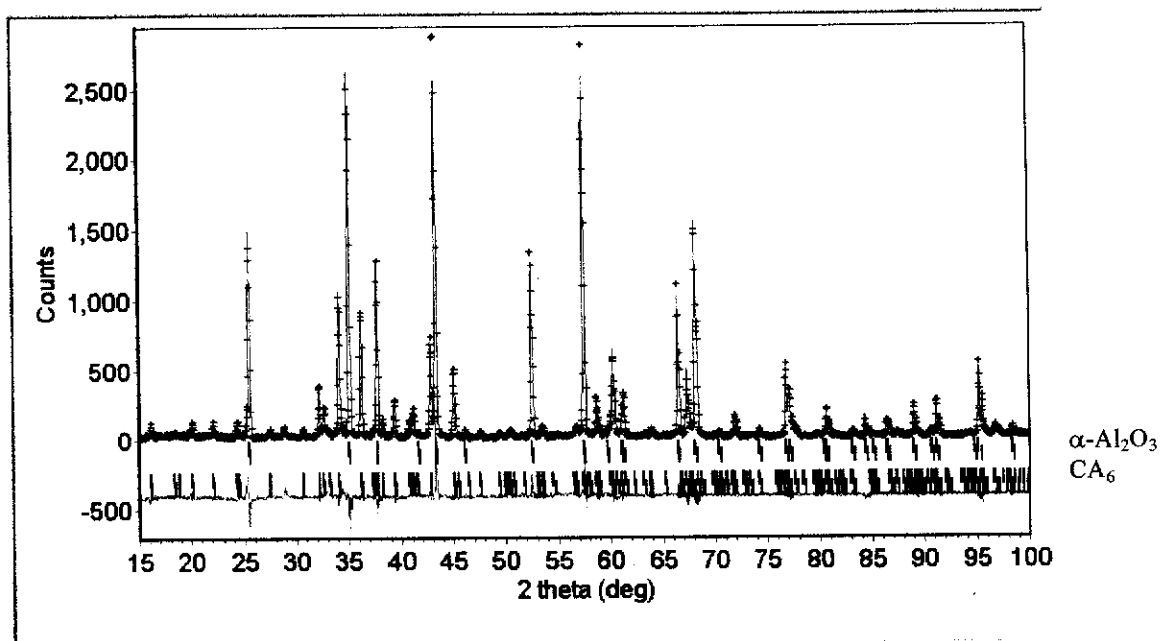


(a)

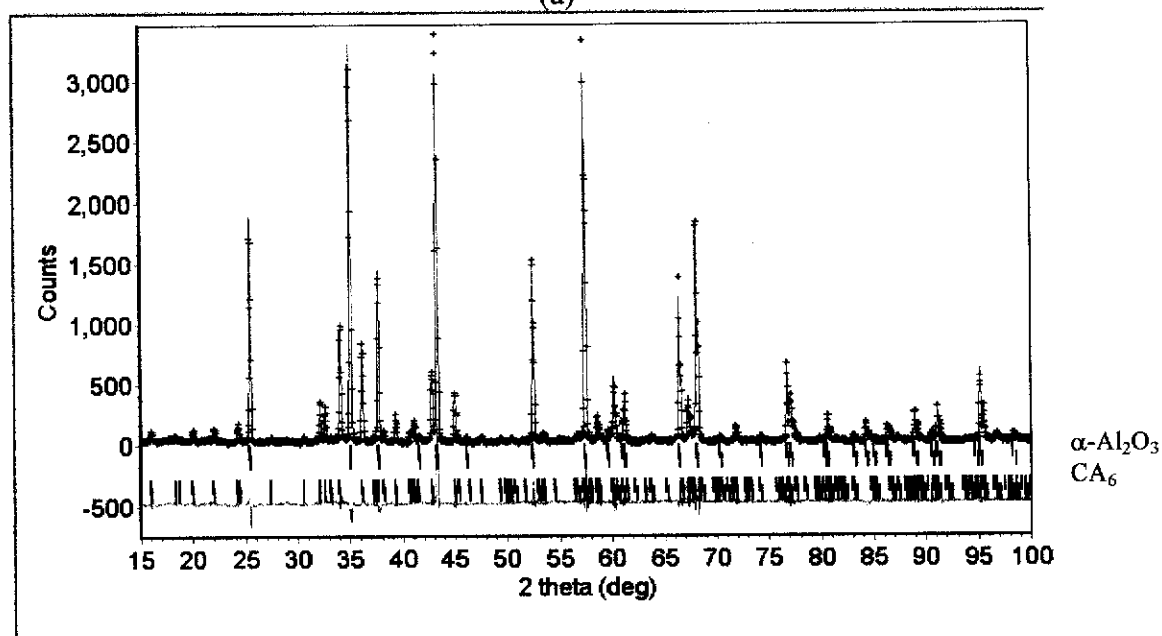


(b)

Figure B.15. XRD Rietveld difference plots for FGM sample at (a) 0 mm (surface) and (b) 1 mm depth. The observed data are shown by a (+) sign, and the calculated data by a solid line. Vertical line represents the positions of diffraction lines of α - Al_2O_3 and CA_6 . The green line below the vertical line is the difference profile.

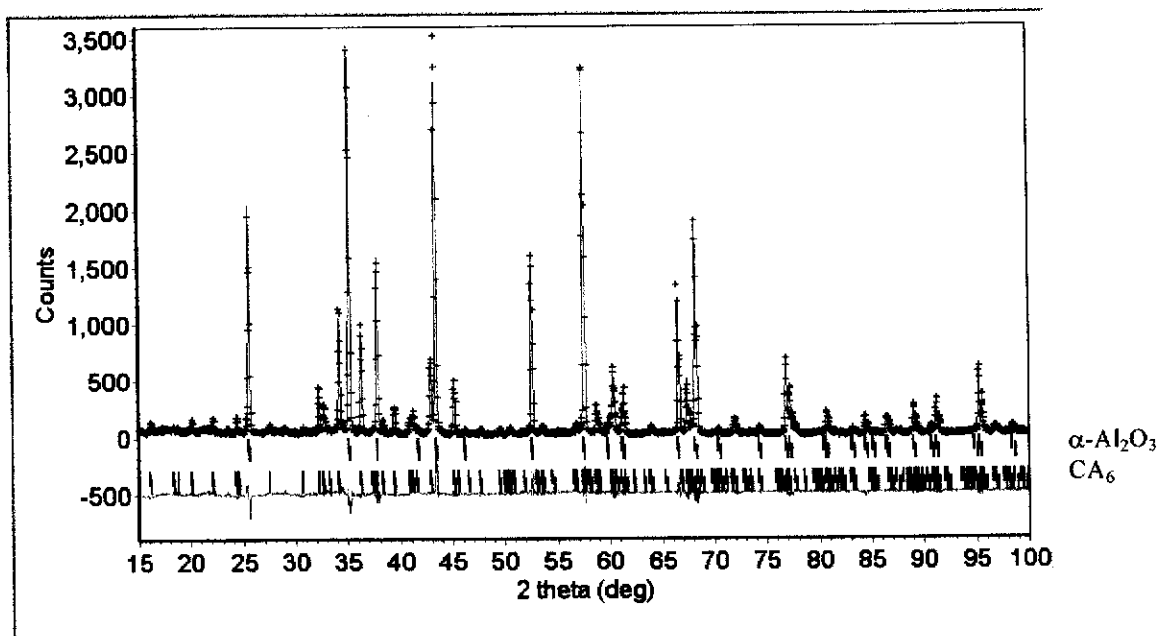


(a)

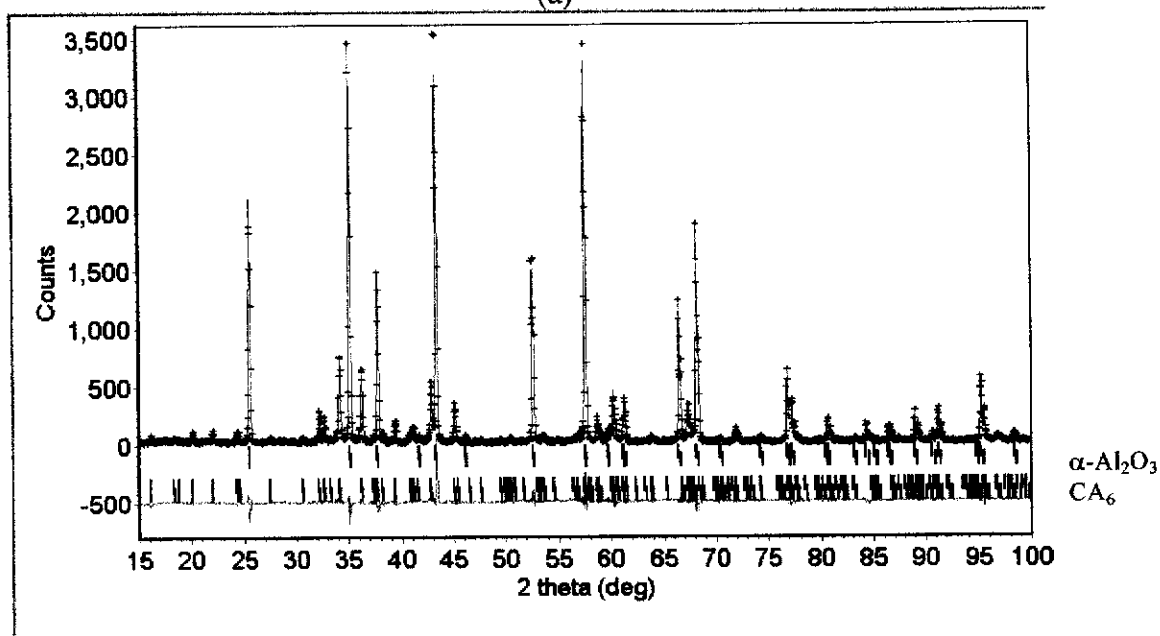


(b)

Figure B.16. XRD Rietveld difference plots for FGM sample at (a) 2 mm and (b) 3 mm depths. The observed data are shown by a (+) sign, and the calculated data by a solid line. Vertical line represents the positions of diffraction lines of $\alpha\text{-Al}_2\text{O}_3$ and CA_6 . The green line below the vertical line is the difference profile.



(a)



(b)

Figure B.17. XRD Rietveld difference plots for FGM sample at (a) 4 mm and (b) 6 mm depths. The observed data are shown by a (+) sign, and the calculated data by a solid line. Vertical line represents the positions of diffraction lines of α - Al_2O_3 and CA_6 . The green line below the vertical line is the difference profile.

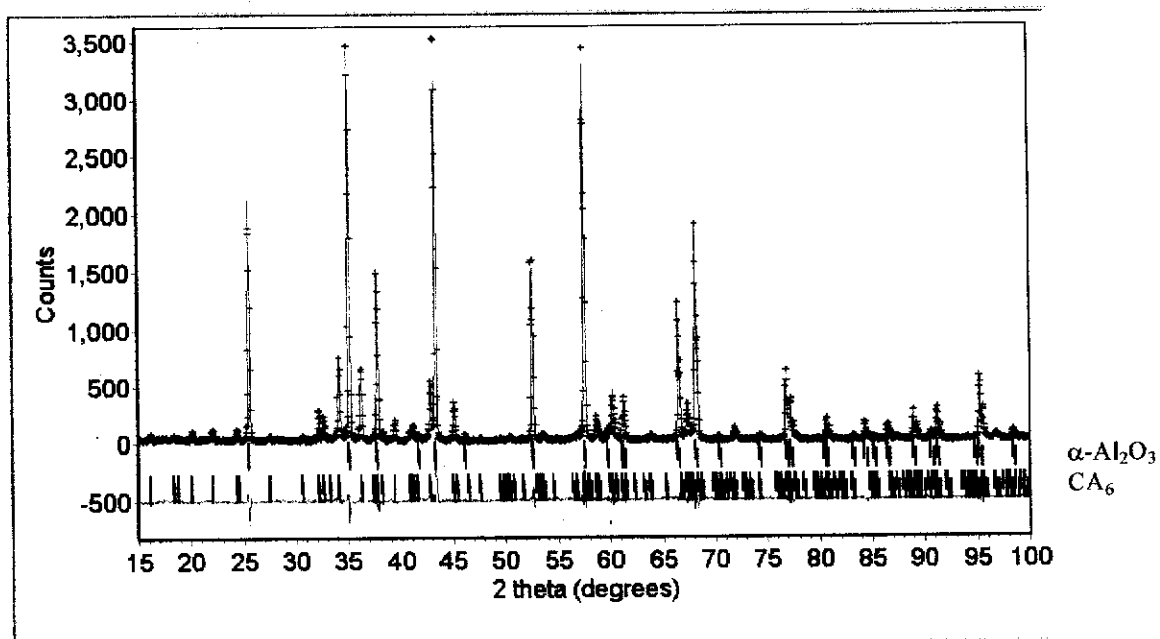
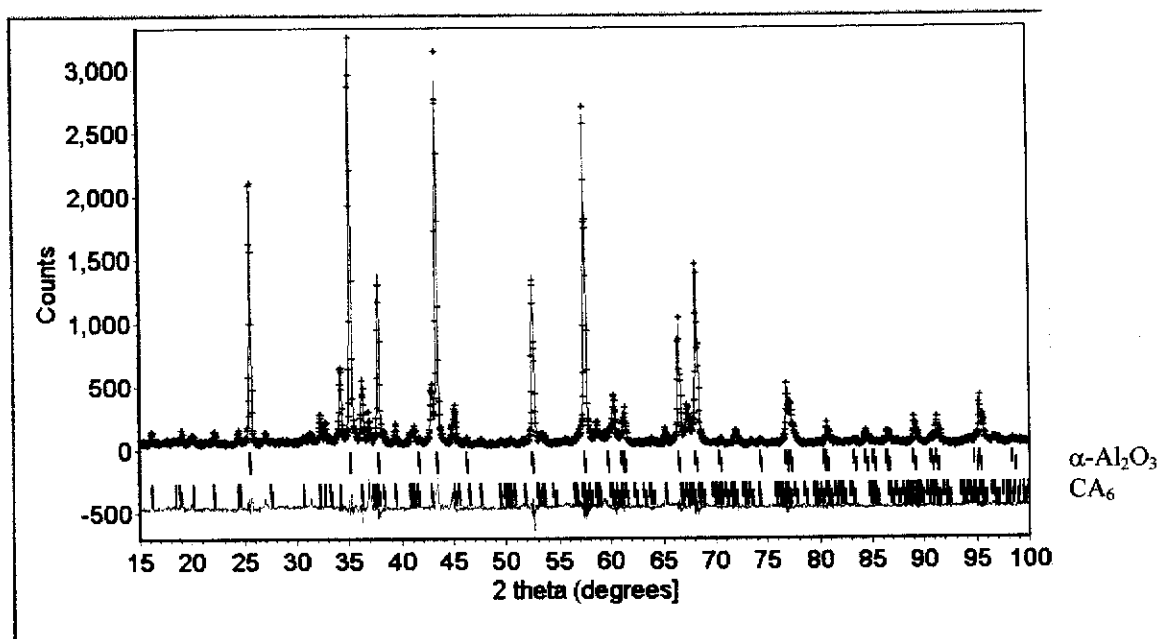
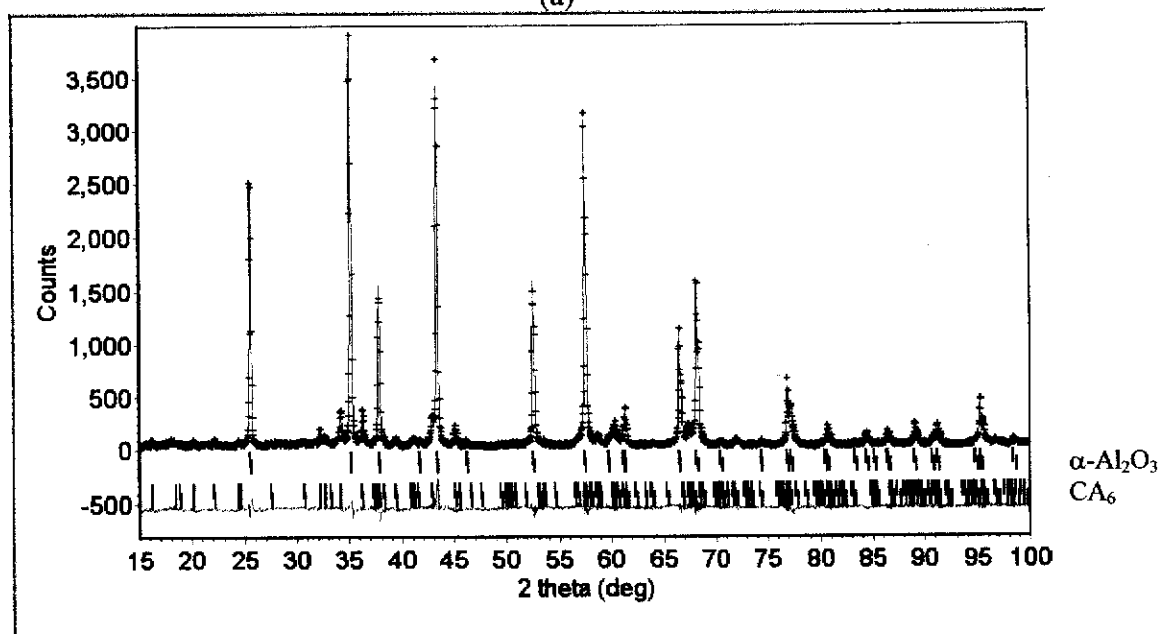


Figure B.18. XRD Rietveld difference plots for FGM sample at 8 mm depth. The observed data are shown by a (+) sign, and the calculated data by a solid line. Vertical line represents the positions of diffraction lines of $\alpha\text{-Al}_2\text{O}_3$ and CA_6 . The green line below the vertical line is the difference profile.



(a)



(b)

Figure B.19. XRD Rietveld difference plots for the FGM obtained by the slicing method for layer 1 (0–2 mm) in (a) and layer 3 (4–6 mm) in (b). The observed data are shown by a (+) sign, and the calculated data by a solid line. Vertical line represents the positions of diffraction lines of α - Al_2O_3 and CA_6 . The green line below the vertical line is the difference profile.

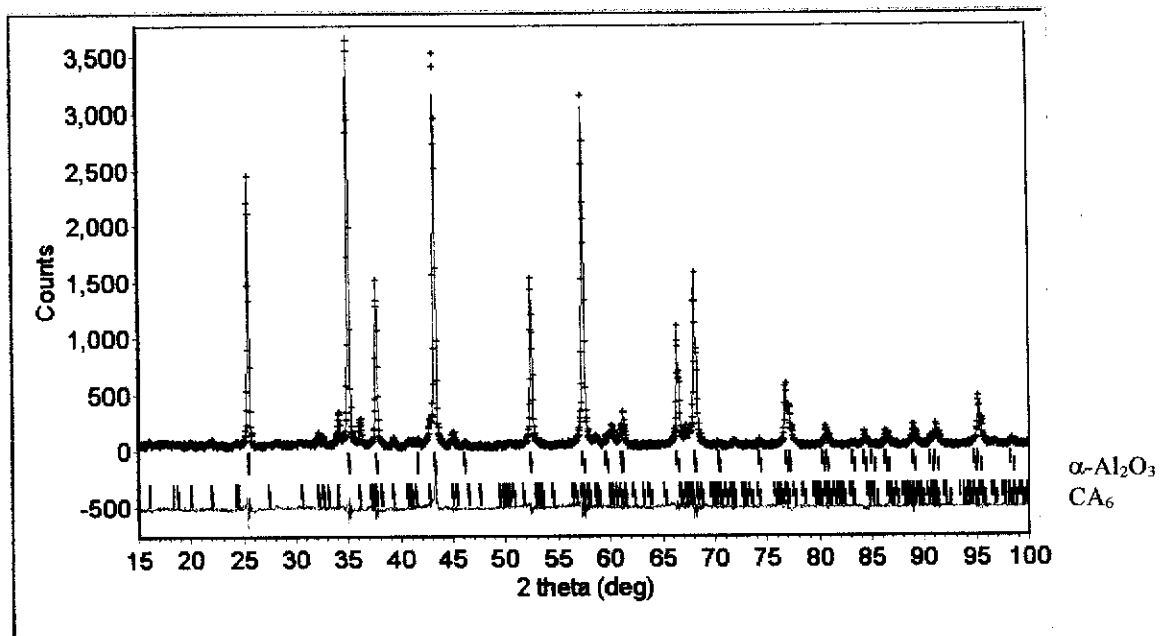
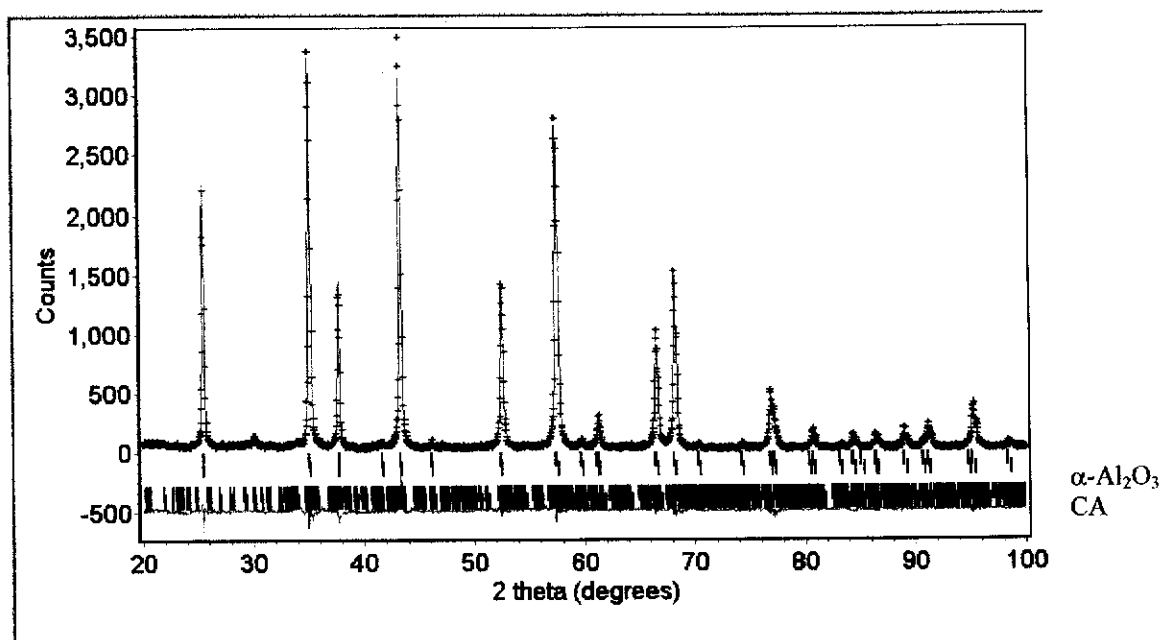
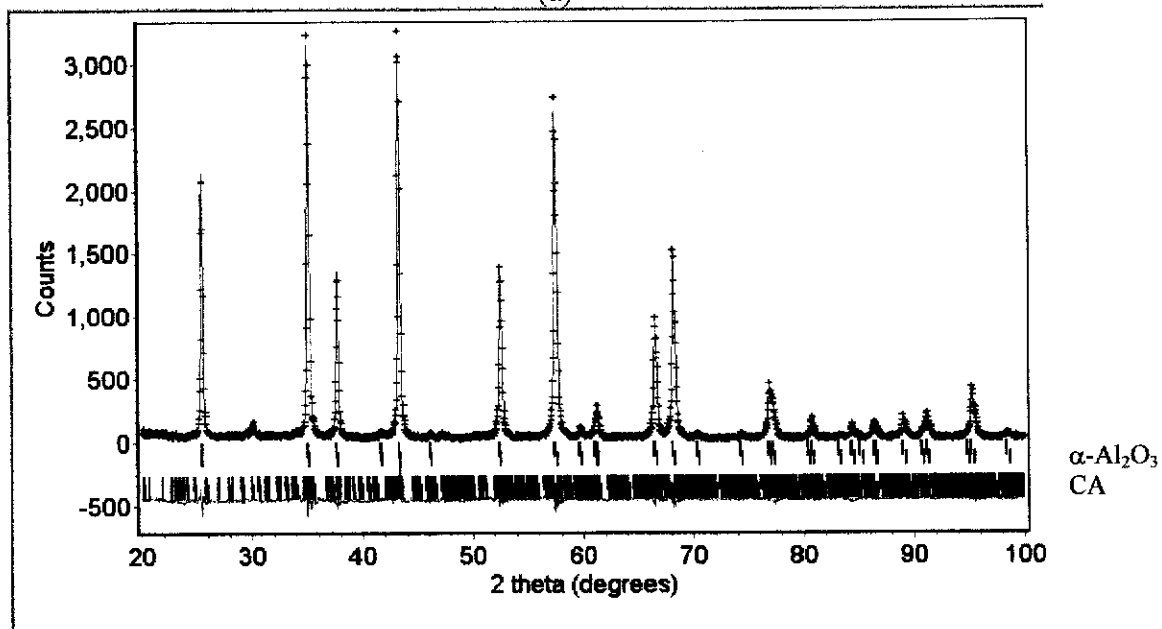


Figure B.20. XRD Rietveld difference plots for the FGM obtained by slicing method for layer 1 (0–2 mm) in (a) and layer 3 (4–6 mm) in (b). The observed data are shown by a (+) sign, and the calculated data by a solid line. Vertical line represents the positions of diffraction lines of $\alpha\text{-Al}_2\text{O}_3$ and CA_6 . The green line below the vertical line is the difference profile.

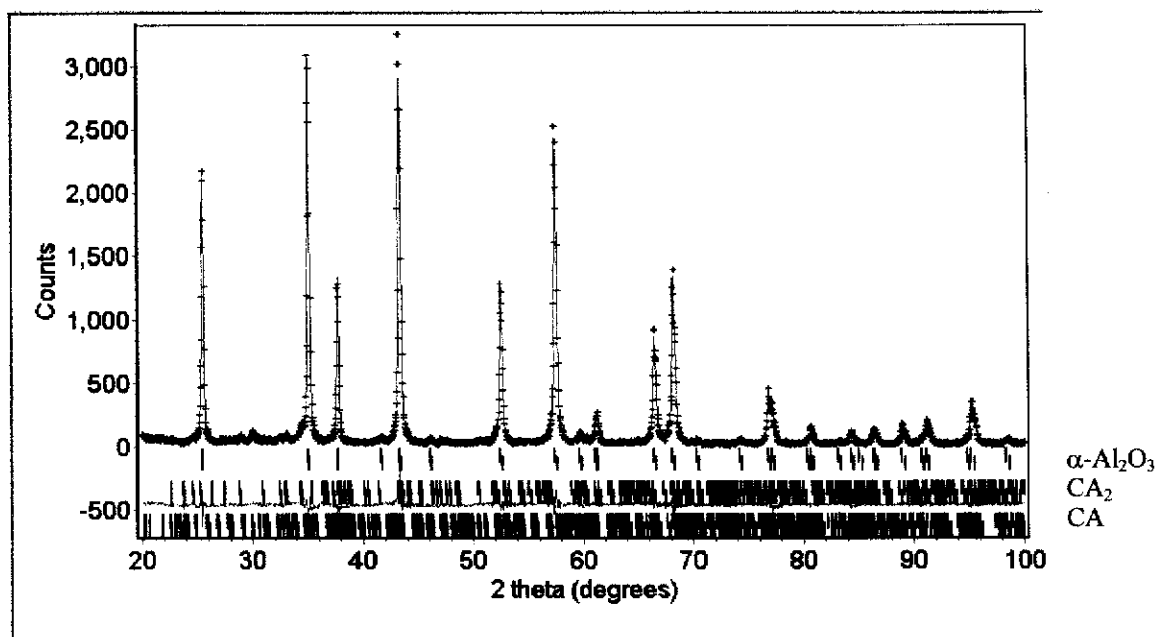


(a)

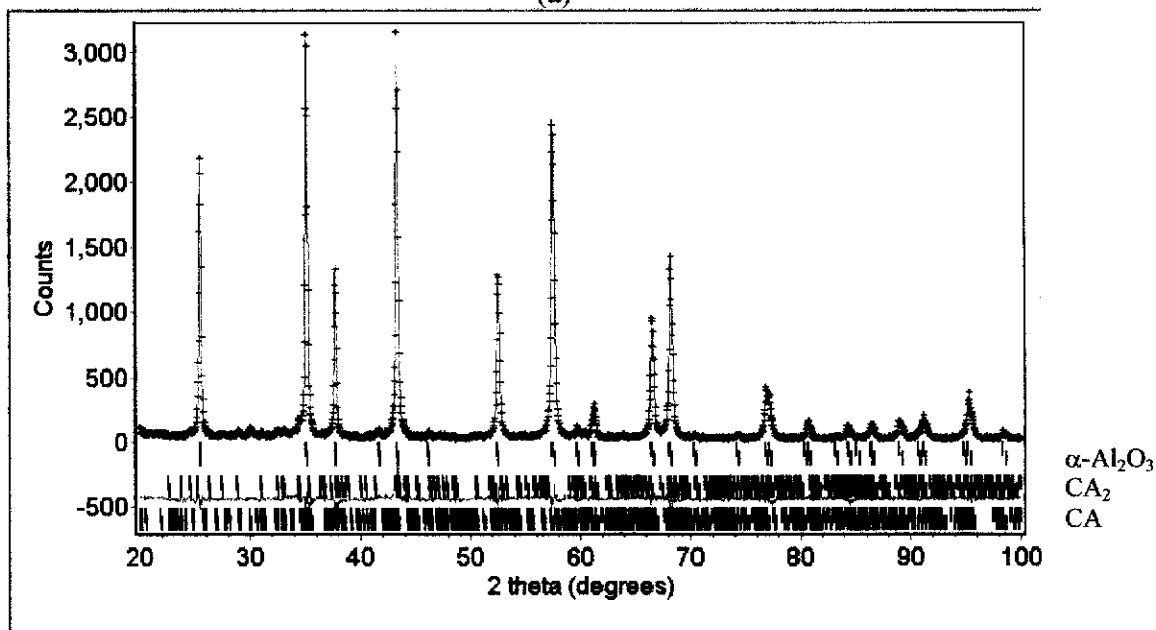


(b)

Figure B.21. XRD Rietveld difference plots for the functionally-graded A/CA₆ composite at 1100 °C in (a) and 1200 °C in (b). The observed data are shown by a (+) sign, and the calculated data by a solid line. Vertical line represents the positions of diffraction lines of $\alpha\text{-Al}_2\text{O}_3$ and CA. The green line below the vertical line is the difference profile.



(a)



(b)

Figure B.22. XRD Rietveld difference plots for the functionally-graded A/CA₆ composite at 1300 °C in (a) and 1350 °C in (b). The observed data are shown by a (+) sign, and the calculated data by a solid line. Vertical line represents the positions of diffraction lines of α -Al₂O₃, CA₂ and CA. The green line below the vertical line is the difference profile.

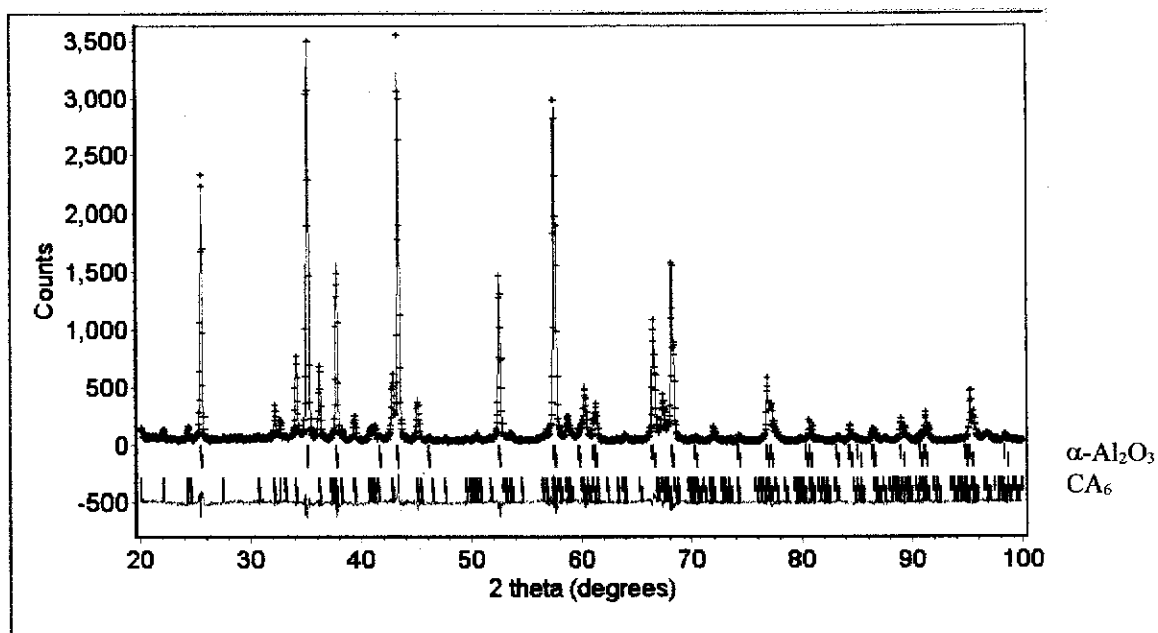
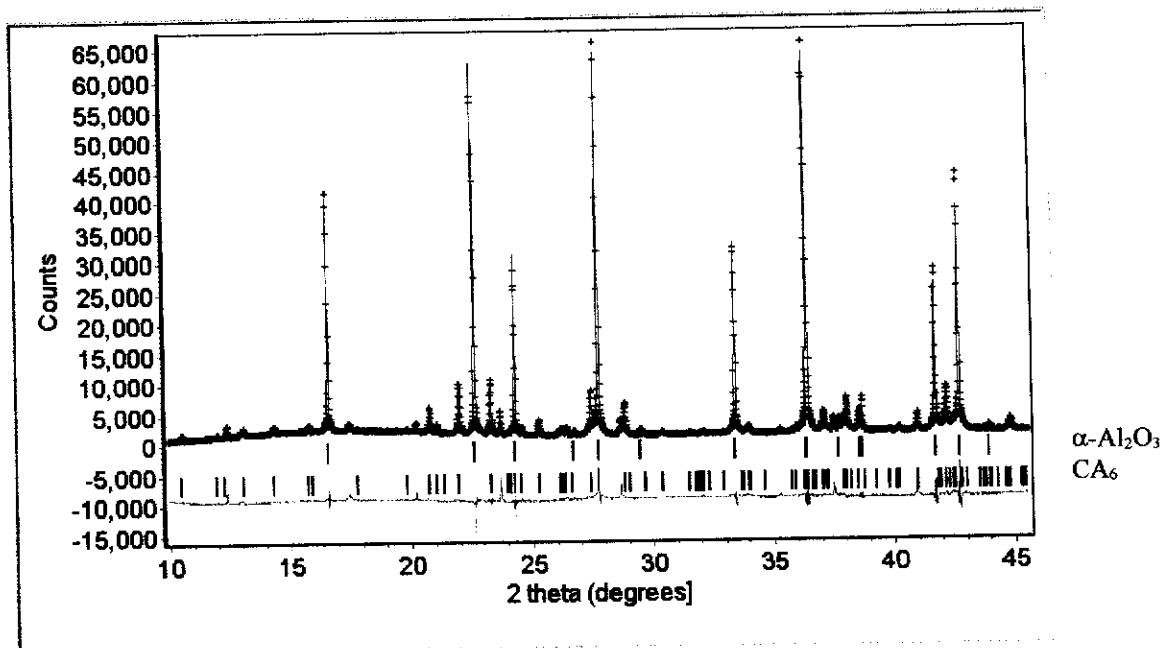
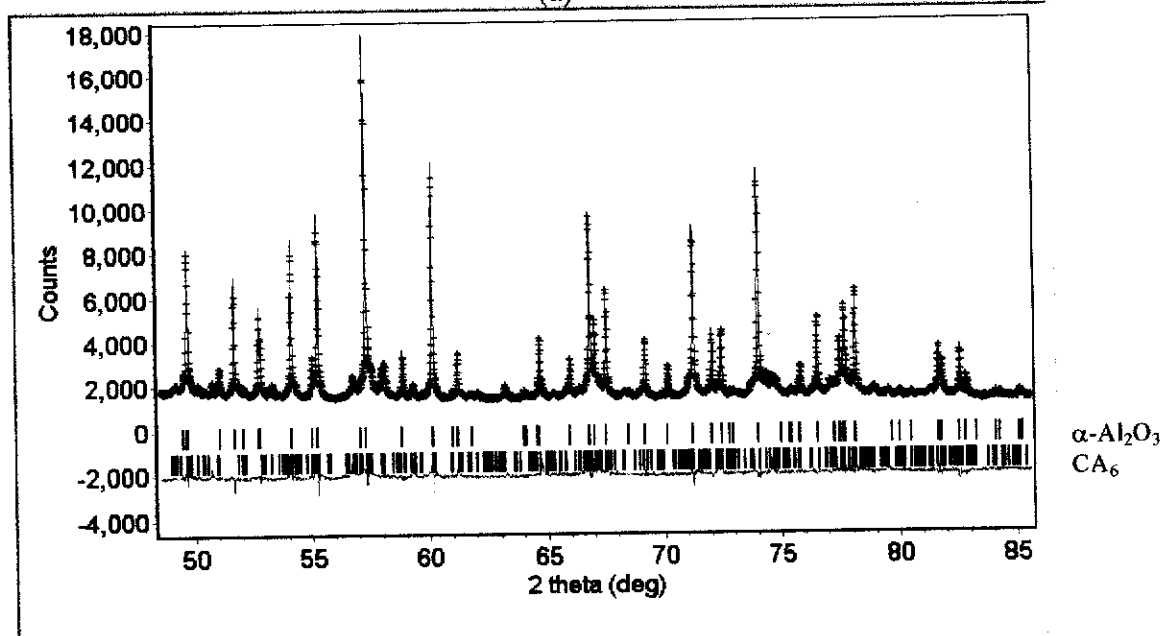


Figure B.23. XRD Rietveld difference plots for the functionally-graded A/CA₆ composite at 1650 °C. The observed data are shown by a (+) sign, and the calculated data by a solid line. Vertical line represents the positions of diffraction lines of α -Al₂O₃ and CA₆. The green line below the vertical line is the difference profile.

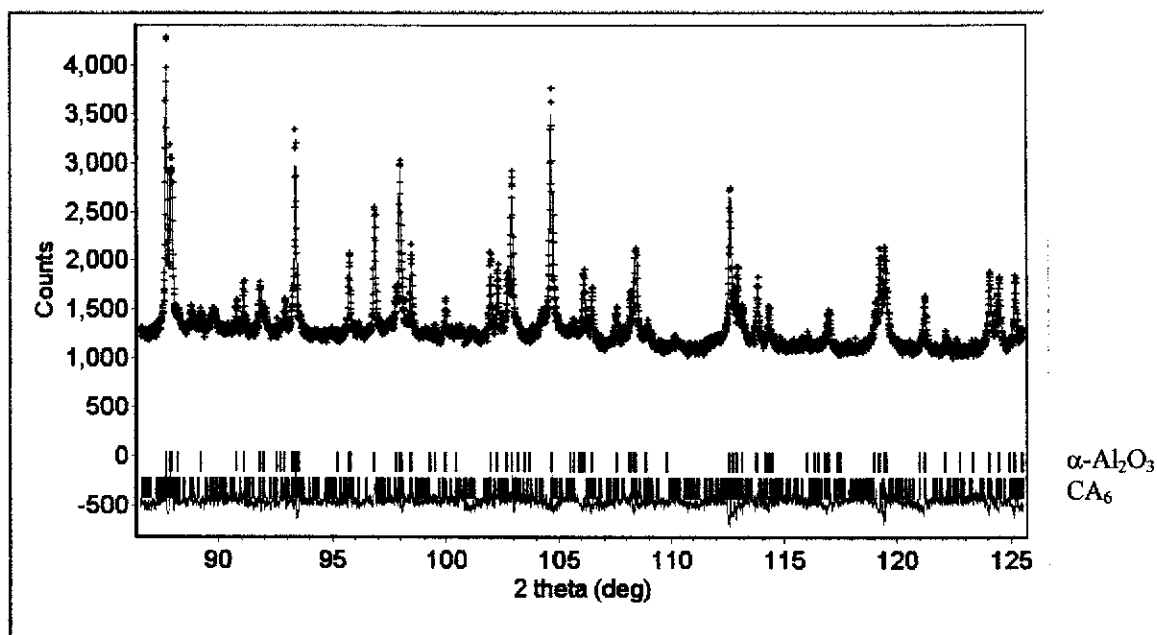


(a)

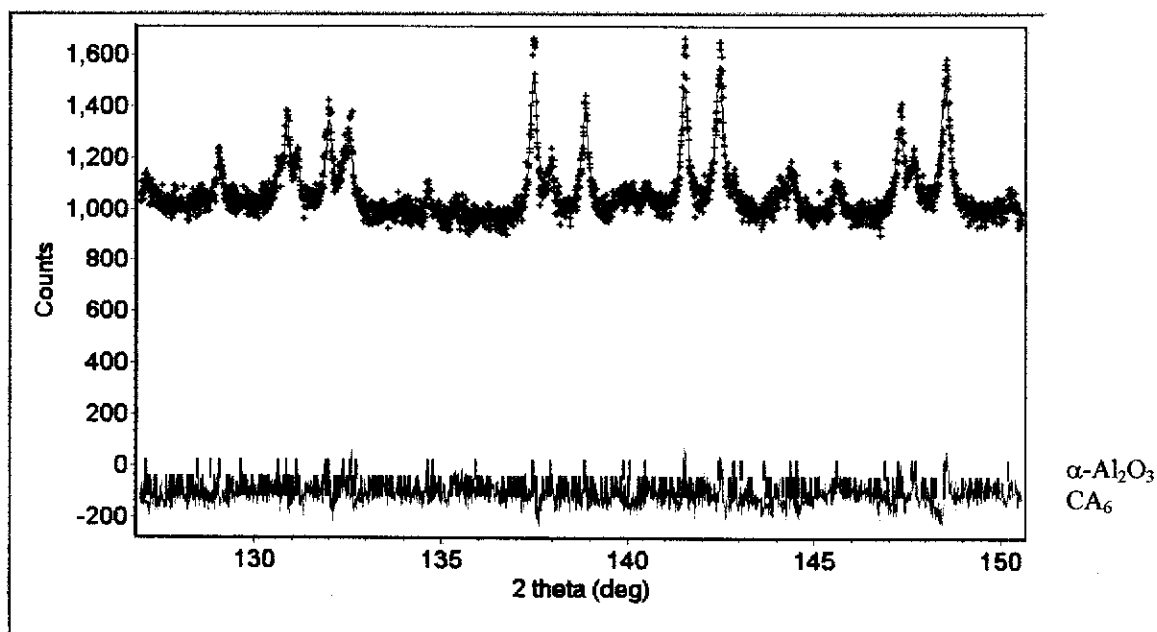


(b)

Figure B.24. SRD Rietveld difference plots for layer 1 of functionally-graded A/CA₆ composite: (a) imaging plate 1 and (b) imaging plate 2. The observed data are shown by a (+) sign, and the calculated data by a solid line. Vertical line represents the positions of diffraction lines of α -Al₂O₃ and CA₆. The green line below the vertical line is the difference profile.

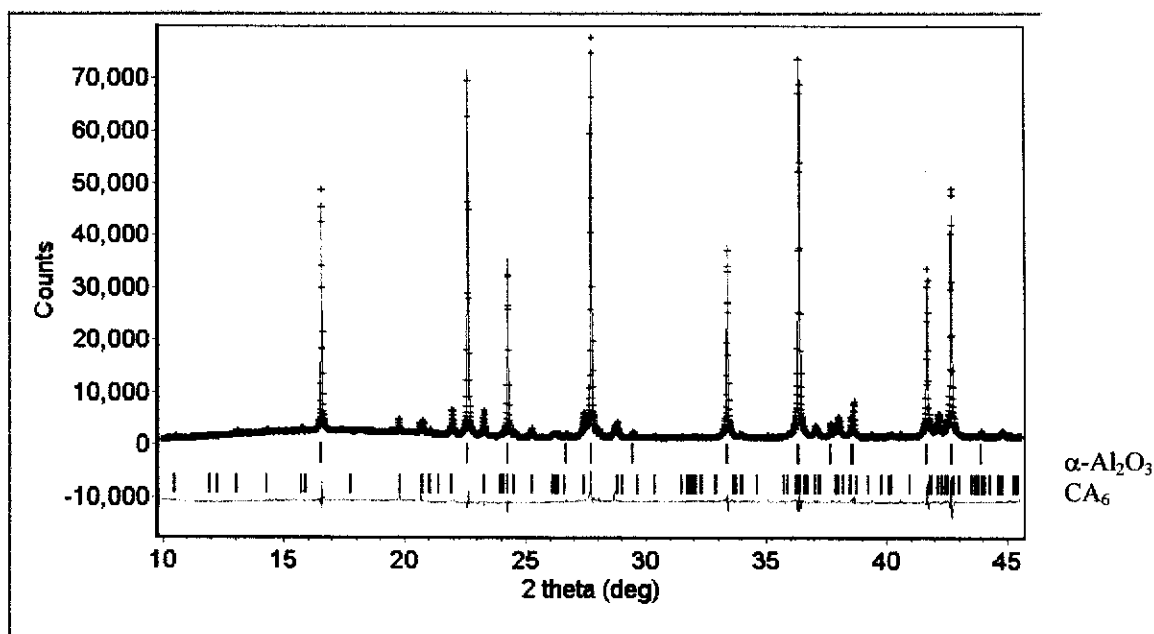


(a)

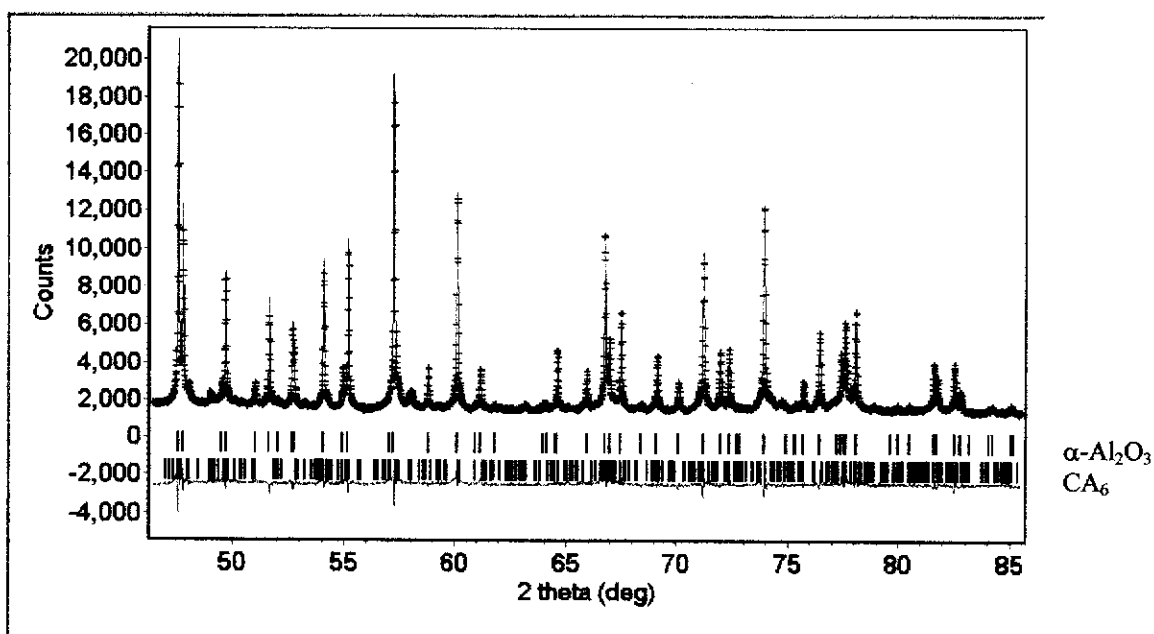


(b)

Figure A2.24. (Continued) SRD Rietveld difference plots for layer 1 of functionally-graded A/CA₆ composites: (a) imaging plate 3 and (b) imaging plate 4. The observed data are shown by a (+) sign, and the calculated data by a solid line. Vertical line represents the positions of diffraction lines of α -Al₂O₃ and CA₆. The green line below the vertical line is the difference profile.

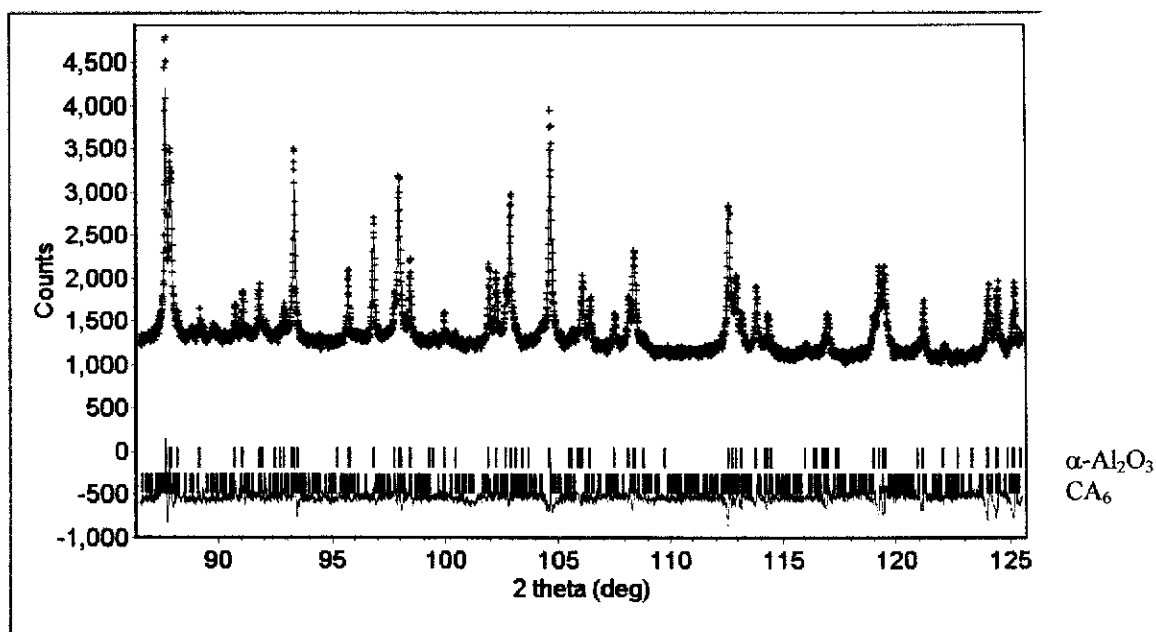


(a)

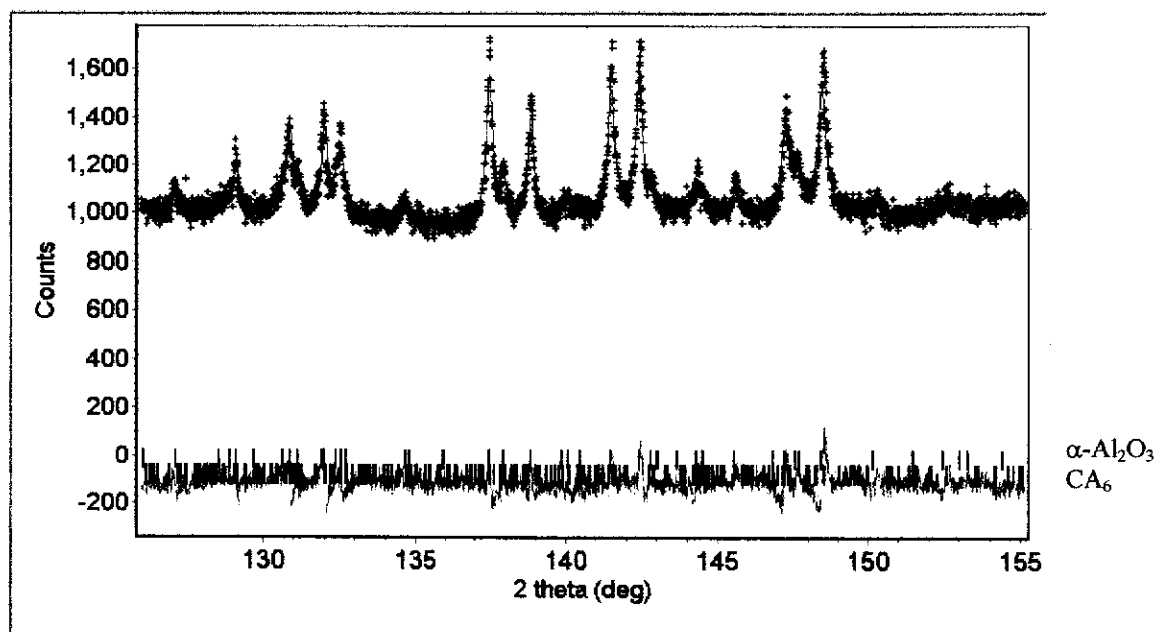


(b)

Figure B.25. SRD Rietveld difference plots for layer 2 of functionally-graded A/CA₆ composite: (a) imaging plate 1 and (b) imaging plate 2. The observed data are shown by a (+) sign, and the calculated data by a solid line. Vertical line represents the positions of diffraction lines of $\alpha\text{-Al}_2\text{O}_3$ and CA₆. The green line below the vertical line is the difference profile.

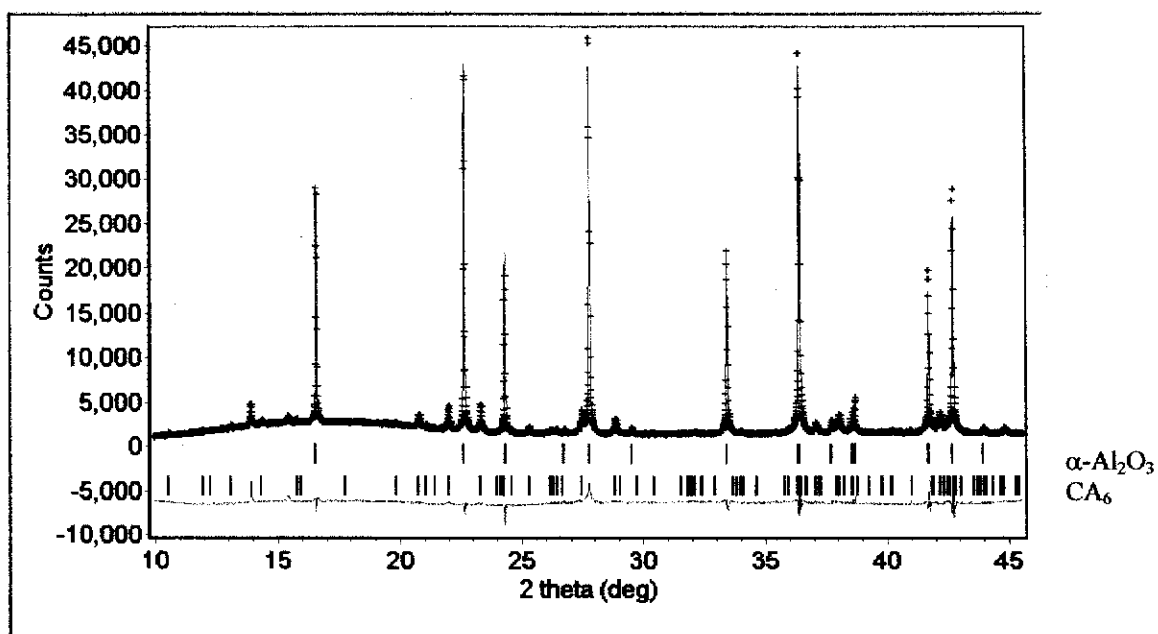


(a)

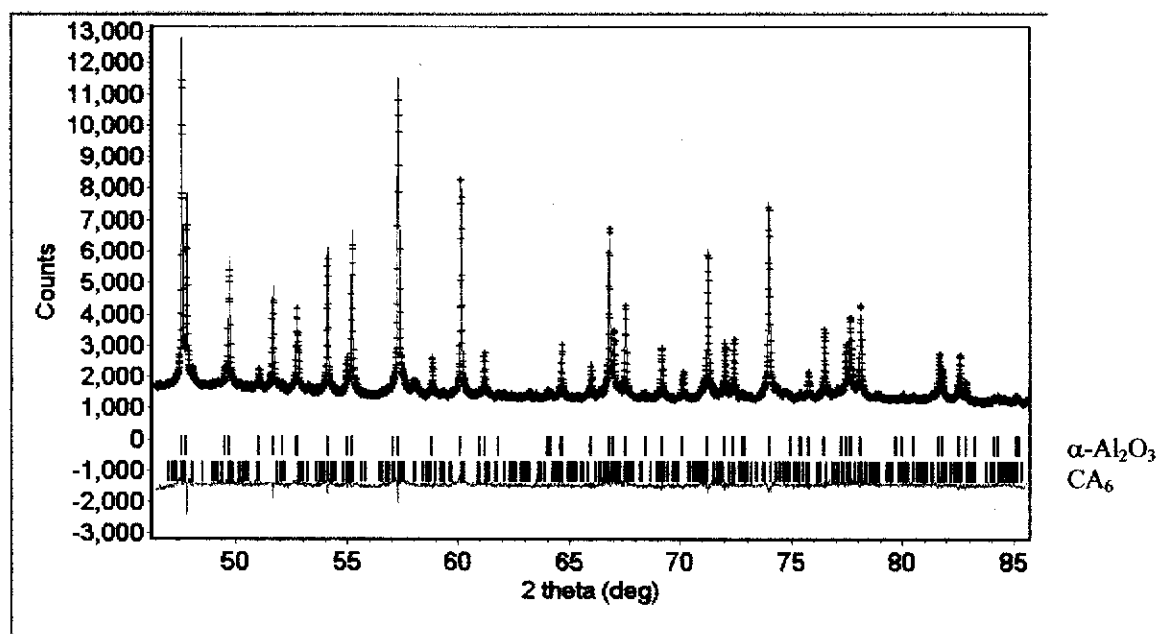


(b)

Figure B.25. (Continued) SRD Rietveld difference plots for layer 2 of functionally-graded A/CA₆ composite: (a) imaging plate 3 and (b) imaging plate 4. The observed data are shown by a (+) sign, and the calculated data by a solid line. Vertical line represents the positions of diffraction lines of α -Al₂O₃ and CA₆. The green line below the vertical line is the difference profile.

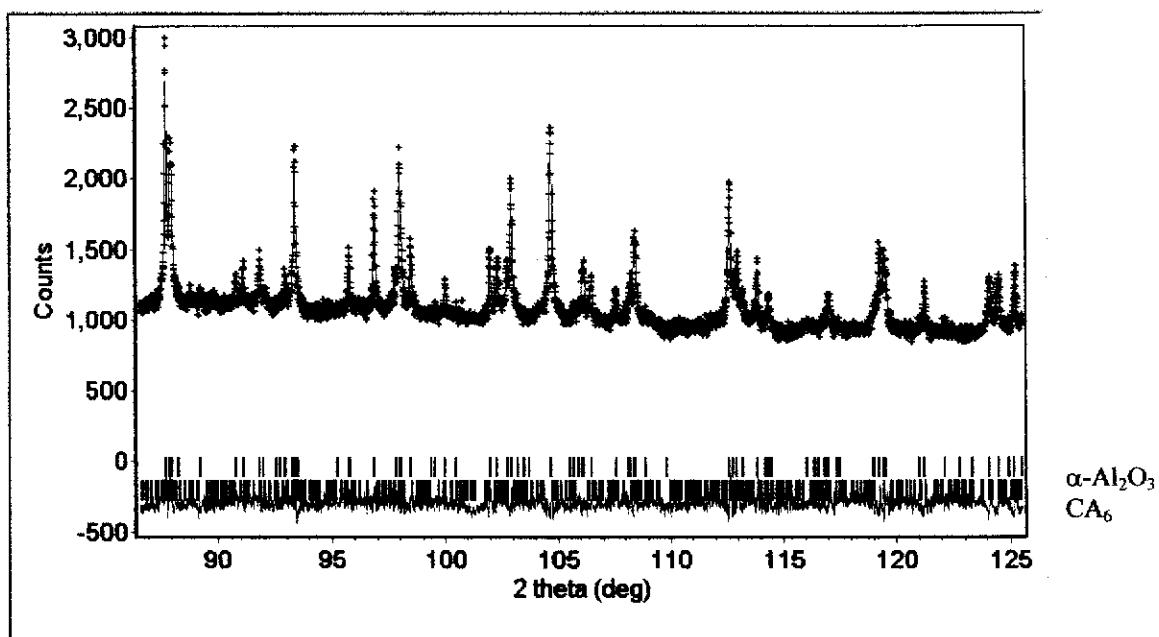


(a)

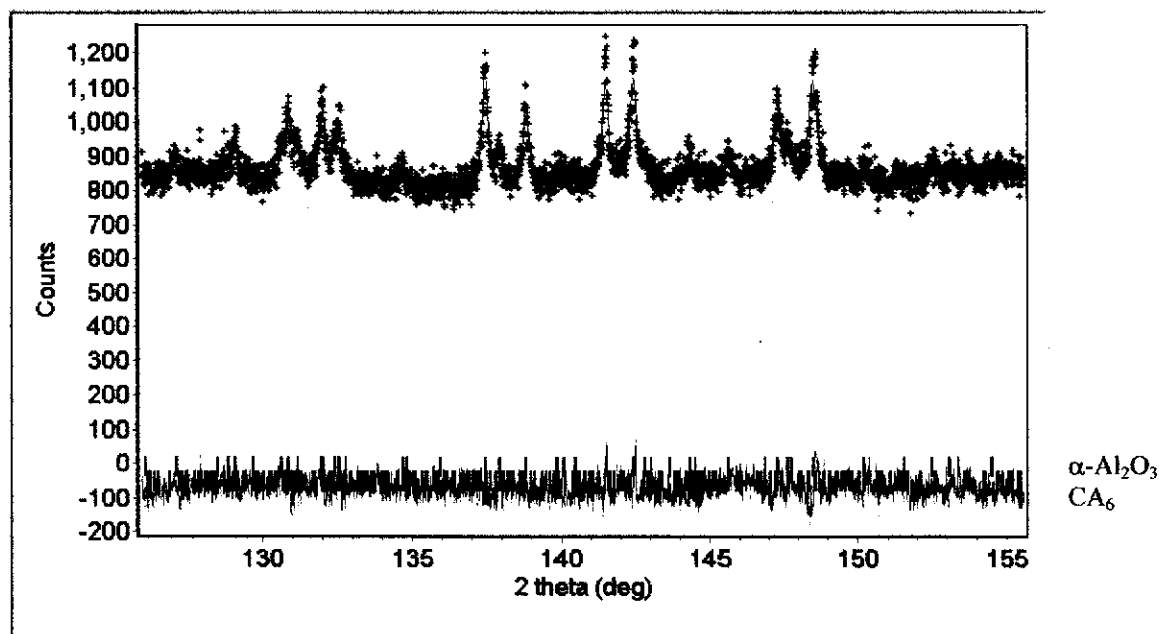


(b)

Figure B.26. SRD Rietveld difference plots for layer 3 of functionally-graded A/CA₆ composite: (a) imaging plate 1 and (b) imaging plate 2. The observed data are shown by a (+) sign, and the calculated data by a solid line. Vertical line represents the positions of diffraction lines of α -Al₂O₃ and CA₆. The green line below the vertical line is the difference profile.

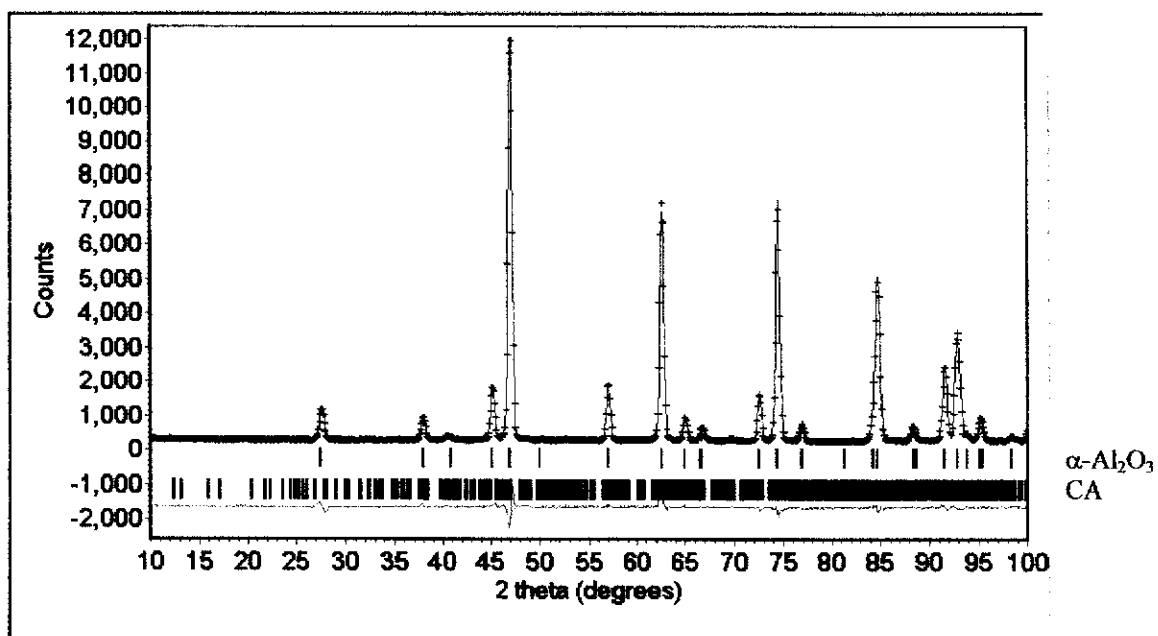


(a)

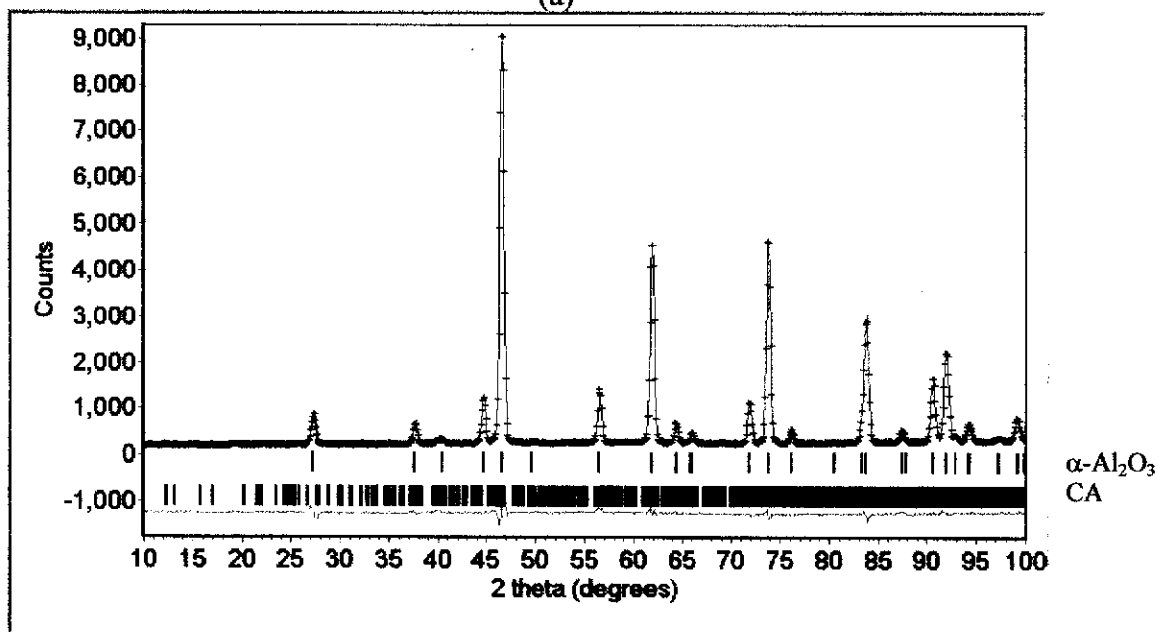


(b)

Figure B.26. (Continued) SRD Rietveld difference plots for layer 3 of functionally graded A/CA₆ composite: (a) imaging plate 3 and (b) imaging plate 4. The observed data are shown by a (+) sign, and the calculated data by a solid line. Vertical line represents the positions of diffraction lines of α -Al₂O₃ and CA₆. The green line below the vertical line is the difference profile.

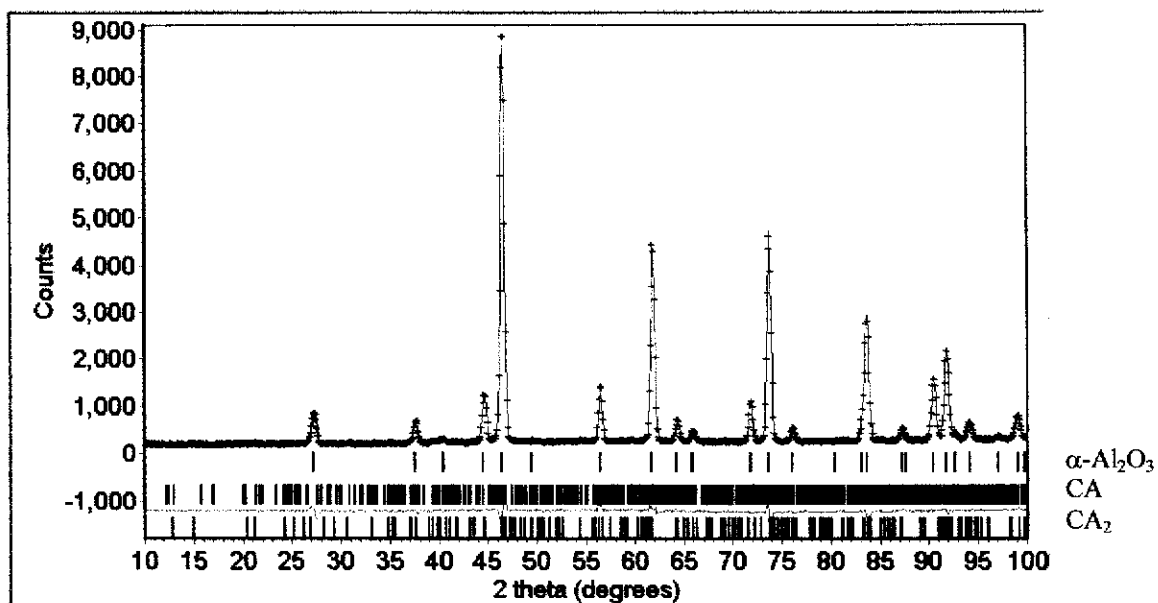


(a)

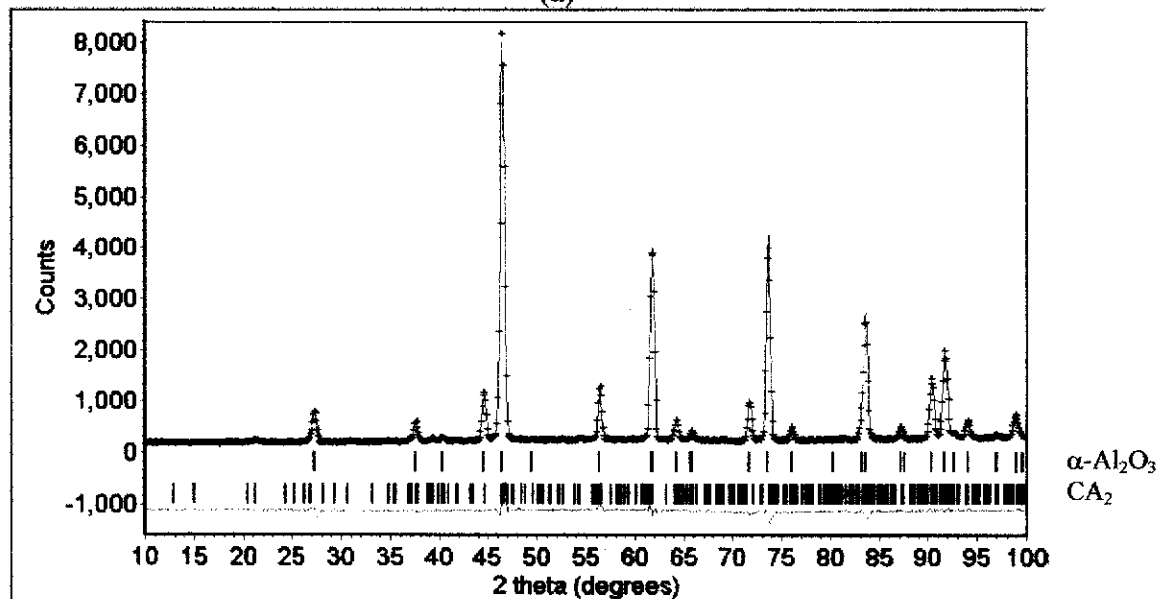


(b)

Figure B.27. HTND Rietveld difference plots for the functionally-graded A/CA₆ composite at RT in (a) and 1100 °C in (b). The observed data are shown by a (+) sign, and the calculated data by a solid line. Vertical line represents the positions of diffraction lines of α -Al₂O₃ and CA. The green line below the vertical line is the difference profile.



(a)



(b)

Figure B.28. HTND Rietveld difference plots for the functionally-graded A/CA₆ composite at 1200 in (a) and 1300 °C in (b). The observed data are shown by a (+) sign, and the calculated data by a solid line. Vertical line represents the positions of diffraction lines of α -Al₂O₃, CA and CA₂ in (a) and α -Al₂O₃ and CA₂ in (b). The green line below the vertical line is the difference profile.

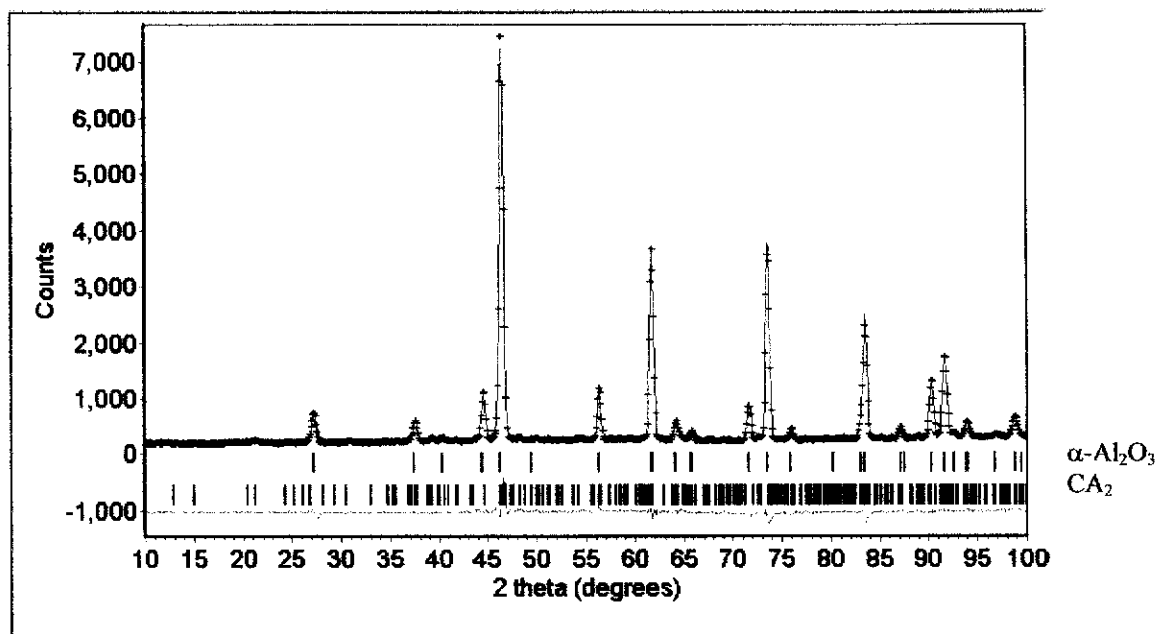


Figure B.29. HTND Rietveld difference plots for the functionally-graded A/CA₆ composite at 1350 °C. The observed data are shown by a (+) sign, and the calculated data by a solid line. Vertical line represents the positions of diffraction lines of $\alpha\text{-Al}_2\text{O}_3$ and CA₂. The green line below the vertical line is the difference profile.